
Technische Universität Kaiserslautern

Fachbereich Chemie

SPIN AND ORBITAL CONTRIBUTIONS TO THE MAGNETIC MOMENT OF TRANSITION METAL CLUSTERS AND COMPLEXES

Am Fachbereich Chemie der Technischen Universität Kaiserslautern zur Erlangung des akademischen Grades "Doktor der Naturwissenschaften" genehmigte

Dissertation
(D386)

vorgelegt von
Dipl.-Chem. Jennifer Meyer

Betreuer: Prof. Dr. G. Niedner-Schatteburg

Tag der wissenschaftlichen Aussprache: 10. Juli 2014
Technische Universität Kaiserslautern

Der experimentelle Teil der vorliegenden Arbeit wurde in der Zeit von November 2009 bis April 2014 im Fachbereich Chemie der Technischen Universität Kaiserslautern unter der Betreuung von Prof. Dr. G. Niedner-Schatteburg angefertigt.

Datum des Antrags der Eröffnung des Promotionsverfahrens: 07.05.2014

Tag der wissenschaftlichen Aussprache: 10.07.2014

Promotionskommission:

Vorsitzender Prof. Dr. W. Thiel

1. Berichterstatter Prof. Dr. G. Niedner-Schatteburg

2. Berichterstatter Prof. Dr. M. Gerhards

für meine Familie

Magnetes Geheimnis, erklär mir das!
Kein größer Geheimnis als Lieb' und Hass.

The magnet's mystery, explain that to me!
No greater mystery but love and hate.

Johann Wolfgang von Goethe

CONTENT

1. Introduction	1
1.1 References.....	4
2. Theoretical background	11
2.1 Classification of magnetic materials.....	11
2.1.1 Diamagnetism.....	12
2.1.2 Paramagnetism.....	12
2.1.3 Collective magnetism.....	13
2.1.3.1 Ferromagnetism.....	14
2.1.3.2 Ferrimagnetism.....	14
2.1.3.3 Antiferromagnetism.....	14
2.2 Magnetism of 3d transition metals.....	15
2.2.1 Magnetic domains.....	18
2.3 Magnetism of nanoparticles and clusters.....	19
2.3.1 Superparamagnetic ensemble.....	19
2.3.2 Magnetic moment of free clusters.....	20
2.3.2.1 The Stern-Gerlach experiment.....	20
2.3.2.2 Enhanced magnetic moments in small clusters.....	22
2.4 X-ray magnetic circular dichroism (XMCD).....	23
2.4.1 X-ray absorption.....	23
2.4.2 Dipole selection rules.....	26
2.4.3 Origin of the x-ray magnetic circular dichroism (XMCD) effect.....	27
2.4.4 Sum rules.....	30
2.4.4.1 Intensity sum rule.....	30
2.4.4.2 Spin and orbital sum rule.....	32
2.4.5 Summary of the XMCD effect.....	33
2.5 References.....	34
3. Experimental methods - the GAMBIT setup	37
3.1 Experimental setup.....	38

3.1.1	Laser vaporization source.....	38
3.1.2	Fourier Transform - Ion Cyclotron Resonance (FT-ICR) mass spectrometry.....	39
3.1.3	FT-ICR mass spectrometer with cryogenic trap.....	42
3.1.4	Synchrotron radiation.....	44
3.1.5	Total Ion Yield spectroscopy of isolated clusters.....	46
3.1.6	Collisional cooling.....	49
3.2	Data acquisition & analysis.....	51
3.2.1	Data acquisition.....	51
3.2.2	Data analysis.....	56
3.2.3	Application of sum rules.....	56
3.2.4	Scaling of experimental magnetic moments.....	59
3.3	References.....	64
3.4	Supplement.....	67
3.4.1	Publication - J. Electron Spectroscopy and related Phenomena, 2011, 184, 113.....	67
3.4.1.0	Abstract.....	68
3.4.1.1	Introduction.....	69
3.4.1.2	Experimental setup.....	70
3.4.1.3	Results and discussion.....	74
3.4.1.4	Summary.....	79
3.4.1.5	Acknowledgement.....	80
3.4.1.6	References.....	80
3.4.2	Draft - J. Electron Spectroscopy and related Phenomena, 2014, accepted.....	81
3.4.2.0	Abstract.....	82
3.4.2.1	Introduction.....	83
3.4.2.2	Experiment.....	84
3.4.2.3	Computational details.....	86
3.4.2.4	Results and discussion.....	87
3.4.2.5	Conclusions.....	93
3.4.2.6	Acknowledgements.....	93
3.4.2.7	References.....	93
4.	Spin and orbital magnetic moments of small cobalt clusters.....	95
4.1	Introduction.....	95
4.2	Coupling of angular moments.....	97

4.3	Comparison of experimental data with:	100
4.3.1	Theoretical data	100
4.3.2	XMCD experiments	102
4.3.3	Stern-Gerlach experiments	103
4.4	References	104
4.5	Supplement - Publication - Phys. Rev. Lett. 2011, 107, 233401	110
4.5.0	Abstract	110
4.5.1	Letter / Content	111
4.5.2	References	118
4.5.3	Supplementary material	120
4.5.3.1	S1 Experimental setup	120
4.5.3.2	S2 Magnetic moments of Co _N clusters	121
4.5.3.3	S3 Langevin scaling factors	122
5.	Spin and orbital magnetic moments of small clusters of the ferromagnetic 3d elements	123
5.1	Introduction	123
5.2	Nickel clusters	125
5.2.1	Spin and orbital magnetic moments of small nickel clusters	125
5.2.2	Comparison of experimental data with:	126
5.2.2.1	Theoretical data	126
5.2.2.2	XMCD experiments	129
5.2.2.3	Stern-Gerlach experiments	130
5.3	Iron clusters	130
5.3.1	Spin and orbital magnetic moments of small iron clusters	130
5.3.2	Comparison of experimental data with:	131
5.3.2.1	Theoretical data	131
5.3.2.2	XMCD experiments	133
5.3.2.3	Stern-Gerlach experiments	134
5.4	References	135
5.5	Supplement - Draft - J. Chem. Phys., 2014, in preparation	140
5.5.0	Abstract	141
5.5.1	Introduction	142
5.5.2	Experimental methods	144
5.5.3	Results and discussion	146

5.5.3.1	Magnetic moments of cobalt clusters.....	146
5.5.3.2	Magnetic moments of iron clusters.....	148
5.5.3.3	Magnetic moments of nickel clusters.....	149
5.5.3.4	Scaling laws of the spin and orbital contributions to the magnetic moments Fe_n^+ , Co_n^+ and Ni_n^+ clusters?.....	152
5.5.4	Summary and outlook.....	156
5.5.5	Acknowledgement.....	157
5.5.6	Appendix.....	157
5.5.8	References.....	157
5.5.9	Supplementary material.....	158
5.5.9.1	S1 Application of scaling laws.....	158
5.5.9.2	S2 Comparison of spin and orbital magnetic moments of XMCD experiments.....	159
5.5.9.3	S3 Numerical values of spin and orbital magnetic moments.....	160
6.	Single Molecule Magnets.....	163
6.1	Introduction.....	163
6.2	Experimental methods.....	166
6.2.1	Electrospray ionization (ESI).....	166
6.2.1.1	ESI process.....	166
6.2.1.2	ESI source.....	167
6.2.2	ClusterNanoTrap.....	168
6.3	$[Fe_4Ln_2]$ Single Molecule Magnets.....	170
6.3.1	X-ray absorption spectra of $[Fe_4Tb_2]^+$ and $[Fe_4Gd_2]^+$	171
6.4	References.....	174
7.	Summary & outlook.....	183
7.1	References.....	187
8.	Zusammenfassung & Ausblick.....	189
8.1	References.....	194
A.	Appendix.....	A.1
A.1	Theoretical background.....	A.1
A.1.1	Spectroscopic splitting factor g & magnetomechanical ratio g'	A.1
A.1.2	References.....	A.2

A.2	Experimental methods - the GAMBIT setup.....	A.3
A.2.1	Total Ion Yield spectroscopy of isolated clusters.....	A.3
A.2.2	Collisional cooling.....	A.5
A.2.3	Scaling of experimental magnetic moments.....	A.8
A.3	List of symbols.....	A.21
A.4	List of publications & conference contributions.....	A.27
A.4.1	Publications.....	A.27
A.4.2	Conference contributions.....	A.27
A.4.2.1	Talks.....	A.27
A.4.2.2	Poster presentations.....	A.28
A.5	Danke.....	A.31
A.6	Curriculum Vitae.....	A.33

ACRONYMS & ABBREVIATIONS

APPLE2	advanced p lanar p olarized l ight e mitter
API	a tmospheric p ressure ionization
BESSY	B erliner E lektronenspeicherring Gesellschaft für S ynchrotronstrahlung.
BESSY II	synchrotron radiation facility, Berlin Adlershof
bcc	b ody c entered c ubic
CRM	c harge r esidue m odel
DFT	d ensity f unctional t heory
Hdpm	d ipivalonyl m ethane
HF-EPR	H igh F requency E lectron P aramagnetic R esonance
EELS	e lectron e nergy l oss s pectroscopy
ESI	e lectrospray ionization
Fe ₈	Single Molecule Magnet; [Fe ₈ O ₂ (OH) ₁₂ (tacn) ₆]Br ₂
Fe ₄	Single Molecule Magnet; [Fe ₄ (L) ₂ (dpm) ₆] H ₃ L = 11-(acetythio)-2,2-bis(hydroxymethyl)undecan-1-ol
[Fe ₄ Ln ₂]	[Fe ₄ Ln ₂ (N ₃) ₄ (Htea) ₄ (piv ₆)]
fcc	f ace c entered c ubic
FDM	f inite d ifference m ethod
FMR	f erromagnetic resonance
FMS	f ull m ultiple s cattering
FT-ICR	F ourier T ransform - I on C yclotron R esonance
GAMBIT	G eneralized A bstraction of M agnetic Moments at B ESSY by I on T rapping
GGA	g eneralized g radient a pproximation
GMR	G iant M agnetoresistance
GV	G eneral V alve
HBL	h exagonal b ilayer
HZB	H elmholtz- Z entrum B erlin für M aterialien und E nergie
hcp	h exagonal c losed p acked
hs	h igh s pin
horz. pol.	h orizontally p olarized photons
ico	i cosahedra
IEM	i on e vaporation m odel

IP	ionization p otential
KIT	K arlsruher Institute of T echnology
Ln	lanthanide
LVap	L aser V aporization source
Mn ₁₂ -ac	Single Molecule Magnet; [Mn ₁₂ O ₁₂ (CH ₃ COO) ₁₆ (H ₂ O) ₄]
neg. circ.	n egatively c ircularly polarized photons
PGM	p lane g rating m onochromator
pos. circ.	p ositively c ircularly polarized photons
Hpiv	p ivalic a cid
RF	r adio f requency
RT	r oom t emperature
SMM	S ingle M olecule M agnet
SOC	s pin o rbit c oupling
SQUID	S uperconduction Q uantum I nterference D evice
tacn	1,4,7-triazacyclononane
H ₃ tea	t riethanolamine
TEY	t otal e lectron y ield
TFY	t otal f luorescent y ield
TIY	t otal i on y ield
TM	t ransition m etal
ToF	t ime o f f light
UE52-PGM	soft x-ray undulator beamline at BESSY II / HZB
UHV	u ltra h igh v acuum
XAS	x -ray a bsorption s pectrum
XANES	x -ray a bsorption n ear e dges s tructure
XMCD	x -ray m agnetic c ircular d ichroism
XPS	x -ray p hotoelectron s pectroscopy

1. INTRODUCTION

Magnetism fascinates mankind since more than 2000 years. Mankind has exploited the naturally occurring magnetism of the mineral magnetite (Fe_3O_4) as "Lodstones". A "Lodstone" magnetized an iron needle to be used as an early navigation device. The first scientific description of the phenomenon "magnetism" was written by W. Gilbert "De Magnete" in 1600^[1]. With the introduction of Maxwell's equations^[2], magnetism could be described in the context of electrodynamics. The concept of magnetic fields interacting with matter still is the foundation of modern magnetism. The concept gave rise to the phenomenological classification of magnetic materials according to their interaction with magnetic fields into: dia-, para-, ferro-, ferri- or antiferromagnetic materials. Quantum mechanics introduced new concepts and continues to do so up to today. New magnetic phenomena are still discovered, e.g. the Giant Magneto Resistance (GMR)^[3,4] or the x-ray magnetic circular dichroism (XMCD) effect^[5].

Magnetism is historically a bulk phenomenon. Thus, the language and concepts describing magnetism mostly developed in the context of solid state physics with the exception of atomic magnetism. The concept of magnetism in solid state physics is based on three pillars^[6]:

- spin

The electron carries an intrinsic angular momentum called spin and additionally an angular momentum due to the electrons spatial motion (orbital angular momentum). Both contributions account for the magnetic moment of the electron.

- long range magnetic order

A strong interaction between the electrons which exceeds the magnetic dipolar interaction drives the formation of a magnetic order. In case of itinerant/band magnetism, this is the exchange interaction between the electrons coupling of the magnetic moment to the crystal lattice

The coupling results in a preferential spatial orientation of the magnetic moment (anisotropy). One microscopic origin of the anisotropy is the spin orbit coupling.

When the dimensions of a sample are reduced, long range interactions are cut off. The influences of the finite size of a system on the spin and orbital magnetic moment and the anisotropy of the system

can be significant. Therefore, magnetic properties can be tailored by controlling the dimensions of the investigated system^[6]. This "tailoring" has been applied to surfaces^[6-9], thin films^[6,9-11], multilayer systems^[6,9], atomic chains^[6,9,12]. Nanoparticles^[13-17] and clusters^[18-23] have been deposited onto numerous supports to produce new magnetic materials.

A cluster or nanoparticle is an aggregate formed of atoms or molecules. It bridges the gap between the 0D (atomic) and 3D (bulk)^[24,25]. However, a cluster is not merely a "piece" of the respective solid^[26]. Particularly in the small size range, a cluster often has individual physical^[24,25,27-34] and / or chemical properties^[35-46]. These unique features are often related to the enhanced ratio of surface to bulk atoms in a cluster or nanoparticle compared to the bulk material. The orbital magnetic moment is almost completely quenched in bulk materials due to crystal field effects. However, the small orbital contribution is central for applications as it is responsible for the magnetic anisotropy of the material, i.e. the coupling to the lattice structures. In clusters, the lower coordination at the surface sites leads to enhanced orbital and spin magnetic moments. Atomic / molecular beam methods, i.e. Stern-Gerlach experiments, of size selected clusters were able to experimentally prove enhanced magnetic moments of free clusters^[47-57]. However, the individual contributions of spin and orbit to the total magnetic moment cannot be deduced from these experiments.

Today, our understanding of the concept of magnetism is based on the spin. An experimental approach allowing us to directly determine the spin and orbital magnetic contributions to the magnetic moment is the XMCD technique. The response of the system after the absorption of circularly polarized x-rays is exploited. A dichroic effect becomes visible if the polarization dependent x-ray absorption spectra of a magnetic sample are compared, e.g. for the dipole allowed transition from the 2p \rightarrow 3d state^[58]. As the magnetic moment of the 3d transition metal (TM) ferromagnets is almost entirely due to the 3d electrons, the XMCD spectrum contains the information about the magnetic moment. The spin and orbital magnetic moments can be accessed with the help of the so called sum rule analysis^[59-62]. The understanding of a magnetic system requires the knowledge about its electronic structure on the microscopic scale. The electronic structure of a 3d TM is highly correlated and theory still does not provide reliable results. Thus, experimental data is important not only to gain a deeper understanding about the evolution of magnetism but also to further advance theory.

The study of magnetic phenomena was always closely related to applications. The deposition of nanoparticles or clusters promises new magnetic materials. The reduced coordination number at the cluster surface can play a crucial role once adsorbates^[50,63-65] or a support material^[15,17,19,20,22,66-68] are involved. A reduced coordination number leads to open coordination sites and thus empty accessible valence states. A charge transfer into empty states can alter the magnetism of the cluster. Thus, for

deposited clusters not only the support material but also its surface structure is important. The system as mentioned is complex and contains more than the sum of the individual parts. The problem is further complicated by the often insufficient knowledge about the cluster itself. Therefore, a reduction of the problem's complexity is desired. We study the isolated cluster in the gas phase without interaction with an environment^[69,70]. This way, we gain information about the cluster without uncertainties caused by the interaction with a support.

The thesis is structured into the following chapters:

A brief introduction into magnetism and the basic concepts needed to understand the presented experiments is given in Chap. 2. The chapter also includes a section on x-ray absorption spectroscopy (XAS) and the XMCD effect. The sum rule analysis used to extract the spin and orbital magnetic moments will be explained.

The experimental methods used to produce and detect the TM clusters are introduced in Chap. 3. The recording of x-ray absorption spectra via Total Ion Yield (TIY) spectroscopy and the subsequent data analysis to extract the spin and orbital magnetic moments will be explained in detail. Additional information on the validity of temperature and field correction of the experimental moments to calculate the intrinsic moments will be given.

We first studied small cobalt clusters. The results will be presented in Chap. 4. The chapter contains a section concerning the controversy about the strength of the spin orbit coupling with respect to the interaction energy with the external magnetic field. The found magnetic moments will be compared to a second XMCD experiment^[71,72], the results of Stern-Gerlach experiments and theory on neutral and cationic cobalt clusters.

The spin and orbital magnetic moments of small clusters of the ferromagnetic 3d TM iron, cobalt and nickel will be presented in Chap. 5. The results will be put into perspective regarding their relation the atomic and bulk values. Cluster properties often follow interpolations between the atomic and bulk value, so called scaling laws. The spin and orbital magnetic moment each follow an interpolation which will be discussed. The magnetic moments will be compared to available theory on neutral and cationic clusters, Stern-Gerlach data and spin and orbital magnetic moments from XMCD experiments^[71-73].

Lately, a new form of magnetism moved into the scientific focus: molecular magnetism. A single molecule with a ferromagnetic core acts like a magnetic entity. The term Single Molecule Magnet (SMM)^[74,75] has been coined for such coordination compounds. SMMs show unique quantum behavior, e.g. quantum tunneling^[76,77]. Again, the investigations of SMMs are driven by a

combination of discovering new physical phenomena^[77,78] and possible applications^[74,79-86]. SMMs have been studied by XMCD spectroscopy as crystals, powders or deposited onto various substrates^[87-95]. The investigation of SMMs in the gas phase is the next step. The molecules are truly isolated in the ultrahigh vacuum (UHV) of the mass spectrometer. We, therefore, implemented an experimental scheme to study isolated SMMs in the gas phase in cooperation with the group of T. Lau (Helmholtz Zentrum Berlin für Materialien und Energie, Berlin, Germany). A brief introduction into the concept of SMMs and the experimental approach together with first results will be given in Chap. 6. First polarization dependent XA spectra of an SMM based on iron and lanthanide ions $[\text{Fe}_4\text{Ln}_2]$ ($[\text{Fe}_4\text{Ln}_2(\text{N}_3)_4(\text{Htea})_4(\text{piv})_6]$) will be presented.

The thesis will be concluded by a summary of the presented results and an outlook on future experiments to further advance the understanding of the magnetism of finite size systems to custom design new materials.

1.1 References

- [1] GILBERT, W., *De Magnete, English translation by Fleury Mottelay*; Dover Publications: New York, **1958**.
- [2] MAXWELL, J. C., *Treatise of Electricity and Mangetism, reprint ot the 3rd edition*; Dover Publications: New York, **1954**.
- [3] BINASCH, G., GRÜNBERG, P., SAURENBACH, F., ZINN, W., *Enhanced magnetoresistance in layered magnetic structures with antiferromagnetic interlayer exchange*, Physical Review B **1989**, 39, 4828.
- [4] BAIBICH, M. N., BROTO, J. M., FERT, A., VAN DAU, F. N., PETROFF, F., ETIENNE, P., CREUZET, G., FRIEDERICH, A., CHAZELAS, J., *Giant Magnetoresistance of (001)Fe/(001)Cr Magnetic Superlattices*, Physical Review Letters **1988**, 61, 2472.
- [5] SCHÜTZ, G., WAGNER, W., WILHELM, W., KIENLE, P., ZELLER, R., FRAHM, R., MATERLIK, G., *Absorption of circularly polarized x rays in iron*, Physical Review Letters **1987**, 58, 737.
- [6] *Lecture Notes Mangetism goes Nano: Electron Correlations, Spin Transport, Molecular Mangetism*; SCHNEIDER, C. M., BLÜGEL, S., BRÜCKEL, T., Eds.; Forschungszentrum Jülich in der Helmholtz Gemeinschaft, **2005**.
- [7] BABERSCHKE, K., *The magnetism of nickel monolayers*, Appl. Phys. A **1996**, 62, 417.
- [8] TISCHER, M., HJORTSTAM, O., ARVANITIS, D., HUNTER DUNN, J., MAY, F., BABERSCHKE, K., TRYGG, J., WILLS, J. M., JOHANSSON, B., ERIKSSON, O., *Enhancement of Orbital Magnetism at Surfaces: Co on Cu(100)*, Physical Review Letters **1995**, 75, 1602.
- [9] STÖHR, J., SIEGMANN, H. C., *Magnetism - From Fundamentals to Nanoscale Dynamics*; Springer, **2006**.
- [10] BORNEMANN, S., ŠIPR, O., MANKOVSKY, S., POLESYA, S., STAUNTON, J. B., WURTH, W., EBERT, H., MINÁR, J., *Trends in the magnetic properties of Fe, Co, and Ni clusters and monolayers on Ir(111), Pt(111), and Au(111)*, Physical Review B **2012**, 86, 104436.

-
- [11] DHESI, S. S., DÜRR, H. A., VAN DER LAAN, G., DUDZIK, E., BROOKES, N. B., *Electronic and magnetic structure of thin Ni films on Co/Cu(001)*, Physical Review B **1999**, *60*, 12852.
- [12] GAMBARDELLA, P., DALLMEYER, A., MAITI, K., MALAGOLI, M. C., EBERHARDT, W., KERN, K., CARBONE, C., *Ferromagnetism in one-dimensional monatomic metal chains*, Nature **2002**, *416*, 301.
- [13] BANSMANN, J., BAKER, S. H., BINNS, C., BLACKMAN, J. A., BUCHER, J. P., DORANTES-DAVILA, J., DUPUIS, V., FAVRE, L., KECHRAKOS, D., KLEIBERT, A., MEIWES-BROER, K. H., PASTOR, G. M., PEREZ, A., TOULEMONDE, O., TROHIDOU, K. N., TUAILLON, J., XIE, Y., *Magnetic and structural properties of isolated and assembled clusters*, Surf. Sci. Rep. **2005**, *56*, 189.
- [14] BANSMANN, J., KLEIBERT, A., GETZLAFF, M., RODRIGUEZ, A. F., NOLTING, F., BOEGLIN, C., MEIWES-BROER, K.-H., *Magnetism of 3d transition metal nanoparticles on surfaces probed with synchrotron radiation - from ensembles towards individual objects*, Physica Status Solidi B-Basic Solid State Physics **2010**, *247*, 1152.
- [15] GAMBARDELLA, P., RUSPONI, S., VERONESE, M., DHESI, S. S., GRAZIOLI, C., DALLMEYER, A., CABRIA, I., ZELLER, R., DEDERICHS, P. H., KERN, K., CARBONE, C., BRUNE, H., *Giant Magnetic Anisotropy of Single Cobalt Atoms and Nanoparticles*, Science **2003**, *300*, 1130.
- [16] EDMONDS, K. W., BINNS, C., BAKER, S. H., THORNTON, S. C., NORRIS, C., GOEDKOOP, J. B., FINAZZI, M., BROOKES, N. B., *Doubling of the orbital magnetic moment in nanoscale Fe clusters*, Physical Review B **1999**, *60*, 472.
- [17] PIETZSCH, O., KUBETZKA, A., BODE, M., WIESENDANGER, R., *Spin-Polarized Scanning Tunneling Spectroscopy of Nanoscale Cobalt Islands on Cu(111)*, Physical Review Letters **2004**, *92*, 057202.
- [18] LAU, J. T., FÖHLISCH, A., MARTINS, M., NIETUBYC, R., REIF, M., WURTH, W., *Spin and orbital magnetic moments of deposited small iron clusters studied by x-ray magnetic circular dichroism spectroscopy*, New Journal of Physics **2002**, *4*, 98.
- [19] LAU, J. T., FÖHLISCH, A., NIETUBYČ, R., REIF, M., WURTH, W., *Size-Dependent Magnetism of Deposited Small Iron Clusters Studied by X-Ray Magnetic Circular Dichroism*, Physical Review Letters **2002**, *89*, 057201.
- [20] FAUTH, K., HESSLER, M., BATCHELOR, D., SCHUTZ, G., *Strong influence of defects on the electronic structure of Pt adatoms and clusters on graphite*, Surface Science **2003**, *529*, 397.
- [21] *Metal clusters at surfaces*; MEIWES-BROER, K. H., Ed.; Springer, **2000**.
- [22] GLASER, L., CHEN, K., FIEDLER, S., WELHÖFER, M., WURTH, W., MARTINS, M., *Magnetic properties of small size-selected Co and CoPt clusters on Ni*, Physical Review B **2012**, *86*, 075435.
- [23] EELBO, T., WAŚNIEWSKA, M., THAKUR, P., GYAMFI, M., SACHS, B., WEHLING, T. O., FORTI, S., STARKE, U., TIEG, C., LICHTENSTEIN, A. I., WIESENDANGER, R., *Adatoms and Clusters of 3d Transition Metals on Graphene: Electronic and Magnetic Configurations*, Physical Review Letters **2013**, *110*, 136804.
- [24] *Clusters of Atoms and Molecules*; HABERLAND, H., Ed.; Springer, **1994**.
- [25] HABERLAND, H., KLEINERMANN, K., TRÄGER, F., Bergmann-Schäfer, *Lehrbuch der Experimentalphysik Band 5 - Gase, Nanosysteme, Flüssigkeiten*, Cluster, 2nd Ed.; Walter de Gruyter, **2006**; pp 819.
- [26] HILLEBRECHT, F. U., *Lecture Notes Magnetism goes Nano: Electron Correlations, Spin Transport, Molecular Magnetism*, X-ray magnetic circular dichroism; Forschungszentrum Jülich in der Helmholtz Gemeinschaft, **2005**.
- [27] KNICKELBEIN, M. B., *Electric dipole polarizabilities of Ni₁₂₋₅₈*, The Journal of Chemical Physics **2001**, *115*, 5957.
-

- [28] WANG, L.-S., LI, X., ZHANG, H.-F., *Probing the electronic structure of iron clusters using photoelectron spectroscopy*, Chemical Physics **2000**, 262, 53.
- [29] SONG, W., LU, W.-C., WANG, C. Z., HO, K. M., *Magnetic and electronic properties of the nickel clusters Ni_n ($n < 30$)*, Computational and Theoretical Chemistry **2011**, 978, 41.
- [30] HARRISON, M. R., EDWARDS, P. P. Electrons in small particles. In *The metallic and non-metallic states of matter*; Edwards, P. P., Rao, C. N. R., Eds.; Francis & Taylor London, 1985.
- [31] BALETTO, F., FERRANDO, R., *Structural properties of nanoclusters: Energetic, thermodynamic, and kinetic effects*, Reviews of Modern Physics **2005**, 77, 371.
- [32] *Quantum Phenomena in Clusters and Nanostructures*; KHANNA, S. N., CASTLEMAN, A. W., Eds.; Springer, **2010**.
- [33] WRIGGE, G., ASTRUC HOFFMANN, M., ISSENDORFF, B., HABERLAND, H., *Ultraviolet photoelectron spectroscopy of Nb_4^- to Nb_{200}^-* , The European Physical Journal D - Atomic, Molecular, Optical and Plasma Physics **2003**, 24, 23.
- [34] WRIGGE, G., HOFFMANN, M. A., ISSENDORFF, B. V., *Photoelectron spectroscopy of sodium clusters: Direct observation of the electronic shell structure*, Physical Review A **2002**, 65, 063201.
- [35] BARZEN, L., TOMBERS, M., MERKERT, C., HEWER, J., NIEDNER-SCHATTEBURG, G., *Benzene activation and H/D isotope effects in reactions of mixed cobalt platinum clusters: The influence of charge and of composition*, International Journal of Mass Spectrometry **2012**, 330, 271.
- [36] TOMBERS, M., BARZEN, L., NIEDNER-SCHATTEBURG, G., *Inverse H/D Isotope Effects in Benzene Activation by Cationic and Anionic Cobalt Clusters*, Journal of Physical Chemistry A **2013**, 117, 1197.
- [37] BERG, C., SCHINDLER, T., NIEDNER-SCHATTEBURG, G., BONDYBEY, V. E., *Reactions of simple hydrocarbons with Nb_n^+ : Chemisorption and physisorption on ionized niobium clusters*, The Journal of Chemical Physics **1995**, 102, 4870.
- [38] PFEFFER, B., JABERG, S., NIEDNER-SCHATTEBURG, G., *Reactions of simple aromatic heterocycles with niobium cluster ions ($n \leq 30$)*, The Journal of Chemical Physics **2009**, 131, 194305.
- [39] ACHATZ, U., BERG, C., JOOS, S., FOX, B. S., BEYER, M. K., NIEDNER-SCHATTEBURG, G., BONDYBEY, V. E., *Methane activation by platinum cluster ions in the gas phase: effects of cluster charge on the Pt_4 tetramer*, Chemical Physics Letters **2000**, 320, 53.
- [40] BÖHME, D. K., SCHWARZ, H., *Gas-Phase Catalysis by Atomic and Cluster Metal Ions: The Ultimate Single-Site Catalysts*, Angewandte Chemie International Edition **2005**, 44, 2336.
- [41] HE, S. G., XIE, Y., DONG, F., BERNSTEIN, E. R., *Reaction of niobium and tantalum neutral clusters with low pressure, unsaturated hydrocarbons in a pickup cell: From dehydrogenation to Met-Car formation*, J. Chem. Phys. **2006**, 125, 10.
- [42] HEINEMANN, C., WESENDROP, R., SCHWARZ, H., *Pt^+ -mediated activation of methane: theory and experiment*, Chemical Physics Letters **1995**, 239, 75.
- [43] IRIKURA, K. K., BEAUCHAMP, J. L., *Methane oligomerization in the gas phase by third-row transition-metal ions*, Journal of the American Chemical Society **1991**, 113, 2769.
- [44] SIMOES, J. A. M., BEAUCHAMP, J. L., *Transition metal-hydrogen and metal-carbon bond strengths: the keys to catalysis*, Chemical Reviews **2002**, 90, 629.
- [45] WESENDROP, R., SCHWARZ, H., *Tantalum-Mediated Coupling of Methane and Carbon-Dioxide in the Gas-Phase*, Angewandte Chemie International Edition **1995**, 34, 2033.
- [46] ZEMSKI, K. A., JUSTES, D. R., CASTLEMAN, A. W., *Reactions of group V transition metal oxide cluster ions with ethane and ethylene*, Journal of Physical Chemistry A **2001**, 105, 10237.
- [47] BILLAS, I. M. L., CHÂTELAIN, A., DE HEER, W. A., *Magnetism from the Atom to the Bulk in Iron, Cobalt, and Nickel Clusters*, Science **1994**, 265, 1682.

-
- [48] XU, X., YIN, S., MORO, R., LIANG, A., BOWLAN, J., DE HEER, W. A., *Metastability of Free Cobalt and Iron Clusters: A Possible Precursor to Bulk Ferromagnetism*, Physical Review Letters **2011**, 107, 057203.
- [49] KNICKELBEIN, M. B., *Experimental Observation of Superparamagnetism in Manganese Clusters*, Physical Review Letters **2001**, 86, 5255.
- [50] KNICKELBEIN, M. B., *Nickel clusters: The influence of adsorbates on magnetic moments*, The Journal of Chemical Physics **2002**, 116, 9703.
- [51] KNICKELBEIN, M. B., *Magnetic ordering in manganese clusters*, Phys. Rev. B: Condens. Matter Mater. Phys. **2004**, 70, 014424/1.
- [52] KNICKELBEIN, M. B., *Magnetic moments of small bimetallic clusters: Co_nMn_m* , Physical Review B **2007**, 75, 014401.
- [53] APSEL, S. E., EMMERT, J. W., DENG, J., BLOOMFIELD, L. A., *Surface-enhanced magnetism in nickel clusters*, Physical Review Letters **1996**, 76, 1441.
- [54] BUCHER, J. P., DOUGLASS, D. C., BLOOMFIELD, L. A., *Magnetic properties of free cobalt clusters*, Physical Review Letters **1991**, 66, 3052.
- [55] COX, A. J., LOUDERBACK, J. G., BLOOMFIELD, L. A., *Experimental observation of magnetism in rhodium clusters*, Physical Review Letters **1993**, 71, 923.
- [56] DOUGLASS, D. C., COX, A. J., BUCHER, J. P., BLOOMFIELD, L. A., *Magnetic properties of free cobalt and gadolinium clusters*, Physical Review B **1993**, 47, 12874.
- [57] PAYNE, F. W., JIANG, W., EMMERT, J. W., DENG, J., BLOOMFIELD, L. A., *Magnetic structure of free cobalt clusters studied with Stern-Gerlach deflection experiments*, Physical Review B **2007**, 75, 094431.
- [58] VAN DER LAAN, G., THOLE, B. T., *Strong magnetic x-ray dichroism in 2p absorption spectra of 3d transition-metal ions*, Physical Review B **1991**, 43, 13401.
- [59] THOLE, B. T., CARRA, P., SETTE, F., VANDERLAAN, G., *X-ray circular dichroism as a probe of orbital magnetization*, Physical Review Letters **1992**, 68, 1943.
- [60] CARRA, P., *X-ray circular dichroism as a probe of orbital and spin magnetizations*, Synchrotron Radiation News **1992**, 5, 21.
- [61] CARRA, P., *Sum rules for X-ray absorption and dichroism*, Journal of Electron Spectroscopy and Related Phenomena **1997**, 86, 139.
- [62] CHEN, C. T., IDZERDA, Y. U., LIN, H. J., SMITH, N. V., MEIGS, G., CHABAN, E., HO, G. H., PELLEGRIN, E., SETTE, F., *Experimental Confirmation of the X-Ray Magnetic Circular Dichroism Sum Rules for Iron and Cobalt*, Physical Review Letters **1995**, 75, 152.
- [63] KNICKELBEIN, M. B., *Magnetic moments of bare and benzene-capped cobalt clusters*, The Journal of Chemical Physics **2006**, 125, 044308.
- [64] KNICKELBEIN, M. B., *Nickel clusters: The influence of adsorbed CO on magnetic moments*, The Journal of Chemical Physics **2001**, 115, 1983.
- [65] KNICKELBEIN, M. B., *Adsorbate-induced enhancement of the magnetic moments of iron clusters*, Chemical Physics Letters **2002**, 353, 221.
- [66] KLEIBERT, A., PASSIG, J., MEIWES-BROER, K. H., GETZLAFF, M., BANSMANN, J., *Structure and magnetic moments of mass-filtered deposited nanoparticles*, Journal of Applied Physics **2007**, 101, 114318.
- [67] CHEN, K., FIEDLER, S., BAEV, I., BEECK, T., WURTH, W., MARTINS, M., *Hybridization and magnetism in small FePt alloy clusters*, New Journal of Physics **2012**, 14, 123005.
- [68] FAUTH, K., GOLD, S., HEßLER, M., SCHNEIDER, N., SCHÜTZ, G., *Cluster surface interactions: small Fe clusters driven nonmagnetic on graphite*, Chemical Physics Letters **2004**, 392, 498.
-

- [69] PEREDKOV, S., NEEB, M., EBERHARDT, W., MEYER, J., TOMBERS, M., KAMPSCHULTE, H., NIEDNER-SCHATTEBURG, G., *Spin and Orbital Magnetic Moments of Free Nanoparticles*, Physical Review Letters **2011**, *107*, 233401.
- [70] PEREDKOV, S., SAVCI, A., PETERS, S., NEEB, M., EBERHARDT, W., KAMPSCHULTE, H., MEYER, J., TOMBERS, M., HOFFERBERTH, B., MENGES, F., NIEDNER-SCHATTEBURG, G., *X-ray absorption spectroscopy of mass-selected transition metal clusters using a cyclotron ion trap: An experimental setup for measuring XMCD spectra of free clusters*, Journal of Electron Spectroscopy and Related Phenomena **2011**, *184*, 113.
- [71] LANGENBERG, A., *Magnetische Momente freier, massenselektierter Eisen-, Cobalt- und Nickelcluster*, Doctoral thesis, **2013**, Technische Universität Berlin.
- [72] LANGENBERG, A., HIRSCH, K., LAWICKI, A., ZAMUDIO-BAYER, V., NIEMEYER, M., CHMIELA, P., LANGBEHN, B., TERASAKI, A., ISSENDORFF, B. V., LAU, J. T., *Spin and orbital magnetic moments of size-selected iron, cobalt, and nickel clusters and their link to the bulk phase diagrams*, arXiv.org, e-Print Arch., Phys. **2014**, 1.
- [73] NIEMEYER, M., HIRSCH, K., ZAMUDIO-BAYER, V., LANGENBERG, A., VOGEL, M., KOSSICK, M., EBRECHT, C., EGASHIRA, K., TERASAKI, A., MÖLLER, T., V. ISSENDORFF, B., LAU, J. T., *Spin Coupling and Orbital Angular Momentum Quenching in Free Iron Clusters*, Physical Review Letters **2012**, *108*, 057201.
- [74] SESSOLI, R., GATTESCHI, D., CANESCHI, A., NOVAK, M. A., *Magnetic bistability in a metal ion cluster*, Nature **1993**, *365*, 141.
- [75] CANESCHI, A., GATTESCHI, D., SESSOLI, R., BARRA, A. L., BRUNEL, L. C., GUILLOT, M., *Alternating-current susceptibility, high-field magnetization, and millimeter band EPR evidence for a ground $S = 10$ state in $Mn_{12}O_{12}(CH_3COO)_{16}(H_2O)_4 \cdot 2CH_3COOH \cdot 4H_2O$* , Journal of the American Chemical Society **1991**, *113*, 5873.
- [76] WERNSDORFER, W., *Adv. Chem. Phys.*, Classical and Quantum Magnetization Reversal Studied in Nanometer-Sized Particles and Clusters; John Wiley & Sons, Inc., **2007**; pp 99.
- [77] GATTESCHI, D., SESSOLI, R., *Quantum tunneling of magnetization and related phenomena in molecular materials*, Angew. Chem., Int. Ed. **2003**, *42*, 268.
- [78] GATTESCHI, D. S., ROBERTA; VILLIAN JACQUES, *Molecular Nanomagnets*; Oxford University Press, **2006**.
- [79] GATTESCHI, D., *Molecular Magnetism: A basis for new materials*, Advanced Materials **1994**, *6*, 635.
- [80] *Localized and itinerant Molecular Magnetism: From Molecular Assemblies to the Devices*; CORONADO, E., DELHAÈS, P., GATTESCHI, D., MILLER, J., Eds.; Kluwer Academic Publishers: Dordrecht, **1996**; Vol. 321.
- [81] SCHNACK, J., *Lecture Notes Magnetism goes Nano - Electron Correlations, Spin Transport, Molecular Magnetism*, Quantum Theory of Molecular Magnetism; Forschungszentrum Jülich in der Helmholtz Gemeinschaft, **2005**.
- [82] LEUENBERGER, M. N., LOSS, D., *Quantum computing in molecular magnets*, Nature **2001**, *410*, 789.
- [83] WANG, X., *Thermal and ground-state entanglement in Heisenberg XX qubit rings*, Phys. Rev. A: At., Mol., Opt. Phys. **2002**, *66*, 034302/1.
- [84] WANG, X., ZANARDI, P., *Quantum entanglement and Bell inequalities in Heisenberg spin chains*, Physics Letters A **2002**, *301*, 1.
- [85] AROMI, G., AGUILA, D., GAMEZ, P., LUIS, F., ROUBEAU, O., *Design of magnetic coordination complexes for quantum computing*, Chemical Society Reviews **2012**, *41*, 537.

- [86] LEE, C.-F., LEIGH, D. A., PRITCHARD, R. G., SCHULTZ, D., TEAT, S. J., TIMCO, G. A., WINPENNY, R. E. P., *Hybrid organic-inorganic rotaxanes and molecular shuttles*, *Nature* **2009**, *458*, 314.
- [87] MANNINI, M., PINEIDER, F., SAINCTAVIT, P., DANIELI, C., OTERO, E., SCIANCALEPORE, C., TALARICO, A. M., ARRIO, M.-A., CORNIA, A., GATTESCHI, D., SESSOLI, R., *Magnetic memory of a single-molecule quantum magnet wired to a gold surface*, *Nat. Mater.* **2009**, *8*, 194.
- [88] MANNINI, M., PINEIDER, F., SAINCTAVIT, P., JOLY, L., FRAILE-RODRÍGUEZ, A., ARRIO, M.-A., CARTIER DIT MOULIN, C., WERNSDORFER, W., CORNIA, A., GATTESCHI, D., SESSOLI, R., *X-Ray Magnetic Circular Dichroism Picks out Single-Molecule Magnets Suitable for Nanodevices*, *Advanced Materials* **2009**, *21*, 167.
- [89] MANNINI, M., SAINCTAVIT, P., SESSOLI, R., CARTIER DIT MOULIN, C., PINEIDER, F., ARRIO, M.-A., CORNIA, A., GATTESCHI, D., *XAS and XMCD Investigation of Mn12 Monolayers on Gold*, *Chemistry – A European Journal* **2008**, *14*, 7530.
- [90] DREISER, J., PEDERSEN, K. S., BIRK, T., SCHAU-MAGNUSSEN, M., PIAMONTEZE, C., RUSPONI, S., WEYHERMUELLER, T., BRUNE, H., NOLTING, F., BENDIX, J., *X-ray Magnetic Circular Dichroism (XMCD) Study of a Methoxide-Bridged Dy-III-Cr-III Cluster Obtained by Fluoride Abstraction from cis-[(CrF₂)-F-III(phen)₂]⁺*, *Journal of Physical Chemistry A* **2012**, *116*, 7842.
- [91] DREISER, J., PEDERSEN, K. S., PIAMONTEZE, C., RUSPONI, S., SALMAN, Z., ALI, M. E., SCHAU-MAGNUSSEN, M., THUESEN, C. A., PILIGKOS, S., WEIHE, H., MUTKA, H., WALDMANN, O., OPPENEER, P., BENDIX, J., NOLTING, F., BRUNE, H., *Direct observation of a ferri-to-ferromagnetic transition in a fluoride-bridged 3d-4f molecular cluster*, *Chemical Science* **2012**, *3*, 1024.
- [92] GHIGNA, P., CAMPANA, A., LASCIALFARI, A., CANESCHI, A., GATTESCHI, D., TAGLIAFERRI, A., BORGATTI, F., *X-ray magnetic-circular-dichroism spectra on the superparamagnetic transition-metal ion clusters Mn-12 and Fe-8*, *Physical Review B* **2001**, *64*.
- [93] GHIGNA, P., CAMPANA, A., LASCIALFARI, A., CANESCHI, A., GATTESCHI, D., TAGLIAFERRI, A., BORGATTI, F., *X-ray magnetic-circular-dichroism spectra of the superparamagnetic transition-metal ion clusters Mn12 and Fe8. [Erratum to document cited in CA136:47067]*, *Phys. Rev. B: Condens. Matter Mater. Phys.* **2002**, *65*, 109903/1.
- [94] MORONI, R., CARTIER, D. M. C., CHAMPION, G., ARRIO, M. A., SAINCTAVIT, P., VERDAGUER, M., GATTESCHI, D., *X-ray magnetic circular dichroism investigation of magnetic contributions from Mn(III) and Mn(IV) ions in Mn12-ac*, *Phys. Rev. B: Condens. Matter Mater. Phys.* **2003**, *68*, 064407/1.
- [95] CORRADINI, V., GHIRRI, A., GARLATTI, E., BIAGI, R., DE RENZI, V., DEL PENNINO, U., BELLINI, V., CARRETTA, S., SANTINI, P., TIMCO, G., WINPENNY, R. E. P., AFFRONTE, M., *Magnetic Anisotropy of Cr7Ni Spin Clusters on Surfaces*, *Advanced Functional Materials* **2012**, *22*, 3706.

2. THEORETICAL BACKGROUND

In the following chapter a brief introduction to the fields of magnetic materials (Chap. 2.1) and especially the magnetism of 3d transition metals (Chap. 2.2) will be given. This is followed by the magnetism of finite sized systems (Chap. 2.3). The paragraphs will deal with the basic concepts needed to understand the experiments presented within this thesis. The reader is referred to the literature for a more detailed introduction into the field of magnetism in general and magnetism of nanoparticles, e.g. Refs. [1-8]. This section is followed by a section on x-ray magnetic circular dichroism (XMCD) (Chap. 2.4). The paragraph is divided into two parts: (i) an introduction into x-ray absorption spectroscopy (Chap. 2.4.1 and 2.4.2) and (ii) the basic concepts of the XMCD effect (Chap. 2.4.3). The chapter will be concluded by the introduction of the sum rule analysis (Chap. 2.4.4). The reader is referred to references [5,9-12] for further reading on the above topics.

2.1 Classification of magnetic materials

A classification of magnetic materials is achieved according to their response to a magnetic field. The magnetic susceptibility is the physical quantity linking the magnetization of a material to an external magnetic field.

$$\mathbf{M} = \chi \mathbf{H} \tag{Eq. 2.1}$$

M	magnetization (total magnetic moment per unit volume)
χ	magnetic susceptibility
H	magnetic field strength

The term "magnetic field" is commonly used to refer to the magnetic field strength **H** and to the magnetic induction **B**. In vacuum both quantities are linearly related via the magnetic permeability of free space μ_0 .

$$\mathbf{B} = \mu_0 \mathbf{H} \tag{Eq. 2.2}$$

If the magnetic induction occurs within a material, the magnetization of the material itself has to be considered, too:

$$\mathbf{B} = \mu_0(\mathbf{H} + \mathbf{M}) = \mu_0(1 + \chi)\mathbf{H} = \mu_0\mu_r\mathbf{H} \quad (\text{Eq. 2.3})$$

μ_r relative permeability

Magnetic materials can be roughly divided into three classes: diamagnetic, paramagnetic and materials showing collective magnetism^[7].

2.1.1 Diamagnetism

Diamagnetism is present in all magnetic materials. A magnetic flux is induced in the material when it is exposed to a magnetic field. The induced moment is oriented antiparallel with respect to the external field following Lenz's law. The diamagnetic susceptibility is negative and mostly temperature independent.

$$\chi^{dia}(T) \approx \text{constant} < 0 \quad (\text{Eq. 2.4})$$

2.1.2 Paramagnetism

A condition for the existence of paramagnetism is the presence of preexisting magnetic dipoles in the material which can be aligned by applying a magnetic field. The average magnetization is parallel to the external magnetic field, i.e. the susceptibility takes on a positive value. The alignment of the magnetic dipoles may be hindered by thermal fluctuations (Fig. 2.1).

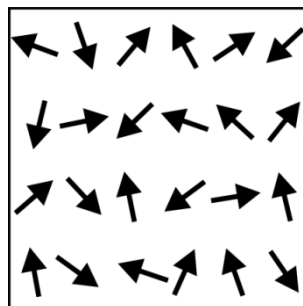


Figure 2.1 random distribution of local magnetic dipoles in a paramagnet due to thermal fluctuations without the presence of a magnetic field

Paramagnets are divided into two groups. The susceptibility of the first group is temperature independent and caused by the itinerant electrons in metals, the so called Pauli-Paramagnetism^[13].

$$\chi^{Pauli} > 0 \quad (\text{Eq. 2.5})$$

$$\frac{\partial \chi^{Pauli}}{\partial T} \approx 0 \quad (\text{Eq. 2.6})$$

Temperature dependent paramagnetism can be found in palladium and platinum and many salts of rare earths^[3,4], which is sometimes called Langevin-Paramagnetism^[7]. The temperature dependence of the susceptibility is described by the Curie-Weiss law^[14]:

$$\chi^{Langevin} > 0 \quad (\text{Eq. 2.7})$$

$$\chi^{Langevin}(T) = \frac{C}{T} \quad (\text{Eq. 2.8})$$

C Curie constant

If the magnitudes of the two paramagnetic susceptibilities are compared, it can be seen that the Pauli-Paramagnetism is much weaker than the Langevin-Paramagnetism.

$$\chi^{Pauli} \ll \chi^{Langevin} \quad (\text{Eq. 2.9})$$

2.1.3 Collective magnetism

In para- and diamagnetic materials, the magnetization of the material depends on the presence of an external magnetic field. A group of materials exhibits a magnetic moment without the presence of an external magnetic field. This behavior is called spontaneous magnetization.

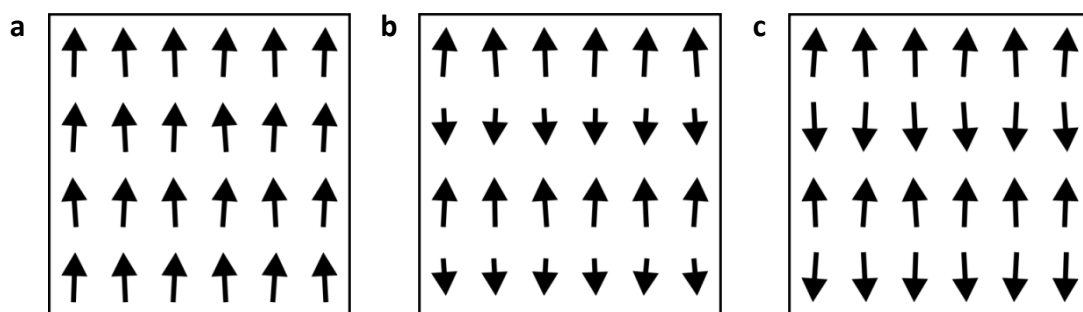


Figure 2.2 spin orientations below the critical temperature for **(a)** a ferromagnet; **(b)** a ferrimagnet; **(c)** an antiferromagnet

The magnetic susceptibility has a complex structure because it does no longer only depend on temperature and applied field but also on the "history" of the material^[7]. The "history" of a material can be seen in a hysteresis loop if the magnetization direction of the sample is reversed.

$$\chi^{collective} = \chi^{collective}(B, T, "history") \quad (\text{Eq. 2.10})$$

A critical temperature is defined below which spontaneous magnetization is present. The spontaneous magnetization is driven by the energy minimization due to exchange interaction between the magnetic dipoles, i.e. the electron spins.

2.1.3.1 Ferromagnetism

All spins are aligned parallel with respect to each other at $T = 0$ K. The spins exhibit a preferential direction at finite temperatures (Fig. 2.2a). The spins can be fully aligned by applying a magnetic field. A ferromagnet retains its magnetization after the external magnetic field is switched off. The critical temperature of a ferromagnet is called Curie temperature T_C . Spontaneous magnetization is present below T_C . If the temperature exceeds T_C the material behaves like a paramagnet. Examples for ferromagnetic materials at room temperature are the 3d metals iron, cobalt and nickel.

2.1.3.2 Ferrimagnetism

Ferrimagnetism occurs if the material can be decomposed into two different sublattices A and B which each show ferromagnetical spin alignment. However, the magnetizations of the sublattices are oriented antiparallel with respect to each other. The material exhibits a total magnetization in one direction because the magnetizations of the individual sublattices differ in magnitude (Fig. 2.2b).

$$\mathbf{M} = \mathbf{M}_A + \mathbf{M}_B \neq 0 \quad (\text{Eq. 2.11})$$

The magnetic order is lost at the Curie temperature T_C and the material becomes paramagnetic.

2.1.3.3 Antiferromagnetism

Antiferromagnetism is a special case of ferrimagnetism. In the case of an antiferromagnetic material, the magnetizations of both sublattices cancel each other out. Hence, the material exhibits no magnetization (Fig. 2.2c).

$$\mathbf{M} = \mathbf{M}_A + \mathbf{M}_B \equiv 0 \quad (\text{Eq. 2.12})$$

The critical temperature for antiferromagnetic materials is called Néel temperature Θ_N . Above the Néel temperature, the spins are randomly orientated and the material behaves paramagnetic.

2.2 Magnetism of 3d transition metals

Iron, cobalt and nickel show a ferromagnetic ordering at room temperature. The magnetic moment per atom in iron (bcc) is about $2.2 \mu_B$ (μ_B = Bohr magneton = magnetic moment of the electron). The non-integer value indicates that a purely localized description of the magnetic moment fails. The magnetism of the 3d metals is usually described by band magnetism or itinerant ferromagnetism^[7]. The spontaneous magnetization is due to a spin splitting of the valence band (Fig. 2.3). The spin splitting of the valence shell occurs if the ferromagnetic alignment of spins becomes energetically favorable over the paramagnetic state. The energy shift of the energy bands with respect to each other is called exchange splitting.

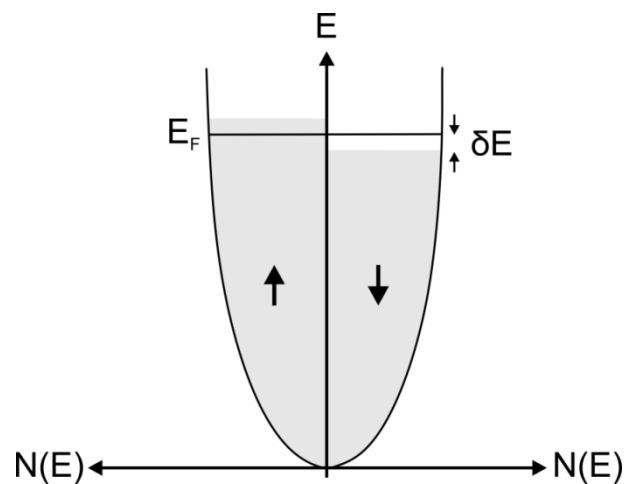


Figure 2.3 Density of states for spin up and spin down electrons exhibiting a spontaneous spin splitting (E_F = Fermi level, δE = exchange splitting, $N(E)$ = density of states)

The spin state with the largest number of electrons is called majority band / spin. Here, the spin down state would be the minority and the spin up the majority spin. Note, that the terms spin up and spin down only have a meaning in relation to a quantization axis.

The exchange interaction between spins aligns them parallel with respect to each other. The mean distance between electrons with a parallel aligned spins is larger than for antiparallel aligned spins. This leads to a reduction of the Coulomb energy. If the reduction of the Coulomb energy, i.e. the gain of exchange energy, was the only criterion for ferromagnetic order, all metals would be ferromagnetic. A parallel alignment of spins is realized by the occupation of higher electronic states within the spin up and spin down band. Thus, the kinetic energy increases (Fig. 2.4). If the kinetic energy increase exceeds the energy gain due to reduced Coulomb interaction the metal is paramagnetic.

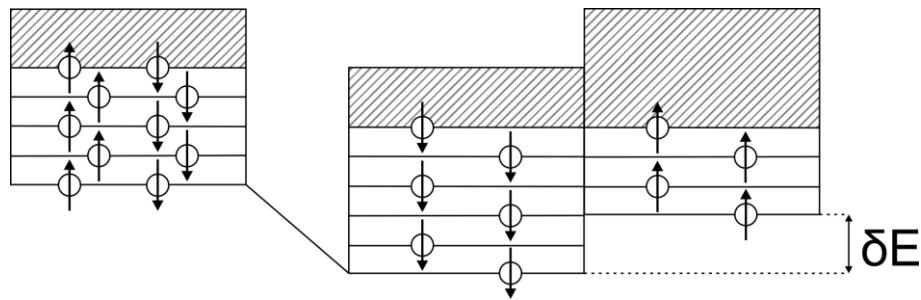


Figure 2.4 redistribution of electrons after exchange splitting into a spin down and spin up band

The energy gain due to the exchange interaction (i.e. the reduced Coulomb energy) exceeds the energy loss because of the enhanced kinetic energy compared to the non-split state.^[3]

Narrow energy bands with high densities of states are advantageous for ferromagnetism as the kinetic energy increase due to the occupation of higher states is relatively small. Stoner and Wohlfarth formulated a criterion for the appearance of ferromagnetism^[3]:

$$JN(E_F)\Omega_0 > 1 \quad (\text{Eq. 2.13})$$

J	exchange energy per atom
$N(E_F)$	density of states at the Fermi level
Ω_0	atomic volume

Three qualitative arguments given here can be formulated from Stoner-Wohlfarth criterion^[3]:

- The exchange integral has to be positive and as large as possible.
- High densities of states decrease the kinetic energy needed to promote electrons into higher electronic states.
- Narrow, half-filled energy bands as in transition metals, are advantageous for high densities of states.

The energy splitting for a given element depends on the atomic distance within the material. If the atomic distance is already large, a further reduction of the Coulomb energy will have no significant influence and no coupling will take place (Fig. 2.5d). On the other hand, if the atomic distance is small, which means a small density of states at the Fermi level, a spontaneous magnetization will be disadvantageous due to the considerable increase of kinetic energy (Fig. 2.5b). However, there is a small range where the Stoner-Wohlfarth criterion is met and ferromagnetic ordering occurs (Fig. 2.5c). A graphical illustration of this phenomenon is given by the Beth-Slater curve^[15,16] which describes the exchange between neighboring atoms in a localized picture. The curve gives the energy

difference between the spontaneously magnetized and unmagnetized state in dependence of the quotient of the interatomic distance and atomic radius r_{AB} / r_d (Fig. 2.5a).

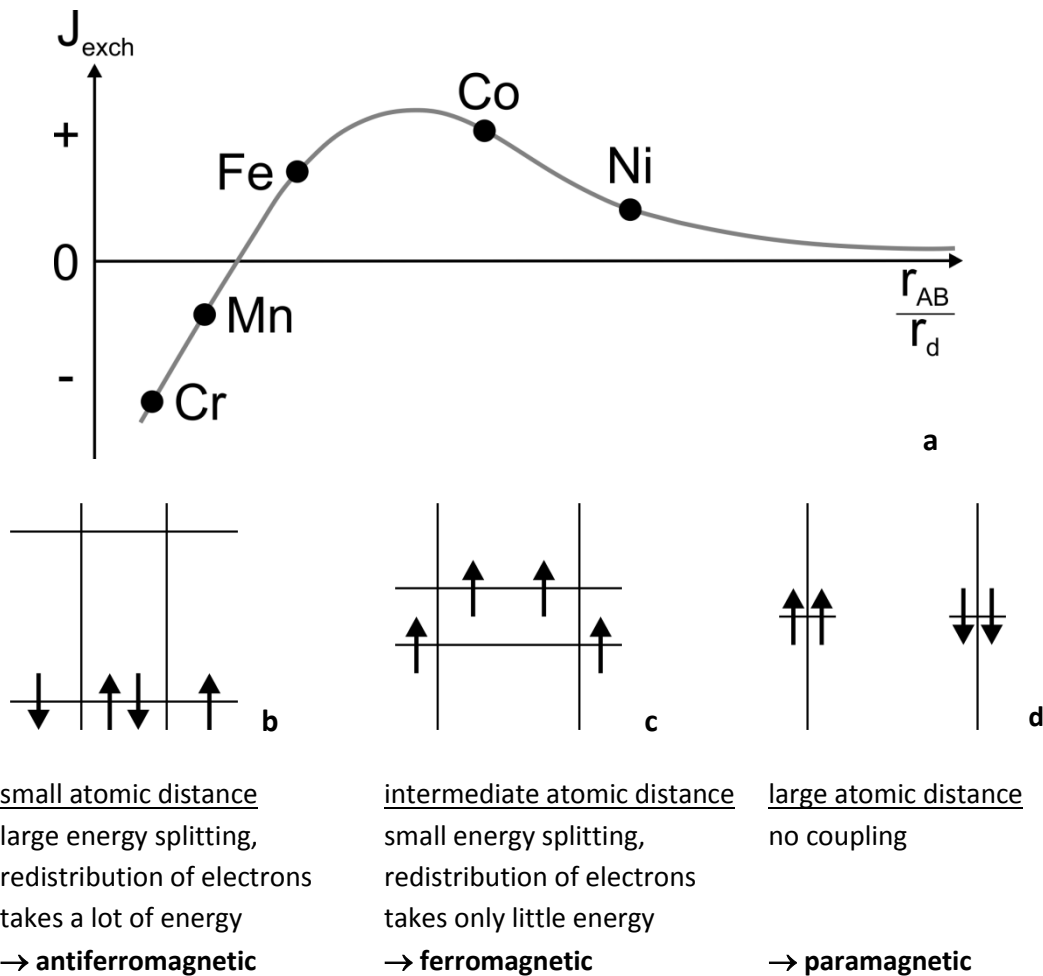


Figure 2.5 Dependence of the magnetic order of the interatomic distance r_{AB} (a) The Bethe Slater curve is an illustration of the exchange energy between the 3d electrons (J_{exch}) in dependence of the quotient of interatomic distance (r_{AB}) and radius of the 3d shell (r_d) in a localized picture. If the value for J_{exch} is negative the material is antiferromagnetic. If J_{exch} is larger than zero than the material has a ferromagnetic ground state. (b-d) energy splitting in dependence of the interatomic distance for antiferromagnetic (b), ferromagnetic (c) and paramagnetic (d) ordering^[3]

Today, the spontaneous magnetization of the 3d metals is usually described by itinerant electrons in the band model. The d-bands partially overlap with the s-bands and electrons are excited from one band into the other and spontaneous magnetization occurs. Nevertheless, the Bethe-Slater curve gives a good illustration of the effect which the atomic order has on magnetism.

2.2.1 Magnetic domains

Even though the Curie temperatures of iron, cobalt and nickel far exceed room temperature, macroscopic samples commonly are not magnetic. In addition to the exchange interaction, we have to consider the magnetic dipolar interaction between two spins to understand this macroscopic behavior. The exchange interaction is about a 1000 times stronger than the magnetic dipolar interaction but it is of a much shorter range^[17]. The exchange interaction drops exponentially with the distance r between two spins whereas the magnetic dipolar interaction drops with the negative power of three ($\sim r^{-3}$) (Eq. 2.14).

$$E = \frac{\mu_0}{4\pi r^3} \left[(\mu_1 \cdot \mu_2) - \frac{3}{r^2} ((\mu_1 \cdot r)(\mu_2 \cdot r)) \right] \quad (\text{Eq. 2.14})$$

μ_1, μ_2	magnetic dipole
r	distance between μ_1 and μ_2
μ_0	Bohr magneton

The long range order of the sample is dominated by contributions from the magnetic dipolar interaction. This can lead to very complex macroscopic structure of the material.

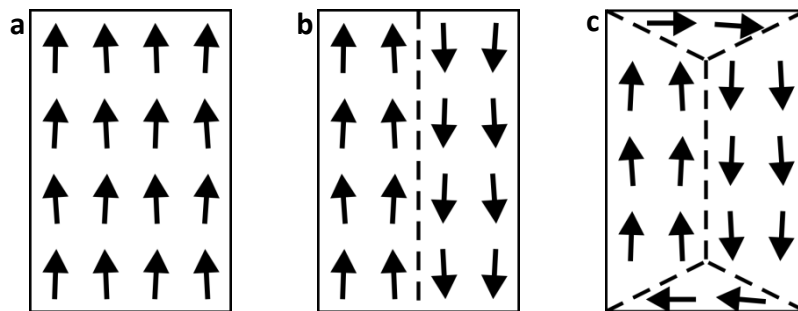


Figure 2.6 A ferromagnetically ordered macroscopic sample can lower its magnetic dipolar energy by the formation of domains. Thus, the structure with only one domain **(a)** has a higher magnetic dipolar energy than a structure with two domains **(b)**. The formation of domains can lead to very complex structures to further reduce the magnetic dipolar energy of the sample. The two domain structure **(b)** can further reduce its energy by forming a four domain structure **(c)**^[17].

The dipolar energy can be significantly lowered by the formation of regions of a homogenous magnetization, so called magnetic domains. The spins are ferromagnetically ordered in each domain. However, the orientation of the magnetization of the individual domains strongly differs from each other (Fig. 2.6). The loss of exchange energy for the few spins located at the domain walls is compensated by the gain of dipolar energy due to the large number of spins. The formation of

domains lowers the dipolar energy of every spin whereas the exchange energy is raised only for a limited number of spins located at the domain walls. This favors the formation of magnetic domains as long as they do not become too small. If domains become too small, the increased exchange energy can no longer be compensated by the gain of dipolar energy.

2.3 Magnetism of nanoparticles and clusters

2.3.1 Superparamagnetic ensemble

If a ferromagnetic sample is made sufficiently small, it will no longer form several domains to reduce its energy but it will become a single domain particle^[1,3,5,18]. This means that all spins will align parallel to each other. An ensemble of single domain ferromagnetic nanoparticles or clusters will behave as a paramagnet because each particle has one effective magnetic moment (Fig. 2.7). Thus, they are called superparamagnetic^[19]. "A superparamagnet is defined as an ensemble of giant magnetic moments which are not interacting and have no effective magnetic anisotropy."^[20]

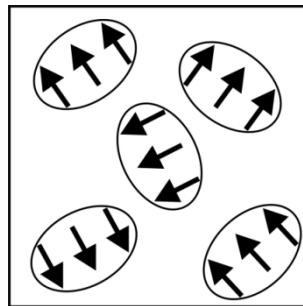


Figure 2.7 arrangement of magnetic moments in a superparamagnet without applied magnetic field

The response of a superparamagnet to a magnetic field depends on the applied field strength and the anisotropy forces within the individual particles. If the anisotropy energy is smaller than the thermal energy, the spins will be able to rotate within the cluster frame. If the so called blocking temperature T_B is reached, the thermal energy is not sufficient enough to rotate the spins anymore. They are locked within the cluster frame, i.e. they are blocked.

$$\frac{E_{anisotropy}}{k_B} = T_B \quad (\text{Eq. 2.15})$$

$E_{anisotropy}$	energy barrier between both energy minima with opposite particle magnetization
k_B	Boltzmann constant

Superparamagnets exhibit no hysteresis because of the absence of anisotropy within a superparamagnet. The magnetization curve of a free superparamagnetic ensemble follows a Langevin function (Eq. 2.16a). The Langevin function describes the magnetization of the superparamagnet in dependence of the temperature T and an external magnetic field H . The lower the temperature and the higher the magnetic field the higher is the magnetization of the superparamagnet (Eq. 2.16). In a superparamagnetic ensemble the magnetization corresponds to the alignment of the magnetic moments of the individual particles.

$$L(y) = \coth(y) - \frac{1}{y} \quad (\text{Eq. 2.16a})$$

$$y = \frac{m_J H}{k_B T} \quad (\text{Eq. 2.16b})$$

$$M(H, T) = N m_J \left(\coth \left(\frac{m_J H}{k_B T} \right) - \frac{k_B T}{m_J H} \right) \quad (\text{Eq. 2.16c})$$

m_J total magnetic moment per particle
 N number of particles

The susceptibility follows the Curie law. Therefore, if the temperature increases beyond T_C , the magnetic order breaks down and the individual particle become paramagnetic.

2.3.2 Magnetic moments of free clusters

2.3.2.1 The Stern-Gerlach experiment

In a Stern-Gerlach experiment, a particle passes through an inhomogeneous magnetic or electric field and the particles deflection from its original trajectory is measured. If a magnetic field is used, the magnitude of the deflection is a measure for the particle's magnetic moment. In the original experiment, Stern and Gerlach passed a beam of silver atoms through an inhomogeneous magnetic field^[21,22]. The electron spin caused the beam to split up due to the space quantization of the spin, i.e. for $s = 1/2$ follows that $m_s = \pm 1/2$.

Magnetic moments of clusters are measured by passing a beam of neutral metal clusters through an inhomogeneous magnetic field. Contrary to the originally used silver atoms, clusters are exclusively deflected towards the high field of the magnet^[2,5,8,23,24] (Fig. 2.8). The cluster behaves like a small ferromagnet. However, the deflection of the cluster is not proportional to the magnetic moment m_J of the cluster but to its projection onto the quantization axis $m_{J,z}$. The passing time through the magnetic field is long enough for a thermal relaxation and thus the magnetic moment can fluctuate within the cluster frame. The cluster ensemble behaves like a superparamagnet and the measured

effective moment follows a Langevin function^[25-28] (Eq. 2.16b/c). Experimental results for iron^[29] clusters are shown in Fig. 2.9. The magnetic moments of the clusters are enhanced compared to the magnetic moment of bulk iron.

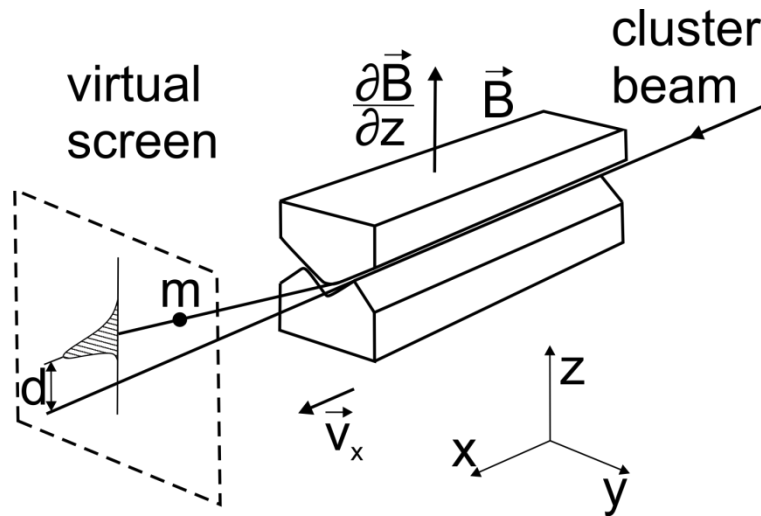


Figure 2.8 Sketch of a Stern-Gerlach experiment which is used to measure the magnetic moments of free metal clusters^[8]

A beam of neutral clusters of defined temperature passes through a magnet with a high magnetic field and a high field gradient. Clusters feel a force which deflects them towards the high field of the inhomogeneous magnetic field. After passing through the magnet, the clusters are ionized by a laser pulse and detected by a position sensitive time of flight mass spectrometer. The deflection d is a measure for the magnetic moment of the clusters.

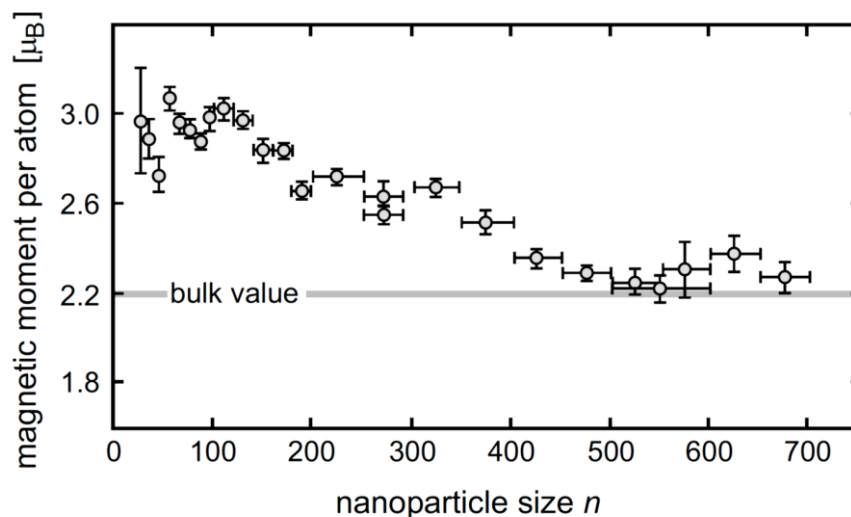


Figure 2.9 magnetic moments in μ_B /atom for iron clusters Fe_n taken by a Stern-Gerlach experiment

The magnetic moments are larger than the bulk value (solid grey line)^[7,23,29].

2.3.2.2 Enhanced magnetic moments in small clusters

The experiments on iron clusters^[23,30,31] reveal an enhanced magnetic moment compared to the respective bulk value of iron (Fig. 2.9). Similar results were found for cobalt^[23,31-34] and nickel^[23,27,35,36] clusters. If the atomic and the bulk magnetic moments are compared, it becomes evident that the magnetic moment of the atom is much larger than that of the respective bulk material (Tab. 2.1). One reason for the reduced magnetic moment in the bulk phase is the almost completely quenched orbital contribution to the magnetic moment in the solid. The total magnetic moment is composed of an orbital and a spin magnetic moment.

$$m_{L,z} = -g_L \mu_B L_z \quad (\text{Eq. 2.17a})$$

$$m_{S,z} = -g_S \mu_B S_z \quad (\text{Eq. 2.17b})$$

$$\begin{aligned} m_{J,z} &= m_{L,z} + m_{S,z} = -\mu_B (g_L L_z + g_S S_z) \\ &= -\mu_B (L_z + 2S_z) = -\mu_B g_J J_z \end{aligned} \quad (\text{Eq. 2.18})$$

$m_{L,z}$	orbital magnetic moment projected onto the quantization axis
L_z	orbital angular momentum projected onto the quantization axis
g_L	g-factor of the orbital moment; $g_L = 1$
μ_B	Bohr magneton
$m_{S,z}$	spin magnetic moment projected onto the quantization axis
S_z	spin angular momentum projected onto the quantization axis
g_S	g-factor the electron spin; $g = 2.0$
$m_{J,z}$	total magnetic moment projected onto the quantization axis
J_z	total angular momentum projected onto the quantization axis
g_J	g-factor of the total magnetic moment

The thermal fluctuations lead to an incomplete alignment of the magnetic moments with respect to the quantization axis. In the case of J, we have to consider the projection of J onto the quantization axis, i.e. J_z . $m_{J,z}$ as a function of magnetic field and temperature is given by a Brillouin function^[4,5,7].

$$B_J(y) = \frac{2J+1}{2J} \coth\left(\frac{2J+1}{2J} y\right) - \frac{1}{2J} \coth\left(\frac{1}{2J} y\right) \quad (\text{Eq. 2.19})$$

$$y = \frac{m_J B}{k_B T} = \frac{g_J \mu_B J B}{k_B T} \quad (\text{Eq. 2.20})$$

The Landé g-factor of the total magnetic moment can be calculated for a free atom, using the fact the g_J is the projection of $(g_L L + g_S S)$ onto J ^[7].

$$g_J = \frac{3}{2} + \frac{S(S+1) - L(L+1)}{2J(J+1)} \quad (\text{Eq. 2.21})$$

From the g-factors of bulk iron, cobalt and nickel it is evident that the magnetic moment in solids is dominated by the spin. The closer the value of g is to two, the more dominant is the spin moment over the orbital moment (Tab. 2.1)

The Brillouin function becomes the Langevin function in the limit of $J \rightarrow \infty$.

$$B_\infty(y) = \coth(y) - \frac{1}{y} = L(y) \quad (\text{Eq. 2.22})$$

Table 2.1 magnetic moments and various g-factors for the atom and the bulk for the ferromagnetic 3d metals Fe, Co and Ni

	atom			bulk		
	magnetic moment ^(*) / μ_B	Landé g-factor ^(#)	magnetic moment / μ_B /atom	spectroscopic splitting factor g-factor ^(§)	magneto-mechanical ratio g' ^(§)	
Fe	6 (5D)	1.50	2.063 ^[37] (bcc)	2.09 ^[5]	1.92 ^[38]	
Co	6 (4F)	1.33	2.25 ^[37] (hcp)	2.18 ^[5]	1.84 ^[39]	
Ni	5 (3F)	1.25	0.66 ^[40,41] (fcc)	2.21 ^[5]	1.84 ^[42]	

^(*) calculated according to Hund's rules

^(#) calculated according to Eq. 2.21

^(§) spectroscopic splitting factor from Ferromagnetic Resonance (FMR) experiments^[43,44]

^(§) magnetomechanical ratio from gyromagnetic experiments (Einstein - de Haas effect)^[43,45]

The relationship between the spectroscopic splitting factor and the magnetomechanical ratio can be found in the appendix (Chap. A.1.1).

2.4 X-ray magnetic circular dichroism

2.4.1 X-ray absorption

An x-ray photon can be absorbed resonantly or non-resonantly. A core electron is excited after the absorption of an x-ray photon given the high photon energy of the x-ray photon of typically a few hundred electron volts. A non-resonant absorption can create a photo electron when the photon energy exceeds the binding energy of the electron. The electron is excited into free electron-like

continuum states. The process is subject to the photo electric effect. Thus, the following function relates the initial x-ray photon energy to that of the excited electron:

$$h\nu \geq E_{bin} + E_{kin} + \phi \quad (\text{Eq. 2.23})$$

$h\nu$	photon energy ($h\nu = \hbar\omega$)
E_{bin}	binding energy
E_{kin}	kinetic energy of the free electron
ϕ	work function

The resulting core hole is filled by a secondary electron dropping down from a higher energy level. The gained energy can either be emitted as radiation (fluorescence) or a second electron (Augé electron).

The resonant excitation of a core electron to a higher electronic state by an x-ray photon is named resonant x-ray absorption. An illustration of the absorption process in a one electron picture is given in Fig. 2.10. The electron absorbs the photon energy which corresponds to the energy difference between the initial core and the final valence state. The one electron picture focuses only on the photo electron and regards all remaining electrons as passive^[5]. The resonant transition can be described by a transition matrix between the core and excited state and thus is subject to selection rules.

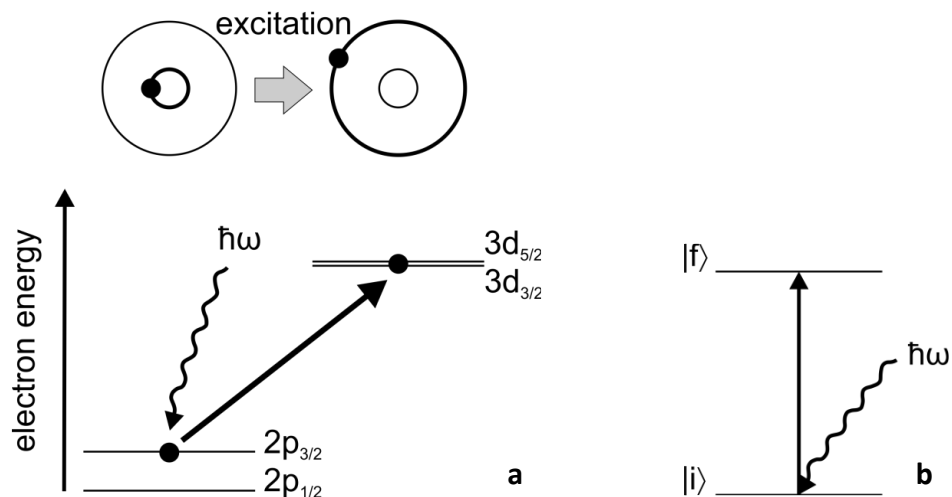


Figure 2.10 Depiction of the resonant $L_{2,3}$ edge absorption ($2p \rightarrow 3d$)^[5] in a one electron picture

(a) An electron is resonantly excited by the absorption of an x-ray photon. The energy levels are labeled by their quantum numbers. **(b)** The core state is the initial state $|i\rangle$ and the valence state into which the electron is excited is the final state $|f\rangle$.

The transition probability between the initial core state $|i\rangle$ and the final valence state $|f\rangle$ can be determined by Fermi's Golden Rule^[46]. The transition probability T_{if} can be written in the form of Eq. 2.24.

$$T_{if} = \frac{2\pi}{\hbar} |\langle f | \hat{H}_{int} | i \rangle|^2 \delta(\varepsilon_i - \varepsilon_f) \rho(\varepsilon_f) \quad (\text{Eq. 2.24})$$

$\rho(\varepsilon_f)$ is the density of final states per unit energy. The interaction Hamiltonian \hat{H}_{int} for resonant x-ray absorption is given by a product of the momentum operator \mathbf{p} and a vector potential \mathbf{A} ^[5,47,48].

$$\hat{H}_{int} = \frac{e}{m_e} \mathbf{p} \cdot \mathbf{A} \quad (\text{Eq. 2.25})$$

\mathbf{p}	momentum operator
\mathbf{A}	vector potential,
e	elementary charge
m_e	electron mass

The states $|i\rangle$ and $|f\rangle$ are combined electron and photon states. The absorption process can also be written as a transition between two electronic states after separating the matrix elements of Eq. 2.24 into a photon and electron part. Eq. 2.26 gives the electronic part^[5,49].

$$M = \langle b | \mathbf{p} \cdot \boldsymbol{\epsilon} e^{i\mathbf{k} \cdot \mathbf{r}} | a \rangle \quad (\text{Eq. 2.26})$$

M	transition matrix element
$ b\rangle$	final electronic state
$ a\rangle$	initial electronic state
\mathbf{p}	electron momentum operator
$\boldsymbol{\epsilon}$	unit photon polarization operator
\mathbf{k}	wave vector
\mathbf{r}	length operator

The momentum operator \mathbf{p} can be rewritten in terms of the length operator \mathbf{r} if the dipole approximation is applied. "The dipole approximation assumes that the size of the absorbing atomic shell is small relative to the X-ray wavelength λ , i.e.

$$|\mathbf{r}| \ll \frac{1}{|k|} = \frac{\lambda}{2\pi} \quad (\text{Eq. 2.27})$$

so that the electric field which drives the electronic transition is constant over the atomic volume."^[5]

The x-ray absorption intensity can therefore be written as:

$$I_{res} = A |\langle b | \boldsymbol{\epsilon} \cdot \mathbf{r} | a \rangle|^2 \quad (\text{Eq. 2.28})$$

$$A = 2\pi^2 \alpha_f \hbar \omega \quad (\text{Eq. 2.29})$$

I_{res}	resonance intensity, [I_{res}] = length ² x energy
α_f	fine structure constant
ω	photon frequency associated with the transition $a \rightarrow b$

2.4.2 Dipole selection rules

In the case polarized photons are used, Eq. 2.28 has to be written in dependence of a polarization dependent dipole operator:

$$I_{res} = A |\langle b | \boldsymbol{\epsilon} \cdot \mathbf{r} | a \rangle|^2 = A |\langle b | \boldsymbol{\epsilon}_\alpha^q \cdot \mathbf{r} | a \rangle|^2 = A |\langle b | P_\alpha^q | a \rangle|^2 \quad (\text{Eq. 2.30})$$

P_α^q	dipole operator
q	photon angular momentum $q = 0$ for linearly polarized light $q = \pm 1$ for circularly polarized light
α	quantization axis in Cartesian coordinates $\alpha = x, y, z$

In a one electron picture, the initial and final state can be described by wave functions of the form:

$$R_{n,l}(r) Y_{l,m_l} \chi_{s,m_s} = |R_{n,l}(r); l, m_l, s, m_s\rangle \quad (\text{Eq. 2.31})$$

$R_{n,l}(r)$	radial component of the wave function
Y_{l,m_l}	angular part of the wave function, expressed in spherical harmonics
χ_{s,m_s}	spin part of the wavefunction
n, l, m_l, s, m_s	quantum numbers

If we consider a transition from an initial core state $|a\rangle$ with an angular momentum c to a final valence state $|b\rangle$ with an angular momentum l , we can write a transition matrix by applying Eq. 2.31 to the electronic states and insert them into Eq. 2.30. Additionally, P_α^q can be written in terms of spherical harmonics $Y_{l,m}(\vartheta, \phi)$ ^[5,50,51]. These, in turn, are expressed in terms of Racah's spherical tensor operators $C_m^{(l)}$ ($e_{\alpha,p}^q$ = coefficients)^[50].

$$\frac{P_\alpha^q}{r} = \sum_{p=0,\pm 1} e_{\alpha,p}^q C_p^{(1)} \quad (\text{Eq. 2.32})$$

$$\langle b | P_{\alpha}^q | a \rangle = \langle R_{n',l}(r); l, m_l, s, m_s' | P_{\alpha}^q | R_{n,c}(r); c, m_c, s, m_s \rangle \quad (\text{Eq. 2.33a/b})$$

$$\langle b | P_{\alpha}^q | a \rangle = \delta(m_s', m_s) \langle R_{n',l}(r) | r | R_{n,c}(r) \rangle \sum_{m_c, m_l, p} \left(e_{\alpha,p}^q \langle l, m_l | C_p^{(1)} | c, m_c \rangle \right)$$

$$\langle b | P_{\alpha}^q | a \rangle = \quad \textit{spin} \quad \quad \textit{radial} \quad \quad \textit{angular} \quad \quad (\text{Eq. 2.33c})$$

The matrix element factors into a spin, angular and radial part. The dipole selection rules can be derived from Eq. 2.33b by inspecting the non-vanishing matrix elements.

- $\Delta l = |l' - l| = \pm 1$
- $\Delta m_l = m_l' - m_l = q = 0, \pm 1$
- $\Delta s = s' - s = 0$
- $\Delta m_s = m_s' - m_s = 0$

2.4.3 Origin of the x-ray magnetic circular dichroism (XMCD) effect

The x-ray magnetic circular dichroism (XMCD) effect occurs when x-ray absorption (XA) spectra of a magnetic sample are measured with circularly polarized x-rays. The shape of the XA spectrum changes upon reversal of the photon helicity, i.e. the relative absorption intensities of the L_2 and L_3 edges shift with respect to each other. A dichroic effect becomes visible when the two spectra are directly compared to each other. The sample magnetization and the photon wave vector are aligned parallel or antiparallel with respect to each other while recording the spectra. Switching the magnetization direction of the sample has the same effect as switching the photon helicity. The relative alignment of wave vector and sample magnetization is important because the quantization axis is defined along the magnetization direction or the external magnetic field and a photon angular momentum q can only be defined according to a quantization axis.

The XMCD effect can be explained by a two-step model. The first step describes the excitation of a core electron by an x-ray photon and the second step concerns the absorption of the excited electron by an empty electronic state, i.e. a hole state. Angular momentum conservation demands that if a circularly polarized photon is absorbed, the angular momentum has to be transferred to the excited electron. Through spin-orbit coupling, a part of the angular momentum can be transferred to the spin and a spin polarized electron is created^[5,9,10,52].

The magnetism is introduced into the model by an imbalance in the occupation of the spin up and spin down band which is present in a magnetic sample. This means that in a simple band model the density of states is exchange split at the Fermi level with an unequal number of spin up and spins

down holes in the valence shell/band (Chap. 2.2). The valence shell acts as a "spin detector". Fig. 2.11 gives the statistical weights for the excitation from the spin orbit split 2p core levels ($2p_{1/2}$ and $2p_{3/2}$) to the 3d valence level. As both spin orientations have opposite signs of the XMCD signal, the dichroic signal vanishes if an equal number of spin up and spin down electrons occupy the 3d band. Thus, the measured signal directly correlates to the spin imbalance at the Fermi-level. This effect can be used to calculate the spin magnetic moment from an experimental spectrum (Chap. 2.2.4 and 3.2.3).

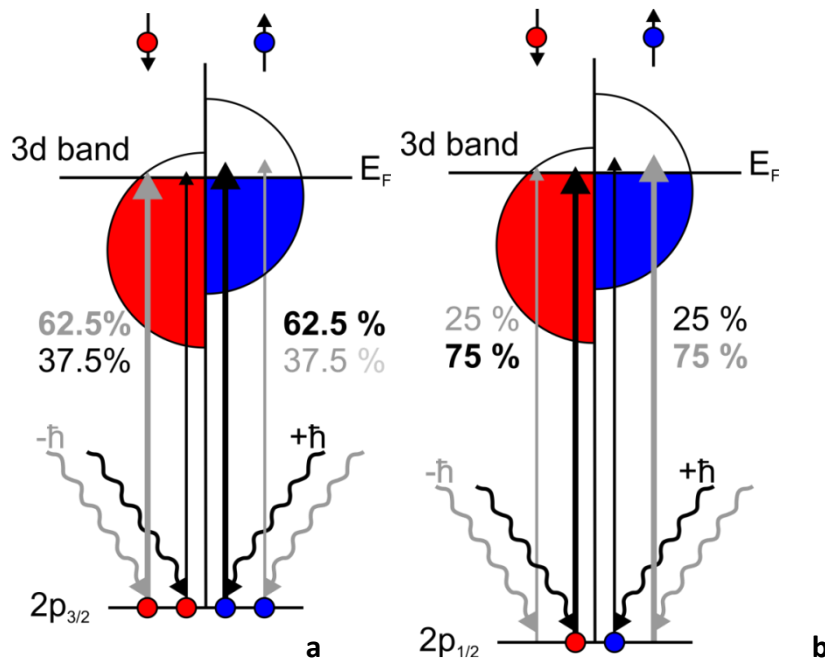


Figure 2.11 Relative transition probabilities for spin up (↑) and spin down (↓) electrons from the spin orbit split 2p levels, i.e. $2p_{3/2}$ (a) and $2p_{1/2}$ (b) level upon excitation with circularly polarized photons with $q = \pm 1$ ($q = -1 = -\hbar =$ transition marked in grey and $q = +1 = +\hbar =$ transitions marked in black)

Transition probabilities for the excitation of spin up or spin down electrons switch when the photon helicity is reversed. Positive ($q = +1$) circularly polarized light predominantly excites spin up electrons at the L_3 edge ($2p_{3/2} \rightarrow 3d$) and at the L_2 edge ($2p_{1/2} \rightarrow 3d$), it mostly excites spin down electrons. The situation is reversed for negative ($q = -1$) circularly polarized photons.

The electronic transitions from a ground state $|a\rangle$ with a configuration $|c, m_c, m_s\rangle$ to a final state $|b\rangle$ with $|l, m_l, m_s\rangle$ have to be evaluated, if relative intensities of the excitation of spin up / spin down electrons for either photon helicity want to be obtained, as e.g. given in Fig. 2.11. The statistical weights of the transition intensities can be calculated from the transition matrix elements under the constraint of the dipole selection rules. An expression for the transition matrix element can be derived from Eq. 2.33b and has the following form according to Stöhr and Wu^[12,52,53].

$$\langle n', l, m_l | P_{(1)}^{+1} | n, c, m_c \rangle = \sqrt{\frac{(c+m_c+2)(c+m_c+1)}{2(2c+3)(2c+1)}} R \quad (\text{Eq. 2.34a})$$

$$\langle n', l, m_l | P_{(1)}^{-1} | n, c, m_c \rangle = \sqrt{\frac{(c-m_c+2)(c-m_c+1)}{2(2c+3)(2c+1)}} R \quad (\text{Eq. 2.34b})$$

$$l = c + 1 \quad (\text{Eq. 2.35})$$

n (n') principal quantum number of the core (final) state
 c (l) orbital angular momentum quantum number of the core (final) state
 m_c (m_l) orbital magnetic quantum number of the core (final) state

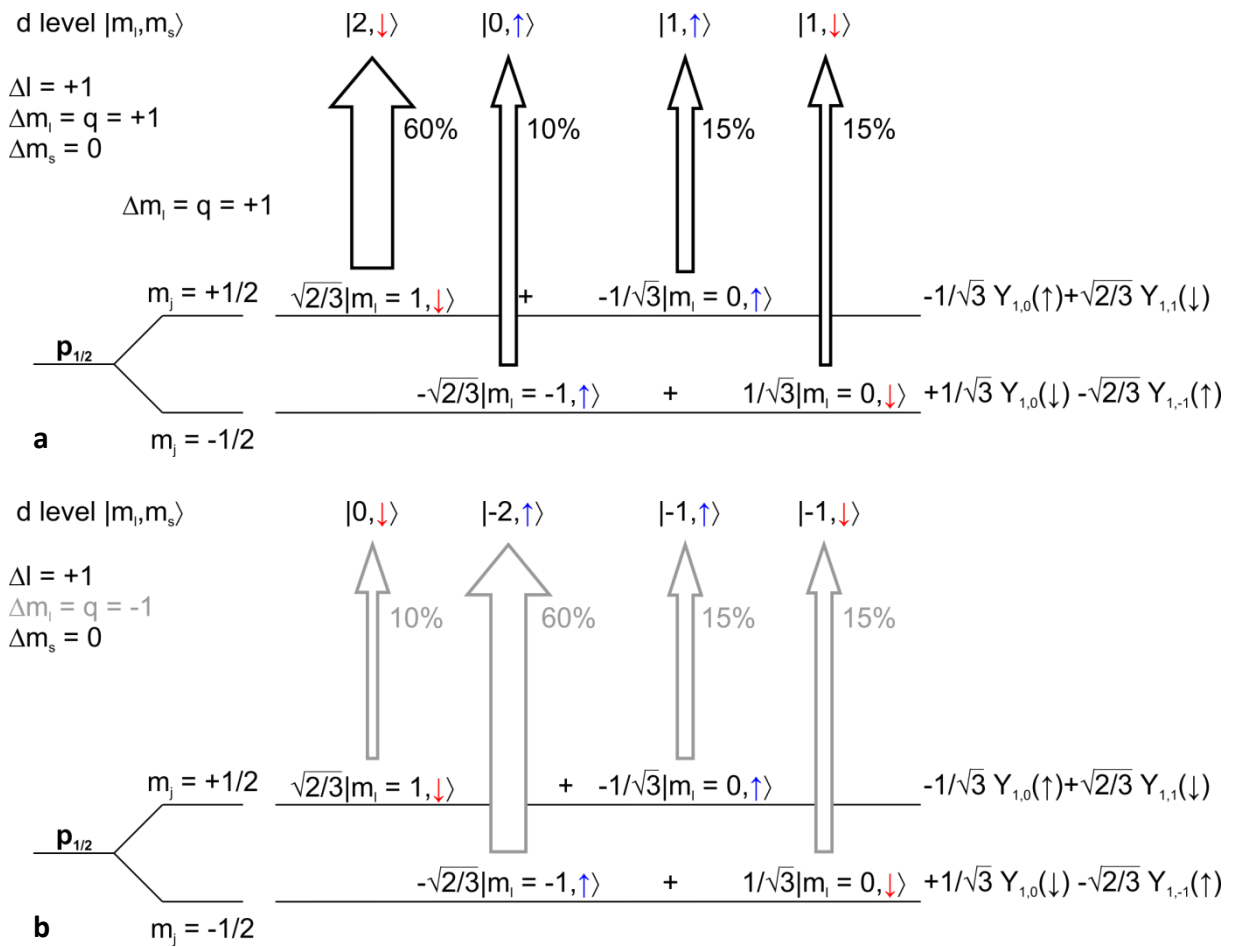


Figure 2.12 Transition probabilities from the different $m_j = \pm 1/2$ states (energetically identical) of the $p_{1/2}$ spin orbit split level into final d states in an LS coupling scheme (modified, from Ref. [9]) The statistical weights of the individual transitions are given for the absorption of either a photon with angular momentum **(a)** $q = +\hbar$ or **(b)** $q = -\hbar$. Thus, Δm_l equals $+1$ for Fig. 2.11a and $\Delta m_l = -1$ for Fig. 2.11b. \uparrow denotes spin up and \downarrow spin down states. The representation of the electronic state in terms of spherical harmonics is given on the right.

An example is given for the $2p_{1/2} \rightarrow 3d$ excitation with positive circularly polarized photons (Fig. 2.12a) and negatively polarized photons (Fig. 2.12b). The dipole transition operator is evaluated using one electron wave function of the form $Y_{l,m_l}\chi_{s,m_s}$ ^[12,52,53]. The total statistical weights for the different photon polarizations and edge combinations given in Fig. 2.11 are calculated by summing over all possible transitions to different m_l states within the 3d level, i.e. $m_l = -2, -1, 0, 1, 2$ for spin up or spin down electrons.

If the valence shell has an orbital angular momentum $l \neq 0$, it can act as orbital angular momentum detector. After the absorption of a negative ($q = -1$) circularly polarized photon, only transitions with $\Delta m_l = -1$ are allowed due to angular momentum conservation. The opposite is true for positive circularly polarized photons. If the final state has an imbalance in the occupation of m_l states, this imbalance can be probed similar to the spin imbalance. Dipole allowed transitions from 2p core states to different m_l valence states are given in Fig. 2.13. The orbital contribution to the magnetic moment can be derived from the experimental spectrum similar to the spin magnetic moments (Chap. 2.4.4 and Chap. 3.2.3).

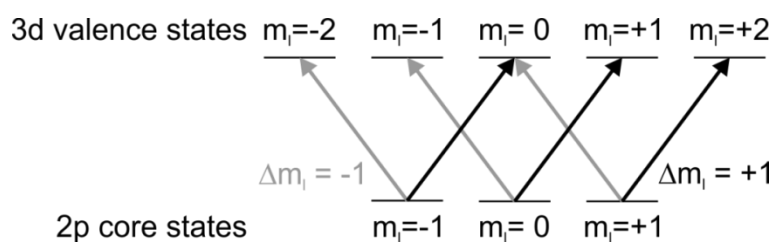


Figure 2.13 Sensitivity of the XMCD effect of orbital magnetism^[54]

The experimental XMCD signal itself is defined as the difference between an absorption spectrum recorded with antiparallel alignment of the photon angular momentum with respect to the sample magnetization axis and an absorption spectrum recorded with parallel alignment.

2.4.4 Sum rules

2.4.4.1 Intensity sum rule

Following Eq. 2.28, the resonant absorption intensity is directly proportional to the number of unoccupied states in the receiving shell. This means for the $L_{2,3}$ edge that the intensity is proportional to the number of empty 3d states. This is schematically illustrated and by the XA spectra of iron, cobalt and nickel. The spectral intensity drops as more and more 3d states become occupied (Fig. 2.14a/b).

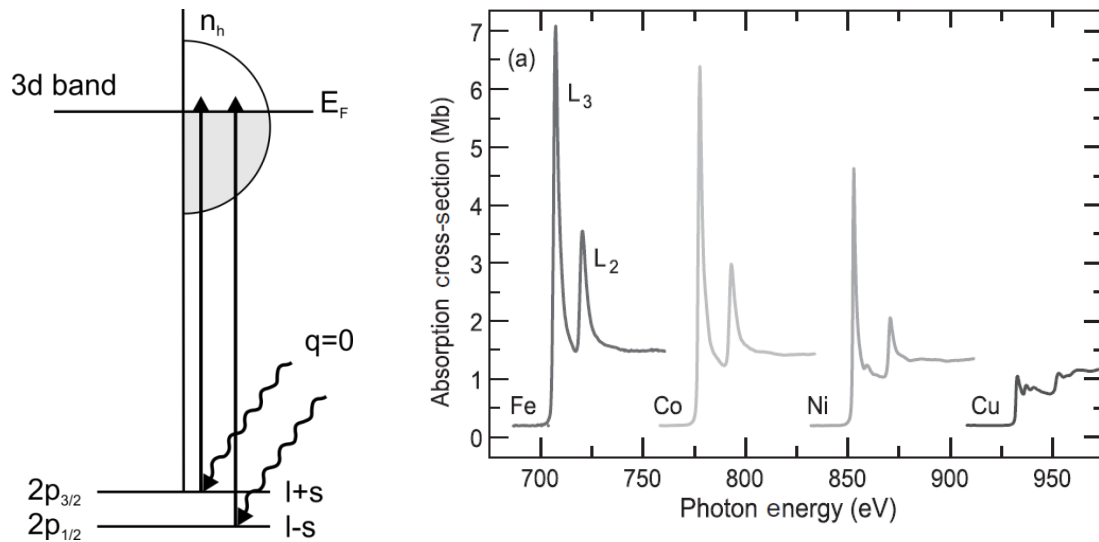


Figure 2.14 Illustration of the intensity sum rule by **(a)** a scheme of the absorption of linearly polarized x-ray photons and **(b)** normalized $L_{2,3}$ edge x-ray absorption spectra of the 3d metals iron, cobalt, nickel and copper^[5]
The absorption intensity drops with increasing number of 3d electrons, i.e. less holes in the valence band.

The absorption intensity I is sometimes called the "white line" intensity. This is a historical term. The strong signals of resonant absorption appeared white on the black background of the then used photographic plates.

The number of valence holes n_h in the ground state can be directly related to the absorption intensity via the so called intensity or charge sum rule for a core to valence transition $n c \rightarrow n' l$ (with $c = l - 1$)

$$I = I_{L_2} + I_{L_3} = C n_h \quad (\text{Eq. 2.36})$$

$$C = A R^2 \frac{l}{3(2l+1)} \quad (\text{Eq. 2.37})$$

C	constant
R	radial transition matrix element
L	orbital angular momentum of the valence / final state
c	orbital angular momentum of the core / initial state
l	orbital angular momentum of the valence / initial state
A	as defined in Eq. 2.29

2.4.4.2 Spin and orbital sum rule

Since the sensitivity of the XMCD effect for the spin has an opposite sign at both edges and the sensitivity for the orbital moment is the same at both edges, a comparison of the dichroic profiles at

both edges through appropriate addition / subtraction can cancel out one contribution^[9]. A set of so called sum rules was derived during the early 1990s which link the spectral intensities to the projection of the spin and orbital magnetic moments of the sample^[37,55-57]. A key issue was the elimination of the radial matrix elements. This was achieved by using the ratio of magnetic and nonmagnetic absorption profiles^[9].

The spin sum rule^[55] links the dichroism intensities to the spin magnetic moment of the sample (Eq. 2.38a/b). The second term in the spin sum rule includes the so-called magnetic dipole term $\langle T_z \rangle$. It might become prominent in anisotropic samples like surfaces or thin films because it takes into account a possible anisotropy in the spin distribution^[58]. The prefactors (a - d) in Eq. 2.38a are chosen for $2p \rightarrow 3d$ transition (Eq. 2.38b). The orbital magnetic moment can also be determined by a sum rule^[56] (Eq. 2.39a/b).

$$\frac{-\left(\int_{j_+} (\mu^+(E) - \mu^-(E)) \cdot dE - b \int_{j_-} (\mu^+(E) - \mu^-(E)) \cdot dE\right)}{\int_{j_+ + j_-} (\mu^+(E) - \mu^-(E) + \mu^0(E)) \cdot dE} = \frac{c \langle S_z \rangle + d \langle T_z \rangle}{n_h} \quad (\text{Eq. 2.38a})$$

$$\frac{-\left(\int_{L_3} (\mu^+(E) - \mu^-(E)) \cdot dE - 2 \int_{L_2} (\mu^+(E) - \mu^-(E)) \cdot dE\right)}{\int_{L_2 + L_3} (\mu^+(E) - \mu^-(E) + \mu^0(E)) \cdot dE} = \frac{\frac{2}{3} \langle S_z \rangle + \frac{7}{3} \langle T_z \rangle}{n_h} \quad (\text{Eq. 2.38b})$$

$$\frac{\int_{j_+ + j_-} (\mu^+(E) - \mu^-(E)) \cdot dE}{\int_{j_+ + j_-} (\mu^+(E) - \mu^-(E) + \mu^0(E)) \cdot dE} = a \frac{\langle L_z \rangle}{n_h} \quad (\text{Eq. 2.39a})$$

$$\frac{\int_{L_2 + L_3} (\mu^+(E) - \mu^-(E)) \cdot dE}{\int_{L_2 + L_3} (\mu^+(E) - \mu^-(E) + \mu^0(E)) \cdot dE} = \frac{1}{2} \frac{\langle L_z \rangle}{n_h} \quad (\text{Eq. 2.39b})$$

j_+, j_-	transitions from spin orbit split core levels
μ^+	XA spectrum recorded with positive circularly polarized light; $q = +\hbar$
μ^-	XA spectrum recorded with negative circularly polarized light; $q = -\hbar$
μ_0	XA spectrum recorded with linearly polarized light; $q = 0$
n_h	number of holes in the final state / shell
a, b, c,	prefactors

An example of the application of the sum rules is given in Chap. 3.2.3. The application of sum rules is restricted by approximations which were done during their derivation. For the derivation of the sum rules, please refer to the literature, e.g. Refs. [55-57,59,60]. Here only the most important conditions will be mentioned for the case of the L edge^[9]:

- the $2p \rightarrow 4s$ transition intensity should be negligible

- The radial matrix element should not strongly vary with energy and should not be significantly different for $j_i = l_i + 1/2$ and $j_i = l_i - 1/2$ excitations.

2.4.5 Summary of the XMCD effect

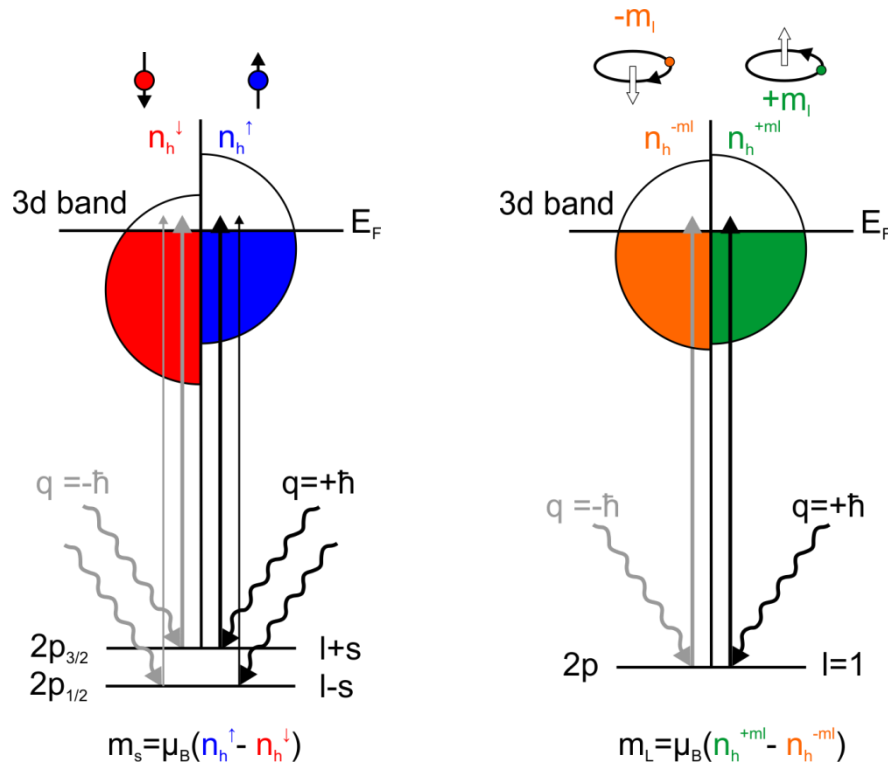


Figure 2.15 Probing of (a) spin and (b) orbital magnetic moment by XMCD spectroscopy

The imbalance of spin up and spin down electrons (or the number of holes) in the valence shell gives rise to a net spin magnetic moment m_s . If the valence shell has an orbital angular momentum quantum number $l \neq 0$, a net orbital angular momentum can arise if the m_l states are not equally occupied.

The dipole selection rules demand that the orbital angular quantum number l changes by ± 1 . If we consider the excitation of electrons from the 2p state, a transition to the 4s state is possible. However, it is about 40 times weaker than the transition to the 3d states ^[61]. Therefore, we can neglect the contributions of the 2p \rightarrow 4s transition in the following when analyzing $L_{2,3}$ edge spectra. The spin and orbital contribution to the total magnetic moment of a sample can be determined by XMCD spectroscopy. An exchange splitting of the valence shell leads to an imbalance in spin up and spin down electrons / holes. This causes a net spin magnetic moment to arise. This imbalance can be probed by circularly polarized x-rays because additional selection rules apply compared to using linearly polarized photons, i.e. $\Delta m_l = q = 0, \pm 1$. These result in different absorption intensities for the various combinations of initial core state and photon helicity (Fig. 2.15a). If the final state has got an

orbital angular momentum $l \neq 0$, it can also be probed by XMCD spectroscopy. The imbalance in m_l holes creates an orbital magnetic moment which can be accessed through the orbital sum rule (Fig. 2.15b).

2.5 References

- [1] ASHCROFT, N. W., MERMIN, N. D., *Solid State Physics*; Brooks / Cole CENGAGE Learning, **1976**
- [2] HABERLAND, H., KLEINERMANN, K., TRÄGER, F., **Bergmann-Schäfer**, *Lehrbuch der Experimentalphysik Band 5 - Gase, Nanosysteme, Flüssigkeiten*, Cluster, 2nd Ed.; Walter de Gruyter, **2006**; pp 819
- [3] KRONMÜLLER, H., LAMBECK, M., *Bergmann-Schäfer Band 6: Festkörper*, Magnetismus im Festkörper, Raith, W., Ed.; Walter de Gruyter, **1992**
- [4] STEFANITA, C.-G., *Magnetism*; Springer, **2012**
- [5] STÖHR, J., SIEGMANN, H. C., *Magnetism - From Fundamentals to Nanoscale Dynamics*; Springer, **2006**
- [6] *Lecture Notes Magnetism goes Nano: Electron Correlation, Spin Transport, Molecular Magnetism*; Forschungszentrum Jülich in der Helmholtz Gemeinschaft, **2005**
- [7] GETZLAFF, M., *Fundamentals of Magnetism*; Springer, **2008**
- [8] *Quantum Phenomena in Clusters and Nanostructures*; KHANNA, S. N., CASTLEMAN, A. W., Eds.; Springer, **2010**
- [9] SCHÜTZ, G., GOERING, E., HERMANN, S. Synchrotron Radiation Techniques Based on X-ray Magnetic Circular Dichroism. In *Handbook of Magnetism and Advanced Magnetic Materials*; Kronmüller, H., Parkin, S., Eds.; John Wiley & Sons, Ltd., 2007; Vol. 3
- [10] STÖHR, J., *X-ray magnetic circular dichroism spectroscopy of transition metal thin films*, Journal of Electron Spectroscopy and Related Phenomena **1995**, 75, 253
- [11] STÖHR, J., *Exploring the microscopic origin of magnetic anisotropies with X-ray magnetic circular dichroism (XMCD) spectroscopy*, Journal of Magnetism and Magnetic Materials **1999**, 200, 470
- [12] FUNK, T., DEB, A., GEORGE, S. J., WANG, H., CRAMER, S. P., *X-ray magnetic circular dichroism-a high energy probe of magnetic properties*, Coord. Chem. Rev. **2005**, 249, 3
- [13] PAULI, W., JR., *Über Gasentartung und Paramagnetismus*, Zeitschrift für Physik **1927**, 41, 81
- [14] CURIE, P., *Lois expérimentales du magnétisme. Propriétés magnétiques des corps à diverses températures*, Ann. Chim. Phys. **1895**, 5, 289
- [15] SLATER, J. C., *Atomic Shielding Constants*, Physical Review **1930**, 36, 57
- [16] SOMMERFELD, A., BETHE, H., **Handbuch der Physik**, *Aufbau der zusammenhängenden Materie*, Elektronentheorie der Metalle, Geiger, H., Scheel, K., Smekal, A., Eds.; Springer, **1933** Vol. 24/2
- [17] ASHCROFT, N. W., MERMIN, N. D., *Festkörperphysik*, 4th ed.; Oldenbourg Verlag München, **2013**
- [18] BECHTHOLD, P. S., *Lecture Notes Magnetism goes Nano: Electron Correlations, Spin Transport, Molecular Magnetism*, Clusters to Nanostructures; Forschungszentrum Jülich in der Helmholtz Gemeinschaft, **2005**
- [19] ELMORE, W. C., *The Magnetization of Ferromagnetic Colloids*, Physical Review **1938**, 54, 1092

-
- [20] FARLE, M., *Lecture Notes Magnetism goes Nano - Electron Correlations, Spin Transport, Molecular Magnetism*, Magnetic Nanoparticles; Forschungszentrum Jülich in der Helmholtz Gemeinschaft, **2005**
- [21] GERLACH, W., STERN, O., *Der experimentelle Nachweis der Richtungsquantelung im Magnetfeld*, Zeitschrift für Physik **1922**, 9, 349
- [22] GERLACH, W., STERN, O., *Der experimentelle Nachweis des magnetischen Moments des Silberatoms*, Zeitschrift für Physik **1922**, 8, 110
- [23] BILLAS, I. M. L., CHÂTELAIN, A., DE HEER, W. A., *Magnetism from the Atom to the Bulk in Iron, Cobalt, and Nickel Clusters*, Science **1994**, 265, 1682
- [24] KNICKELBEIN, M. B., *Spin relaxation in isolated molecules and clusters: The interpretation of Stern-Gerlach experiments*, Journal of Chemical Physics **2004**, 121, 5281
- [25] BUCHER, J. P., DOUGLASS, D. C., BLOOMFIELD, L. A., *Magnetic properties of free cobalt clusters*, Physical Review Letters **1991**, 66, 3052
- [26] KHANNA, S. N., LINDEROTH, S., *magnetic behavior of clusters of ferromagnetic transition metals*, Physical Review Letters **1991**, 67, 742
- [27] KNICKELBEIN, M. B., *Nickel clusters: The influence of adsorbates on magnetic moments*, The Journal of Chemical Physics **2002**, 116, 9703
- [28] REDDY, B. V., NAYAK, S. K., KHANNA, S. N., RAO, B. K., JENA, P., *Physics of nickel clusters. 2. Electronic structure and magnetic properties*, Journal of Physical Chemistry A **1998**, 102, 1748
- [29] BILLAS, I. M. L., BECKER, J. A., CHÂTELAIN, A., DE HEER, W. A., *Magnetic moments of iron clusters with 25 to 700 atoms and their dependence on temperature*, Physical Review Letters **1993**, 71, 4067
- [30] KNICKELBEIN, M. B., *Adsorbate-induced enhancement of the magnetic moments of iron clusters*, Chemical Physics Letters **2002**, 353, 221
- [31] XU, X., YIN, S., MORO, R., LIANG, A., BOWLAN, J., DE HEER, W. A., *Metastability of Free Cobalt and Iron Clusters: A Possible Precursor to Bulk Ferromagnetism*, Physical Review Letters **2011**, 107, 057203
- [32] KNICKELBEIN, M. B., *Magnetic moments of bare and benzene-capped cobalt clusters*, The Journal of Chemical Physics **2006**, 125, 044308
- [33] PAYNE, F. W., JIANG, W., EMMERT, J. W., DENG, J., BLOOMFIELD, L. A., *Magnetic structure of free cobalt clusters studied with Stern-Gerlach deflection experiments*, Physical Review B **2007**, 75, 094431
- [34] XU, X. S., YIN, S. Y., MORO, R., DE HEER, W. A., *Magnetic moments and adiabatic magnetization of free cobalt clusters*, Physical Review Letters **2005**, 95, 237209
- [35] KNICKELBEIN, M. B., *Nickel clusters: The influence of adsorbed CO on magnetic moments*, The Journal of Chemical Physics **2001**, 115, 1983
- [36] APSEL, S. E., EMMERT, J. W., DENG, J., BLOOMFIELD, L. A., *Surface-enhanced magnetism in nickel clusters*, Physical Review Letters **1996**, 76, 1441
- [37] CHEN, C. T., IDZERDA, Y. U., LIN, H. J., SMITH, N. V., MEIGS, G., CHABAN, E., HO, G. H., PELLEGRIN, E., SETTE, F., *Experimental Confirmation of the X-Ray Magnetic Circular Dichroism Sum Rules for Iron and Cobalt*, Physical Review Letters **1995**, 75, 152
- [38] SCOTT, G. G., STURNER, H. W., *Magnetomechanical ratios for iron-cobalt alloys*, Phys. Rev. **1969**, 184, 490
- [39] SCOTT, G. G., *Investigation of the Einstein-de Haas Effect for Cobalt and for the Co-Ni Alloys*, Physical Review **1966**, 148, 525
-

- [40] CHEN, C. T., SMITH, N. V., SETTE, F., *Exchange, spin-orbit, and correlation effects in the soft-x-ray magnetic-circular-dichroism spectrum of nickel*, Physical Review B **1991**, 43, 6785
- [41] VOGEL, J., SACCHI, M., *Polarization and angular dependence of the $L_{2,3}$ absorption edges in Ni(110)*, Physical Review B **1994**, 49, 3230
- [42] SCOTT, G. G., RECK, R. A., *Magnetomechanical ratios and spin and orbital moments for nickel-copper alloys*, Phys. Rev. B **1973**, 8, 233
- [43] KITTEL, C., *On the Gyromagnetic Ratio and Spectroscopic Splitting Factor of Ferromagnetic Substances*, Physical Review **1949**, 76, 743
- [44] PELZL, J., MECKENSTOCK, R., SPODDIG, D., SCHREIBER, F., PFLAUM, J., FRAIT, Z., *Spin-orbit-coupling effects on g -value and damping factor of the ferromagnetic resonance in Co and Fe films*, Journal of Physics: Condensed Matter **2003**, 15, S451
- [45] EINSTEIN, A., DE HAAS, W. J., *Experimenteller Nachweis der Ampereschen Molekularströme*, Verhandlungen Deutsch Physikalische Gesellschaft **1915**, 17, 152
- [46] FERMI, E., *Nuclear Physics*; Univeristy Chicago Press: Chicago, **1950**
- [47] SCHIFF, L. I., *Quantum Mechanics*, 3rd ed.; McGraw-Hill: New York, **1968**
- [48] MANDL, F., SHAW, G., *Quantum Field Theory*; Wiley: New York, **1993**
- [49] LOUDON, R., *The Quantum Theory of Light*; Clarendon: Oxford, **1973**
- [50] SHORE, B. W., MENZEL, D. H., *Principle of atomic spectra*; Wiley New York, **1968**
- [51] COWAN, R. D., *Theory of atomic structure and spectra*; University of California Press Berkley, **1981**
- [52] STÖHR, J., WU, Y. X-ray Magnetic Circular Dichroism: Basic concepts and theory for 3d transition metal atoms. In *New Direction in Research with Third-Generation Soft X-ray Synchrotron Radiation Sources*; Schlachter, A. S., Wuillemumier, F. J., Eds.; Kluwer: Amsterdam, 1994
- [53] BETHE, H. A., SALPETER, E. E., *Quantum Mechanics on one and two electron atoms*; Plenum Press: New York, **1977**
- [54] LAU, J. T., *Magnetische Eigenschaften kleiner massenseparierter Übergangsmetallcluster*, **Doctoral Thesis**, 2002, Universität Hamburg
- [55] CARRA, P., THOLE, B. T., ALTARELLI, M., WANG, X., *X-ray circular dichroism and local magnetic fields*, Physical Review Letters **1993**, 70, 694
- [56] THOLE, B. T., CARRA, P., SETTE, F., VANDERLAAN, G., *X-ray circular dichroism as a probe of orbital magnetization*, Physical Review Letters **1992**, 68, 1943
- [57] CARRA, P., *X-ray circular dichroism as a probe of orbital and spin magnetizations*, Synchrotron Radiation News **1992**, 5, 21
- [58] SIPR, O., MINAR, J., EBERT, H., *On the importance of the magnetic dipole term T_z in analyzing X-ray magnetic circular dichroism spectra of clusters*, Europhysics Letters **2009**, 87
- [59] THOLE, B. T., LAAN, G. V. D., *Systematics of the Relation between Spin-Orbit Splitting in the Valence Band and the Branching Ratio in X-Ray Absorption Spectra*, EPL (Europhysics Letters) **1987**, 4, 1083
- [60] CARRA, P., *Sum rules for X-ray absorption and dichroism*, Journal of Electron Spectroscopy and Related Phenomena **1997**, 86, 139
- [61] EBERT, H., STÖHR, J., PARKIN, S. S. P., SAMANT, M., NILSSON, A., *L-edge x-ray absorption in fcc and bcc Cu metal: Comparison of experimental and first-principles theoretical results*, Physical Review B **1996**, 53, 16067

3. EXPERIMENTAL METHODS - THE GAMBIT SETUP

The experimental approach we followed to record XMCD spectra of isolated clusters in the gas phase will be explained in this chapter. Cluster generation by laser vaporization (Chap. 3.1.1) and detection via Fourier Transform-Ion Cyclotron Resonance (FT-ICR) mass spectrometry (Chap. 3.1.2) are introduced. A paragraph will deal with the modifications of the FT-ICR done to be able to record XMCD spectra (Chap. 3.1.3). These modifications are discussed in detail in the doctoral thesis of Heinrich Kampschulte^[1]. A brief introduction about synchrotron radiation is given in Chap. 3.1.4. Total Ion Yield spectroscopy as recording principle of x-ray absorption spectra is explained (Chap. 3.1.5) and followed by a paragraph on the collisional cooling procedure employed to reach cluster temperatures of about 20 K (Chap. 3.1.6). The data acquisition (Chap. 3.2.1), data analysis (Chap. 3.2.2) and application of sum rules (Chap. 3.2.3) are explained. The used procedures were developed together with my co-workers Sergey Peredkov and Matthias Tombers. Sergey Peredkov also programmed the data evaluation program which I used for the evaluation of all spectra presented within this thesis. The chapter is concluded by a paragraph on the scaling of the experimental moments extracted from the experimental spectra. Scaling means the calculation of the intrinsic magnetic moment from the measured projection onto the quantization axis (Chap. 3.2.5).

All spectra shown in this chapter were recorded by an experimental team consisting of Sergey Peredkov, Matthias Tombers and myself. A first paper the experimental procedure of recording x-ray absorption spectra by our experimental approach was published in 2011 (Chap. 3.4.1). The manuscript was mainly drafted by our collaboration partners Sergey Peredkov and Matthias Neeb. Together with S. Peredkov I recorded the XA spectra of the vanadium clusters, Nb_{13}^+ and Co_{22}^+ and assisted S. Peredkov with the data evaluation. Chap. 3.4.2 contains a manuscript about the x-ray absorption spectrum of Nb_{13}^+ which was drafted by a theory group from the Research Center for Nanoscale Structure of Matter, Southern Federal University, Rostov-on-Don, Russia. My contribution relates to the presented experiments.

3.1 Experimental setup

3.1.1 Laser vaporization source

A laser vaporization^[2,3] (LVap) source is used to produce ionic transition metal clusters (Fig. 3.1). The source consists of three major building blocks, i.e. the piezoelectric valve, the expansion / interaction block and the expansion channel.

The second harmonic of a Nd:YAG Laser (Spitlight 200, Innolas; 20 Hz) is focused onto a rotating metal target. A homebuilt piezoelectric valve^[4] produces a gas pulse (40 μ s, helium backing pressure in the range of 10 - 20 bar) prior to the laser shots. Target and valve are oriented in a 90° angle with respect to each other (Fig. 3.2). The metal plasma, created by the laser pulse, is cooled down within the supersonic expansion of the helium gas. Cluster formation takes place in the connecting expansion channel. No further ionization step is needed as positive as well as negative ions are formed^[5,6]. The charge of the cluster ions, which will be investigated, is selected by the bias of the following ion optics. The size distribution within the cluster beam ranges from the singly charged ion to clusters of about 30 - 40 atoms per cluster^[5-8]. The center of the cluster distribution can be influenced by adjusting the source parameters, i.e. the timing between gas pulse and laser shot, the amount of gas expanded into the chamber, laser power and applied source voltages.

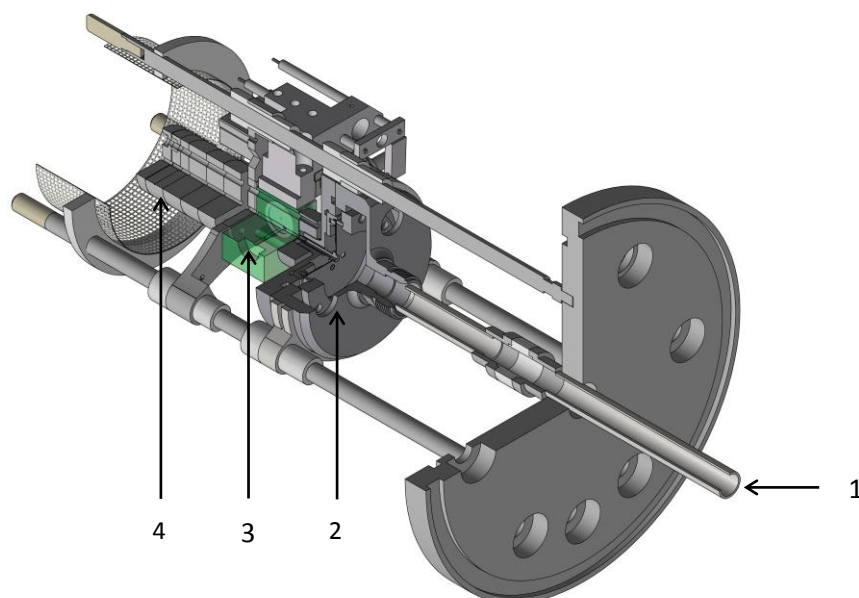


Figure 3.1 Schematic drawing LVap source^[9]

(1) gas inlet (2) piezoelectric valve, (3) expansion / interaction block, (4) expansion channel of variable length

Thin metals foils were used as target material (thickness 0.4 - 0.5 mm). The cobalt foil was purchased from Alfa Aesar (purity 99,95 %). In the cases of iron and nickel mono isotopic target materials were

purchased (Oak Ridge National Laboratory, Fe-56, purity 99.93 % and Ni-58, purity 99.61 %). This was necessary to prevent signal dilution due to intensity distribution over several peaks because of the different iron or nickel isotopes.

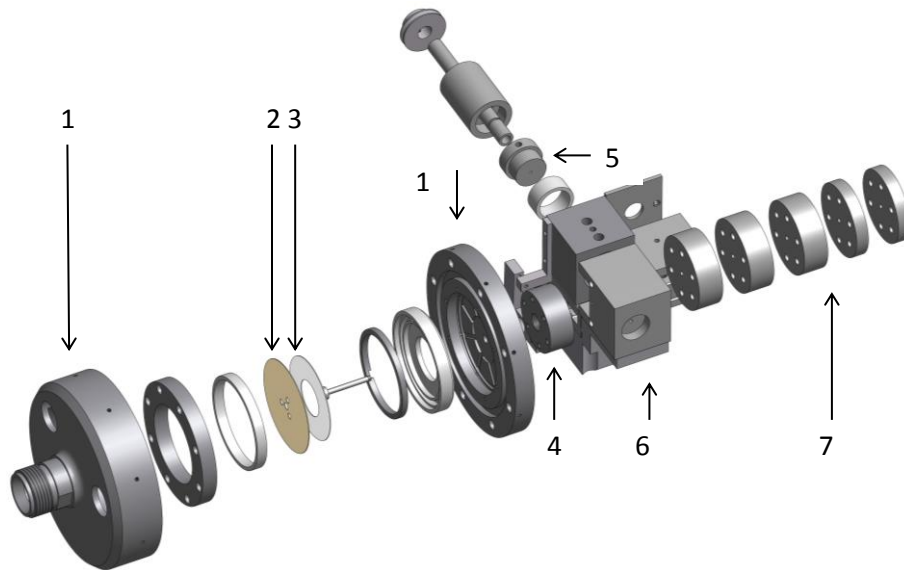


Figure 3.2 Schematic drawing of the piezoelectric valve & source block^[9] (1) housing, (2) titanium disk, (3) piezo ceramic, (4) expansion nozzle, (5) target mount with target, (6) expansion / interaction block, (7) single element of the expansion channel

3.1.2 Fourier Transform - Ion Cyclotron Resonance (FT-ICR) mass spectrometry

The concept of ion cyclotron resonance was discovered during the 1930s by E. O. Lawrence^[10,11]. Ions will be trapped on circular orbits if an alternating electric field is applied perpendicular to a high magnetic field. The angular frequency (ion cyclotron resonance) of the ion motion is independent of the radius of the orbit the ions are circling on. The principle was used to construct the first ICR-mass spectrometers in the beginning of the 1950s^[12,13]. In the mid-1970s Fourier Transform (FT) - ICR was introduced by Comisarov and Marshall^[14-16].

The radius of the ion motion is influenced by two opposing forcing, i.e. the Lorentz and Centrifugal force.

$$F_L = qv_{xy}B \quad (\text{Eq. 3.1})$$

$$F_{cf} = \frac{mv_{xy}^2}{r} \quad (\text{Eq. 3.2})$$

F_L	Lorentz force
q	charge of the ion ($q = z \cdot e$)
z	number of charges
e	elementary charge
v_{xy}	velocity of the ion in the xy plane
B	magnetic field
F_{cf}	Centrifugal Force
m	ion mass
r	radius of the ion's orbit

Thus, the ion radius can be described by the following equation:

$$r = \frac{mv_{xy}}{qB} \quad (\text{Eq. 3.3})$$

Upon substitution of v_{xy} by the angular velocity ω_c , we insert the cyclotron frequency f_c into the equation:

$$v_{xy} = r\omega_c \quad (\text{Eq. 3.4})$$

$$\omega_c = 2\pi f_c = \frac{qB}{m} \quad (\text{Eq. 3.5a})$$

$$f_c = \frac{qB}{2\pi m} \quad (\text{Eq. 3.5b})$$

The cyclotron frequency is proportional to the mass to charge (m/z) ratio but independent of the initial ion velocity in the xy-plane (Eq. 3.5b).

An ICR cell consists of two excitation plates facing each other and providing the radio frequency for the alternating electric field. A frequency sweep is applied to the excitation plates to accelerate the ions and their orbits increase. The spectrum is recorded by measuring an image current induced in two detection plates when the ions pass by the plates (Fig. 3.3).

Two additional plates to the excitation and detection plates, the so called trapping plates, confine the ions in the z-axis^[13]. As a result, an ion can be stored within the cell for minutes^[17,18] or even up to hours^[19,20]. However, as the ions have an initial velocity along the z-axis, the trapping leads to an oscillatory motion, which is called trapping motion. Additionally, the ions move along an electrostatic

potential. This motion is mass independent and called magnetron motion. The cyclotron and the trapping motion are superimposed on the magnetron motion ^[21,22] (Fig. 3.4).

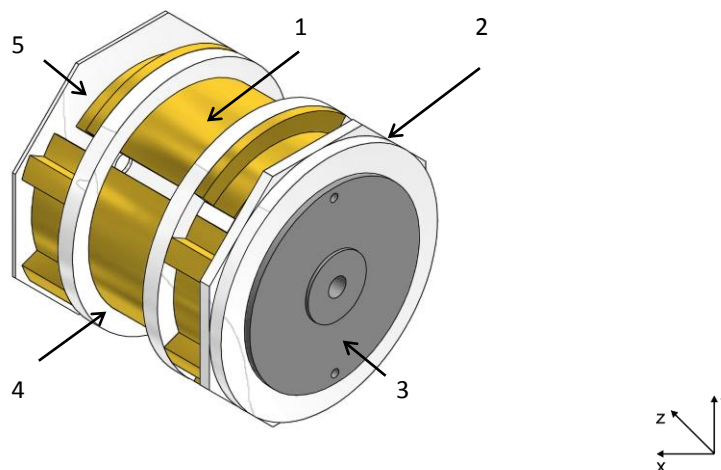


Figure 3.3 Sketch of the an ICR cell^[9] (design: Bruker Infinity Cell™)

(1) detection plate, (2) front trapping plate, (3) front electrode, (4) excitation plate, (5) back trapping plate

The ICR cell body consists of four plates, two trapping and two detection plates. Plates of the same designation face each other. Two additional plates are installed in the horizontal axis of the cell. These are the so called trapping plates which confine the ion along the z-axis. A hole in the front trapping plate allows the ions to enter. A light or electron beam can be coupled into the ICR cell through a hole in the back trapping plate.

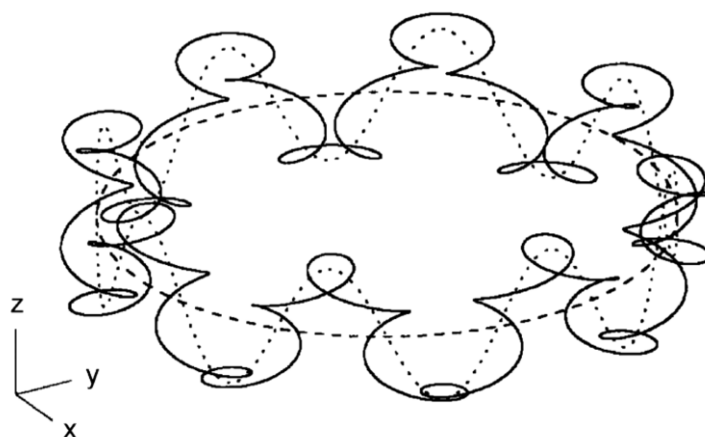


Figure 3.4 Representation of the ion motions within an Infinity trap^[22]

The pure magnetron motion is shown as dashed line and the magnetron motion plus the trapping motion as dotted line. The solid line shows the overall motion including the cyclotron motion

The ICR cell installed in the Bruker Apex IV FT-ICR mass spectrometer, used for the experiments presented in this thesis, is a so called Infinity Cell^[23]. The trapping plates are segmented. The resulting electrostatic potential causes a virtual expansion of the ICR cell to infinity along the z-axis^[19]. This allows longer storage times because of a more effective trapping of the ions.

The ICR cell does not only function as an ion trap but can also be used as a mass selector. Mass selection is achieved by application of a frequency sweep excluding the resonance frequency of the selected m/z-ratio. All remaining ions are excited onto much higher orbits than for detection. These orbits are unstable and thus ions are ejected from the ICR cell.

3.1.3 FT-ICR mass spectrometer with cryogenic trap

A commercially available Bruker Apex IV FT-ICR mass spectrometer has been modified. A quadrupole bending unit was installed to allow the attachment of multiple ion sources at the same time. An ion beam produced by the LVap is bent by 90° onto the magnetic field axis and transferred into the ICR cell (Fig. 3.5a).

Additionally, a cryogenic ICR cell was installed. A brief description will be given in this thesis for further reading refer to the doctoral thesis of H. Kampschulte^[1]. The cryo trap consists of two actively cooled copper tubes which are connected to a two stage Sumitomo cold head (model cold head SRDK-408S2, compressing unit W-71D). The copper tubes are connected to the ICR cell and thus enable the heat transport from the cell to the cold head. Three passive copper shields are installed to prevent radiative heating of the actively cooled inner stages and the ICR cell by the vacuum housing. Three thermocouples are placed within the instrument to constantly monitor the temperature (CernoxTM, calibrated from 4 - 325 K, LakeShore) (Fig. 3.4b).

The first sensor (sensor A) is directly attached to the inner (i.e. the colder) cooling stage at the base of cold head. The second sensor (sensor B) is mounted within the copper shielding and attached to the outer active cooling stage (i.e. the warmer). The third sensor (sensor C) is located at the ICR cell and mounted on the copper base supporting the ICR cell. The temperature within the system can be adjusted by a heating element located at the first cooling stage. The temperature can be varied by adjusting the output power of the element while the cold head is working. Temperatures up to 130 K at the ICR cell can be stabilized. The ICR cell itself can be cooled down as low as 18 K.

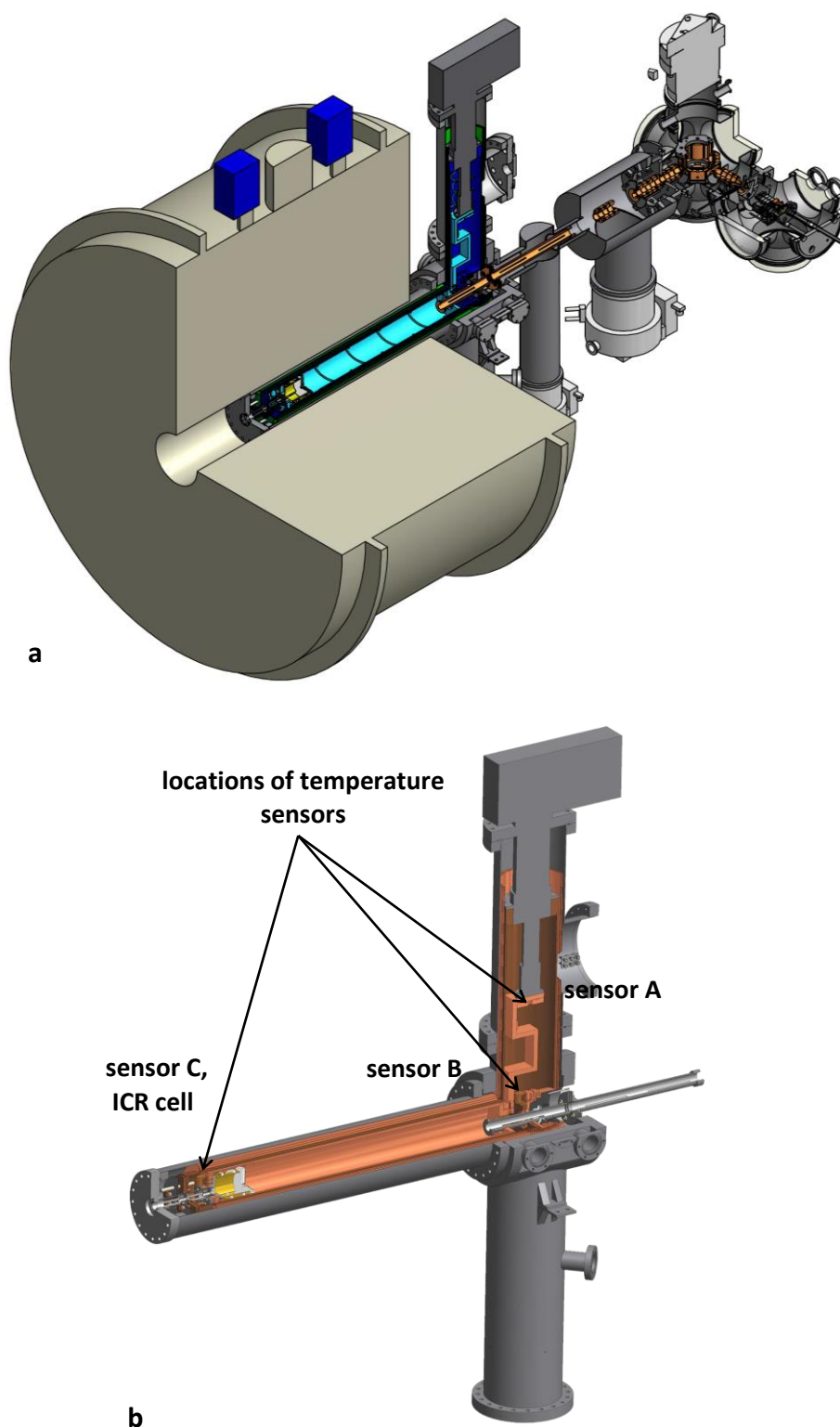


Figure 3.5 Experimental setup^[9]

(a) modified FT-ICR mass spectrometer as used for the experiments (GAMBIT setup). Ions are produced by the LVac and transferred into the high field region of the superconducting solenoid ($B = 7$ T) via electrostatic lenses and a quadrupole bending unit where the ICR cell is located. Ion storage, mass selection and detection all take place inside the ICR cell. **(b)** Detailed view of the cryogenic modifications, including the location of the temperature sensors used to monitor the temperatures within the setup.

3.1.4 Synchrotron radiation

The FT-ICR mass spectrometer was coupled to an undulator beamline at the synchrotron radiation facility BESSY II of the "Helmholtz Zentrum Berlin für Materialien und Energie". All x-ray absorption spectra presented in this thesis were recorded at the soft x-ray undulator beamline UE52-PGM. Only a brief introduction into synchrotron radiation will be given here. Detailed introductions into the field of synchrotron radiation can be found in the literature, e.g. in references [24-26].

Synchrotron radiation is emitted by relativistic particles when they are radially accelerated. In the case of BESSY II, electrons with a kinetic energy of 1.7 GeV are produced, accelerated and transferred into a storage ring. The storage ring consists of straight segments and deflecting dipole magnets. Every time an electron passes through a dipole magnet synchrotron radiation is emitted. The x-ray beam is then transferred via a beamline to an experimental endstation. Energy losses of the electrons due to light emittance are compensated by reacceleration of the electrons within three radio frequency (RF) cavities located within the storage ring.

A further enhancement of the photon flux can be achieved by using an undulator instead of a bending magnet as outcoupling device. Undulators are located within the straight segments of the storage ring. An additional oscillary motion of the electron is induced by the magnets of the undulator (Fig. 3.6a). If the light wave emitted by an electron interferes constructively with second light wave emitted by the same electron further along its orbit, x-ray radiation will be emitted. Undulator radiation is more brilliant compared to x-ray radiation emitted by bending magnets. However, the photon energy has to be continuously adjusted as the undulator is "a line source"^[27]. Undulator radiation shows sharp peaks at characteristic energies, i.e. the so called harmonics. This is achieved by varying the magnetic field the electrons experience when passing through the undulator by adjusting the gap between the two magnetic arrays of the undulator (Fig. 3.6).

The property of an undulator to produce circularly polarized x-ray radiation is important for the experiments presented in this thesis. The magnetic arrays above and below the electron orbit are each split in half. Circularly polarized light is emitted by shifting the magnetic arrays with respect to each other and thus forcing the electron onto an elliptical orbit (Fig. 3.6b)

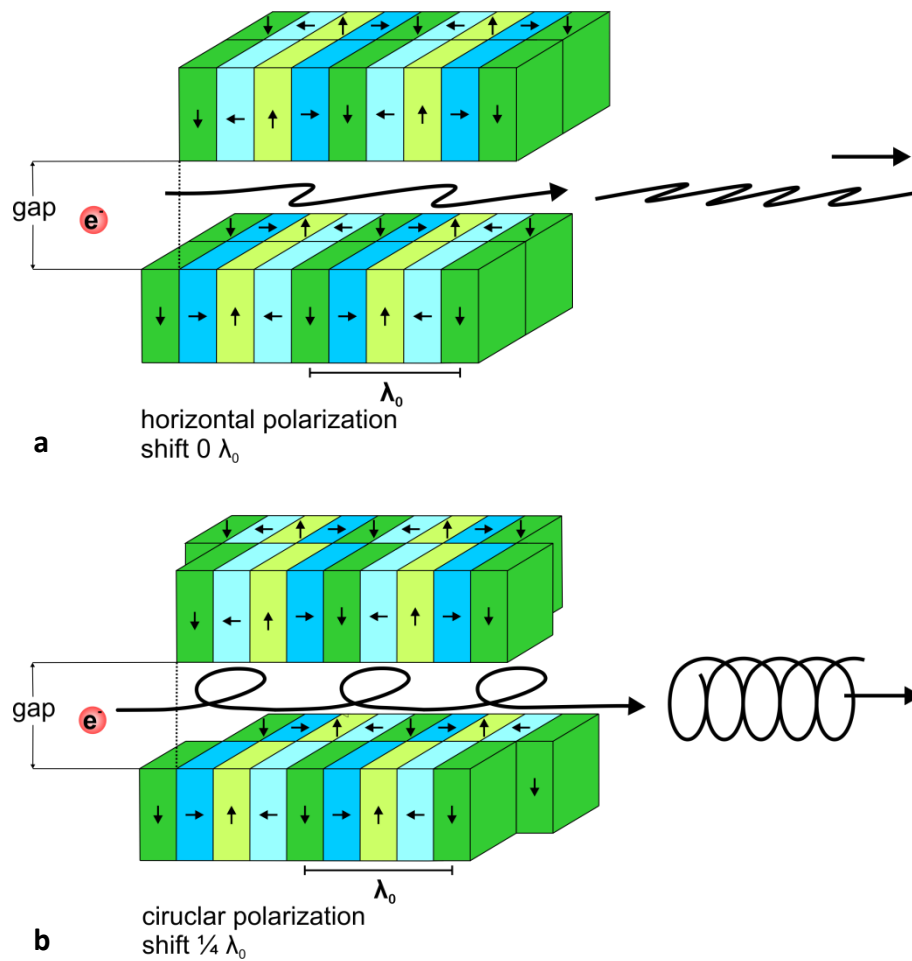


Figure 3.6 Magnetic structure of an APPLE2 undulator (advanced planar polarized light emitter)^[28-30] **(a)** setting of the permanent magnets for horizontal photon polarization **(b)** Setting of the permanent magnets for circular photon polarization
The polarization of the outgoing x-ray beam can be varied by horizontal movement / shifting of the permanent magnets with respect to each other. λ_0 denotes the period length of the magnetic array. The emitted photon energy can be adjusted by varying the gap between the upper and lower panel, i.e. the magnetic field the electrons experience while passing through the undulator. Taken from Wende, *et al.*^[27]

Table 3.1 Technical specifications of the UE52-PGM undulator beamline at BESSY II^[31]

energy range	85 - 1600 eV (soft x-ray regime)
resolving power at 400 eV	> 10000
polarization	variable
degree of polarization	90 %
photon flux (500 eV - 1000 eV)	> 10^{12} photons / s
divergence	0.8 mrad x 0.2 mrad

3.1.5 Total Ion Yield spectroscopy of isolated clusters

X-ray absorption spectra in the soft x-ray regime are typically measured in total electron yield (TEY) or total fluorescence yield (TFY)^[32,33]. Both methods measure the response of a sample after the absorption of x-ray photons. In TEY the electron drain in a sample is measured after the emission of electrons due to the formation of core holes after the absorption of an x-ray photon and subsequent excitation of core electrons. TFY monitors the occurrence of fluorescence after the formation of a core hole. A direct transmission experiment as for hard x-rays is unfavorable due to the low penetration depth of the soft x-rays^[32]. The enhanced absorption coefficient for soft x-rays compared to hard x-rays results in a penetration depth of a few nanometers.

Our sample is a cloud of cluster ions in gas phase. The ions are trapped within the ICR cell and can be exposed to the x-ray beam for a given amount of time. TEY is not applicable as means of detection as we do not have a stationary sample which we could measure an electron drain from. TFY would be a possible way of detection for a gas phase sample. However, our experimental geometry and the extremely low target density rule out this method, too. A direct absorption spectroscopy would be compatible with our experimental geometry but the target density is too low to measure an attenuation of the incident x-ray beam after passing through the sample. The clusters density within the ion cloud is about 10^6 cluster ions per cubic centimeters.

We are exploiting a secondary process following the photon absorption comparable to TEY and TFY. Both methods monitor processes which happen after a core hole is formed and an Auger electron emitted. We do not monitor the secondary electrons directly or the charging of the sample but the subsequent fragmentation of our clusters upon charging up. Auger electrons and secondary electrons are emitted from the clusters which will lead to a fragmentation of the cluster once the charge accumulated on the cluster can no longer be stabilized. Monitoring the fragment intensity is therefore a measure of the x-ray absorption. As the clusters are stored within the ICR cell, i.e. an ion trap, also the ionic fragments will be trapped. The fragment intensity can be measured by recording a mass spectrum after the exposure to the x-ray beam. This method of detection has been termed Total Ion Yield (TIY) spectroscopy^[34-37].

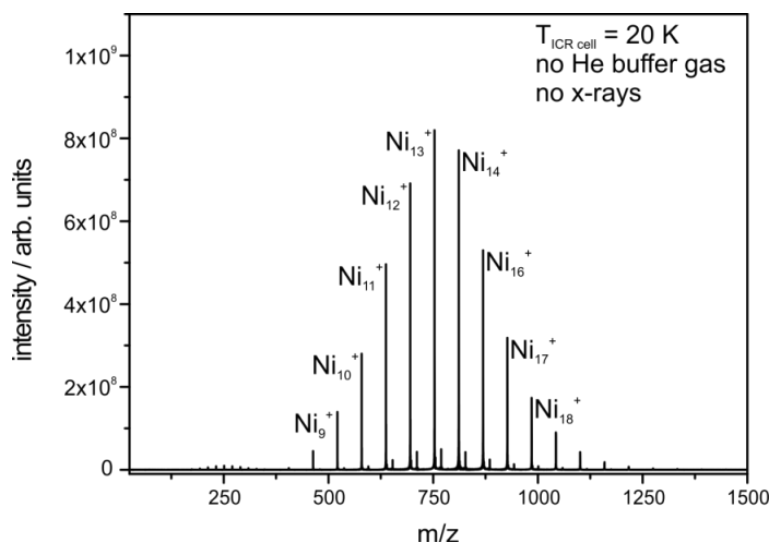


Figure 3.7 cluster distribution for nickel cluster cations with Ni_{13}^+ as central peak
The small peak to higher m/z with respect to the cluster signals is due to oxygen contamination in the source region.

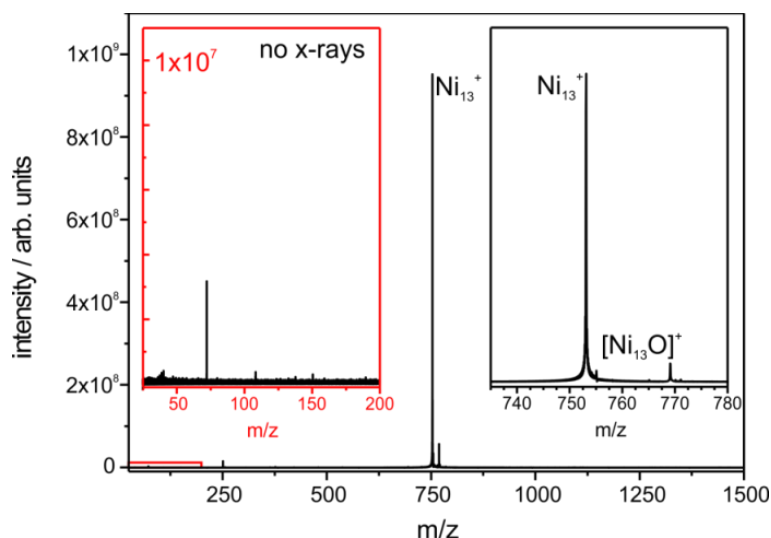


Figure 3.8 mass spectrum of Ni_{13}^+ after isolation, no x-ray exposure

A pulse of helium buffer gas was added to the ICR to cool down the clusters (see Chap. 3.1.6). No fragmentation products are visible in the low mass range (left (red) inset). The peak at m/z 72 in the left inset is a noise peak due to stray frequencies detected by the electronics. The right (black) inset shows a zoom of the parent cluster.

The x-ray absorption spectrum of one cluster size is measured by isolating this m/z prior to exposure to the x-ray beam. The cluster distribution is adjusted for the later to be selected cluster size to be the central peak within the distribution (Fig. 3.7). The cluster size is then selected. A mass spectrum with the experimental settings used in TIY mode is recorded to ensure no fragmentation without x-ray beam is present (Fig. 3.8).

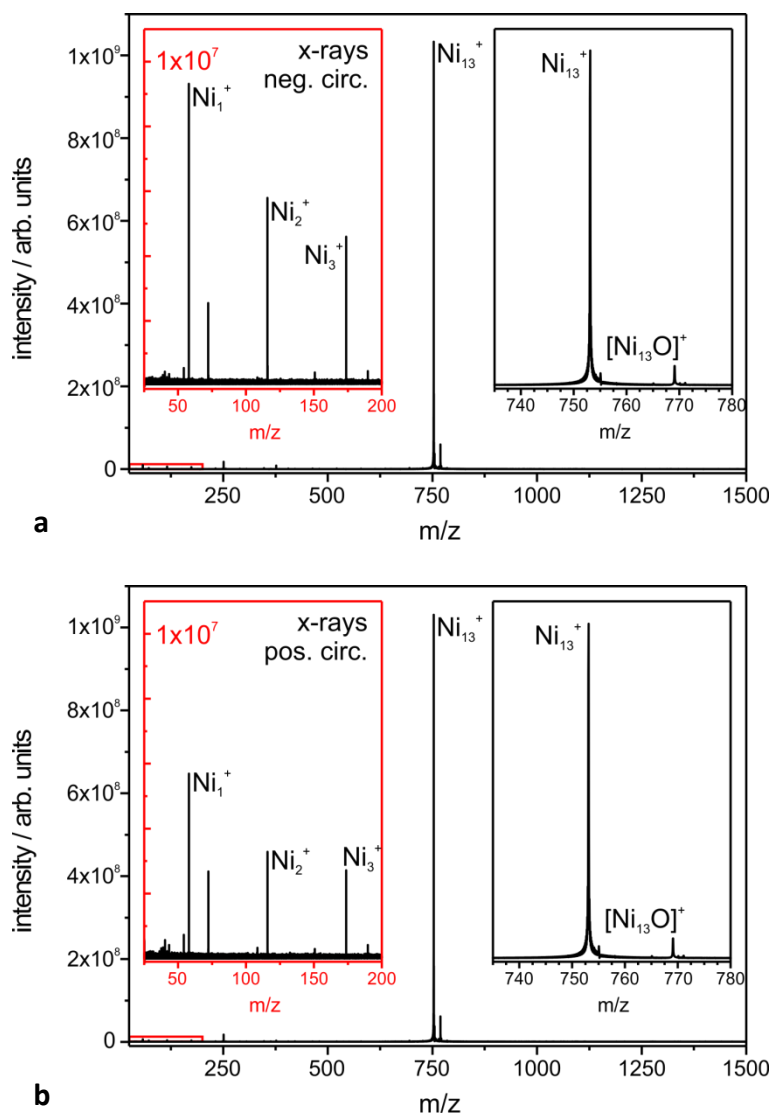


Figure 3.9 Mass spectra of Ni_{13}^+ after isolation and exposure to x-rays

(a) Ni_{13}^+ isolated and exposed to negative circularly polarized x-rays

The photon energy was set to 853 eV, i.e. the L_3 edge, with a photon flux of about $2 \cdot 10^{12}$ photons / s (ring current = 280 mA).

(b) Ni_{13}^+ isolated and exposed to positive circularly polarized x-rays

The photon energy was set to 853 eV, i.e. the L_3 edge, with a photon flux of about $1.5 \cdot 10^{12}$ photons / s (ring current = 250 mA).

The ICR cell was held at a temperature of 20 K. A pulse of helium buffer gas was added to the ICR to cool down the clusters (Chap. 3.1.6). The left (red) inset shows the main fragments Ni_1^+ , Ni_2^+ and Ni_3^+ . The peak visible in the left inset at m/z 72 is a noise peak due to stray frequencies detected by the electronics. The right inset shows a zoom of the parent cluster.

An illustration of the practical application of TIY spectroscopy is given in Fig. 3.9. The mass spectra for Ni_{13}^+ are measured after exposure to the x-ray beam for both circular photon polarizations with a photon energy which corresponds to the resonance at the L_3 edge. The differences in the fragment

intensities for Ni_1^+ , Ni_2^+ and Ni_3^+ stem from the different absorption cross sections for positive and negative circular photon polarizations. A second example can be found in the appendix (Chap. A.2.1). A comparison between mass spectra recorded with three different photon energies is given. The photon energies vary by one electron volt with the second corresponding to the resonance at the L_3 edge.

3.1.6 Collisional cooling

A defined cluster temperature is important to later extract the intrinsic magnetic moments from the experimental spectra. The experimentally accessible magnetic moments are the projections upon the quantization axis. In our experimental setup the quantization axis denoted z lies along the magnetic field axis which coincides with the propagation axis of the x-ray beam. The experimental accessible dichroic effect scales with the applied magnetic field and the cluster temperature according to a Brillouin / Langevin function. A cluster temperature in the low Kelvin range is necessary for a successful experiment because of the small magnetic moment of the clusters (Chap. 2.3.1, Chap. 2.3.2.2 and Chap. 2.4.3).

Cooling of the clusters can be achieved by introducing pre cooled helium buffer gas into the ICR cell. This procedure is termed collisional cooling. The clusters collide with the helium atoms and thereby transfer energy. If the amount of collisions a single cluster undergoes with the buffer gas is sufficient, it will thermalize to the temperature of the helium buffer gas.

Our experimental implementation of the collisional cooling will be briefly described in the following. Helium is pulsed into the ICR cell region using a General Valve (P/N 009-1632-900 VAC-1250PSIG). The gas is transported to the ICR cell through a spiral which is located at the inner (colder) cooling stage (Fig. 3.5). This ensures sufficient collisions between the helium and the tube wall to cool down the helium to the desired temperature. Once introduced into the ICR cell the cluster ions cool down via collisions with the cold helium atoms. The amount of gas is controlled by the helium backing pressure at the General Valve and the opening time of the General Valve. A vacuum gauge located in the UHV part of the instrument is used to monitor the amount of gas introduced into the instrument.

We conducted a set of experiments to ensure that a sufficient number of collisions occur to reach the desired cluster temperature. Afterwards, a "pump down delay" was introduced to reach a pressure of approximately $2 \cdot 10^{-8}$ mbar or lower before admitting the x-ray beam into the ICR cell. Polarization dependent XA spectra of Co_{11}^+ were recorded for different amounts of helium buffer gas and the resulting XMCD effect compared. Spectra were recorded for five different pressure readings at the ion gauge while the ICR cell temperature was kept constant at 20 K (individual XA spectra Fig. A.5 - A.9, individual experimental settings Tab. A.1). If the normalized XMCD spectra are compared to

each other, one finds that the dichroic effect at the L_3 edge is similar for all five experiments (Fig. 3.10). However, the effect at the L_2 edge shows a clear dependence of the amount of gas used. There is hardly any dichroic effect visible at the L_2 -edge for the two lowest pressure readings. A dichroic effect becomes visible when increasing the pressure reading up to approximately $9 \cdot 10^{-7}$ mbar. A further increase does not alter the spectral shape any more.

The above defined procedure for cooling the cluster ions was used for all experiments presented in this thesis. The final parameter set was taken from the experiment with a pressure reading of $1 \cdot 10^{-6}$ mbar (Tab. A.1). The parameters were gradually adjusted with time to keep the amount of gas used stable as the General Valve deteriorated with age.

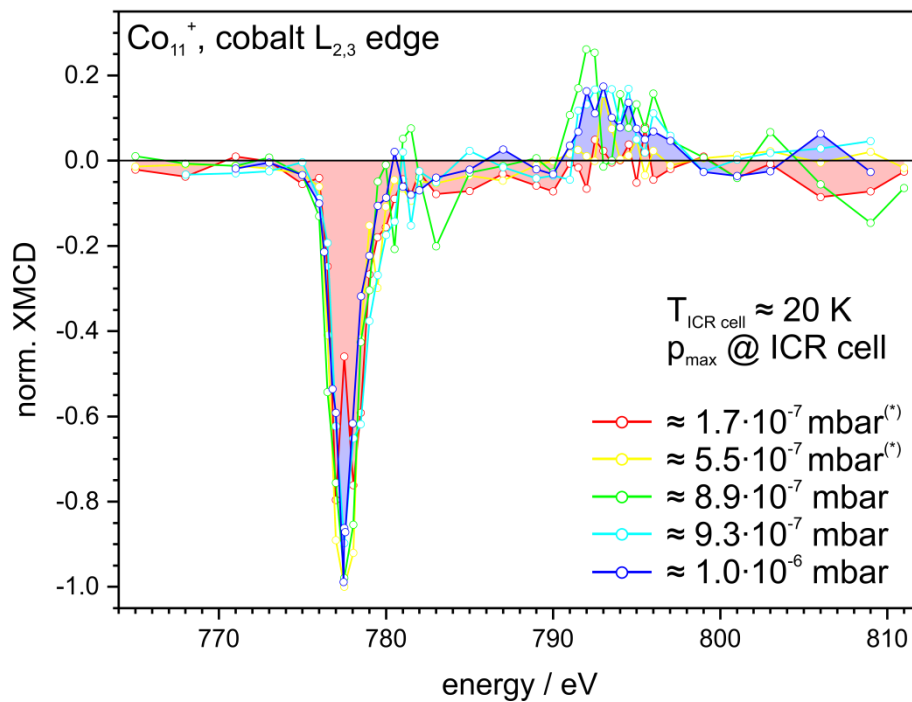


Figure 3.10 normalized XMCD intensity for helium buffer gas dependent experiments of Co_{11}^+

The individual XMCD spectra are calculated from a normalized pair of XA spectra. The XMCD spectra are normalized to the largest dichroic effect within the set of experiments. The red shaded area indicates the dichroic effect of the experiment with the least amount of gas. Whereas the blue area indicates the experiment in which the highest amount of buffer gas was used. One should note that the ion gauge is not located near the ICR cell and therefore the actual pressure in the ICR may differ from the recorded reading to monitor the used amount helium gas.

(*) Experiments of isolated Co_{11}^+ were not possible at the time of the experiment. A set of three clusters Co_{10}^+ , Co_{11}^+ and Co_{12}^+ was instead isolated with Co_{11}^+ as central peak.

3.2 Data acquisition & analysis

3.2.1 Data acquisition

In the following paragraph a description of the experimental procedure, which was followed to record an XMCD spectrum for an isolated cluster in the gas phase, will be given. Fig. 3.11 illustrates the process in a flow chart. While Fig. 3.11a states the main objective of each step, Fig. 3.11b gives a more detailed account on how the objective is achieved.

The inner most loop represents the recording of a single mass spectrum for a given photon energy. The ICR cell is filled by a certain number of "ion packages", each generated by a single laser shot. The exact number of shots depends on the performance of the cluster source and the ablation laser but usually ranged from ten to twenty shots. In the next step, the cluster size to be investigated is isolated. The clusters are cooled down by collisional cooling (Chap. 3.1.6). The introduced "pump down delay" before the admittance of the x-ray beam into the ICR cell is necessary to efficiently trap the fragment ions in the ICR cell. Immediately after the gas pulse, the background pressure in the ICR cell is too high to confine the low m/z fragments from the parent cluster fragmentation on stable orbits. The collisions with the helium atoms result in the loss of these stable orbits and subsequently fragments are ejected from the ICR cell, i.e. they collide with the ICR cell itself. Therefore, a pump down delay, i.e. a waiting time, was introduced before the clusters are irradiated by the x-ray beam. A beam shutter was used to control and time the admission of photons into the ICR cell. Typical irradiation times range from eight to thirteen seconds per mass spectrum.

A mass spectrum was recorded for each photon energy. Each saved mass spectrum was the sum of two individual mass spectra. At the same time the ring current in the storage ring was saved. The ring current was used to normalize the spectra to the incident photon flux. Therefore, the ring current was transformed to a flux value by means of a prior recorded calibration curve. The calibration curve takes the absorption of optical elements in the beamline into account. A table containing the photon energies, which were to be measured, was constructed before the experiment. The energy range and step size was adjusted according to the investigated transition metal and planned experiment. Once the mass spectra for all photon energies were measured, a file was saved that contained all mass spectra, the photon polarization was changed. This is done by changing the undulator shift from positive to negative or vice versa (Fig. 3.6b). The next XA spectrum was measured. Polarization dependent XA spectra were always taken in pairs to account for possible changes of the experimental conditions, i.e. either of the cluster source or of the x-ray beam.

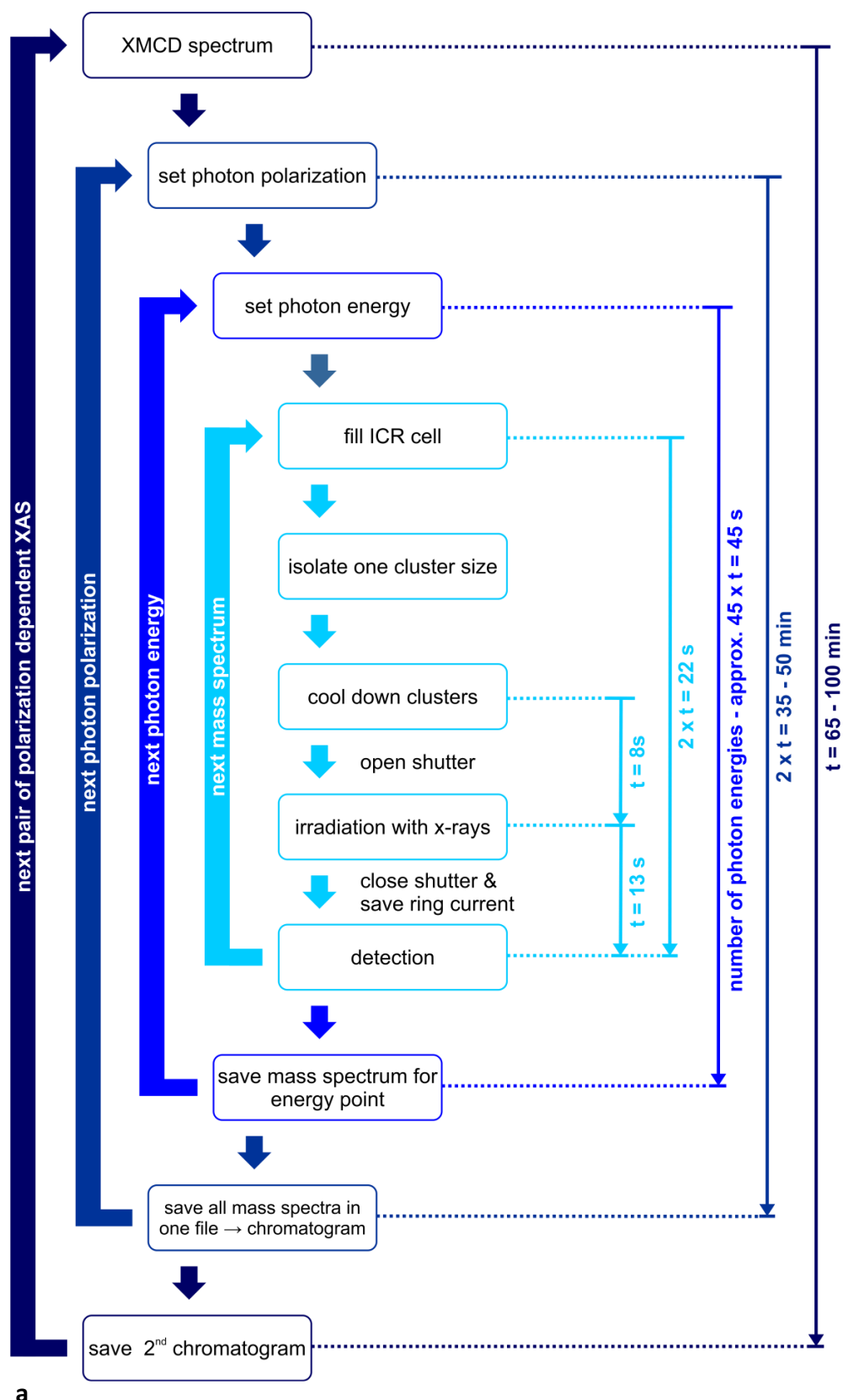


Figure 3.11 generalized acquisition procedure for recording XMCD spectra
(a) main objectives **(b)** realization of objectives
 The loops indicate the individual cycles needed to obtain an XMCD spectrum for a single cluster size: (1st, inner most) mass spectrum, (2nd) XAS, (3rd) pair of polarization dependent XAS, (4th, outer) XMCD spectrum

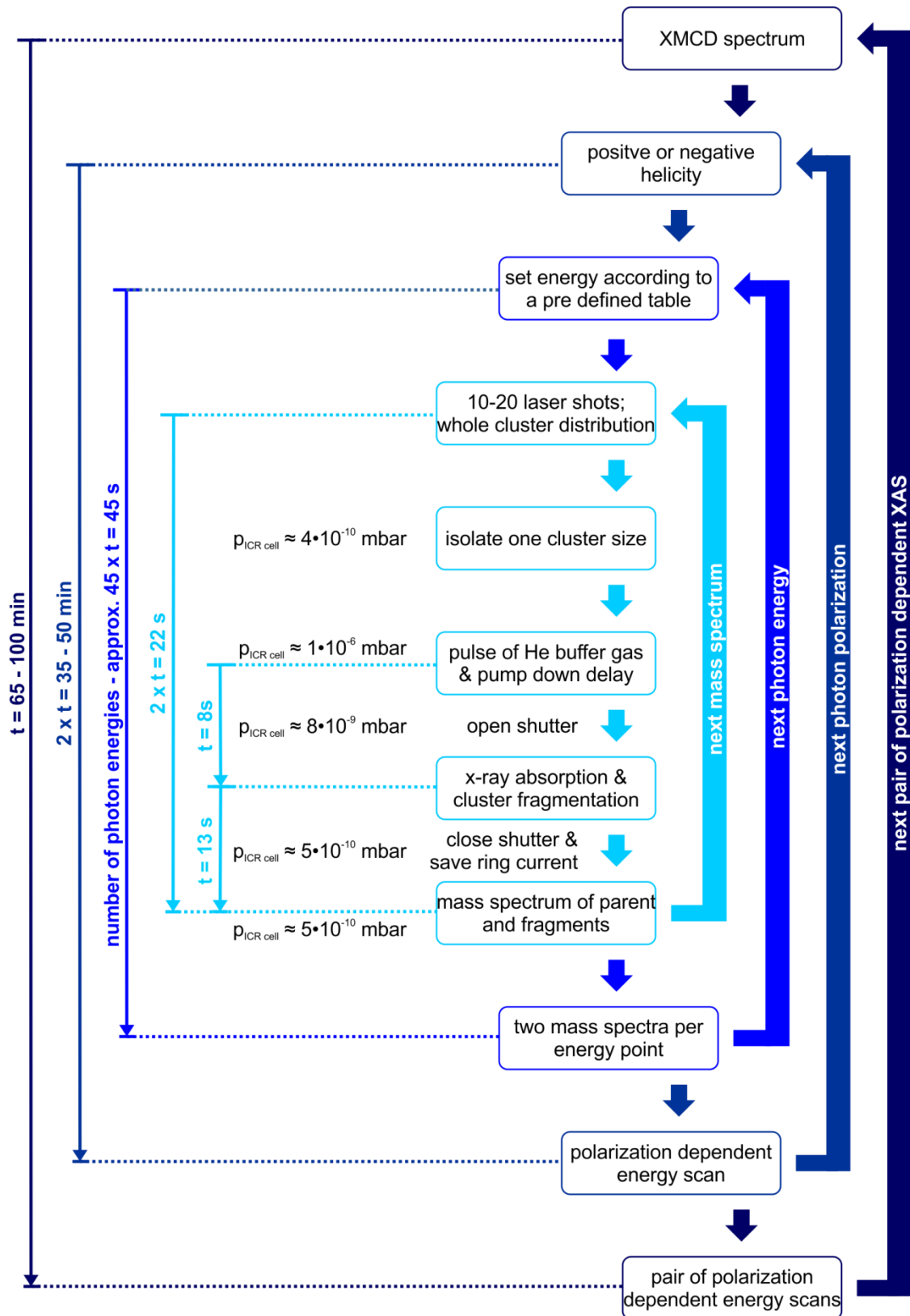


Figure 3.11 Photon energies are set prior to experiment according to the desired energy range and spectral resolution. The outer loop would be repeated until sufficient statistics were achieved to calculate magnetic moments from the XMCD spectrum. The times given in Fig. 3.11 are typical values needed to complete the indicated experimental step.

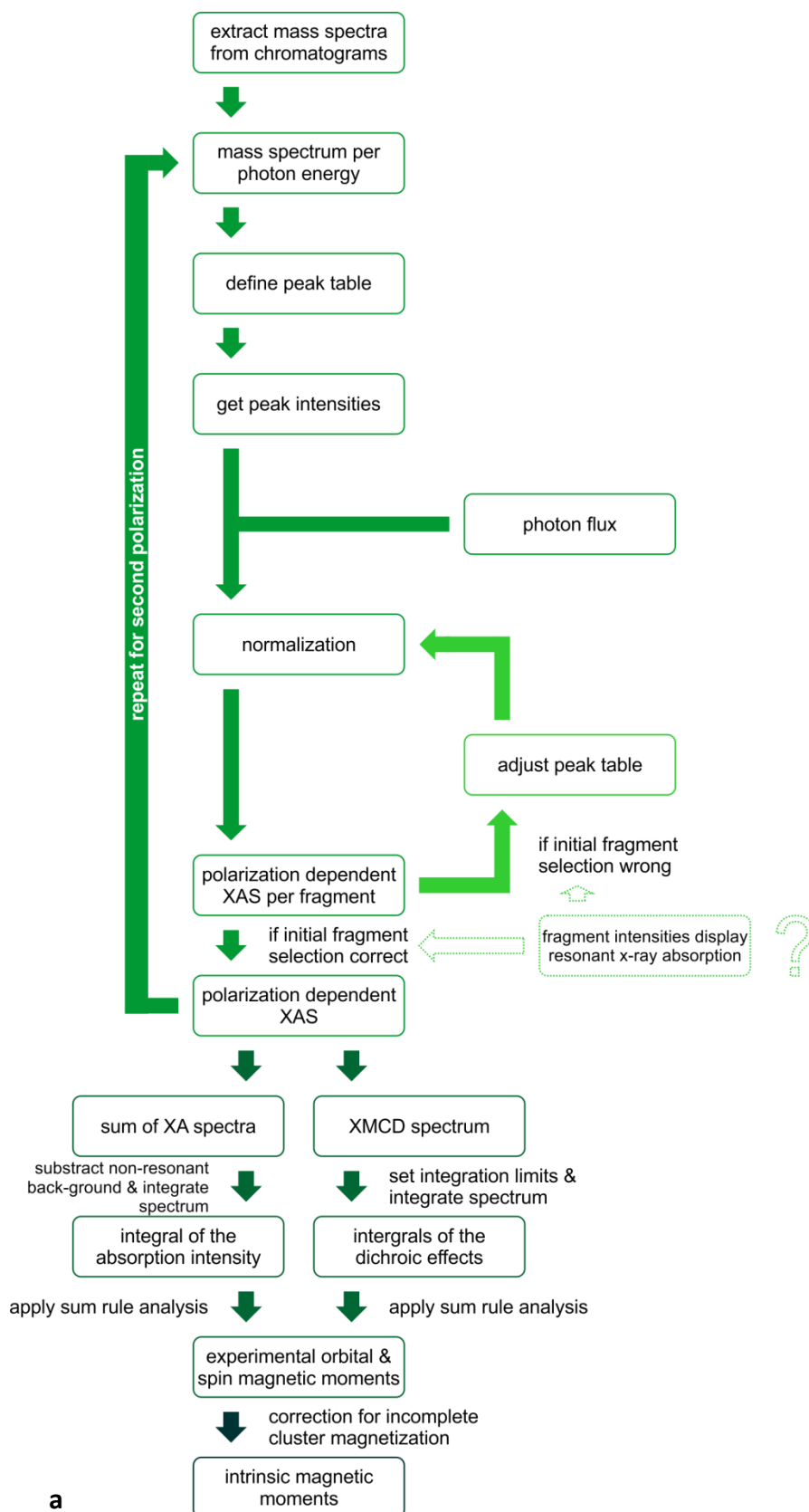
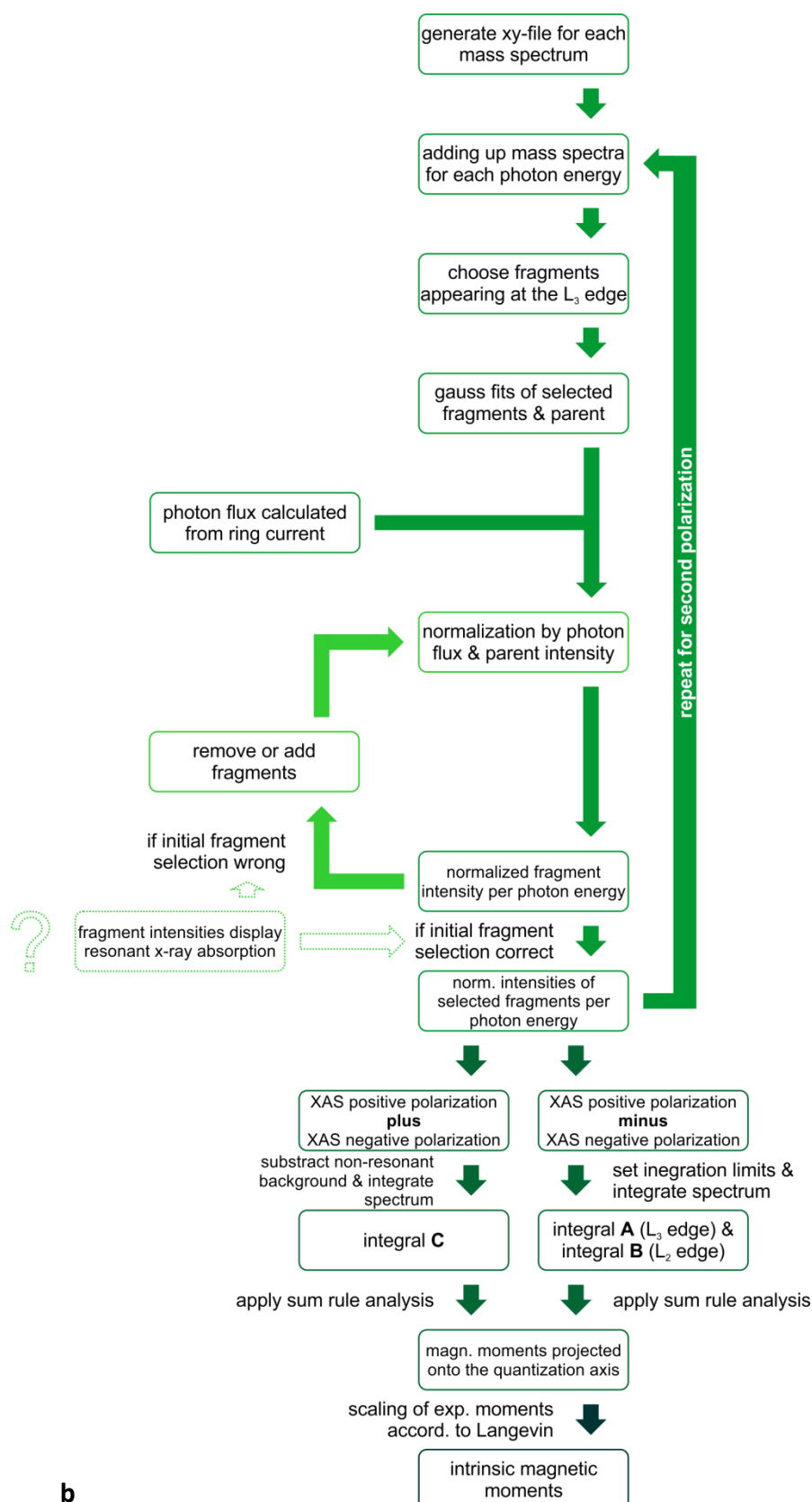


Figure 3.12 Scheme of the data analysis

(a) main objectives **(b)** realization of objectives

The main steps needed to extract magnetic moments from experimental data are illustrated in the flow charts.



b

Figure 3.12 The scheme illustrates how the data is processed to generate an XA spectrum. The outer loop corresponds to the calculation of the XA spectra for both polarizations. The small inner loop refers to the verification if all selected fragments show resonant behavior. Then the experimental magnetic moments $m_{L,z}$ and $m_{S,z}$ are extracted from the XMCD spectrum by sum rule analysis.

The outer cycle corresponds to the measurement of a pair of polarization dependent XA spectra. This cycle was repeated until the number of XA spectra per polarization yielded sufficient statistics to extract magnetic moments from the XMCD spectrum by sum rule analysis^[38-41].

3.2.2 Data analysis

The x-ray absorption spectra were calculated from the recorded mass spectra for each photon energy. The first step is the adding up of all individual mass spectra for one polarization to one final pair of mass spectra. This results in a better signal to noise ratio in the mass spectra and thus leads to a better statistic in the final XA spectrum (Fig. 3.11, outer loop). The fragment and parent intensities are extracted from these two final mass spectra by Gauss fits to the individual mass peaks.

The fragments which are used in the analysis are defined in a table which is individually adjusted for each parent cluster. A mass spectrum, which is accumulated of up to twenty individual mass spectra recorded at the L_3 resonance, is used to identify resonant fragments by checking against a mass spectrum taken without x-ray beam. The primary selection is again checked after the XA spectra are calculated. If the XA spectrum calculated from a single fragment shows the resonant structure of the L-edge, the fragment will be taken into account. The most common fragments in our experiment are the singly charged cation, dimer and trimer. However, depending on the cluster size other fragments might be added to the list. All fragments showing a resonant absorption structure are used in the final evaluation. A scheme including the individual steps done during the data analysis is given in Fig. 3.12a and 3.12b. Fig. 3.12a names the steps followed during the analysis while Fig. 3.12b indicates in more detail how each step is accomplished.

Each energy point is normalized to the parent cluster intensity to account for intensity variations of the cluster source with time. Additionally, the spectra are normalized to the photon flux which is calculated from the ring current in the storage ring and a calibration curve which accounts for photon absorption of optical elements in the beamline.

Once the XA spectra for both polarizations are calculated the magnetic moments can be extracted by the application of the sum rules (Chap. 3.2.3). The last step in the flow chart is the scaling of the experimental magnetic moments. This step is needed because under our experimental conditions the magnetic moments of the clusters are not completely aligned to the external magnetic field due to their temperature of $T > 0$ K and the finite external magnetic field. (Chap. 3.2.4)

3.2.3 Application of sum rules

The magnetic moments are extracted from the measured spectra by the application of the so called sum rules^[39-41] (Chap. 2.4.3 and 2.4.4). In this paragraph an example of the practical application of the

sum rules will be given. Fig. 3.13a shows the polarization dependent x-ray absorption spectra for Co_{16}^{+} . The integral intensities of the dichroic effects for both absorption edges have to be calculated from the XMCD spectrum (Fig. 3.13b). The XMCD spectrum is the difference of the XAS for positive (μ^+) and negative (μ^-) polarization. The absorption spectrum of horizontally polarized light (μ^0) is also needed for the application of the sum rules. However, it is rarely measured along with the positive and negative spectra and usually approximated by the average of both circular polarizations (μ^+ and μ^-) (Eq. 3.6a). Therefore, the integral in the denominator of the original formulation of the sum rules (Eq. 2.4.4) reduces to:

$$\mu^0(E) = \frac{\mu^-(E) + \mu^+(E)}{2} \quad (\text{Eq. 3.6a})$$

$$\mu^+(E) + \mu^-(E) + \mu^0(E) \approx \mu^+(E) + \mu^-(E) + \frac{(\mu^-(E) + \mu^+(E))}{2} \quad (\text{Eq. 3.6b})$$

$$\mu^+(E) + \mu^-(E) + \mu^0(E) \approx \frac{3}{2}(\mu^-(E) + \mu^+(E)) \quad (\text{Eq. 3.6c})$$

The integral experimental spectrum of ($\mu^+ + \mu^-$) has to be corrected for the non-resonant absorption caused by direct photo ionization processes before the integration^[32,33]. This is done by fitting a two-step function to the spectrum. The height of the steps is given as two thirds and one third of the tail intensity. This corresponds to the ratio of electrons located in the $2p_{3/2}$ and $2p_{1/2}$ orbitals (Fig. 3.13c). We follow the procedure published by Chen *et al.*^[40].

The formulation of the sum rules in terms of the integrals calculated from the experimental spectra reads as follows:

$$\langle m_{L,z} \rangle = -\frac{4}{3} \cdot \frac{A+B}{C} \cdot n_h \cdot \mu_B \quad (\text{Eq. 3.7})$$

$$\langle m_{S,z} \rangle + 7\langle T_z \rangle = -2 \cdot \frac{A-2B}{C} \cdot n_h \cdot \mu_B \quad (\text{Eq. 3.8})$$

$\langle m_{L,z} \rangle$	orbital magnetic moment projected onto the quantization axis
$\langle m_{S,z} \rangle$	spin magnetic moment projected onto the quantization axis
A	integral dichroic effect at the L_3 edge
B	integral dichroic effect at the L_2 edge
C	integral intensity of ($\mu^+(E) + \mu^-(E)$) corrected for non-resonant absorption
n_h	number of holes in the 3d shell
μ_B	Bohr magneton
$\langle T_z \rangle$	spin dipole term

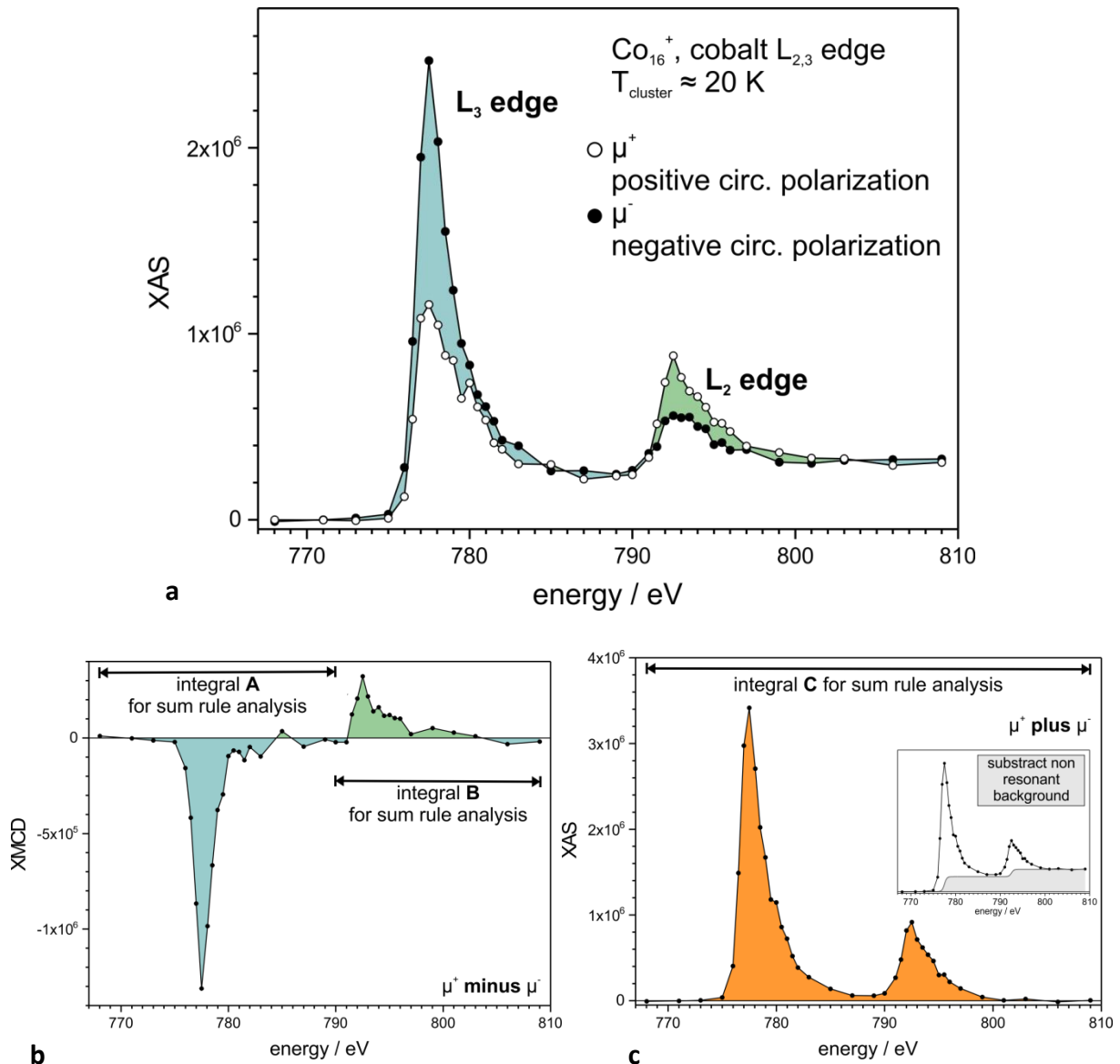


Figure 3.13 Illustration of the integral areas used in the sum rule analysis

(a) Polarization dependent XA spectra taken with negative (μ^-) and positive (μ^+) circularly polarized x-ray photons of Co_{16}^+ **(b)** XMCD spectrum calculated by subtracting the negative from the positive XAS ($\mu^+(E) - \mu^-(E)$). The areas used for integration are indicated. Integral **A** corresponds to the dichroic effect at the L_3 edge and integral **B** to the dichroic effect at the L_2 edge. **(c)** The sum of positive and negative XAS ($\mu^+(E) + \mu^-(E)$) is used to calculate the integral **C**. The integral corresponds to the integration of the resonant absorption intensity over both absorption edges. The non-resonant background is subtracted prior to the integration by fitting a two-step function as indicated in the inset. We follow the procedure described by Chen *et al.* for fitting the background^[40].

The left hand side of Eq. 3.8 is called *effective XMCD spin*^[32] as the spin magnetic moment is not directly accessible from the spin sum rule. The $\langle T_z \rangle$ term account for anisotropy in the spin distribution of the sample with respect to the chosen quantization axis. It is the expectation value of

the spin magnetic dipole operator for the spin quantization axis oriented along z ^[40,42]. The contributions of $\langle T_z \rangle$ can be quite significant in an anisotropic bonding environment, e.g. thin films^[42,43]. However, if an angle averaging XMCD experiment is performed it cancels out close to zero^[32,44] because it is a highly directional value. In our experiment the clusters are freely rotating within the ICR cell and thus we perform an angle averaged experiment. Therefore, we can justify neglecting the $\langle T_z \rangle$ term in the analysis and directly calculate a spin magnetic moment^[36,45] from our experimental spectra.

3.2.4 Scaling of experimental magnetic moments

The application of the sum rule analysis as described in the previous paragraphs allows the calculation of the spin and orbital magnetic moments projected onto the quantization axis z which coincides with the magnetic field axis. The value of this projection depends on the experimental conditions, i.e. magnetic field and sample temperature which define how well the magnetic moment of the sample is aligned with respect to the external magnetic field. The alignment as a function of external magnetic field B and temperature T follows a Brillouin function for small moments^[46] or the classical Langevin function for larger moments^[47-52] (Chap. 2.3).

Table 3.2 Cluster temperatures and corresponding temperature readings at the three different sensors for the temperature dependent experiments of Co_{11}^+

T cluster	T ICR cell / K	T sensor A / K	T sensor B / K
150±50	20	8.5	42
80±1	88	100	68
65±1	67	70	55
50±1	50	50	no reading ^(§)
40±1	43	40	50
30±1	33	30	no reading ^(§)
20±2	20	9	no reading ^(§)
18.5±5	19.5	9	no reading ^(§)
16±5	20	8.5	42

^(§) Temperature sensor B did not give a reading at the time of the experiment.

Please Note that the cross over of the temperatures measured by sensors A and B is due to an active heating element (Chap. 3.1.3) This cross over may lead to additional / larger uncertainties of the assigned cluster temperature T_{cluster} .

We measured a set of temperature dependent XMCD spectra for Co_{11}^+ (Fig. 3.4) to confirm that the magnetization of the clusters follows a Langevin curve as function of cluster temperature and external magnetic field for our experimental scheme^[36]. XMCD spectra were measured for nine different temperatures (Tab. 3.2).

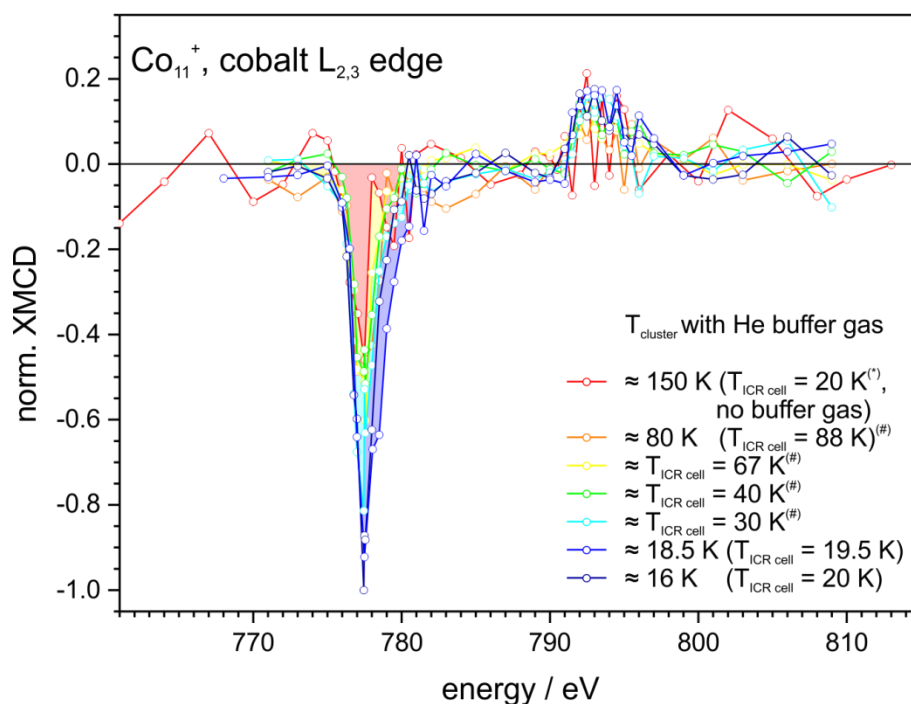


Figure 3.14 Normalized XMCD intensity for the temperature dependent experiments of Co_{11}^+

The individual XMCD spectra are calculated from a normalized pair of XA spectra (Fig. A.9 - A.17). The XMCD spectra are normalized to the largest dichroic effect within the set of experiments. The shaded areas indicate the increasing dichroic effect at the L_3 edge for decreasing temperatures. The dichroic effects for $T_{\text{cluster}} = 80$ K and 40 K are not shaded to due clarity.

(*) Experiments of isolated Co_{11}^+ were not possible at the time of the experiment. A set of three clusters Co_{10}^+ , Co_{11}^+ and Co_{12}^+ was instead isolated with Co_{11}^+ as central peak. The energy scale for the $T_{\text{cluster}} = 150$ K experiment was shifted by 1 eV to lower energy due to energy shifts in the beamline at the time of the experiment. This was done to align the spectrum to the remaining spectra.

(#) Experiments of isolated Co_{11}^+ were not possible. The isolation of only Co_{11}^+ led to a strong reduction of the cluster intensity. $[\text{Co}_{11}\text{H}_2]^+$ had to be included in the experiments to ensure a sufficient parent cluster intensity.

The temperature dependent effect is largest at the L_3 edge (Fig. 3.14). The dichroic effect increases as the temperature decreases, i.e. the better the alignment of the magnetic moment of the cluster the larger the experimentally accessible effect. The effect at the L_2 edge is less pronounced than for the L_3 edge. However, an increase of the dichroic effect is visible. The experiment for $T_{\text{cluster}} = 150$ K was

done with an ICR cell temperature of 20 K but without the use of helium buffer gas to thermalize the clusters. The temperature of 150 K is estimated to be the cluster temperature after the supersonic expansion in the source region. The remaining cluster temperatures were achieved by turning on a heating element which output could be controlled to obtain defined temperatures. Temperatures were controlled by a feedback loop which adjusted the output power of the heating element to stabilize the temperatures within a range 0.5 K.

The experimental values for the total magnetic moments were fitted either by Langevin^[53] (Eq. 3.9a - 3.9c) or Brillouin^[53] (Eq. 3.10a - 3.10c).

$$m_{J,z} = m_J \left(\coth \left(\frac{m_J B}{k_B T} \right) - \frac{k_B T}{m_J B} \right) \quad (\text{Eq. 3.9a})$$

$$m_{L,z} = m_L \left(\coth \left(\frac{m_L B}{k_B T} \right) - \frac{k_B T}{m_L B} \right) \quad (\text{Eq. 3.9b})$$

$$m_{S,z} = g_S S \left(\coth \left(\frac{m_S B}{k_B T} \right) - \frac{k_B T}{m_S B} \right) \quad (\text{Eq. 3.9c})$$

$$m_{J,z} = g_J J \left(\frac{2J+1}{2J} \coth \left(\frac{2J+1}{2J} \frac{\mu_B g_J J B}{k_B T} \right) - \frac{1}{2J} \coth \frac{1}{2L} \frac{\mu_B g_J J B}{k_B T} \right) \quad (\text{Eq. 3.10a})$$

$$m_{L,z} = g_L L \left(\frac{2L+1}{2L} \coth \left(\frac{2L+1}{2L} \frac{\mu_B g_L L B}{k_B T} \right) - \frac{1}{2L} \coth \frac{1}{2L} \frac{\mu_B g_L L B}{k_B T} \right) \quad (\text{Eq. 3.10b})$$

$$m_{S,z} = g_S S \left(\frac{2S+1}{2S} \coth \left(\frac{2S+1}{2S} \frac{\mu_B g_S S B}{k_B T} \right) - \frac{1}{2L} \coth \frac{1}{2S} \frac{\mu_B g_S S B}{k_B T} \right) \quad (\text{Eq. 3.10c})$$

$m_{J,z}$, $m_{L,z}$, $m_{S,z}$	effective (experimental) total, spin, orbital magnetic moment of the cluster in units of μ_B
L	total orbital angular momentum of the cluster
m_L	orbital magnetic moment of the cluster
g_L	Landé-factor of the orbital magnetic moment; $g_L = 1.0$
S	total spin angular momentum of the cluster
m_S	spin magnetic moment of the cluster
g_S	Landé-factor of the electron; $g_S = 2.0$
J	total angular momentum of the cluster; $J = S + L$
m_J	total magnetic moment of the cluster
g_J	Landé-factor of the total magnetic moment
B	magnetic field

A pulse of helium buffer gas was used to thermalize the clusters to the desired temperatures (experimental settings for the experiments at different temperatures see Tab. A.3). The temperature of the helium gas has an uncertainty to it because of the temperature gradient within the experimental setup itself (Tab. 3.2). The cluster temperature is assumed to be the temperatures of

the ICR cell. The magnetic field was kept constant at 7 T for all experiments. Fig. 3.14 does not include the spectra for $T_{\text{cluster}} = 50$ K and 20 K (Fig. A.12 and A.15). The magnetic moments for 50 K and 80 K were extrapolated from the dichroic effect at the L_3 edge^[38].

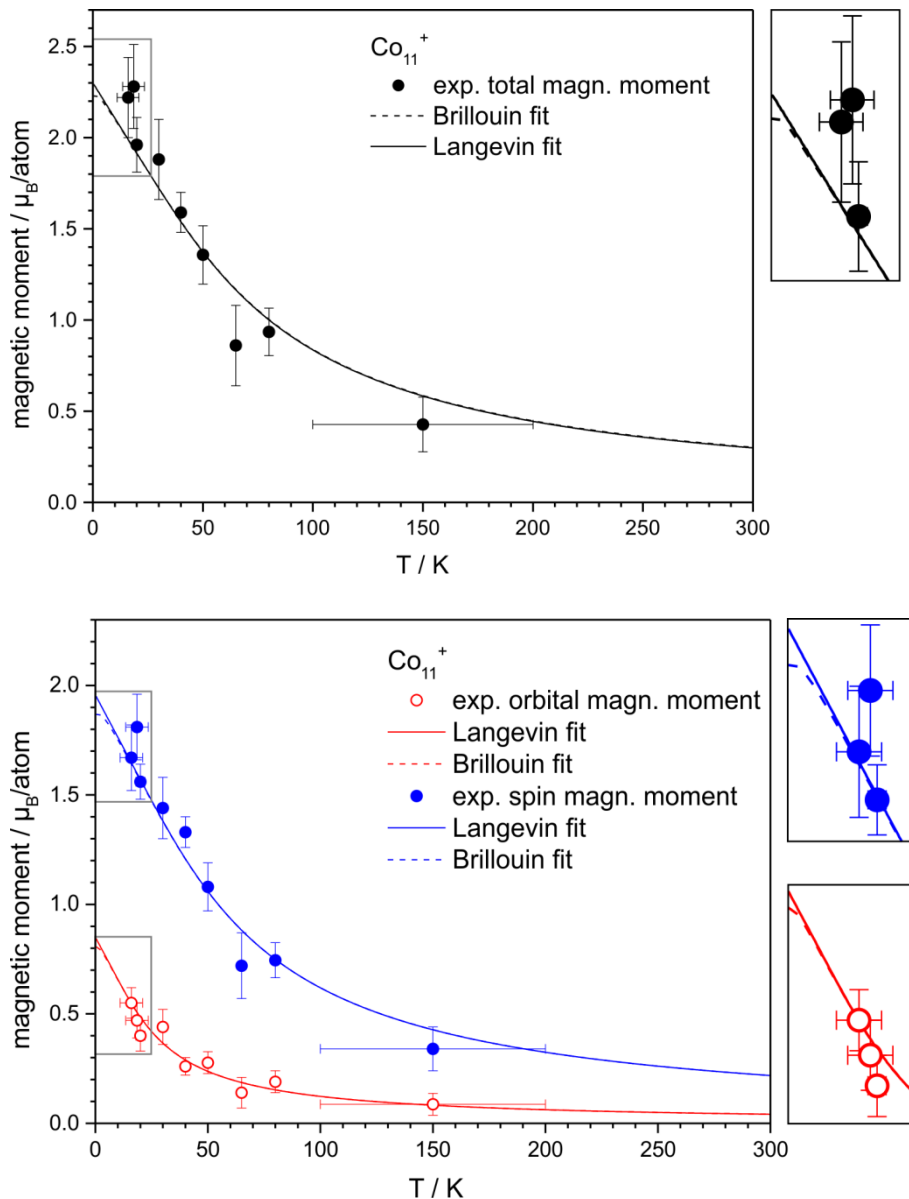


Figure 3.15 scaling of experimental magnetic moments according to the Langevin and Brillouin formula

(a) The total magnetic moment m_J is scaled. The experimental moments $m_{J,z}$ (solid black symbols) are extrapolated to the intrinsic magnetic moment m_J according to Langevin (solid line) or Brillouin (dashed line). **(b)** The spin magnetic moment and orbital magnetic moment are scaled independently. The experimental moments $m_{S,z}$ (solid blue symbols) and $m_{L,z}$ (open red symbols) are extrapolated to the intrinsic magnetic moment m_S and m_L according to Langevin (solid line) or Brillouin (dashed line).

The Langevin and Brillouin scaling curves for each individual experiment are given in Fig. A.19 - A.24. The g_J -factors for all individual experiments can be found in Fig. A.18.

The curves overlap over almost the whole temperature range (0 - 300 K). A small deviation only occurs for temperatures below 10 K (Fig. 3.15a, zoom). The total magnetic moment of Co_{11}^+ calculated from the Langevin fit is $2.300 \mu_B/\text{atom}$ and from the Brillouin fit it is $2.256 \mu_B/\text{atom}$. The deviation is well within our experimental error.

The total magnetic moment for $T_{\text{cluster}} = 65 \text{ K}$ lies below the curve whereas the moments for the two lowest temperatures lie above the fits. The Langevin-like behavior of the magnetization for free clusters trapped in an ICR cell is confirmed. Therefore, we can correct our experimental magnetic moments for the insufficient alignment and obtain the intrinsic magnetic moments of the clusters.

Fig. 3.15b shows the Langevin and Brillouin fits as they have been published before: individually done for spin and orbital magnetic moment^[36]. This individual scaling of both contributions to the magnetic moment corresponds to a decoupling of spin and angular momentum and an individual alignment to the external field and has been proven wrong in the meantime^[45,54,55] (Chap. 4.2). Therefore, the Langevin correction was applied to the total magnetic moment $m_{J,z}$ for all experiments presented within this thesis if not explicitly indicated otherwise.

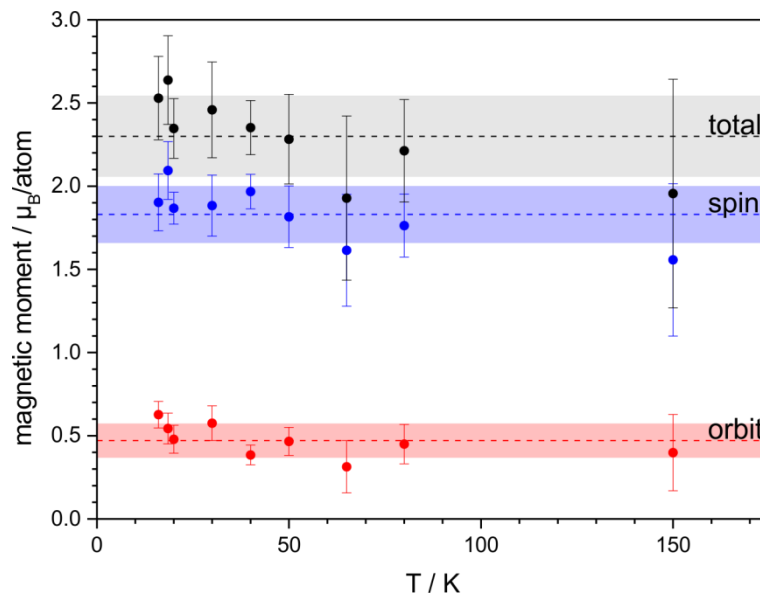


Figure 3.16 Total magnetic moments m_J of Co_{11}^+ after Langevin scaling of m_J . The scaling of the total magnetic moments m_J preserves the ratio of $m_{L,z} / m_{S,z}$. Thus, the ratio of $m_{S,z} / m_{J,z}$ and $m_{L,z} / m_{J,z}$ respectively are preserved too and the values for m_S and m_L can be calculated from m_J . The three dashed lines give the mean values of m_S , m_L and m_J . The shaded area represents two times the standard deviation from the mean value ($\sigma(m_J) = 0.240$, $\sigma(m_S) = 0.167$, $\sigma(m_L) = 0.099$). The Brillouin scaling of $m_{J,z}$ and the results for the individual scaling of $m_{S,z}$ and $m_{L,z}$ according to Langevin and Brillouin are given in Fig. A.25 - A.27.

The total magnetic moment m_J after the Langevin correction for Co_{11}^+ is $2.3 \mu_B/\text{atom}$. It separates into $m_S = 1.83 \mu_B/\text{atom}$ and $m_L = 0.471 \mu_B/\text{atom}$. The total, spin and orbital magnetic moments for all nine temperatures after Langevin correction are displayed in Fig. 3.16. If spin and orbital magnetic moment are individually scaled the m_L / m_S ratio will change (Fig. 3.17). The small orbital moment is harder to align and will therefore be scaled more than the larger spin moment. The case of individually scaled moments would lead to $m_J = 2.797 \mu_B/\text{atom}$, $m_S = 1.947 \mu_B/\text{atom}$ and $m_L = 0.849 \mu_B/\text{atom}$ (Fig. 3.17).

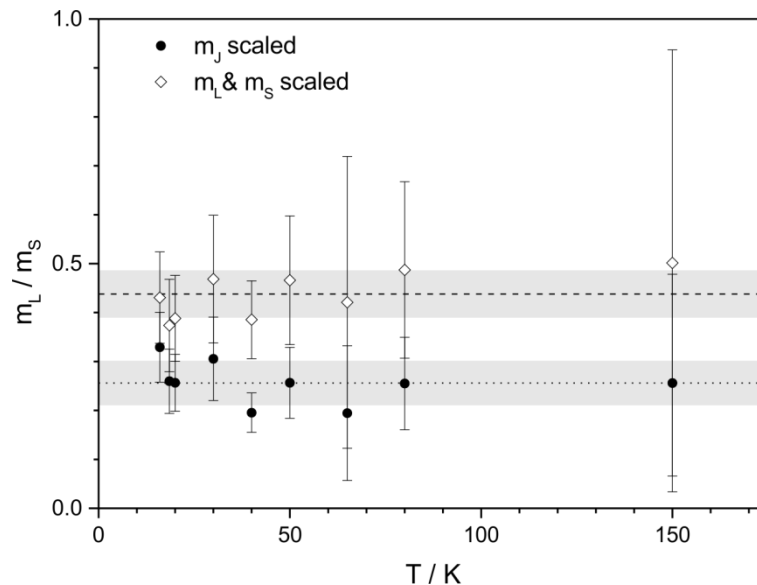


Figure 3.17 ratio of orbital to spin magnetic moment m_L / m_S after Langevin correction

If m_J is scaled the m_L / m_S ratio is the same as the $m_{L,z} / m_{S,z}$ ratio (solid symbols; the dotted line gives the mean value and the shaded area is two times the standard deviation, $\sigma = 0.044$). If spin and orbital magnetic moment are independently scaled the m_L / m_S ratio differs from the $m_{L,z} / m_{S,z}$ ratio (open symbols; the dashed line gives the mean value and the shaded area is two times the standard deviation, $\sigma = 0.047$). The graphic for the Brillouin correction is given in the appendix (Fig. A.28).

3.3 References

- [1] KAMPSCHULTE, H., *Entwicklung einer Tieftemperatur FT-ICR Zelle und ihre Charakterisierung mittels Reaktionskinetiken und Synchrotron-Spektroskopie*, **Doctoral Thesis**, 2010, Technische Universität Kaiserslautern
- [2] BONDYBEY, V. E., ENGLISH, J. H., *Laser-Induced Fluorescence of Metal-Clusters Produced by Laser Vaporization - Gas-Phase Spectrum of Pb-2*, *Journal of Chemical Physics* **1981**, 74, 6978
- [3] DIETZ, T. G., DUNCAN, M. A., POWERS, D. E., SMALLEY, R. E., *Laser Production of Supersonic Metal Cluster Beams*, *Journal of Chemical Physics* **1981**, 74, 6511
- [4] PROCH, D., TRICKL, T., *A high-intensity multi-purpose piezoelectric pulsed molecular beam source*, *Review of Scientific Instruments* **1989**, 60, 713

-
- [5] BARZEN, L., TOMBERS, M., MERKERT, C., HEWER, J., NIEDNER-SCHATTEBURG, G., *Benzene activation and H/D isotope effects in reactions of mixed cobalt platinum clusters: The influence of charge and of composition*, International Journal of Mass Spectrometry **2012**, 330, 271
- [6] TOMBERS, M., BARZEN, L., NIEDNER-SCHATTEBURG, G., *Inverse H/D Isotope Effects in Benzene Activation by Cationic and Anionic Cobalt Clusters*, Journal of Physical Chemistry A **2013**, 117, 1197
- [7] PFEFFER, B., JABERG, S., NIEDNER-SCHATTEBURG, G., *Reactions of simple aromatic heterocycles with niobium cluster ions ($n \leq 30$)*, The Journal of Chemical Physics **2009**, 131, 194305
- [8] BERG, C., SCHINDLER, T., NIEDNER-SCHATTEBURG, G., BONDYBEY, V. E., *Reactions of simple hydrocarbons with Nb_n^+ : Chemisorption and physisorption on ionized niobium clusters*, The Journal of Chemical Physics **1995**, 102, 4870
- [9] KAMPSCHULTE, H., KOLLING, T. Autodesk Inventor
- [10] LAWRENCE, E. O., COOKSEY, D., *On the Apparatus for the Multiple Acceleration of Light Ions to High Speeds*, Physical Review **1936**, 50, 1131
- [11] LAWRENCE, E. O., LIVINGSTON, M. S., *The Production of High Speed Light Ions Without the Use of High Voltages*, Physical Review **1932**, 40, 19
- [12] SMITH, L. G., *A New Magnetic Period Mass Spectrometer*, Review of Scientific Instruments **1951**, 22, 115
- [13] SOMMER, H., THOMAS, H. A., HIPPLE, J. A., *The Measurement of e/M by Cyclotron Resonance*, Physical Review **1951**, 82, 697
- [14] COMISAROW, M. B., MARSHALL, A. G., *Fourier transform ion cyclotron resonance spectroscopy*, Chemical Physics Letters **1974**, 25, 282
- [15] COMISAROW, M. B., MARSHALL, A. G., *Frequency-sweep fourier transform ion cyclotron resonance spectroscopy*, Chemical Physics Letters **1974**, 26, 489
- [16] COMISAROW, M. B., MARSHALL, A. G., *The Early Development of Fourier Transform Ion Cyclotron Resonance (FT-ICR) Spectroscopy*, Journal of Mass Spectrometry **1996**, 31, 581
- [17] MENGES, F., *Structure and Reactivity of Isolated Mononuclear and Oligonuclear Metal Complexes*, **Doctoral Thesis**, 2013, Technische Universität Kaiserslautern
- [18] BHUNIA, A., GAMER, M. T., UNGUR, L., CHIBOTARU, L. F., POWELL, A. K., LAN, Y., ROESKY, P. W., MENGES, F., RIEHN, C., NIEDNER-SCHATTEBURG, G., *From a Dy(III) Single Molecule Magnet (SMM) to a Ferromagnetic [Mn(II)Dy(III)Mn(II)] Trinuclear Complex*, Inorg. Chem. **2012**, 51, 9589
- [19] GROSS, J. H., *Mass Spectrometry*; Springer, **2011**
- [20] MARSHALL, A. G., HENDRICKSON, C. L., JACKSON, G. S., *Fourier transform ion cyclotron resonance mass spectrometry: A primer*, Mass Spectrometry Reviews **1998**, 17, 1
- [21] BROWN, L. S., GABRIELSE, G., *Geonium theory: Physics of a single electron or ion in a Penning trap*, Reviews of Modern Physics **1986**, 58, 233
- [22] SCHWEIKHARD, L., ZIEGLER, J., BOPP, H., LÜTZENKIRCHEN, K., *The trapping condition and a new instability of the ion motion in the ion cyclotron resonance trap*, International Journal of Mass Spectrometry and Ion Processes **1995**, 141, 77
- [23] CARAVATTI, P., ALLEMANN, M., *The 'infinity cell': A new trapped-ion cell with radiofrequency covered trapping electrodes for fourier transform ion cyclotron resonance mass spectrometry*, Organic Mass Spectrometry **1991**, 26, 514
- [24] FALTA, J., MÖLLER THOMAS, *Forschung mit Synchrotron Strahlung*; Vieweg+Teubner Verlag, **2010**
-

- [25] MARGARITONDO, G., *A Primer in Synchrotron Radiation: Everything You Wanted to Know about SEX (Synchrotron Emission of X-rays) but Were Afraid to Ask*, Journal of Synchrotron Radiation **1995**, 2, 148
- [26] MARGARITONDO, G., *Synchrotron light in a nutshell*, Surface Review and Letters **2000**, 07, 379
- [27] WENDE, H., *Recent advances in x-ray absorption spectroscopy*, Reports on Progress in Physics **2004**, 67, 2105
- [28] SASAKI, S., KAKUNO, K., TAKADA, T., SHIMADA, T., YANAGIDA, K.-I., MIYAHARA, Y., *Design of a new type of planar undulator for generating variably polarized radiation*, Nuclear Instruments and Methods in Physics Research Section A: Accelerators, Spectrometers, Detectors and Associated Equipment **1993**, 331, 763
- [29] SASAKI, S., *Analyses for a planar variably-polarizing undulator*, Nuclear Instruments and Methods in Physics Research Section A: Accelerators, Spectrometers, Detectors and Associated Equipment **1994**, 347, 83
- [30] BAHRDT, J., FRENRUP, W., GAUPP, A., SCHEER, M., GUDAT, W., INGOLD, G., SASAKI, S., *A quasi periodic hybrid undulator at BESSY II* Nuclear Instruments & Methods in Physics Research Section A: Accelerators, Spectrometers, Detectors and associated Equipment **2001**, 467, 130
- [31] http://www.helmholtz-berlin.de/pubbin/igama_output?modus=einzel&sprache=en&gid=1927&typoid=35512, 2013
- [32] SCHÜTZ, G., GOERING, E., HERMANN, S. Synchrotron Radiation Techniques Based on X-ray Magnetic Circular Dichroism. In *Handbook of Magnetism and Advanced Magnetic Materials*; Kronmüller, H., Parkin, S., Eds.; John Wiley & Sons, Ltd., 2007; Vol. 3
- [33] STÖHR, J., SIEGMANN, H. C., *Magnetism - From Fundamentals to Nanoscale Dynamics*; Springer, **2006**
- [34] HIRSCH, K., LAU, J. T., KLAR, P., LANGENBERG, A., PROBST, J., RITTMANN, J., VOGEL, M., ZAMUDIO-BAYER, V., MOELLER, T., VON ISSENDORFF, B., *X-ray spectroscopy on size-selected clusters in an ion trap: from the molecular limit to bulk properties*, Journal of Physics B-Atomic Molecular and Optical Physics **2009**, 42
- [35] LAU, J. T., RITTMANN, J., ZAMUDIO-BAYER, V., VOGEL, M., HIRSCH, K., KLAR, P., LOFINK, F., MOELLER, T., VON ISSENDORFF, B., *Size Dependence of $L_{2,3}$ Branching Ratio and $2p$ Core-Hole Screening in X-Ray Absorption of Metal Clusters*, Physical Review Letters **2008**, 101
- [36] PEREDKOV, S., NEEB, M., EBERHARDT, W., MEYER, J., TOMBERS, M., KAMPSCHULTE, H., NIEDNER-SCHATTEBURG, G., *Spin and Orbital Magnetic Moments of Free Nanoparticles*, Physical Review Letters **2011**, 107, 233401
- [37] PEREDKOV, S., SAVCI, A., PETERS, S., NEEB, M., EBERHARDT, W., KAMPSCHULTE, H., MEYER, J., TOMBERS, M., HOFFERBERTH, B., MENGES, F., NIEDNER-SCHATTEBURG, G., *X-ray absorption spectroscopy of mass-selected transition metal clusters using a cyclotron ion trap: An experimental setup for measuring XMCD spectra of free clusters*, Journal of Electron Spectroscopy and Related Phenomena **2011**, 184, 113
- [38] This was done by S. Peredkov who held a PostDoc position within the project at the time.
- [39] CARRA, P., THOLE, B. T., ALTARELLI, M., WANG, X., *X-ray circular dichroism and local magnetic fields*, Physical Review Letters **1993**, 70, 694
- [40] CHEN, C. T., IDZERDA, Y. U., LIN, H. J., SMITH, N. V., MEIGS, G., CHABAN, E., HO, G. H., PELLEGRIN, E., SETTE, F., *Experimental Confirmation of the X-Ray Magnetic Circular Dichroism Sum Rules for Iron and Cobalt*, Physical Review Letters **1995**, 75, 152
- [41] THOLE, B. T., CARRA, P., SETTE, F., VANDERLAAN, G., *X-ray circular dichroism as a probe of orbital magnetization*, Physical Review Letters **1992**, 68, 1943

- [42] SIPR, O., MINAR, J., EBERT, H., *On the importance of the magnetic dipole term T_z in analyzing X-ray magnetic circular dichroism spectra of clusters*, Europhysics Letters **2009**, 87
- [43] WU, R., FREEMAN, A. J., *Limitation of the Magnetic-Circular-Dichroism Spin Sum Rule for Transition Metals and Importance of the Magnetic Dipole Term*, Physical Review Letters **1994**, 73, 1994
- [44] STÖHR, J., KÖNIG, H., *Determination of Spin- and Orbital-Moment Anisotropies in Transition Metals by Angle-Dependent X-Ray Magnetic Circular Dichroism*, Physical Review Letters **1995**, 75, 3748
- [45] NIEMEYER, M., HIRSCH, K., ZAMUDIO-BAYER, V., LANGENBERG, A., VOGEL, M., KOSSICK, M., EBRECHT, C., EGASHIRA, K., TERASAKI, A., MÖLLER, T., V. ISSENDORFF, B., LAU, J. T., *Spin Coupling and Orbital Angular Momentum Quenching in Free Iron Clusters*, Physical Review Letters **2012**, 108, 057201
- [46] LUEKEN, H., *Magnetochemie: Eine Einführung in Theorie und Methoden*; Teubner Verlag, **1999**
- [47] BARRA, A.-L., CANESCHI, A., CORNIA, A., GATTESCHI, D., GORINI, L., HEINIGER, L.-P., SESSOLI, R., SORACE, L., *The Origin of Transverse Anisotropy in Axially Symmetric Single Molecule Magnets*, J. Am. Chem. Soc. **2007**, 129, 10754
- [48] BUCHER, J. P., DOUGLASS, D. C., BLOOMFIELD, L. A., *Magnetic properties of free cobalt clusters*, Physical Review Letters **1991**, 66, 3052
- [49] KHANNA, S. N., LINDEROTH, S., *magnetic behavior of clusters of ferromagnetic transition metals*, Physical Review Letters **1991**, 67, 742
- [50] KNICKELBEIN, M. B., *Nickel clusters: The influence of adsorbates on magnetic moments*, The Journal of Chemical Physics **2002**, 116, 9703
- [51] REDDY, B. V., NAYAK, S. K., KHANNA, S. N., RAO, B. K., JENA, P., *Physics of nickel clusters. 2. Electronic structure and magnetic properties*, Journal of Physical Chemistry A **1998**, 102, 1748
- [52] XU, X., YIN, S., MORO, R., DE HEER, W. A., *Distribution of magnetization of a cold ferromagnetic cluster beam*, Physical Review B **2008**, 78, 054430
- [53] numerical solution of equation by FindRoot function, *Mathematica 9.0.1.0*, Wolfram Research, Inc
- [54] FAUTH, K., MÜNZING, B., *Unterdrückter Impuls*, Physik Journal **2012**, 05/2012
- [55] LANGENBERG, A., *Magnetische Momente freier, massenselektierter Eisen-, Cobalt- und Nickelcluster*, **Doctoral Thesis**, 2013, Technische Universität Berlin

3.4 Supplement

3.4.1 Publication - J. Electron Spectroscopy and related Phenomena 2011, 184, 113

The manuscript was mainly drafted by our collaboration partners Sergey Peredkov and Matthias Neeb. Together with S. Peredkov I recorded the XA spectra of the vanadium clusters, Nb_{13}^+ and Co_{22}^+ and assisted S. Peredkov with the data evaluation. Matthias Tombers joined the experimental work on the XA spectra of Co_{22}^+ .

PEREDKOV, S., SAVCI, A., PETERS, S., NEEB, M., EBERHARDT, W., KAMPSCHULTE, H., MEYER, J., TOMBERS, M., HOFFERBERTH, B., MENGES, F., NIEDNER-SCHATTEBURG, G., *X-ray absorption spectroscopy of mass-selected transition metal clusters using a cyclotron ion trap: An experimental setup for measuring XMCD spectra of free clusters*, Journal of Electron Spectroscopy and Related Phenomena **2011**, 184, 113

<http://www.sciencedirect.com/science/article/pii/S0368204810003>

X-ray absorption spectroscopy of mass-selected transition metal clusters using a cyclotron ion trap: An experimental setup for measuring XMCD spectra of free clusters

Sergey Peredkov^{a,1}, Ali Savci^b, Sven Peters^b, Matthias Neeb^{b,*}, Wolfgang Eberhardt^b, Heinrich Kampschulte^c, Jennifer Meyer^c, Matthias Tombers^c, Bernd Hofferberth^{c,2}, Fabian Menges^c, Gereon Niedner-Schatteburg^c

^a Technische Universität Berlin, Institut für Optik und Atomare Physik, Hardenbergstr. 36, 10623 Berlin, Germany

^b Helmholtz-Zentrum Berlin für Materialien und Energie, Wilhelm-Conrad-Röntgen-Campus Adlershof, Elektronenspeicherring BESSY II, Albert-Einstein-Straße 15, Germany

^c Fachbereich Chemie und Forschungszentrum OPTIMAS, TU Kaiserslautern, 67663 Kaiserslautern, Germany

3.4.1.0 Abstract

A Fourier Transform-Ion Cyclotron Resonance mass spectrometer has been installed at the BESSY II storage ring. This unique setup enables to record soft X-ray absorption and magnetic circular dichroism spectra (XMCD) of mass-selected clusters in the photon energy range 200 - 1200 eV. The photoabsorption signal is obtained by recording the fragmentation pattern as produced after X-ray absorption and subsequent Auger decay of the core-excited parent cluster ion. The experimental setup and first X-ray absorption spectra on V_{13}^+ and Nb_{13}^+ are discussed. The feasibility of recording X-ray induced XMCD spectra is demonstrated for Co_{22}^+ . Improvements that allow for quantitative determination of spin and orbital momenta in the future are briefly outlined.

3.4.1.1 Introduction

In recent years X-ray magnetic circular dichroism (XMCD) has developed into an important magnetometry tool for studying dilute samples such as sub-monolayers [1], quantum wires [2], nanoparticles [3], as well as supported monodispersed clusters [4,5]. In general XMCD allows for separation of spin and orbital magnetic moments, and it provides for a route to determine magnetic anisotropies of selected samples [6,7]. XMCD has the particular advantage of being sensitive to low sample concentrations and being element specific.

Various deposited metal clusters have been investigated by XMCD. The total moments of these clusters increase with respect to bulk values, and the relative contributions of spin- and orbital moments differ from those of corresponding bulk samples [4,5]. However, the deposition of the clusters inevitably alters intrinsic cluster properties through substrate induced electronic reorganization. It is a challenge to accurately model the electronic coupling within the cluster-surface system [8]. Even the modelling of individual clusters causes such challenge and requires highly correlated relativistic ab initio levels of computation [9,10]. These circumstances request for additional investigation, i.e. XMCD experiments on free mass-selected clusters as those do not interact with any environment. Our present setup is designed to serve this purpose, i.e. to analyse the spin and orbit magnetic moments of free mass-selected cluster ions by recording the X-ray induced dichroic difference signal using circularly polarised soft X-ray undulator radiation.

Total magnetic moments of mass-selected metal clusters have been recorded by Stern-Gerlach experiments [11-14]. It turns out that the total moments of free clusters are clearly enhanced with respect to the bulk. Moreover the Stern-Gerlach measurements show that mass-selection is mandatory for the exploration of small clusters as the magnetic moments vary in a non-scalable way as function of size. This is particularly true for clusters with less than 100 atoms. As the relative contribution of orbital and spin moments cannot be received by Stern-Gerlach experiments XMCD spectroscopy serves as complementary tool for the investigation of the magnetic properties of free clusters.

Ion trapping has successfully been applied for exploring massselected clusters with respect to e.g. photofragmentation [15], charge states [16], vibrational frequencies [17] and structure [18]. Moreover, ion trapping has recently been used to explore free nanoparticles and mass-selected clusters by soft X-ray absorption [19,20]. Ion trapping provides a spatially confined target density. Using an average photon flux of an undulator X-ray source of $\sim 10^{12} \text{ s}^{-1}$ as well as a typical atomic photoionization cross sections in the soft X-ray region ($= 1 - 10 \text{ Mb}$ [21]) we estimate that a target density of $\geq 10^7 \text{ clusters/cm}^3$ should provide a reasonable signal-to-noise ratio (> 3) for doing soft

X-ray photoabsorption spectroscopy. For this estimation we assumed a detection limit of > 200 ions [22], 10 atoms/cluster and 100 % photon and ion beam overlap. Photoabsorption of X-ray's and subsequent Auger decay creates multiply charged cluster ions. These final state ions are very likely to dissociate, in analogy to what has been observed in molecular X-ray spectroscopy [23]. The total fragment ion intensity is proportional to the X-ray absorption probability. Thus an absorption spectrum of the stored parent cluster is recorded by scanning the photon energy over an inner-shell absorption edge and detecting the fragment ion yield.

We built an experimental setup in order to perform XMCD spectroscopy on free clusters. This new setup, branded GAMBIT (General Abstraction of Magnetic Moments at BESSY by Ion Trapping), utilizes a cyclotron ion trap (combination of DC electric and static magnetic fields) which serves both as ion trap and mass detector (m/z). In contrast to dynamical RF traps which have recently been used for X-ray absorption spectroscopy of mass-selected ions and clusters [19,20] the Penning-like setup uses a strong homogeneous magnetic field for radial confinement of the cluster ions. This trapping field also defines the magnetization direction of the cluster ensemble for XMCD measurements.

We have taken first X-ray absorption spectra for V_{13}^+ and Nb_{13}^+ using linear polarisation. These clusters are supposed to have an icosahedral-like geometry. Circular polarisation has been used to record the absorption spectra of Co_{22}^+ which can be assumed to be superparamagnetic [13]. These cluster sizes have been chosen as these could be produced with highest intensity for the time being. Moreover, any higher harmonics (3^{rd} , 5^{th} , 7^{th}) of the parent mass peak resulting from Fourier analysis of the recorded frequency spectra do not overlap with the fragment peaks.

3.4.1.2 Experimental setup

The setup is based on a commercial Fourier-Transform Ion Cyclotron Resonance (FT-ICR) instrument (Bruker Apex III). The instrument was modified according to a similar instrument that serves to investigate transition metal cluster reactions [24]. The latter experiment is not combined with a synchrotron beamline, however. Metal clusters are formed by pulsed laser vaporisation (20 Hz, 532 nm, ~ 10 mJ/pulse) of a rotating thin foil into pulses of Helium carrier gas from a home-built piezo valve [17]. The valve opens shortly (60 - 120 μ s) in order to allow for the admittance of high backing pressures (up to 15 bar). The cluster/gas mixture of the source region propagates along a channel (80 mm \times 2 mm diameter), expands adiabatically into vacuum, and passes through a gas dynamic skimmer (opening 0.2 mm) for differential pumping. Subsequently, the cluster ion beam is bent by a home-built 90° electrostatic quadrupole deflector. Multiple electrostatic ion lenses, steering elements and biased apertures guide the cluster ion beam into the high magnetic field region of a shielded superconducting solenoid (7.05 T with a bore diameter of 155 mm). Trapping, RF

excitation and detection of the ions inside the trap takes place by a cylindrical ICR cell ($\varnothing = 6$ mm, $l = 60$ mm) that comprises multi segmented planar trapping end caps (a so-called Infinity cell [25]). The cluster and X-ray beam enter the ICR-cell through axial apertures (diameter 6 mm) on either side of the trap. The vacuum housing of the trapping cell is connected to the X-ray beamline by a non-magnetic stainless steel tube (316 Ti). A schematic layout of the experimental setup including cluster source, ion optics and ICR ion trap is provided in Fig. 1.

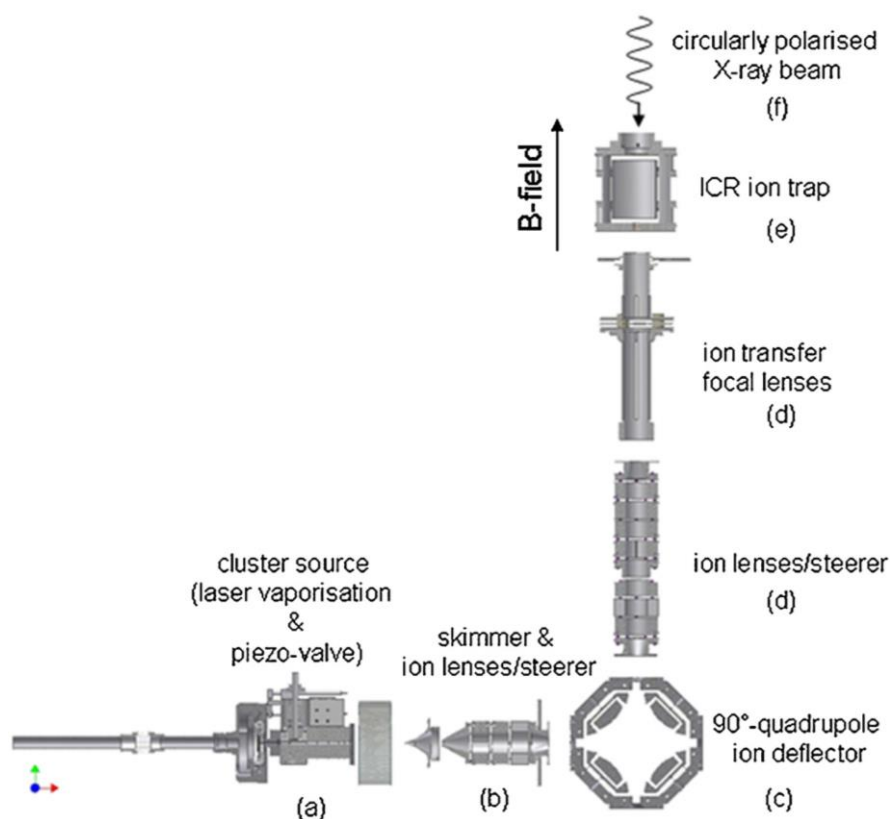


Fig. 1 Scheme of the experimental setup for XAS and XMCD measurements on free mass-selected clusters: (a) cluster source, (b) skimmer and extraction optics, (c) electrostatic quadrupole deflector, (d) focussing and transfer optics, (e) FT-ICR cell for trapping and analyzing the cluster ions, and (f) counter propagating X-ray photon beam. The FT-ICR cell is placed in the center of a superconducting magnet (7T).

The ICR ion trap is filled with clusters from a sequence of 5 - 20 laser shots (at 20 Hz repetition rate) by synchronized gating of the axial front trapping plate. Typical mass spectra of transition metal clusters reveal a Gaussian-like intensity distributions (Fig. 2 (top panel) for e.g. V_n^+ -clusters, with a maximum at V_{13}^+ that can be shifted towards higher or lower cluster sizes by variation of timing delays, e.g. ICR-cell opening to laser pulse for ion time-of-flight variation, vaporisation laser to piezo valve for cluster production. Mass-selection is achieved inside the trap by isolation of a particular cluster mass using resonant RF-ejection of all unwanted cluster as shown in the center of Fig. 2 for V_{13}^+ . Upon mass-selection the intensity of the mass-selected mother ion reduces by ca. 30 - 50 %.

The center of the superconducting magnet is installed ~ 4 m downstream of the focus of the UE52-PGM beamline at the BESSY II storage ring. The horizontal X-ray beam width was determined to be ~ 0.5 mm at the location of the ICR-cell.

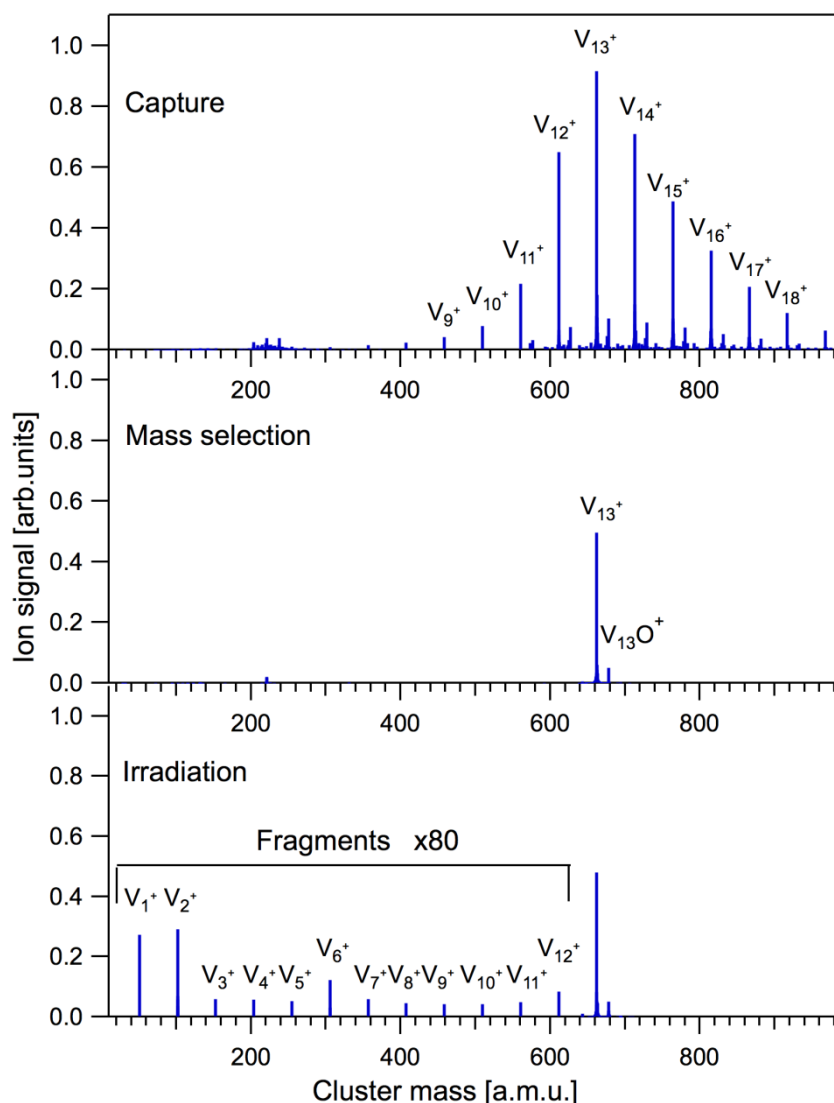


Fig. 2 ICR-mass spectrum of V_n^+ clusters. Initial cluster distribution as captured from the cluster ion source (top), after mass-selection of a particular cluster size (center) and after X-ray exposure for 4 s (bottom). The strongest satellite mass peak next to each pristine cluster (top panel) can be assigned as a monatomic vanadium oxide ($V_nO_1^+$) which is captured from the cluster beam.

The vertical X-ray beam width is approximately equal to the variable exit slit setting of the monochromator (20, 50, 100, 200, or 500 μm). All absorption spectra discussed in the following were recorded with an exit slit setting of 500 μm , which leads to a spectral resolution of ~ 1 eV and to a flux of $0.5 - 1 \times 10^{12}$ photons/s (300 - 900 eV). The magnetic field is aligned parallel to the X-ray

propagation direction. Hence a maximum dichroic signal is observed when left and right circular X-ray polarisation is used for recording XMCD spectra.

Admittance of the X-ray photon beam to the ICR cell is controlled via an electrically triggered pneumatic beam shutter in front of the magnet. Exposure of stored cluster ions for a few seconds yields ionic fragments sufficient for subsequent RF excitation and detection. Within the exposure time the detected fragment yield increases to $\sim 1\%$ of the precursor intensity (see Fig. 2, bottom panel). This large mother-to-daughter ratio ensures photoabsorption of the mother ion but not by the fragment ions. After irradiation and detection of the fragments the ICR cell is quenched and reloaded with new clusters. Both parent ions as well as fragment ions are detected. Application of an RF frequency chirp to the ICR-cell electrodes yields a superposition of sinusoidal response functions. Fast Fourier transformation (FFT) converts this transient signal into a frequency spectrum. These frequencies are inversely proportional to the mass (m/z) of the detected ions and thus a traditional mass spectrum is obtained from frequency-to-mass conversion. The mass calibration took place with a standard ion trap tuning mix (G2431A, Omnilab-Laborzentrum GmbH, Bremen) and using a standard electrospray ion source. The mass resolution m/m is proportional to the detection time t (resolving power = $0.5 \times \omega_{\text{cyc}} \times t$), e.g. up to 10^4 for 100 ms detection at 500 - 1000 amu ($\omega_{\text{cyc}} = 100 - 200$ kHz).

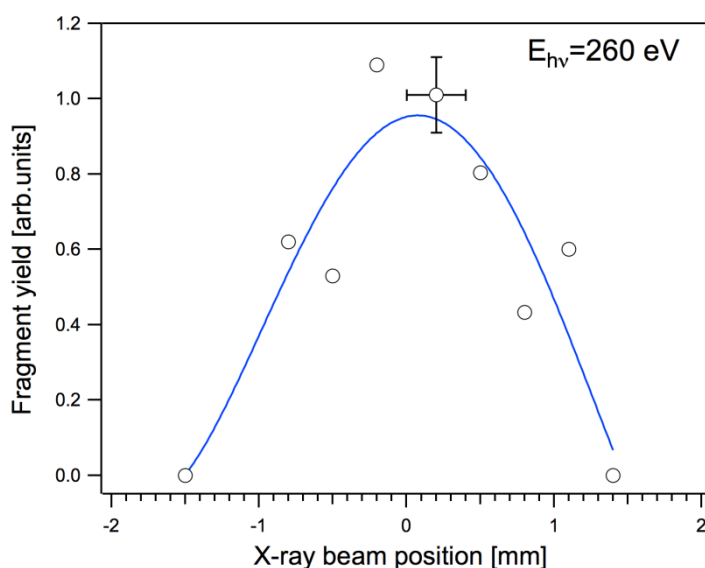


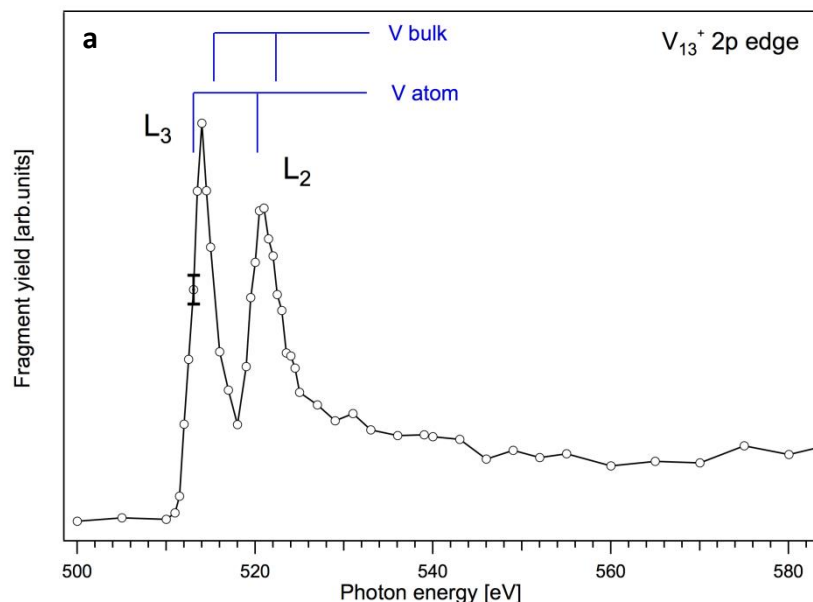
Fig. 3 Intensity distribution of the cluster ion cloud inside the ICR-cell. By sweeping the X-ray beam across the cell the recorded fragment intensities reveal the spatial distribution of the Nb_{13}^+ -cloud. The error bar for the intensity near zero beam position is the standard deviation ($\pm 2\sigma$) from several measurements. The uncertainty of the x-coordinate is caused by determining the position of the X-ray spot on a phosphor-plated window. Spectra have been taken with 4 s irradiation time.

We estimate an ion cloud diameter of 2 mm inside the trap by spatially scanning the X-ray beam across the trapped ion cloud while recording the fragment yield. The cloud size is determined by the combined cyclotron and magnetron motion of the ions as a result of the crossed radial component of the electric trapping field and axial magnetic field [26]. The measured radius has independently been confirmed by SIMION simulations [27] using a B-field strength of 7 T, trapping potentials of 3 V, an ion beam width of 1 mm as well as an ion beam expansion velocity of 1000 m/s. From the measured ion cloud diameter (see Fig. 3), the ion current entering our ion trap (~ 1 pA), as well as the length of the ion trap (6 cm) we calculate an ion density of $\sim 3 \times 10^7/\text{cm}^3$. This cluster density exceeds the minimum ion density necessary to record X-ray absorption spectra of acceptable signal-to-noise ratio at reasonable time (see estimation above).

3.4.1.3 Results and discussion

Vanadium

An X-ray absorption spectrum (XAS) of V_{13}^+ is displayed in Fig. 4a. It has been recorded with linearly polarised X-rays. The spectrum shows the accumulated fragment intensity ($\text{V}_{13}^+ - \text{V}_9^+$) versus photon energy within the L-edge absorption region (2p). Each data point has been accumulated with a total X-ray exposure time of ~ 6 min (6 s per data point, 60 scans). The spectrum is normalized to the mass-selected mother peak intensity and the BESSY storage ring current, which is proportional to the delivered X-ray intensity.



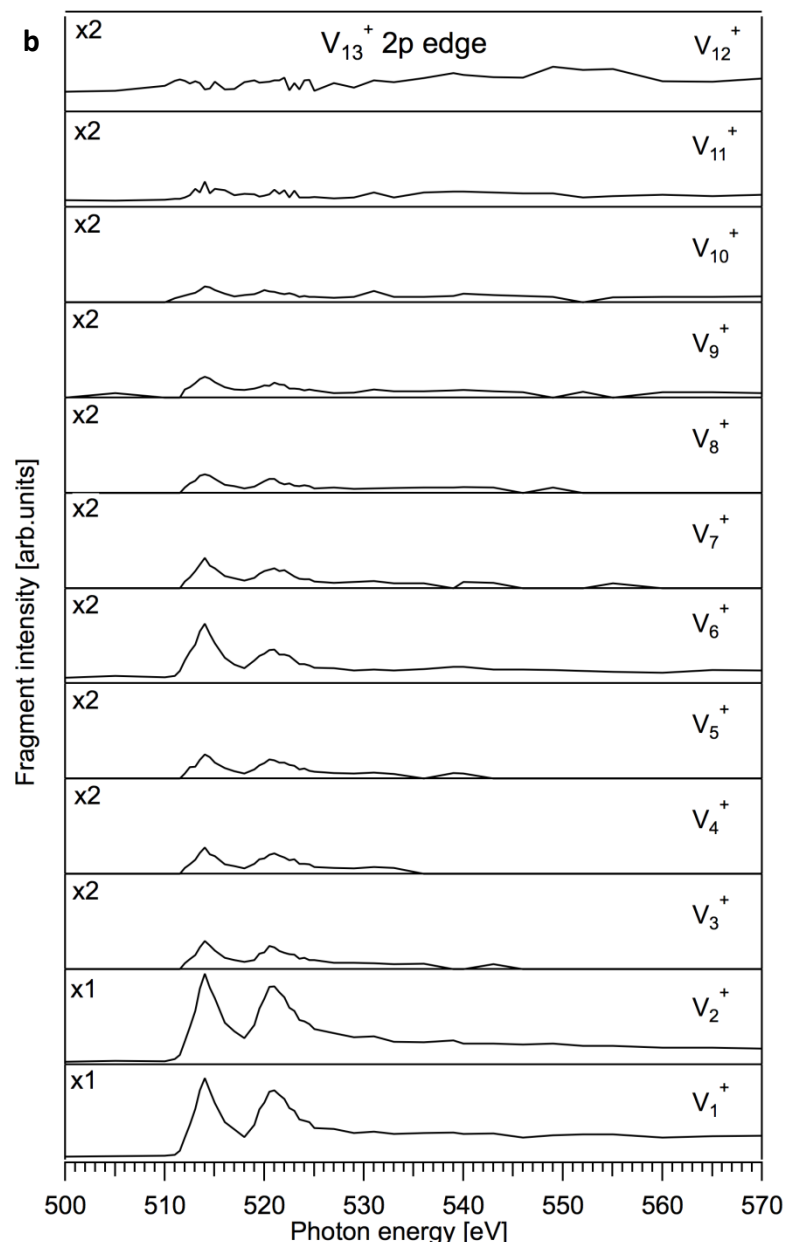
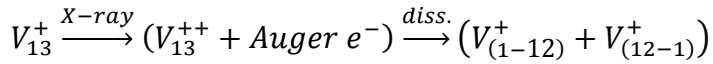


Fig. 4 (a) X-ray absorption spectrum (XAS) at the L-edge of V_{13}^+ . The signal intensity is proportional to the accumulated fragmentation signal ($V_1^+ - V_9^+$). The signal intensity is normalized to the BESSY storage ring current and to the intensity of the V_{13}^+ mother ion. The L_3 and L_2 edges of bulk vanadium [32] and the atom [31] are indicated. **(b)** Partial ion yield X-ray absorption spectra of V_{13}^+ (L-edge). The accumulated ion yield was experimentally optimized by maximizing the intensity of the monomer and dimer (V_1^+ and V_2^+). The displayed intensities of larger fragment ions are scaled by a factor of two.

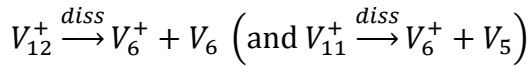
The two spin-orbit components are well resolved at 512 eV (L_3 edge) and 520 eV (L_2), respectively. The threshold energy of the cluster is shifted by +0.8 eV with respect to the atom and by -1.3 eV with respect to the bulk. This spectrum agrees nicely with corresponding results from previous XAS measurements on a series of V_n^+ -clusters that were recorded within a linear RF ion trap but without

external magnetic field [28]. We assume that a variation of the trapped cluster density after each refill is the main source of error. This density variation is caused by pulse-to-pulse fluctuations cluster beam. The error bar in Fig. 4a is the two standard deviation ($\pm 2\sigma$) from repeated measurements at 513 eV.

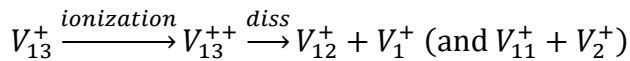
X-ray exposure of V_{13}^+ leads to various fragment ions ranging from V_1^+ to V_{12}^+ as displayed in Fig. 4b. The relative intensity of the fragment ions varies somewhat by the excitation and detection conditions, which were optimized for recording the monomer (V_1^+) and dimer (V_2^+). The appearance of all possible fragment sizes might be explained by a stepwise dissociation mechanism: core excitation of the initially ionized cluster and Auger decay is followed by Coulomb-driven dissociation of the doubly charged final state mother ions, i.e.



Note that the largest fragment ions V_{12}^+ and V_{11}^+ are hardly ever observed on-resonance while the corresponding sister ions V_1^+ and V_2^+ , respectively, are particularly intense at the maximum of the L_3 and L_2 resonance. Also, the intensity of V_6^+ is particularly strong with respect to all other daughter ions for $n \geq 3$. Thus it seems likely that the primary fragments V_{12}^+ and V_{11}^+ , which are produced via core excitation and dissociation of V_{13}^+ , are metastable and dissociate further into the hexamer ion. Such secondary "symmetric" fission would explain the relative enhancement of the V_6^+ yield, i.e.



Most of the fragment ions occur exclusively within the resonant region and not in the pre-edge region (V_{3-10}^+ , except V_6^+). Note, however, that some fragment intensity of V_{11}^+ and V_{12}^+ appears before the L-edge. This is also true for V_1^+ , V_2^+ and V_6^+ . It is worth mentioning that absolutely no fragment intensity is seen for all singly charged daughter ions without X-ray exposure. Thus we attribute the non L-edge specific fragmentation yield to direct photoionization (outer core: 3s, 3p, valence 3d, 4s) and subsequent dissociation, i.e.



The pre-edge intensity of the hexamer fragment (V_6^+) might be due to direct fission of the doubly ionized parent ion or might result from symmetric fission of the primary daughter fragments (V_{12}^+ and V_{11}^+) as explained above.

We do not observe doubly charged fragment ions with an odd number of atoms. This cannot definitely stated for the occurrence of doubly charged even-numbered fragment ions due to their

m/z-coincidence with singly charged fragments having half the number of atoms. An exclusive production of even-numbered doubly charged ions seems unlikely, however. Thus we have no evidence for the production of stable doubly charged fragments.

We note that the final state of the L_3 (L_2) absorption transition in V_{13}^+ (valence ionized initial state) is equal to the $2p_{3/2}$ ($2p_{1/2}$) XPS final state of neutral V_{13} . Thus from the peak maxima we can deduce the corresponding XPS binding energy of the neutral cluster by adding the first ionization potential of neutral V_{13} . As this value is experimentally unknown we use the electrostatic liquid drop model [29] for approximation of the ionization potential $IP(V_{13}) = W_{\text{solid}} + Ae^2/4\epsilon_0R$. A is a constant which has been found to be 0.5 in classical electrostatics and 3/8 if quantum effects are considered. W_{solid} is the corresponding bulk work function of vanadium (4.3 eV). R is the radius of a spherical droplet given by $R = N^{1/3}r_{\text{WS}}$ where r_{WS} is the Wigner-Seitz radius of vanadium (1.25 Å [30]). These parameters yield an XPS ionization energy of 519.1 eV using $IP_{\text{core}}(2p_{3/2}, V_{13}) = IP_{\text{core}}(2p_{3/2}, \text{bulk}) + Ae^2/4\epsilon_0R$. Thus the approximated XPS energy of neutral V_{13} is ~ 9 eV lower than that of the V-atom [31], while it is ~ 3.5 eV higher than the corresponding XPS ionization energy of solid vanadium as calculated from the XPS binding energy [32] and work function (4.3 eV [33]) of vanadium, i.e. $IP_{\text{core}}(2p_{3/2}, \text{bulk}) = XPS(2p_{3/2}, \text{bulk}) + W_{\text{solid}} = 516.6$ eV).

Niobium

An M-edge XAS spectrum of Nb_{13}^+ is shown in Fig. 5. It results from accumulation of the total fragment ion yield. Similar to the bulk spectrum, the cluster absorption spectrum exhibits a heavily shifted maximum which is located about 80 eV beyond the 3d XPS threshold of ~ 210 eV for solid niobium [34]. This so-called "delayed absorption maximum" has been explained for the solid by a strong centrifugal barrier of the atomic-like $3d \rightarrow 4f$ channel [34].

Note that a corresponding but distinctly different fine structure is observed for crystalline Nb of bcc structure [35] (shown as dotted line in Fig. 5). The recorded data thus nicely show the sensitivity of XAS towards structural features of mass-selected clusters. The apparent fine structure in the continuum is qualitatively reproduced by FeFF simulations [36]. In these simulations an icosahedral structure of Nb_{13}^+ has been assumed and one of the twelve equivalent cage atoms has been chosen as the atomic absorber.

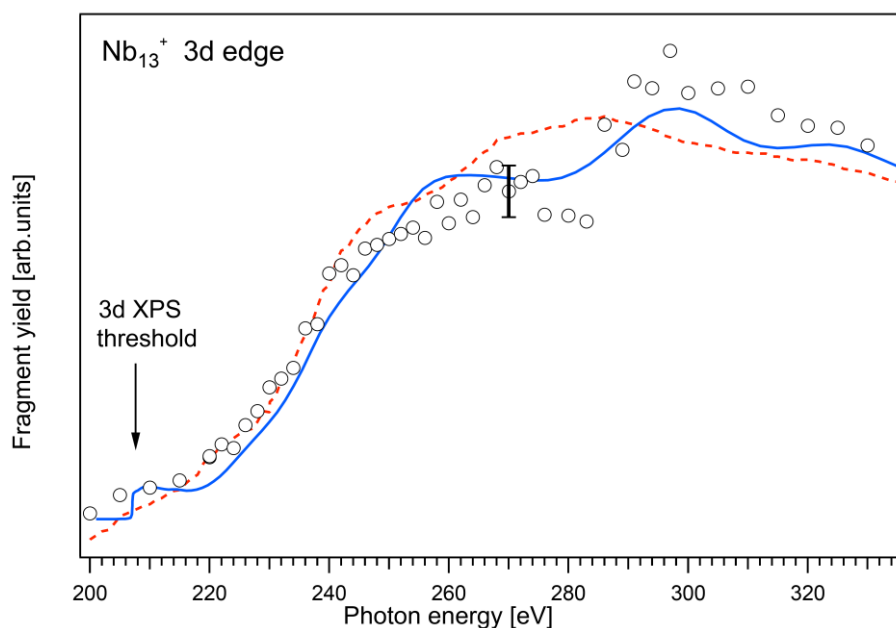


Fig. 5 X-ray absorption spectrum at the M-edge of Nb_{13}^+ . The displayed signal (open circles) comprises the accumulated fragmentation signals as normalized to the BESSY ring current and to the intensity of the Nb_{13}^+ mother ion. The error bar is the standard deviation ($\pm 2\sigma$) of several measurements at 270 eV. Using the FeFF code a simulation of the X-ray absorption spectrum agrees reasonably well with an icosahedral structure of Nb_{13} (absorption by cage atom, solid blue line). The absorption spectrum of bulk niobium [35] (dotted red line) reveals a distinctly different fine structure. (For interpretation of the references to color in this figure legend, the reader is referred to the web version of the article.)

Cobalt

In order to check for the feasibility of XMCD spectroscopy on mass-selected cluster ions circular polarisation of the X-ray beam has been used to record the helicity-dependent L-edge absorption spectra of Co_{22}^+ (Fig. 6). As the cluster magnetic moment scales with the number of atoms we explored the biggest cluster we could produce with sufficient intensity at that time. The X-ray absorption spectra of Co_{22}^+ are normalized to the mother cluster intensity and photon flux. The degree of circular polarisation amounts to 90 %. The cluster ions were cooled inside the ICR cell [37] by multiple collisions with a pulsed He buffer gas (10^{-6} mbar, $> 5 \times 10^{-7}$ mbar for 1 s). For this purpose the ICR trap was cryogenically cooled to 100 K.

As shown in Fig. 6 the L_3 and L_2 edge are clearly resolved. The two recorded curves - taken with negative circular polarization (σ^- , anticlockwise rotation of E-vector in light propagation direction according to [7], see Fig. 6) and with positive polarisation (black open circles) - reveal clearly resolved L_3 and L_2 edges with a striking intensity difference. The dichroic intensity is large at the L_3 edge but

almost vanishes at the L_2 in clear contrast to the dichroic spectrum of the bulk [38]. This dichroic signal shows that the superparamagnetic moment [12-14] of the clusters gets partially aligned along the strong magnetic trapping field at a cluster temperature of ~ 100 K. According to the classical Langevin formula [12-14] the magnetic saturation behaviour of superparamagnetic particles scales inversely with the temperature. Quantitative determination of spin and orbital momenta becomes possible by magneto-optical sum rule analysis [38] under saturation conditions. In order to enable such experiments we aim at further cooling of the ICR cell in order to achieve cluster temperatures as low as 20 K in the future [37].

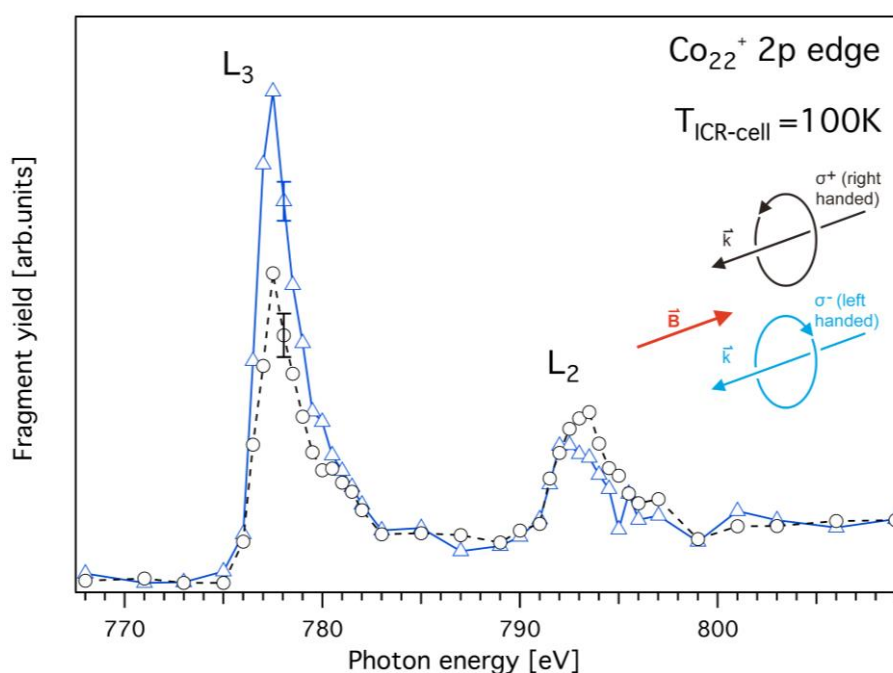


Fig. 6 Circularly polarised X-ray absorption spectra of Co_{22}^+ at the L-edge (negative polarisation (σ^-) = triangles (blue), positive polarisation (σ^+) = open dots (black); the relative orientation of polarisation, light propagation (k), and magnetic field (B) is shown in the cartoon). The signal intensity comprises of the integrated fragment yield and is normalized to the BESSY storage ring current and intensity of the mother ion. The error bar is the standard deviation ($\pm 2\sigma$) from repeated measurements at 778 eV. The spectra have been taken at an ICR-cell temperature of 100 K. The clusters are cooled inside the trap by collisional cooling (see text). (For interpretation of the references to color in this figure legend, the reader is referred to the web version of the article.)

3.4.1.4 Summary

A new setup for recording XAS and XMCD spectra of free mass selected metal clusters has been devised and put into operation at BESSY. First XAS data on clusters of vanadium, niobium, and cobalt were recorded. The spectra of free V_{13}^+ and Co_{22}^+ show well resolved L_3 and L_2 edges, respectively.

The M-edge absorption spectrum of Nb_{13}^+ shows a delayed absorption maximum according to a strong centrifugal barrier in the effective potential. The dependence of recorded signals on the helicity of the X-ray beam was investigated for Co_{22}^+ at a temperature of 100 K. A dichroic signal is clearly evident in the spectrum. Further cooling of the clusters is mandatory for a quantitative determination of the spin and orbital magnetic moments of the clusters under magnetic saturation conditions. Efforts in this direction are underway.

3.4.1.5 Acknowledgements

We acknowledge funding of the FT-ICR experiment by the Deutsche Forschungsgemeinschaft (Nie325/10-1). Furthermore we are grateful to A. Lugatschenko, P. Bischoff, P. Hoffmann, C. Kalus, C. Jung, G. Reichardt, R. Follath, T. Schroeter, G. Meyer, A. Meißner, and P. Gutmann for diverse technical, optical, alignment, vacuum, electronics and software support. We acknowledge fruitful discussions on the initial definition of the experiment with W. Wurth, and valuable suggestions by the referees.

3.4.1.6 References

- [1] L.H. Tjeng, Y.U. Idzerda, P. Rudolf, F. Sette, C.T. Chen, J. Magn. Magn. Mater. 109 (1992) 288.
- [2] P. Gambardella, A. Dallmeyer, K. Maiti, M.C. Malagoli, W. Eberhardt, K. Kern, C. Carbone, Nature 416 (2002) 301.
- [3] M. Getzlaff, A. Kleibert, R. Methling, J. Bansmann, K.-H. Meiwes-Broer, Surf. Sci. 566 (2004) 332.
- [4] J.T. Lau, A. Foehlich, R. Nietubyc, M. Reif, W. Wurth, Phys. Rev. Lett. 89 (2002) 57202.
- [5] K. Fauth, M. Heßler, D. Batchelor, G. Schütz, Surf. Sci. 529 (2003) 397.
- [6] G. Schütz, W. Wagner, W. Wilhelm, P. Kienle, R. Zeller, R. Frahm, G. Materlik, Phys. Rev. Lett. 58 (1987) 737.
- [7] J. Stöhr, J. Electron Spectrosc. Relat. Phenom. 75 (1995) 253.
- [8] O. Sipr, J. Minar, H. Ebert, Eur. Phys. Lett. 87 (2009) 67007.
- [9] C. Van Wüllen, J. Chem. Phys. 130 (2009) 194109.
- [10] C. Van Wüllen, J. Phys. Chem. A 113 (2009) 11535.
- [11] I.M.L. Billas, A. Chatelain, W.A. de Heer, Science 265 (1994) 1682.
- [12] X. Xu, S. Yin, R. Moro, W.A. de Heer, Phys. Rev. Lett. 95 (2005) 237209.
- [13] M.B. Knickelbein, J. Chem. Phys. 125 (2006) 044308.
- [14] F.W. Payne, W. Jiang, J.W. Emmert, J. Deng, L.A. Bloomfield, Phys. Rev. B 75 (2007) 094431.
- [15] C. Walther, St. Becker, G. Dietrich, H.-J. Kluge, M. Lindinger, K. Lützenkirchen, L. Schweikhard, J. Ziegler, Z. Phys. D 38 (1996) 51.
- [16] S. Krückeberg, P. Beiersdorfer, G. Dietrich, K. Lützenkirchen, L. Schweikhard, C. Walther, Rapid Commun. Mass Spectrosc. 11 (1997) 45.
- [17] B.M. Reinhard, A. Lagutschenkov, J. Lemaire, P. Boissel, P. Maitre, G. NiednerSchatteburg, J. Phys. Chem. A 108 (2004) 3350.
- [18] S. Krückeberg, D. Schooss, M. Maier-Borst, J.H. Parks, Phys. Rev. Lett. 85 (2000) 4494.

- [19] M. Grimm, B. Langer, S. Schlemmer, T. Lischke, U. Becker, W. Widdra, D. Gerlich, R. Flesch, E. Rühl, Phys. Rev. Lett. 96 (2006) 066801.
- [20] J.T. Lau, J. Rittmann, V. Zamudio-Bayer, R. Richter, M. Vogel, K. Hirsch, Ph. Klar, F. Lofink, T. Moeller, B.V. Issendorff, Phys. Rev. Lett. 101 (2008) 153401.
- [21] J.J. Yeh, I. Lindau, Atom. Data Nucl. Data Tables 32 (1985) 1-155.
- [22] H.G. Jürgen, Mass Spectrometry: A Textbook, Springer Verlag, Berlin, Heidelberg, New York, 2004.
- [23] W. Eberhardt, J. Stöhr, J. Feldhaus, E.W. Plummer, F. Sette, Phys. Rev. Lett. 51 (1983) 2370.
- [24] B. Pfeffer, S. Jaberg, G. Niedner-Schatteburg, J. Chem. Phys. 131 (2009) 194305.
- [25] P. Caravatti, M. Allemann, Org. Mass Spectrom. 26 (1991) 514.
- [26] A.G. Marshall, P.B. Grosshans, Anal. Chem. 63 (1991) 215A.
- [27] D.A. Dahl, SIMION 3D Version 6.0, Users' Manual Publication No. INEL-95/0403, Lockheed Idaho Technologies Company, Idaho Falls, ID, USA, 1995; D.A. Dahl, T.R. McJunkin, J.R. Scott, Intl. J. Mass Spectrom. 266 (2007) 156.
- [28] J.T. Lau, K. Hirsch, Ph. Klar, A. Langenberg, F. Lofink, R. Richter, J. Rittmann, M. Vogel, V. Zamudio-Bayer, T. Moeller, B.V. Issendorff, Phys. Rev. A 79 (2009) 053201.
- [29] M. Seidl, J.P. Perdew, Phys. Rev. B 50 (1994) 5744.
- [30] A. Pramann, K. Koyasu, A. Nakajima, K. Kaya, J. Phys. Chem. A 106 (2002) 2483.
- [31] M. Martins, K. Godehusen, T. Richter, P. Wernet, P. Zimmermann, J. Phys. B 39 (2006) R79.
- [32] V. Ilakovac, M. Kralj, P. Pervan, M.C. Richter, A. Goldoni, R. Larciprete, L. Petaccia, K. Hricovini, Phys. Rev. B 71 (2005) 085413.
- [33] <http://environmentalchemistry.com/yogi/periodic/V.html#Physical>.
- [34] R.D. Leapman, P. Rez, D.F. Mayers, J. Chem. Phys. 72 (1979) 1232.
- [35] M.J. Olszta, J. Wang, E.C. Dickey, J. Microsc. 224 (2006) 233.
- [36] FEFF 8 program package S.I. Zabinsky, J.J. Rehr, A. Ankudinov, R.C. Albers, M.J. Eller, Phys. Rev. B 52 (1995) 2995.
- [37] H. Kampschulte, PhD thesis, "Entwicklung einer Tieftemperatur FT-ICR Zelle und Charakterisierung mittels Reaktionskinetiken und SynchrotronSpektroskopie", TU Kaiserslautern, 2011.
- [38] C.T. Chen, Y.U. Idzerda, H.-J. Lin, N.V. Smith, G. Meigs, E. Chaban, G.H. Ho, E. Pellegrin, F. Sette, Phys. Rev. Lett. 75 (1995) 152.

3.4.2 Draft - J. Electron Spectroscopy and related Phenomena 2014, accepted

The manuscript was drafted by the group from the Southern Federal University, Rostov-on-Don, Russia. The focus of the manuscript is on the theoretical simulation and description of the x-ray absorption spectrum of Nb_{13}^+ . My contribution to this manuscript relates to the experiment described in the manuscript. I took part in the beamtime in which the x-ray absorption spectrum of Nb_{13}^+ was recorded.

This draft has been accepted in a slightly modified version for publication by the "Journal of Electron Spectroscopy and Related Phenomena" in July 2014.

Atomic and electronic structure of free niobium nanoclusters: simulation of the $M_{4,5}$ -XANES spectrum of Nb_{13}^+

KRAVTSOVA, A., LOMACHENKO, K., SOLDATOV, A., MEYER, J., NIEDNER-SCHATTEBURG, G., PEREDKOV, S., EBERHARDT, W., NEEB, M.

Journal of Electron Spectroscopy and Related Phenomena, **2014**, accepted July 2014, DOI: 10.1016/j.elspec.2014.07.005

<http://www.sciencedirect.com/science/article/pii/S0368204814001534>

**Atomic and electronic structure of free niobium nanoclusters:
simulation of the $M_{4,5}$ -XANES spectrum of Nb_{13}^+**

Antonina N. Kravtsova ^{a,*}, Kirill A. Lomachenko ^{a,b}, Alexander V. Soldatov ^{a,*}, Jennifer Meyer, Gereon Niedner-Schatteburg ^c, Sergey Peredkov ^{d,1}, Wolfgang Eberhardt ^e, Matthias Neeb ^{d,*}

^a *Research Center for Nanoscale Structure of Matter, Southern Federal University, Sorgestr. 5, 344090 Rostov-on-Don, Russia*

^b *Department of Chemistry and NIS Centre of Excellence, University of Turin, Via P. Giuria 7, 10125 Turin, Italy*

Department of Chemistry and State Research Center OPTIMAS, Technische Universität Kaiserslautern, Erwin-Schrödinger Straße, 67663 Kaiserslautern, Germany

^d *Helmholtz-Zentrum Berlin für Materialien und Energie, Wilhelm-Conrad-Röntgen-Campus Adlershof, Elektronenspeicherring BESSY II, Albert-Einstein-Straße 15, Germany*

^e *Technische Universität Berlin, IOAP, Straße des 17. Juni 135, 10623 Berlin, Germany*

¹ Present address: Max-Planck-Institut fuer Chemische Energiekonversion, Stiftstr. 34 - 36, 45470, Mülheim an der Ruhr, Germany

3.4.2.0 Abstract

The atomic and electronic structure of free niobium nanoclusters has been studied on the basis of X-ray absorption near edge structure (XANES) spectroscopy and density functional theory. $M_{4,5}$ -

XANES spectra have been calculated for several structural models of the 13-atomic niobium cluster. The calculations have been done on the basis of both full multiple scattering theory within the muffin-tin approximation for a potential and full-potential finite difference method. The comparison of the experimental $M_{4,5}$ -edge XANES spectrum [1] with the simulated X-ray absorption spectra of Nb_{13}^+ hints to a highly-symmetric icosahedral structure of the cluster. An internuclear distance of $2.2 \pm 0.1 \text{ \AA}$ between neighboring "surface" atoms of the icosahedron and 2.09 \AA between the central "bulk" atom and "surface" atoms, respectively, has been found upon comparison of the experimental and theoretical XANES spectra.

3.4.2.1 Introduction

Nanoclusters attract significant attention both from the fundamental point of view and from the standpoint of their possible applications in nanotechnologies. The properties of nanoclusters change significantly with size and atomic structure [2-3]. Thus, a deep insight into the nature of nanoclusters is impossible without the data on their atomic structure. Such data can most reliably be obtained by studying free clusters, because deposition on any kind of substrate might cause major changes in clusters geometry and electronic structure.

Among the wide variety of different types of clusters, nanoclusters of $4d$ transition metals are of particular interest because of their fundamental importance and potential applications as magnetic materials and nanocatalysts. Niobium nanoclusters are among the most extensively investigated transition-metal clusters due to the several features, such as the relatively large propensity for clusterization and the existence of ferroelectric state related to superconductivity [4]. Atomic and electronic structure of niobium nanoclusters has been previously studied by various experimental and theoretical methods. Niobium trimers Nb_3 in argon matrices have been investigated based on an analysis of absorption (scattering depletion) and Raman spectra [5]. Photoelectron spectra of mass-separated Nb_n^- clusters ($n = 6 - 17$) have been discussed by Kietzmann *et al.* [6], indicating a closed electronic shell of the neutral even-numbered clusters. Time-of-flight mass spectra of free niobium clusters Nb_n produced by laser vaporization have been measured and magic numbers were observed at $n = 7, 13, 15, 22$ [7]. Theoretical methods of investigation have been applied to determine the most stable atomic geometries and electronic properties of niobium nanoclusters in the size range from 2 till 52 atoms [8-15]. Atomic structure and magnetic moment of $4d$ transition-metal clusters with 13 atoms (including Nb_{13} cluster) have been discussed [16-19].

An effective modern technique for the analysis of nanoscale atomic structure (as well as the density of unoccupied electronic states near the bottom of the conduction band) is the X-ray absorption near edge structure (XANES) spectroscopy [20,21]. XANES spectroscopy could give full information on the

local atomic structure around the absorbing atom (coordination numbers, bond lengths and bond angles) with high precision, even for materials without long-range order in the atomic arrangement, such as nanoclusters. The bond length distances can be determined using XANES spectroscopy with the accuracy up to 0.02 Å, bond angles - with the accuracy of few degrees [22]. At the same time, the extraction of structural data from XANES spectra demands complicated theoretical analysis [23,24]. Recently, XANES spectroscopy has been successfully applied to investigate titanium and copper nanoclusters [25-27]. In the present work, the theoretical analysis of the $M_{4,5}$ -XANES spectrum of free Nb_{13}^+ has been performed and compared with the recently measured experimental spectrum [1] in order to extract information on the geometry of the nanoclusters.

3.4.2.2 Experiment

The experimental setup used to measure $M_{4,5}$ -XANES spectra of free mass-selected niobium clusters has been described in detail elsewhere [1,28]. In short, X-ray absorption spectra of free Nb_{13}^+ were measured at UE52-PGM beamline ($\sim 10^{12}$ photons/s, 1st undulator harmonic) of the synchrotron source BESSY II (Helmholtz Zentrum Berlin, Germany). A cluster beam has been produced by pulsed laser vaporization (532 nm, 20 Hz) and supersonic expansion using a synchronized pulsed He buffer gas. Clusters have been mass-selected by using a Penning-like ion trap and FT-ICR mass spectrometer (7 Tesla, Bruker). Fig. 1 shows the ICR-mass spectrum of mass isolated Nb_{13}^+ clusters. Note the low degree of contamination after mass-selection and isolation.

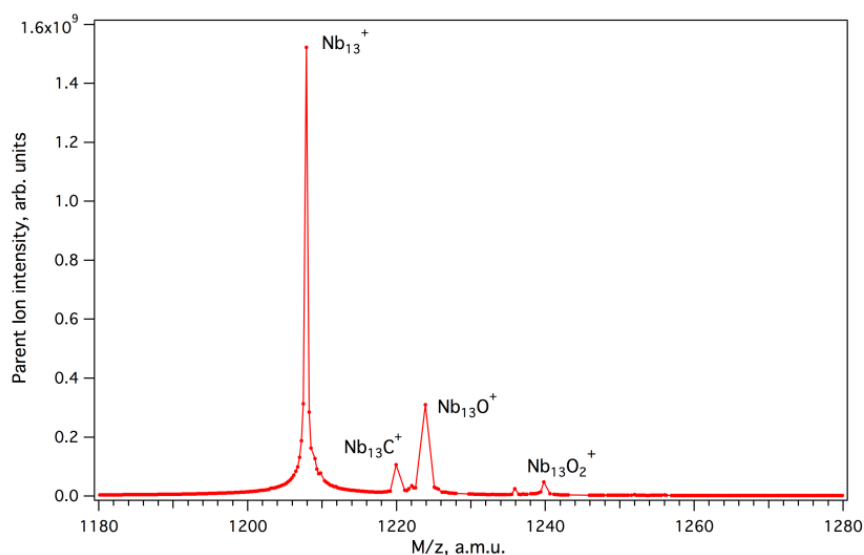


Fig. 1 ICR-mass spectrum of parent Nb_{13}^+ clusters after mass isolation.

X-ray absorption spectra on Nb_{13}^+ have been recorded near the $M_{4,5}$ -absorption edge of niobium using linearly polarized X-ray undulator radiation. As absorption signal, the number of ionic fragments has been recorded inside the ion trap (Fig. 2). The two smallest fragment ions (Nb_1^+ , Nb_2^+)

were the dominant ones and therefore they have been accumulated to represent the absorption spectrum of Nb_{13}^+ at best signal-to-noise ratio.

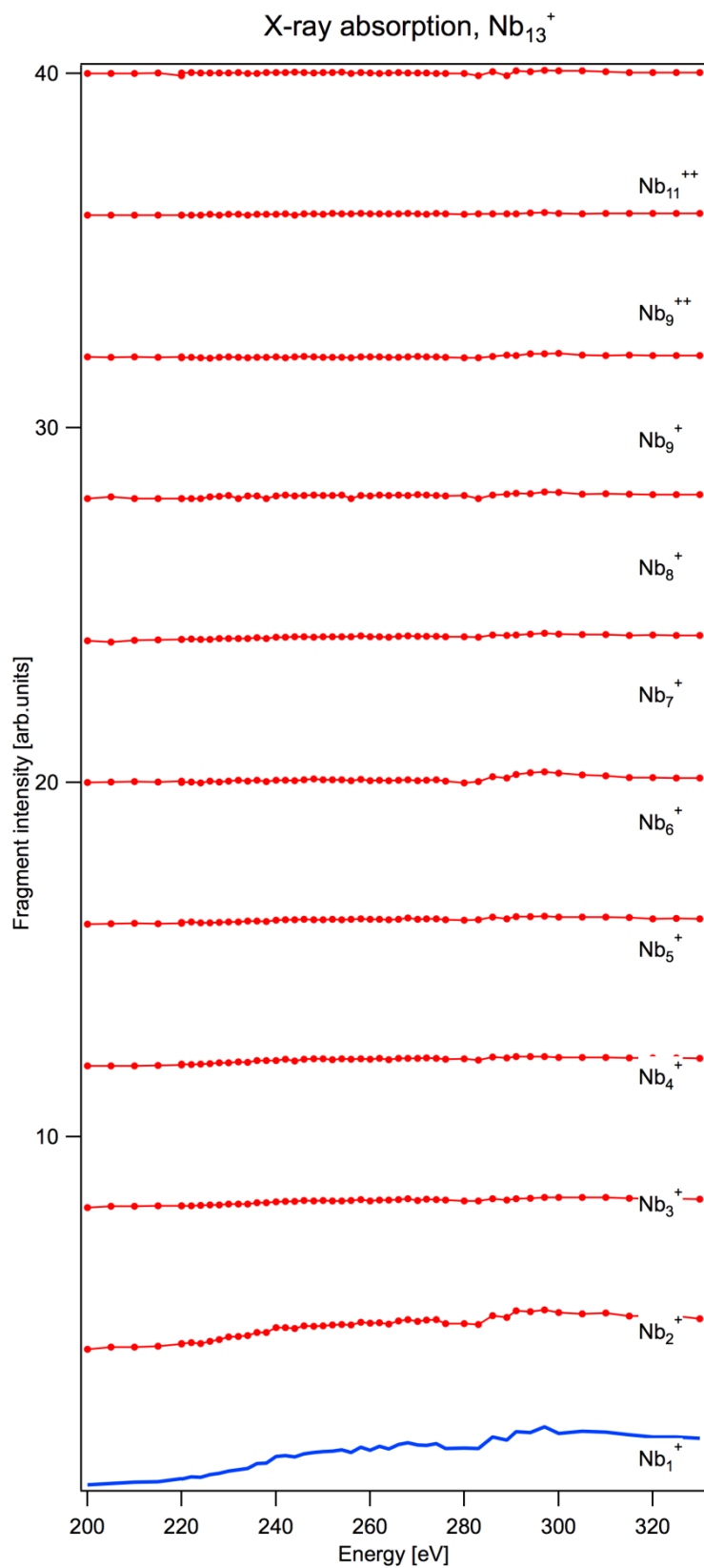


Fig. 2 Mass resolved ion yield absorption spectra of Nb_{13}^+ recorded at the $M_{4,5}$ -edge using soft X-ray undulator radiation (linear polarisation).

The accumulated absorption spectra are shown as top curves in Fig. 4 and 5 (experimental spectrum). The fragmentation yield has been normalized to the photon flux of the beamline, which was recorded by a GaAs-diode behind the monochromator exit slit. Therefore any absorption by the carbon contamination of the beamline optics should not falsify our Nb absorption signal, even though the photon range of the niobium M -edge overlaps with the K -edge of carbon.

The second order light intensity (> 500 eV) transmitted by the monochromator (plane grating) has been measured by us to be 2 - 3 % of the first order intensity. Absorption by carbon and oxygen contaminated Nb_{13}^+ clusters can be ruled out by the tiny degree of contamination (Fig. 1) and the low degree of transmitted second order light. The ICR-cell has been quenched and refilled by new mother clusters after a few seconds of irradiation.

3.4.2.3 Computational details

Theoretical Nb $M_{4,5}$ -XANES spectra for several structural models of 13-atomic niobium cluster have been calculated on the basis of two approaches. Firstly, the self-consistent real-space full multiple-scattering (FMS) theory has been used. The calculations are based on the formalism of the relativistic Green's function in the real space. The muffin-tin approximation [29] for the potential shape has been employed. This theory is implemented into the X-ray absorption spectra and electronic structure FEFF 8.4 code [30]. Secondly, the real-space full-potential finite difference method (FDM) realized in FDMNES-2009 program code [31] has been applied. Its main advantage is the possibility to have a totally free potential shape, thus avoiding limitations associated with the classical muffin-tin approximation for a cluster potential. Calculations of the Nb $M_{4,5}$ -XANES spectra using both methods have been done within the Hedin-Lundquist model of the exchange-correlation potential taking into consideration a core hole effect.

Recently, FEFF code based on muffin-tin approximation has been applied to calculate the $M_{4,5}$ -XANES spectrum of icosahedral Nb_{13} in which the surface atoms have been considered as absorbing atom [1]. In the present study we use not only FEFF, but also FDMNES code, to exhibit the influence of non-muffin-tin effects. Such effects are particularly important to be considered in the simulations of nanoclusters due to the significant "surface" atoms contribution to the cluster's electronic structure. Moreover, Nb $M_{4,5}$ -edge spectra have independently been simulated for both the "surface" and central ("bulk") atom of the icosahedron.

The atomic geometry of the structural models of Nb_{13}^+ has been optimized on the basis of the Kohn-Sham density functional theory using the ADF2009 program code [32] within the generalized gradient approximation (GGA) using the OLYP [33,34] model for the exchange-correlation potential. This model was chosen among other tested models (PBE, OPBE, BLYP), as it results in better

agreement between theoretical and experimental values of the dimer bond length. The experimental value of the Nb₂-bond length is equal to $d_{\text{Nb}} \sim 2.08 \text{ \AA}$ [35,36]. Our calculation of the dimer bond length performed within the OLYP exchange-correlation model results in a value of $d_{\text{Nb}} = 2.07 \text{ \AA}$, while the calculation done within the OPBE model results in $d_{\text{Nb}} = 2.03 \text{ \AA}$. For cluster geometry optimization a core double zeta, valence triple zeta, polarized basis set (TZP) [37] of Slater-type orbitals has been used. The positive charge of Nb₁₃⁺ cluster has been taken into account.

The FDM scheme has previously been successfully applied to compute X-ray absorption near-edge spectra of metal nanoclusters, for example, small titanium [25] and copper [26,27] nanoclusters. The DFT approach as realized in ADF code, on the other hand, has been successfully used to study the atomic geometries and electronic properties of free copper [27,26] and titanium [38] nanoclusters.

3.2.2.4 Results and discussion

At the first step the Nb $M_{4,5}$ -edge XANES spectrum of bulk niobium was calculated to check the adequacy of the used theoretical approaches. The bulk niobium crystallizes in *bcc* structure with the lattice parameter $a = 3.30 \text{ \AA}$ [39]. A comparison of the theoretical Nb $M_{4,5}$ -XANES spectrum of bulk niobium simulated on the basis of the full-potential finite difference method with the corresponding experimental EELS spectrum taken from Olszta *et al.* [40] is presented in Fig. 3.

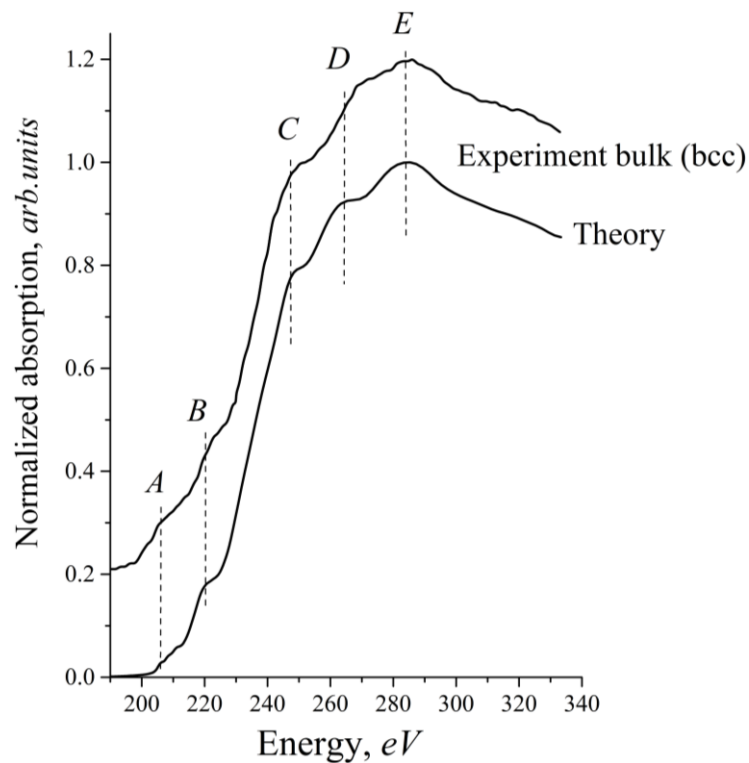


Fig. 3. Comparison of the $M_{4,5}$ -XANES spectrum of bulk niobium (*bcc* structure) calculated on the basis of the full-potential finite difference method (FDMNES code) with the corresponding experimental EELS spectrum from Olszta *et al.* [40].

It can be seen that the calculated spectrum is in good agreement with the experimental one. Minor discrepancies between the experimental and theoretical spectra may be caused by the sample surface oxidation. An agreement between the theoretical and experimental spectra of bulk niobium supports the application of the finite difference method for the analysis of XANES of niobium nanoclusters. Initially, the icosahedral model of the Nb_{13} cluster structure was considered. The lattice parameter $a = 3.30 \text{ \AA}$ of a *bcc* niobium crystal gives rise to an interatomic bulk distance of $r = 2.86 \text{ \AA}$ ($r = a/2 \cdot \sqrt{3}$) which was used as initial guess of the distance between the "surface" atoms ($d_{\text{surf-surf}}$) of icosahedral Nb_{13} . The distance between the central atom and the "surface" atoms ($d_{\text{cent-surf}}$) of an icosahedron is generally related to $d_{\text{cent-surf}} = 1/2 \sqrt{(1 + \phi^2)} d_{\text{surf-surf}}$ where ϕ is the so-called Fibonacci number 1.618. Using the interatomic bulk distance as initial guess for the distance of the surface atoms of the icosahedron ($d_{\text{surf-surf}} = 2.86 \text{ \AA}$) the distance between the central and "surface" atoms is equal to 2.72 \AA .

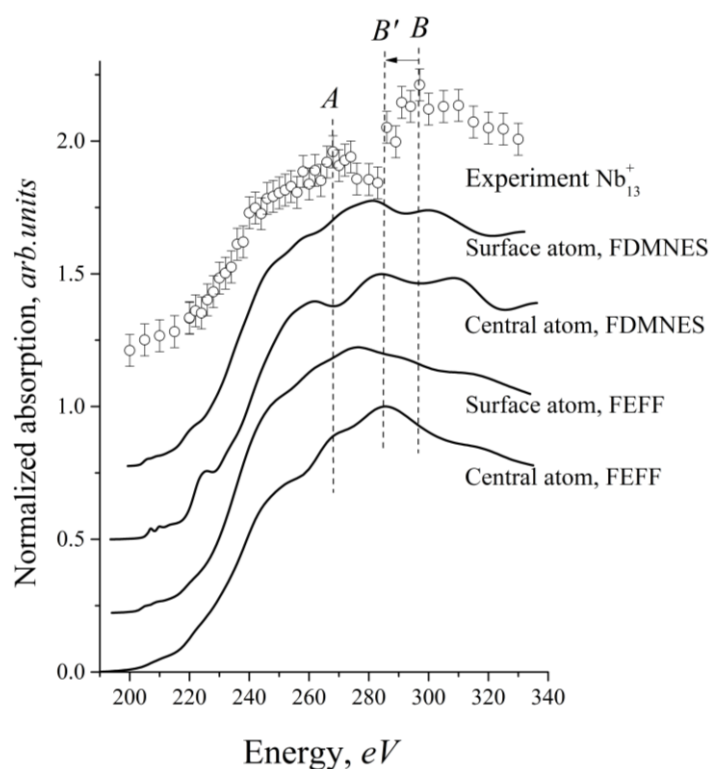


Fig. 4 Experimental $M_{4,5}$ -XANES spectrum of free Nb_{13}^+ from Peredkov *et al.* [1] compared to the theoretical spectra (FDMNES and FEFF) calculated for the icosahedral model with an atomic distance between surface atoms equal to that of the crystalline bulk (2.86 \AA).

Fig. 4 compares the experimental $M_{4,5}$ -edge X-ray absorption spectrum of Nb_{13}^+ ($M_{4,5}$ -edge) with the theoretical spectra calculated for the icosahedral structure of the 13-atomic cluster using the bulk atomic distance as initial guess for the "surface" atom distance. The displayed theoretical spectra are

computed on the basis of both full-multiple scattering theory within the muffin-tin approximation for the potential shape (FEFF 8.4 program) and full-potential finite difference method (FDMNES code).

The spectra were simulated for the cases when both "surface" and central atoms were sequentially set as the absorbers. It can be seen from Fig. 4 that fine structures of the experimental and theoretical spectra contain features marked as *A* and *B*. However, maxima *B* of the theoretical spectra calculated on the basis of both FMS and FDM methods are shifted to the lower energy region as compared to maximum *B* of the experimental spectrum. The disagreement between the experimental and theoretical data (difference in the intensity of peak *A* and energy position of peak *B*) suggests for a refinement of the initially considered structural model of 13-atomic niobium cluster which is described in the following paragraph.

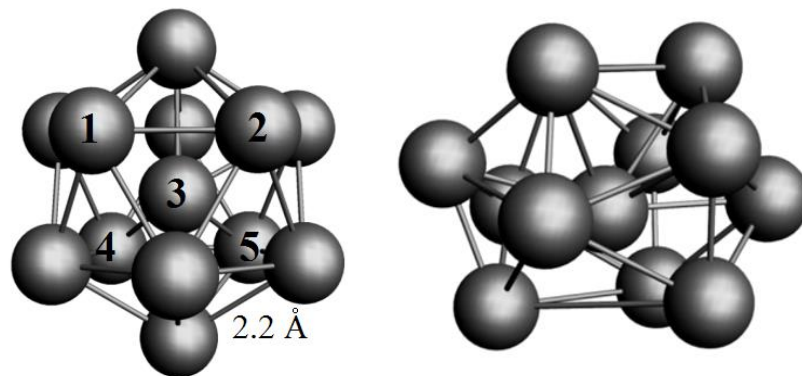


Fig. 5 (a) Schematic representation of the icosahedral structure of the Nb₁₃ cluster used for calculation of the $M_{4,5}$ -XANES spectra shown in Fig. 6. Labels 1-2-3-4-5 mark atoms laying in the plane used for calculations of a contour map of the potential of the niobium cluster (Fig. 7). **(b)** Scheme of the "amorphous" structure obtained by atomic geometry optimization based on density functional theory implemented in the ADF code (see text).

To further improve the agreement between theory and experiment, the calculations of the Nb $M_{4,5}$ -XANES spectra have been carried out for the icosahedral structural model of Nb₁₃ varying the interatomic distances (calculations have been done for $d_{\text{surf-surf}}$ equal to 2.86 Å, 2.36 Å, 2.2 Å, 2.1 Å). A good agreement between experiment and theory is achieved when the internuclear distance between neighboring "surface" atoms is equal to $d_{\text{surf-surf}} = 2.2$ Å. For this surface atom separation a distance from the center atom to the surface atoms of $d_{\text{cent-surf}} = 2.09$ Å results (Fig. 5a). This bond-length reduction agrees with the general tendency of decreasing interatomic distances with decreasing nanoparticles size [41]. We suppose that the significant bond length reduction in Nb₁₃ as compared to bulk niobium is not only due to coordination change but also due to change in chemical bonding from metallic (in macroscopic particles) to covalent one (in small clusters). Note that the

interatomic distance of molecular Nb_2 is 2.08 Å [35,36], i.e. similar to the bond length between the central and surface atoms of the Nb_{13}^+ -icosahedron which results in the best agreement of the theoretical with the experimental XANES spectrum as shown in Fig. 6.

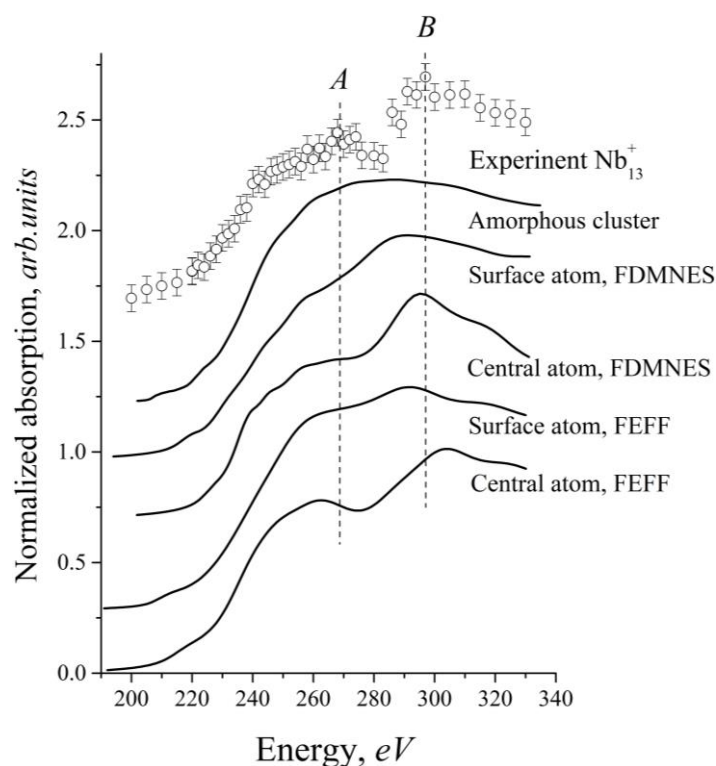


Fig. 6 Experimental $M_{4,5}$ -edge XANES spectrum of free Nb_{13}^+ from Peredkov *et al.* [1] with the corresponding theoretical spectra (FDMNES, FEFF) calculated for the icosahedral structure having a distance between the "surface" atoms of 2.2 Å. Note that the simulated FDMNES spectrum of the amorphous structure shows definitely less fine structure than the spectra of the icosahedrons.

Fig. 6 shows theoretical XANES spectra simulated for the icosahedron of Nb_{13}^+ with distances $d_{\text{surf-surf}} = 2.2$ Å and $d_{\text{cent-surf}} = 2.09$ Å. The simulations have been done on the basis of the full multiple scattering theory within the muffin-tin approximation for the potential shape (FEFF 8.4 code) and the full-potential finite difference method (FDMNES code). For both types of calculations the "surface" and center "bulk" atom have been individually chosen as photon absorber. It can be seen that FDMNES calculations of XANES spectra are in slightly better agreement with the experiment as compared with FEFF 8.4 calculations, what can be explained by the presence of non-muffin-tin effects due to the surface contribution to the electronic structure of the cluster.

Finally, the optimization of the atomic geometry of the Nb_{13}^+ cluster was additionally performed based on the DFT implemented in the ADF code [32]. As described above the icosahedral model was used as starting structure for the optimization. Without symmetry restrictions during the

optimization, an "amorphous" cluster is obtained. In other words, all atoms of the cluster become nonequivalent (Fig. 5b). Theoretical Nb $M_{4,5}$ -XANES spectra of the amorphous cluster structure have been calculated based on the full-potential finite difference method (FDMNES code) for all nonequivalent niobium positions of the obtained structure (every nonequivalent niobium atom was sequentially set up as an absorbing one). To get a final theoretical $M_{4,5}$ -edge inner-shell absorption curve, XANES spectra for all nonequivalent positions were summed up. The theoretical $M_{4,5}$ -edge XANES spectrum for the "amorphous" structure of Nb_{13}^+ cluster is presented in Fig. 6. It can be seen that the calculated spectrum of the "amorphous" cluster shows much less fine structure than those of the icosahedron (experimental features marked as *A* and *B* are not reproduced in the theoretical spectrum of the "amorphous" structure). The inequivalent atoms of the amorphous structure gives rise to slightly different absorption spectra which superimpose to a featureless total spectrum. Thus the insufficient agreement between experiment and theory indicates that the "amorphous" structure is less likely. In other words, the measured spectral fine structure favors a high symmetry of the 13-atomic niobium cluster which is formed under the chosen experimental conditions. The performed analysis allows for the conclusion that the icosahedron with the distance between the "surface" atoms of $\sim 2.2 \text{ \AA}$ is the most preferable structure of the 13-atomic niobium cluster among the considered models.

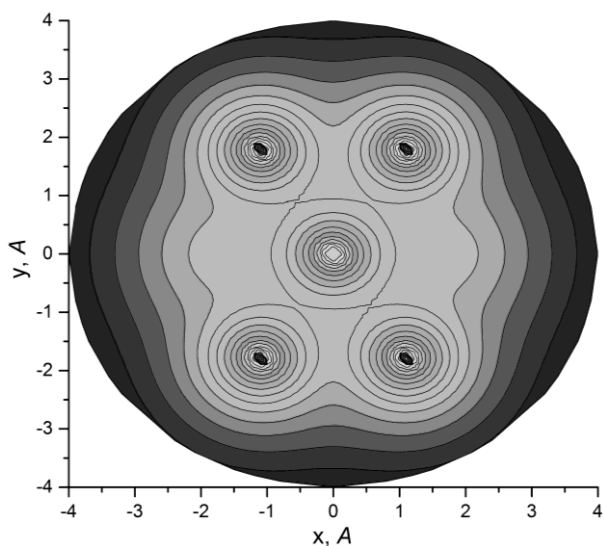


Fig. 7 Contour map of the potential of the 13-atomic icosahedral niobium cluster along the plane containing the central atom and four "surface" atoms. Darker areas correspond to weaker potential.

The FDMNES code was also used to calculate a contour map of the potential of the 13-atomic icosahedral niobium cluster within one of the icosahedral symmetry planes containing the central atom and four "surface" atoms (the plane containing atoms marked as 1-2-3-4-5 in Fig. 5a). The

contour map of the potential of Nb_{13} is shown in Fig. 7. One can see that the muffin-tin approximation [29] is not valid for "surface" atoms of the Nb_{13} cluster. Within the muffin-tin approximation, the potential between atoms must be constant; thus, the potential along the line from the surface atoms to the outer region must be constant. From Fig. 7 it can be seen that this is not the case of Nb_{13} cluster, as the potential is changing significantly. Thus, full-potential methods like FDMNES seems to be most appropriate to simulate XANES spectra of small niobium nanoclusters.

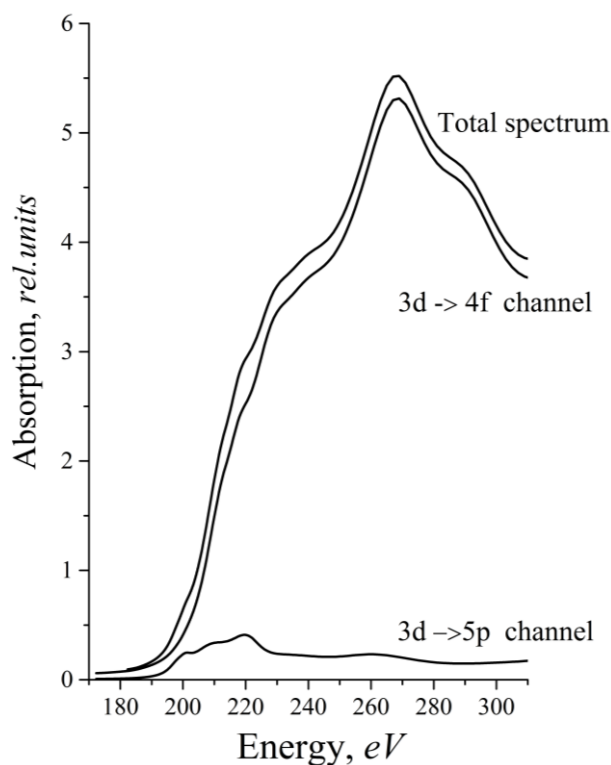


Fig. 8 Calculated $3d \rightarrow 4f$ and $3d \rightarrow 5p$ electronic transitions corresponding to the $M_{4,5}$ -XANES of central niobium atom of icosahedral structure of 13-atomic niobium cluster (distance between the "surface" atoms is 2.2 Å). The total $M_{4,5}$ -XANES spectrum calculated with the consideration of both Nb $3d \rightarrow 4f$ and Nb $3d \rightarrow 5p$ channels are also presented.

According to dipole selection rules, the electronic transition corresponding to the Nb $M_{4,5}$ -XANES includes two $\Delta l = \pm 1$ channels: $3d \rightarrow 4f$ and $3d \rightarrow 5p$. In the present work $M_{4,5}$ -XANES spectra for all considered structural models of niobium clusters have been calculated as a sum of two dipole allowed channels. The possibility of different transitions of $3d$ electrons by photon absorption in niobium has been discussed earlier [42]. As an example, Fig. 8 shows the calculations of two channels ($d \rightarrow f$ and $d \rightarrow p$) corresponding to the $M_{4,5}$ -XANES of central niobium of icosahedral structure of 13-atomic niobium cluster with 2.2 Å distance between the "surface" atoms. It can be seen that the

$d \rightarrow f$ transition contributes much more than the $d \rightarrow p$ transition to the Nb $M_{4,5}$ -XANES spectrum, which is similar to earlier results on bulk niobium [42].

3.4.2.5 Conclusions

Theoretical analysis of the $M_{4,5}$ -edge X-ray absorption spectra of Nb_{13}^+ clusters has been performed and compared with experimental results. The Nb $M_{4,5}$ -XANES spectra have been calculated on the basis of the full multiple scattering theory (FEFF 8.4 code) and the full-potential finite difference method (FDMNES code) for several structural models of the cluster. XANES analysis has shown that high-symmetrical icosahedral structure of the 13-atomic niobium cluster is more preferable than the thermodynamically more stable "amorphous" one. The best agreement of the theoretical $M_{4,5}$ -XANES with the experiment has been obtained for the icosahedral niobium clusters with the distances between the "surface" atoms of $2.2 \pm 0.1 \text{ \AA}$.

3.4.2.6 Acknowledgements

This research has been supported by the German-Russian Interdisciplinary Science Center (G-RISC). A.V.S. acknowledges the Mega-grant of the Russian Federation Government to support scientific research under the supervision of the leading scientist at Southern Federal University, No. 14.Y26.31.0001. The authors thank the referee for valuable comments finding consideration in the paper.

3.4.2.7 References

- [1] Peredkov, S., Savci, A., Peters, S., Neeb, M., Eberhardt, W., Kampschulte, H., Meyer, J., Tombers, M., Hofferberth, B., Menges, F., Niedner-Schatteburg, G., J. Electron Spectros. Relat. Phenomena 184 (2011) 113-118.
- [2] Johnston, R.L. (2002) Atomic and molecular clusters, Taylor and Francis, London and New York.
- [3] Eberhardt, W., Surface Science 500 (2002) 242-270.
- [4] Moro, R., Yin, Sh., Xu, X., de Heer, W.A., Phys. Rev. Lett. 93 (2004) 086803.
- [5] Wang, H., Craig, R., Haouari, H., Liu, Y., Lombardi, J.R., Lindsay, D.M., J. Chem. Phys. 105 (1996) 5355-5357.
- [6] Kietzmann, H., Morenzin, J., Bechthold, P.S., Ganteför, G., Eberhardt, W., J. Chem. Phys. 109 (1998) 2275-2278.
- [7] Sakurai, M., Watanabe, K., Sumiyama, K., Suzuki, K., J. Chem. Phys. 111 (1999) 235-238.
- [8] Fa, W, Luo, Ch., Dong, J., Phys. Rev. B 71 (2005) 245415.
- [9] Fournier, R., Pang, T., Chen, Ch., Phys. Rev. A 57 (1998) 3683-3691.
- [10] Goodwin, L., Salahub, D.R., Phys. Rev. A 47 (1993) R774-R777.
- [11] Grönbeck, H., Rosen, A., Phys. Rev. B 54 (1996) 1549-1552.
- [12] Grönbeck, H., Rosen, A., Andreoni, W., Phys. Rev. A 58 (1998) 4630-4636.
- [13] Kumar, V., Kawazoe, Y., Phys. Rev. B 65 (2002) 125403.
- [14] Nayak, S.K., Rao, B.K., Khanna, S.N., Jena, P., Chem. Phys. Lett. 259 (1996) 588-592.

- [15] Ren, F.-Zh., Wang, Y.-X., Zhang, G.-B., Wei, Sh.-K., Luo, Y.-H., *Chin. Phys. B* 18 (2009)1491-1497.
- [16] Chang, C.M., Chou, M.Y., *Phys. Rev. Lett.* 93 (2004) 133401.
- [17] Kaiming, D., Jinlong, Y., Chuanyun, X., Kelin, W., *Phys. Rev. B* 54(1996) 11907-11910.
- [18] Sun, Y., Zhang, M., Fournier, R., *Phys. Rev. B* 77 (2008) 075435.
- [19] Sun, Y., Fournier, R., Zhang, M., 2009, *Phys. Rev. A* 79 (2009) 043202.
- [20] Bianconi, A. (1988) XANES spectroscopy, in: Prins, R., Koningsberger, D.C. (Eds.), *X-ray absorption: principles, applications and techniques of EXAFS, SEXAFS and XANES*, John Wiley and sons, New York, pp. 573-662.
- [21] Bunker, G. (2011) *Introduction to XAFS: a practical guide to x-ray absorption fine structure spectroscopy*, Cambridge University Press.
- [22] Smolentsev, G., Soldatov, A.V., Feiters, M.C., *Phys. Rev. B* 75 (2007) 144106.
- [23] Smolentsev, G., Soldatov, A., *J. Synchrotron Radiat.* 13 (2006) 19-29.
- [24] Smolentsev, G., Soldatov, A.V., *Comp. Matter. Science* 39 (2007) 569-574.
- [25] Mazalova, V., Kravtsova, A., Yalovega, G., Soldatov, A., Piseri, P., Coreno, M., Mazza, T., Lenardi, C., Bongiorno, G., Milani, P., 2007, *Nucl. Instrum. Methods Phys. Res. A* 575 (2007) 165-167.
- [26] Mazalova, V.L., Soldatov, A.V., Adam, S., Yakovlev, A., Möller, T., Johnston, R.L., *J. Phys. Chem. C* 113 (2009) 9086-9091.
- [27] Mazalova, V.L., Soldatov, A.V., 2008, *J. Struct. Chem.* 49 (2008) Supplement, S107-S115.
- [28] Peredkov, S., Neeb, M., Eberhardt, W., Meyer, J., Tombers, M., Kampschulte, H., Niedner-Schatteburg, G., *Phys. Rev. Lett.*, 107 (2011) 233401.
- [29] Rehr, J.J., Albers, R.C., *Rev. Mod. Phys.* 72 (2000) 621-654.
- [30] Rehr, J.J., Ankudinov, A.L., *Coord. Chem. Rev.* 249 (2005) 131-140.
- [31] Joly, Y., *Phys. Rev. B* 63 (2001) 125120.
- [32] te Velde, G., Bickelhaupt, F.M., Baerends, E.J., Fonseca Guerra, C., van Gisbergen, S.J.A., Snijders, J.G., Ziegler, T., *J. Comput. Chem.*, 22 (2001) 931-967.
- [33] Handy, N.C., Cohen, A.J., *Mol. Phys.* 99 (2001) 403-412.
- [34] Hoe, W.-M., Cohen, A.J., Handy, N.C., *Chem. Phys. Lett.* 341 (2001) 319-328.
- [35] Hales, D.A., Lian, L., Armentrout, P.B., *Int. J. Mass Spectrom. Ion Process.* 102 (1990) 269-301.
- [36] James, A.M., Kowalczyk, P., Fournier, R., Simard, B., *J. Chem. Phys.* 99 (1993) 8504.
- [37] van Lenthe, E., Baerends, E.J., *J. Comp. Chem.* 24 (2003) 1142-1156.
- [38] Kravtsova, A.N., Guda, A.A., Mazalova, V.L., Soldatov, A.V., Johnston., R.L., *Nanostructures: Mathematical physics and modeling* 4 (2011) 15-22 (in Russian).
- [39] Barns, R.L., *J. Appl. Phys.* 39 (1968) 4044-4045.
- [40] Olszta, M.J., Wang, J., Dickey, E.C., 2006, *J. Microsc.* 224 (2006) 233-241.
- [41] Riedler, M., de Castro, A.R.B., Kolmakov, A., Löfken, J.O., Nowak, C., Soldatov, A.V., Wark, A., Yalovega, G., Möller, T., 2001, *J. Chem. Phys.* 115 (2001) 1319-1323.
- [42] Leapman, R.D., Rez, P., Mayers, D.F., *J. Chem. Phys.* 72 (1980) 1232-1243.

4. SPIN AND ORBITAL MAGNETIC MOMENTS OF SMALL COBALT CLUSTERS

We investigated the magnetic structure of small cobalt clusters Co_n^+ in close cooperation with S. Peredkov^{*}, M. Neeb[#] and W. Eberhardt^{*} (*Institut für Optik und Atomare Physik, Technische Universität Berlin, Germany, [#]Helmholtz Zentrum Berlin für Materialien und Energie, BESSY II, Germany). The experimental setup was located at the synchrotron facility BESSY II/HZB. Experiments were carried out by a team. The core members of this team were S. Peredkov, M. Tombers and me. Data evaluation was done by S. Peredkov and me. Preliminary results are included in the Diploma thesis of M. Tombers^[1]. The spin and orbital magnetic moments of the small cobalt clusters Co_n^+ were published in 2011. The first draft was written by S. Peredkov and M. Neeb. The final draft after internal revision within the group was accepted by Physical Review Letters.

PEREDKOV, S., NEEB, M., EBERHARDT, W., MEYER, J., TOMBERS, M., KAMPSCHULTE, H., NIEDNER-SCHATTEBURG, G., *Spin and Orbital Magnetic Moments of Free Nanoparticles*, Physical Review Letters **2011**, *107*, 233401

<http://link.aps.org/doi/10.1103/PhysRevLett.107.233401>

4.1 Introduction

Cobalt is one of the few elements which show a ferromagnetic order at room temperature. The spin and orbital magnetic moments of bulk cobalt are reduced compared to the atomic value. Especially, the orbital moment is almost completely quenched due to orbital hybridization, symmetry breaking, delocalization and the formation of a band structure. The evolution of the orbital and spin magnetic moments upon size reduction of the sample, i.e. the magnetic moment of nanoparticles, thin films, and clusters has been at the focus of numerous theoretical^[2-16] and experimental^[17-22] studies within the last years. One technique to experimentally access magnetic moments is x-ray magnetic circular dichroism^[23-26] (XMCD) spectroscopy. Most important XMCD allows the determination of the spin and orbital contributions to the total magnetic moment even of dilute samples such as surfaces^[27,28], thin films^[29-33], deposited nanoparticles^[34-41] or clusters^[42-47] and adatoms^[48-50]. Enhanced magnetic moments were found in low dimensional samples. This enhancement^[42-44] can be explained by the

reduced coordination of surface atoms and more localized electronic states or in other words narrower bands. Particularly for clusters the ratio of surface to bulk atoms is strongly enhanced^[51-53].

The influence of the support on the magnetic properties can be significant for deposited clusters, i.e. leading to an enhancement^[42-44,54] or quenching^[55] of the magnetic moments depending on the individual combination of cluster and support material. This complex interaction makes predictions of the magnetic properties of new magnetic materials highly demanding. This predictability would be important for the design of new data storage materials. In case of nanostructures and especially in the case of clusters not only the material but also the geometrical structure of the cluster has to be considered^[56,57]. The geometrical structure of clusters is closely related to their electronic structure and thus to the magnetic moment of the clusters. Therefore, knowledge about the magnetic structure of isolated clusters becomes more important. The complex system of cluster plus support has first to be divided into its individual parts before the complex interaction between cluster and support can be taken into account.

The total magnetic moment of free transition metal clusters can be determined by Stern-Gerlach experiments^[58-67]. Stern-Gerlach experiments of elements with magnetic ordering in the bulk revealed enhanced magnetic moments compared to the bulk phase. Clusters of elements having no magnetic order in the bulk even showed a magnetic moment once the clusters became small enough^[63,68-70]. Spin and orbital magnetic moments are not accessible by Stern-Gerlach experiments. XMCD spectroscopy of free clusters enables us to experimentally determine spin and orbital magnetic moments^[71-76].

The magnetic moments of small cobalt clusters Co_n^+ will be discussed in the following chapter. The results have been published in 2011^[71]. Note, that only $m_{S,L,z}$, i.e. the projection onto the quantization axis, can be directly determined from the experimental x-ray absorption spectra (Chap. 2.4.4 and 3.2.3). The experimental values depend on the cluster temperature and on the magnetic field used to align the magnetic moments with respect to the external magnetic field. The experimental moments can be extrapolated to the intrinsic moments via a Langevin or Brillouin function which describe the field and temperature dependence of the magnetic moments of the clusters (Chap. 2.3 and 3.2.4). The coupling of the spin and orbital magnetic moments is a key issue. In our initial interpretation, we assumed decoupled spin and orbital magnetic moments. A controversy arose if this interpretation was valid^[73,77]. The magnetic interaction energy of the moments with the external magnetic field has to exceed the spin orbit coupling for the spin and orbital moments to decouple. Otherwise, LS coupling prevails. Our initial interpretation of decoupled moments was proven wrong.

Chap. 4.1 gives the reevaluation of the experimental magnetic moments of Co_n^+ clusters. The effect of the different coupling schemes on the final intrinsic magnetic moments will be discussed (Fig. 4.3). The magnetic moments from the present work will be compared to calculated spin magnetic moments of neutral Co_n and singly positively charged Co_n^+ clusters (Chap. 4.3.1). Spin and total magnetic moments of the present work will be discussed in relation to total magnetic moments of neutral cobalt clusters Co_n from Stern-Gerlach experiments (Chap. 4.3.2). Recently, Lau *et al.*^[74,78] published XMCD results of cobalt clusters Co_n^+ . This allows us not only to compare results (Chap. 4.3.3) but also gauge the validity of the experimental approach of Total Ion Yield spectroscopy^[71-74,79-81] (TIY) (Chap. 3.1.5). This chapter will be concluded by the publication in "Physical Review Letters"^[71].

4.2 Coupling of angular moments

The by XMCD spectroscopy experimentally accessible magnetic moments are the projections of the magnetic moments onto a quantization axis (Chap. 2.4.4 and 3.2.3). These measured moments are dependent on the experimental conditions at which the spectra are recorded. The alignment of magnetic moments depend on two parameters, i.e. the external magnetic field B and the cluster temperature T . The stronger the external magnetic field is the better is the alignment. Thermal fluctuations oppose the alignment of magnetic moments and thus high temperatures are unfavorable for the experiments (Fig. 4.1).

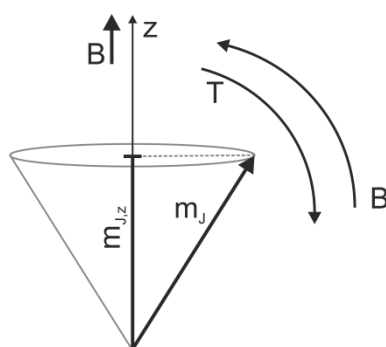


Figure 4.1 Influence of the magnetic field and temperature on the alignment of magnetic moments. A lower temperature leads to a better alignment due to reduced thermal fluctuations. A high external magnetic field is advantageous.

The intrinsic magnetic moments can be calculated from the experimental magnetic moments. The projection of a magnetic moment at a given temperature T and external magnetic field B follows a Langevin / Brillouin function^[82-84] (Chap. 2.3 and 3.2.4). In our case, it is important to know the

interaction between angular moments and external magnetic field (Fig. 4.2a). If LS coupling prevails, the total angular momentum will align to the external field. Therefore, the total angular momentum has to be corrected according to Langevin / Brillouin. If the magnetic field is strong enough, it will be able to decouple spin and orbital angular momentum. In that case both moments have to be scaled individually (Fig. 4.2b). We assumed decoupled moments at our experimental conditions and subsequently scaled both contributions separately^[71]. A controversy about the (de)coupling of spin and orbital magnetic moment surfaced after Lau *et al.* published a data set on iron clusters ($T_{\text{cluster}} < 15 \text{ K}$ and $B = 5 \text{ T}$)^[73]. They assumed LS coupling and subsequently the alignment of the total magnetic moment.

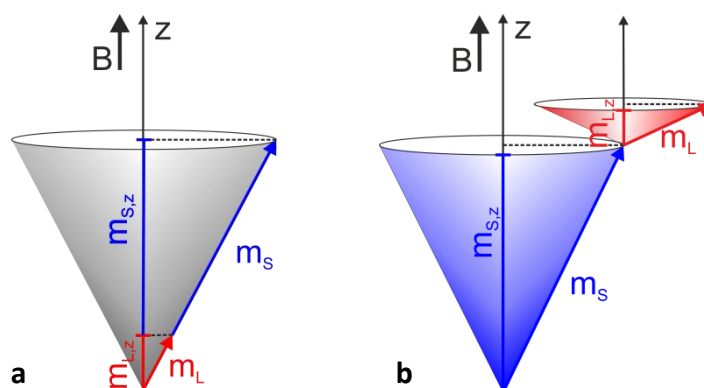


Figure 4.2 coupling schemes for spin and orbital magnetic moments (the magnetic field axis coincides with the quantization axis z) **(a)** Spin and orbital magnetic moment couple to a total magnetic moment which aligns to the external magnetic field. **(b)** The external magnetic field is strong enough to overcome the spin orbit coupling and decouples m_s and m_L . Spin and orbital magnetic moment align individually to the external magnetic field.

Since then, several discussions led to the conclusion that the spin orbit coupling exceeds the interaction with the magnetic field, i.e. LS coupling is present at the experimental conditions of both experiments ($T < 20 \text{ K}$, $B = 5$ or 7 T)^[77]. Thus, our initial evaluation was proven wrong. Reevaluation of our experimental data with assumed LS coupling revealed that there are only minor changes in the spin magnetic moment (Fig. 4.3a/b). The orbital magnetic moment changes quite significantly. Due to its lower magnitude, it is harder to align (Fig. 4.2b). The ratio of $m_{L,z} / m_L$ is much smaller than that of $m_{s,z} / m_s$. The orbital moment is scaled more than the spin magnetic moment (Fig. 4.4). The magnetic moments plotted in Fig. 4.3a are given in Tab. 4.1. The individually scaled values plotted in Fig. 4.3b are given in Chap. 4.5.

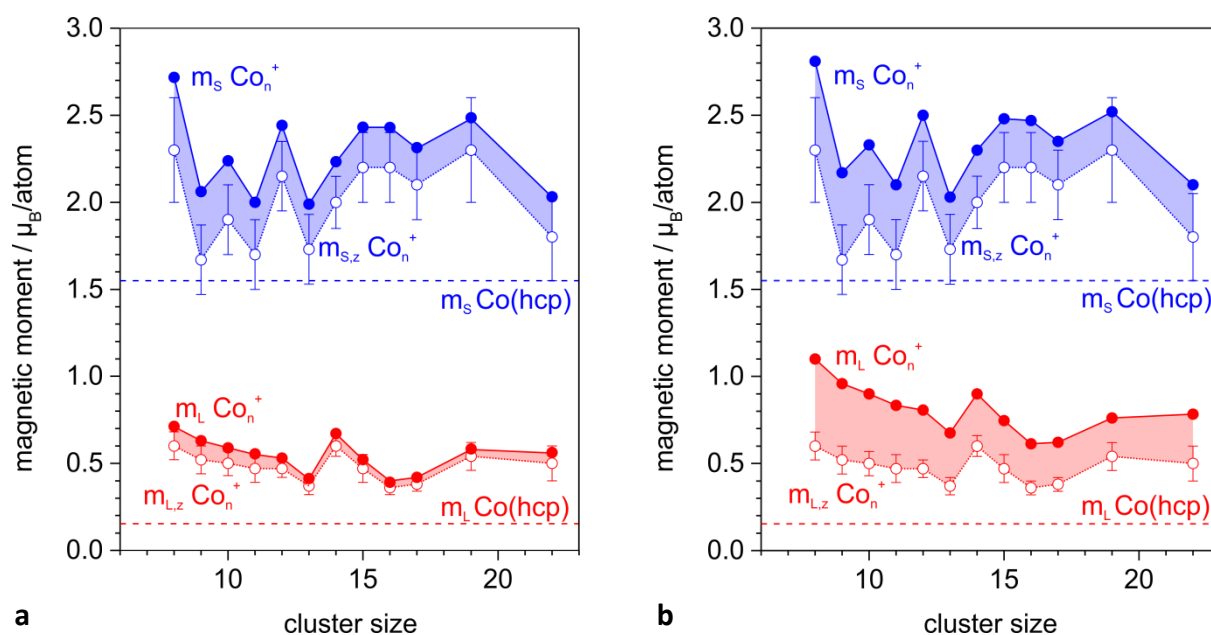


Figure 4.3 Experimental spin $m_{s,z}$ (blue open circles) and orbital $m_{L,z}$ (red open circles) magnetic moments of small Co_n^+ clusters in comparison with intrinsic magnetic moments after (a) assumed LS coupling and scaling of the total magnetic moment and (b) decoupled spin and orbital magnetic moments and individual scaling of spin and orbital magnetic moment. The shaded areas indicate the change in spin and orbital magnetic moment due to Langevin correction (blue (red) filled circles = spin (orbital) magnetic moments after scaling). Errors of the scaled magnetic moments are omitted for clarity. (bulk values taken from Ref. [29])

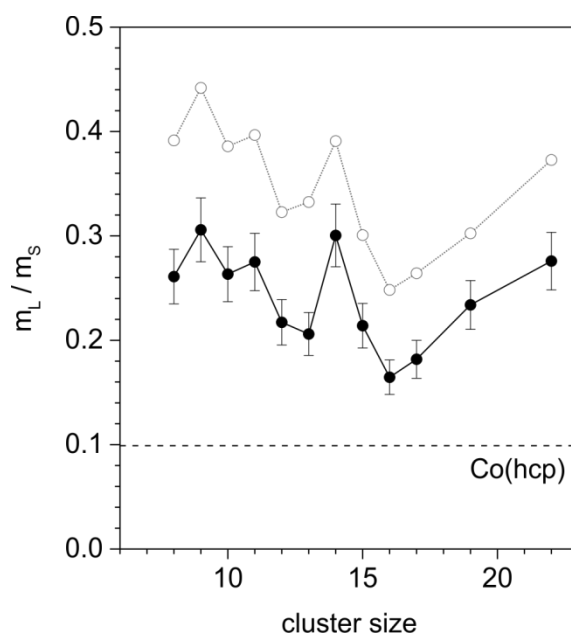


Figure 4.4 ratio of orbital to spin magnetic m_L / m_s moment of Co_n^+ clusters (filled black circles). The m_L / m_s ratio (open grey circles) after individual scaling of the spin and orbital magnetic moment is larger than for scaling of m_j . (bulk values were taken from Ref. [29])

Table 4.1 Experimental orbital $m_{L,z}$ and spin $m_{S,z}$ and intrinsic orbital m_L , spin m_S and total m_J magnetic moments of small cobalt clusters Co_n^+ with assumed LS coupling

	Experimental magnetic moments		Magnetic moments		
	/ μ_B /atom		/ μ_B /atom		
	$m_{L,z}$	$m_{S,z}$	m_L	m_S	m_J
Co_8^+	0.60 ± 0.08	2.3 ± 0.25	0.71 ± 0.10	2.7 ± 0.30	3.4 ± 0.40
Co_9^+	0.52 ± 0.07	1.7 ± 0.20	0.63 ± 0.09	2.05 ± 0.25	2.7 ± 0.30
Co_{10}^+	0.50 ± 0.07	2.15 ± 0.20	0.59 ± 0.08	2.25 ± 0.25	2.8 ± 0.30
Co_{11}^+	0.47 ± 0.04	1.7 ± 0.15	0.55 ± 0.08	2.0 ± 0.20	2.55 ± 0.30
Co_{12}^+	0.47 ± 0.05	2.15 ± 0.20	0.53 ± 0.05	2.45 ± 0.20	3.0 ± 0.30
Co_{13}^+	0.37 ± 0.06	1.7 ± 0.20	0.41 ± 0.06	2.0 ± 0.20	2.4 ± 0.30
Co_{14}^+	0.60 ± 0.08	2.0 ± 0.15	0.67 ± 0.07	2.2 ± 0.20	2.9 ± 0.25
Co_{15}^+	0.47 ± 0.04	2.2 ± 0.15	0.52 ± 0.09	2.4 ± 0.20	2.95 ± 0.30
Co_{16}^+	0.36 ± 0.04	2.2 ± 0.20	0.40 ± 0.04	2.4 ± 0.20	2.8 ± 0.30
Co_{17}^+	0.38 ± 0.04	2.1 ± 0.20	0.42 ± 0.04	2.3 ± 0.20	2.7 ± 0.25
Co_{19}^+	0.54 ± 0.07	2.3 ± 0.30	0.58 ± 0.06	2.5 ± 0.30	3.1 ± 0.40
Co_{22}^+	0.50 ± 0.07	1.8 ± 0.25	0.56 ± 0.08	2.0 ± 0.30	2.6 ± 0.35

4.3 Comparison of experimental magnetic moments by XMCD with:

4.3.1 Theoretical data

Numerous theoretical studies on the spin magnetic moment of neutral cobalt clusters Co_n have been published within the last years. They either employ a tight binding method^[10,85,86] or density functional theory (DFT)^[9,15,16,57,87-92]. The values oscillate around a spin magnetic moment of $2 \mu_B$ /atom for clusters containing more than seven atoms per cluster (Fig. 4.5a). Only the spin magnetic moments of Rodriguez-Lopez *et al.*^[10] deviate from the general trend. They are closer to $2.4 - 2.5 \mu_B$ /atom. In general, the agreement between theory and experiment is reasonably well. However, no single theoretical series agrees with the experimental results over the whole investigated size range. They either agree with the cluster sizes representing local minima within the experimental data, i.e. Co_9^+ , Co_{11}^+ , Co_{13}^+ and Co_{22}^+ or in case of the data of Rodriguez-Lopez *et al.* agree with the higher spin magnetic moments of for example Co_8^+ , Co_{12}^+ or Co_{16}^+ . Values for $\text{Co}_2 - \text{Co}_7$ are included to indicate possible trends towards smaller cluster sizes. Deviations between the individual theoretical works seem to be even larger for clusters with less than ten atoms per clusters than for larger cluster sizes. This might be due to the enhanced influence of the cluster geometry on the electronic / magnetic structure.

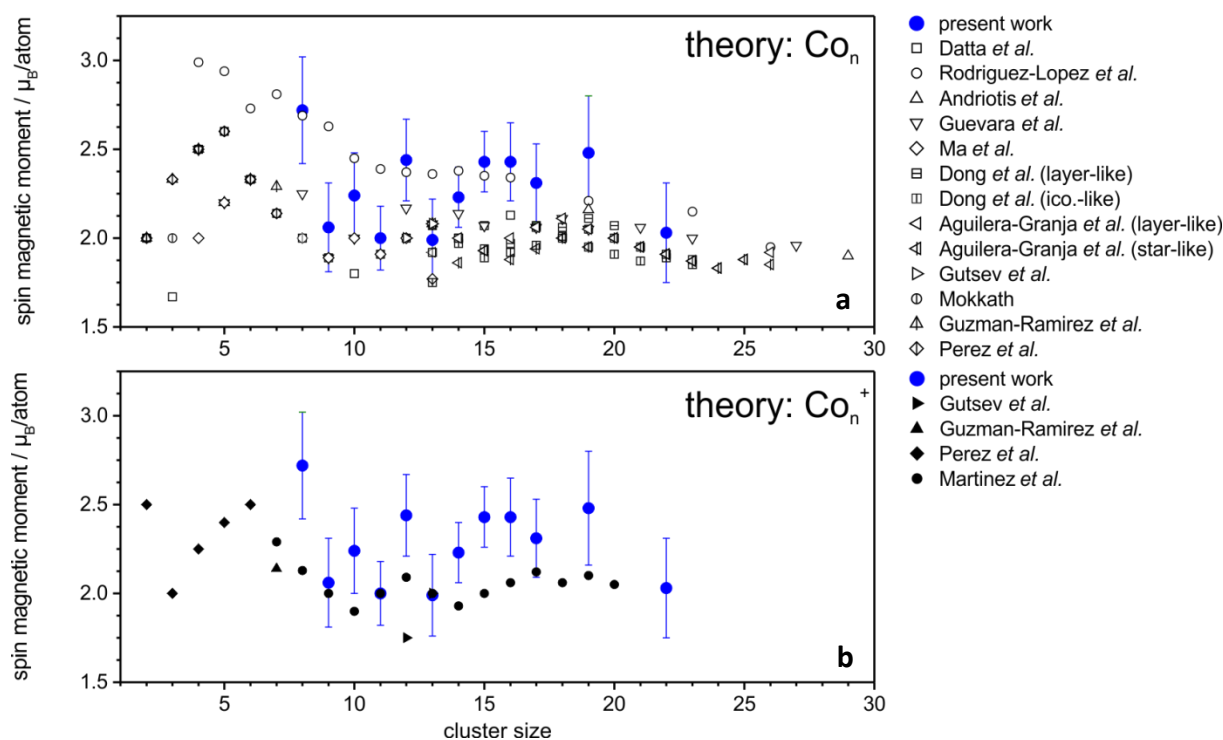


Figure 4.5 Comparison between the spin magnetic moments of Co_n^+ clusters (filled blue circles) of the present work with theoretical data of **(a)** neutral cobalt clusters Co_n ^[9,10,15,16,57,85-89,92] and **(b)** cationic cobalt clusters Co_n^+ ^[15,16,91,92] (The spin magnetic moment of the lowest energy isomer was taken from the references in case of several structural isomers for one cluster size, if not indicated otherwise.)

The theoretical values for the spin magnetic moments of neutral cobalt clusters match reasonably well with the experimental results, but no theoretical series agrees with the experiment over the whole investigated size range. The spin magnetic moments of Rodriguez-Lopez *et al.*^[10] are slightly larger than the general trend of the theoretical values for Co_n . Spin magnetic moments calculated by Martinez *et al.*^[91] for cationic cobalt clusters Co_n^+ are smaller than the experimental values except for Co_9^+ , Co_{11}^+ and Co_{13}^+ which represent minima within the experimental series. The data of Martinez *et al.* mostly reproduces the trend of the data for neutral cobalt clusters Co_n .

Fewer theoretical studies of singly positively charged cobalt clusters Co_n^+ ^[15,16,91,92] have been published (Fig. 4.5b). All are based on DFT methods. Gutsev *et al.*^[15] only investigated Co_{12}^+ and Co_{13}^+ . Their value for Co_{12}^+ is lower than for Co_{13}^+ which does not agree with the experiment in which Co_{13}^+ has the smaller spin magnetic moment. The value for Co_{13}^+ , however, agrees with the experimental one. Interestingly, the optimized structure is not based on an icosahedral motif, like for Co_{12}^+ , but on a hexagonal bilayer (HBL). Martinez *et al.*^[91] investigated cationic cobalt clusters Co_n^+ in a size range overlapping with our investigated size range, i.e. $7 \leq n \leq 20$. Comparable to the results on neutral cobalt clusters, their theoretical spin magnetic moments oscillate around $2 \mu_B/\text{atom}$ and thus are in general too low compared to our results except for Co_9^+ , Co_{11}^+ and Co_{13}^+ . Their spin magnetic

moments agree well with the experimental spin magnetic moments for these cluster sizes. Results from Perez *et al.*^[92] and Guzman-Ramirez *et al.*^[16] for smaller cluster sizes than we investigated are included for comparison.

4.3.2 XMCD experiments

Spin and orbital magnetic moments of singly positively charged cobalt clusters Co_n^+ have been published by Lau *et al.*^[74,78]. Lau *et al.* employ a different experimental approach than we do. A gas aggregation cluster ion source developed by B. von Issendorff is used for the cluster generation. They employ a linear quadrupole ion trap located within the homogenous field of a superconducting solenoid ($B = 5 \text{ T}$). The mass detection is done by time of flight mass spectrometry^[73,74,78,93,94]. For further details of the experimental setup see Chap. 6.2.2.

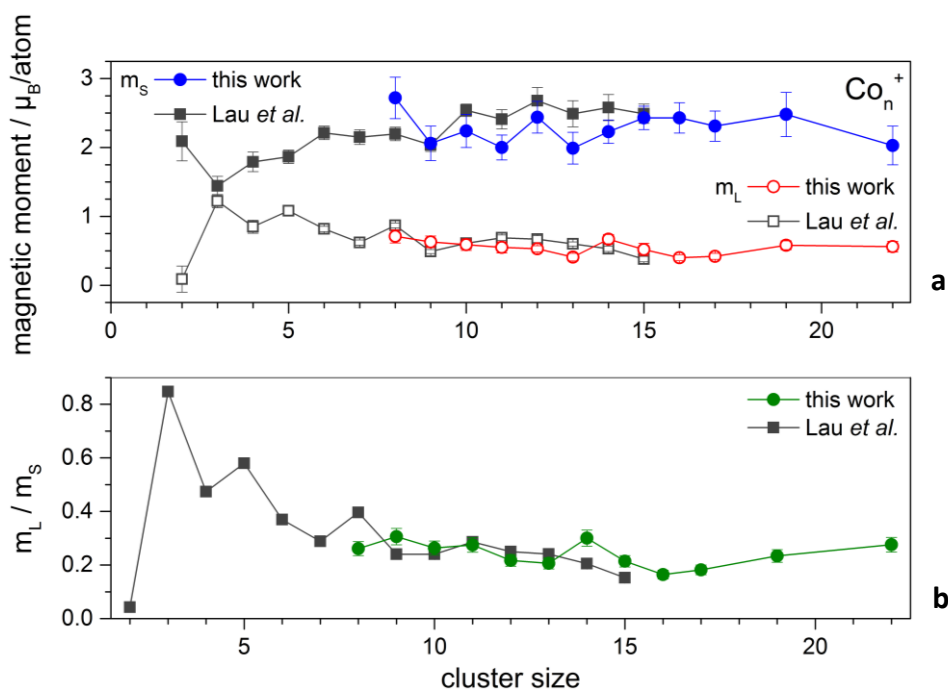


Figure 4.6 Comparison between experimental values for cobalt clusters Co_n^+ from the present work and from Lau *et al.*^[74,78] for the **(a)** spin (this work filled blue circles; Lau *et al.* filled grey squares) and orbital (this work red open circles; Lau *et al.* open grey squares) magnetic moments and **(b)** ratio of orbital to spin magnetic moment m_L/m_s (this work green filled circles; Lau *et al.* filled grey squares). The magnetic moments agree well with each other. The m_L/m_s ratios agree even better between both experiments than m_s and m_L . Thus, indicating the validity of the experimental approach of determining spin and orbital magnetic moments of size selected clusters in the gas phase. And especially the recording of XMCD spectra by means of Total Ion Yield spectroscopy.

The orbital magnetic moments from both experiments agree with each other within the uncertainties of both experiments (Fig. 4.6a). The spin magnetic moments deviate more from each other, but still almost agree within the experimental uncertainties. The spin magnetic moments of the present experiment are in general lower than those published by Lau *et al.*. The only exception is Co_8^+ . However, both data series show almost similar trends. A comparison of the ratio of the orbital to spin magnetic moment m_L / m_S is given in Fig. 4.6b. If the m_L / m_S is compared the choice of the number of 3d holes n_h , which is needed to calculate a magnetic moment, does not matter as n_h is eliminated from the equation. Additionally, the normalization to the isotropic x-ray absorption intensity cancels out (Chap. 2.4.4 and 3.2.3). Thus, a comparison of the m_L / m_S ratio is more reliable as the m_L / m_S ratio contains fewer uncertainties due to data processing and evaluation. The ratios agree well with each other. Larger deviations only occur for Co_8^+ , Co_{14}^+ and Co_{15}^+ . In the case of Co_8^+ , the ratio obtained by us is lower than the one found by Lau *et al.*. The situation is reversed for Co_{14}^+ and Co_{15}^+ .

4.3.3 Stern-Gerlach experiments

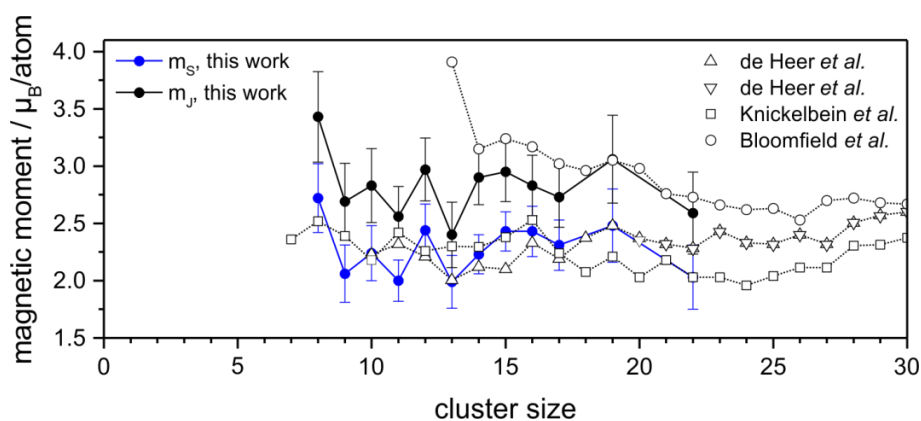


Figure 4.7 Spin and orbital magnetic moment of Co_n^+ clusters compared to total magnetic moments found by Stern-Gerlach experiments for neutral cobalt clusters Co_n [61,64,66,67]. The data of de Heer *et al.* [66,67] and Knickelbein *et al.* [61] agree with our spin magnetic moments for Co_n^+ clusters. The magnetic moments found by Bloomfield *et al.* [64] are larger than the ones found by de Heer *et al.* and Knickelbein *et al.*. They agree better with the total magnetic moments found by us for the ionic Co_n^+ clusters. However, the magnetic moments of Bloomfield *et al.* already exceed the moments found by us for clusters with less than eighteen atoms per cluster.

The total magnetic moments of transition metal clusters can be determined by Stern-Gerlach experiments (Chap. 2.3.2.1). Several experiments were performed on cobalt clusters [58,61,64,66,67]. One has to keep in mind that Stern-Gerlach experiments are conducted with neutral clusters Co_n . If we

compare the spin and total magnetic moment from our XMCD experiments to results from Stern-Gerlach experiments, we find that the spin magnetic moments agree with the total magnetic moments found by the groups of de Heer^[66,67] and Knickelbein^[61]. The magnetic moments found by Bloomfield *et al.*^[64] are larger and agree better with the total magnetic moment found in our XMCD experiments (Fig. 4.7) for clusters with less than eighteen atoms per cluster.

A further discussion of this topic can be found in the publication attached to this chapter as supplement (Chap. 4.5) and in Chap. 5.5 in comparison with the findings on iron and nickel clusters.

4.4 References

- [1] TOMBERS, M., *Kinetische und magnetische Studien an ionischen Cobalt-Clustern mittels Fourier Transform Ionen-Zyklotron Resonanz (FT-ICR) Massenspektrometrie und röntgenbasiertem magnetischem Zirkulardichroismus (XMCD)*, Diploma thesis, **2011**, Technische Universität Kaiserslautern.
- [2] LAZAROVITS, B., SZUNYOGH, L., WEINBERGER, P., *Fully relativistic calculation of magnetic properties of Fe, Co, and Ni adclusters on Ag(100)*, Physical Review B **2002**, *65*, 104441.
- [3] YUANNAN, X., JOHN, A. B., *On the oscillation of the magnetic moment of free transition metal clusters*, Journal of Physics: Condensed Matter **2003**, *15*, L615.
- [4] XIE, Y., BLACKMAN, J. A., *Enhanced effect of magnetic anisotropy on free clusters*, Applied Physics Letters **2003**, *82*, 1446.
- [5] HJORTSTAM, O., TRYGG, J., WILLS, J. M., JOHANSSON, B., ERIKSSON, O., *Calculated spin and orbital moments in the surfaces of the 3d metals Fe, Co, and Ni and their overlayers on Cu(001)*, Physical Review B **1996**, *53*, 9204.
- [6] RUIZ-DÍAZ, P., GARIBAY-ALONSO, R., DORANTES-DÁVILA, J., PASTOR, G. M., *Noncollinear magnetism in transition metal nanostructures: Exchange interaction and local environment effects in free and deposited clusters*, Physical Review B **2011**, *84*, 024431.
- [7] AGUILERA-GRANJA, F., GARCÍA-FUENTE, A., VEGA, A., *Comparative ab initio study of the structural, electronic, and magnetic trends of isoelectronic late 3d and 4d transition metal clusters*, Physical Review B **2008**, *78*, 134425.
- [8] GUIRADO-LOPEZ, R. A., DORANTES-DAVILA, J., PASTOR, G. M., *Orbital magnetism in transition-metal clusters: From Hund's rules to bulk quenching*, Physical Review Letters **2003**, *90*, 226402.
- [9] DATTA, S., KABIR, M., GANGULY, S., SANYAL, B., SAHA-DASGUPTA, T., MOOKERJEE, A., *Structure, bonding, and magnetism of cobalt clusters from first-principles calculations*, Physical Review B **2007**, *76*, 014429.
- [10] RODRÍGUEZ-LÓPEZ, J. L., AGUILERA-GRANJA, F., MICHAELIAN, K., VEGA, A., *Structure and magnetism of cobalt clusters*, Physical Review B **2003**, *67*, 174413.
- [11] MCENIRY, E. J., DRAUTZ, R., K. H. MADSEN, G., *Environmental tight-binding modeling of nickel and cobalt clusters*, Journal of Physics: Condensed Matter **2013**, *25*, 115502.
- [12] GUTSEV, G. L., JOHNSON, L. E., BELAY, K. G., WEATHERFORD, C. A., GUTSEV, L. G., RAMACHANDRAN, B. R., *Structure and magnetic properties of Fe₁₂X clusters*, Chemical Physics **2014**, *430*, 62.
- [13] GUTSEV, G. L., KHANNA, S. N., JENA, P., *Magnetic excitations of Co₂ dimer*, Chemical Physics Letters **2001**, *345*, 481.

- [14] GUTSEV, G. L., WEATHERFORD, C. A., JENA, P., JOHNSON, E., RAMACHANDRAN, B. R., *Structure and Properties of Fe_n , Fe_n^- , and Fe_n^+ Clusters, $n = 7 - 20$* , The Journal of Physical Chemistry A **2012**, *116*, 10218.
- [15] GUTSEV, G. L., WEATHERFORD, C. W., BELAY, K. G., RAMACHANDRAN, B. R., JENA, P., *An all-electron density functional theory study of the structure and properties of the neutral and singly charged M_{12} and M_{13} clusters: $M = Sc - Zn$* , The Journal of Chemical Physics **2013**, *138*, 164303.
- [16] GUZMÁN-RAMÍREZ, G., SALVADOR, P., ROBLES, J., VEGA, A., AGUILERA-GRANJA, F., *Density functional study of ternary $Fe_x Co_y Ni_z$ ($x + y + z = 7$) clusters*, Theor Chem Acc **2012**, *132*, 1.
- [17] WIESENDANGER, R., GÜNTHERODT, H. J., GÜNTHERODT, G., GAMBINO, R. J., RUF, R., *Observation of vacuum tunneling of spin-polarized electrons with the scanning tunneling microscope*, Physical Review Letters **1990**, *65*, 247.
- [18] BRUNE, H., *Assembly and Probing of Spin Chains of Finite Size*, Science **2006**, *312*, 1005.
- [19] STÖHR, J., KÖNIG, H., *Determination of Spin- and Orbital-Moment Anisotropies in Transition Metals by Angle-Dependent X-Ray Magnetic Circular Dichroism*, Physical Review Letters **1995**, *75*, 3748.
- [20] HIRJIBEHDIN, C. F., LIN, C.-Y., OTTE, A. F., TERNES, M., LUTZ, C. P., JONES, B. A., HEINRICH, A. J., *Large Magnetic Anisotropy of a Single Atomic Spin Embedded in a Surface Molecular Network*, Science **2007**, *317*, 1199.
- [21] BALASHOV, T., SCHUH, T., TAKÁCS, A. F., ERNST, A., OStanIN, S., HENK, J., MERTIG, I., BRUNO, P., MIYAMACHI, T., SUGA, S., WULFHEKEL, W., *Magnetic Anisotropy and Magnetization Dynamics of Individual Atoms and Clusters of Fe and Co on Pt(111)*, Physical Review Letters **2009**, *102*, 257203.
- [22] DONATI, F., DUBOUT, Q., AUTÈS, G., PATTHEY, F., CALLEJA, F., GAMBARDELLA, P., YAZYEV, O. V., BRUNE, H., *Magnetic Moment and Anisotropy of Individual Co Atoms on Graphene*, Physical Review Letters **2013**, *111*, 236801.
- [23] SCHÜTZ, G., GOERING, E., HERMANN, S. Synchrotron Radiation Techniques Based on X-ray Magnetic Circular Dichroism. In *Handbook of Magnetism and Advanced Magnetic Materials*; Kronmüller, H., Parkin, S., Eds.; John Wiley & Sons, Ltd., 2007; Vol. 3.
- [24] SCHÜTZ, G., WAGNER, W., WILHELM, W., KIENLE, P., ZELLER, R., FRAHM, R., MATERLIK, G., *Absorption of circularly polarized x rays in iron*, Physical Review Letters **1987**, *58*, 737.
- [25] STÖHR, J., *X-ray magnetic circular dichroism spectroscopy of transition metal thin films*, Journal of Electron Spectroscopy and Related Phenomena **1995**, *75*, 253.
- [26] STÖHR, J., *Exploring the microscopic origin of magnetic anisotropies with X-ray magnetic circular dichroism (XMCD) spectroscopy*, Journal of Magnetism and Magnetic Materials **1999**, *200*, 470.
- [27] TISCHER, M., HJORTSTAM, O., ARVANITIS, D., HUNTER DUNN, J., MAY, F., BABERSCHKE, K., TRYGG, J., WILLS, J. M., JOHANSSON, B., ERIKSSON, O., *Enhancement of Orbital Magnetism at Surfaces: Co on Cu(100)*, Physical Review Letters **1995**, *75*, 1602.
- [28] BABERSCHKE, K., *The magnetism of nickel monolayers*, Appl. Phys. A **1996**, *62*, 417.
- [29] CHEN, C. T., IDZERDA, Y. U., LIN, H. J., SMITH, N. V., MEIGS, G., CHABAN, E., HO, G. H., PELLEGRIN, E., SETTE, F., *Experimental Confirmation of the X-Ray Magnetic Circular Dichroism Sum Rules for Iron and Cobalt*, Physical Review Letters **1995**, *75*, 152.
- [30] CHEN, C. T., SETTE, F., MA, Y., MODESTI, S., *Soft-x-ray magnetic circular dichroism at the $L_{2,3}$ edges of nickel*, Physical Review B **1990**, *42*, 7262.

- [31] BORNEMANN, S., ŠIPR, O., MANKOVSKY, S., POLESYA, S., STAUNTON, J. B., WURTH, W., EBERT, H., MINÁR, J., *Trends in the magnetic properties of Fe, Co, and Ni clusters and monolayers on Ir(111), Pt(111), and Au(111)*, Physical Review B **2012**, 86, 104436.
- [32] DHESI, S. S., DUDZIK, E., DÜRR, H. A., BROOKES, N. B., VAN DER LAAN, G., *Correlation between L3 absorption satellite intensity and spin moment in ultrathin Ni films*, Surface Science **2000**, 454–456, 930.
- [33] DHESI, S. S., DÜRR, H. A., VAN DER LAAN, G., DUDZIK, E., BROOKES, N. B., *Electronic and magnetic structure of thin Ni films on Co/Cu(001)*, Physical Review B **1999**, 60, 12852.
- [34] BANIODEH, A., MEREACRE, V., MAGNANI, N., LAN, Y., WOLNY, J. A., SCHUENEMANN, V., ANSON, C. E., POWELL, A. K., *Para versus meta ligand substituents as a means of directing magnetic anisotropy in Fe₂Dy₂ coordination clusters*, Chem. Commun. (Cambridge, U. K.) **2013**, 49, 9666.
- [35] BANSMANN, J., BAKER, S. H., BINNS, C., BLACKMAN, J. A., BUCHER, J. P., DORANTES-DAVILA, J., DUPUIS, V., FAVRE, L., KECHRAKOS, D., KLEIBERT, A., MEIWES-BROER, K. H., PASTOR, G. M., PEREZ, A., TOULEMONDE, O., TROHIDOU, K. N., TUAILLON, J., XIE, Y., *Magnetic and structural properties of isolated and assembled clusters*, Surf. Sci. Rep. **2005**, 56, 189.
- [36] BANSMANN, J., KLEIBERT, A., GETZLAFF, M., RODRIGUEZ, A. F., NOLTING, F., BOEGLIN, C., MEIWES-BROER, K.-H., *Magnetism of 3d transition metal nanoparticles on surfaces probed with synchrotron radiation - from ensembles towards individual objects*, Physica Status Solidi B-Basic Solid State Physics **2010**, 247, 1152.
- [37] KLEIBERT, A., PASSIG, J., MEIWES-BROER, K. H., GETZLAFF, M., BANSMANN, J., *Structure and magnetic moments of mass-filtered deposited nanoparticles*, Journal of Applied Physics **2007**, 101, 114318.
- [38] GAMBARDELLA, P., RUSPONI, S., VERONESE, M., DHESI, S. S., GRAZIOLI, C., DALLMEYER, A., CABRIA, I., ZELLER, R., DEDERICHS, P. H., KERN, K., CARBONE, C., BRUNE, H., *Giant Magnetic Anisotropy of Single Cobalt Atoms and Nanoparticles*, Science **2003**, 300, 1130.
- [39] DURR, H. A., DHESI, S. S., DUDZIK, E., KNABBEN, D., VAN DER LAAN, G., GOEDKOOP, J. B., HILLEBRECHT, F. U., *Spin and orbital magnetization in self-assembled Co clusters on Au(111)*, Physical Review B **1999**, 59, R701.
- [40] EDMONDS, K. W., BINNS, C., BAKER, S. H., THORNTON, S. C., NORRIS, C., GOEDKOOP, J. B., FINAZZI, M., BROOKES, N. B., *Doubling of the orbital magnetic moment in nanoscale Fe clusters*, Physical Review B **1999**, 60, 472.
- [41] PIETZSCH, O., KUBETZKA, A., BODE, M., WIESENDANGER, R., *Spin-Polarized Scanning Tunneling Spectroscopy of Nanoscale Cobalt Islands on Cu(111)*, Physical Review Letters **2004**, 92, 057202.
- [42] GLASER, L., CHEN, K., FIEDLER, S., WELLHÖFER, M., WURTH, W., MARTINS, M., *Magnetic properties of small size-selected Co and CoPt clusters on Ni*, Physical Review B **2012**, 86, 075435.
- [43] LAU, J. T., FÖHLISCH, A., MARTINS, M., NIETUBYC, R., REIF, M., WURTH, W., *Spin and orbital magnetic moments of deposited small iron clusters studied by x-ray magnetic circular dichroism spectroscopy*, New Journal of Physics **2002**, 4, 98.
- [44] LAU, J. T., FÖHLISCH, A., NIETUBYČ, R., REIF, M., WURTH, W., *Size-Dependent Magnetism of Deposited Small Iron Clusters Studied by X-Ray Magnetic Circular Dichroism*, Physical Review Letters **2002**, 89, 057201.
- [45] FAUTH, K., HESSLER, M., BATCHELOR, D., SCHUTZ, G., *Strong influence of defects on the electronic structure of Pt adatoms and clusters on graphite*, Surface Science **2003**, 529, 397.

-
- [46] BALLENTINE, G., HEßLER, M., KINZA, M., FAUTH, K., *Superparamagnetism in small Fe clusters on Cu(111)*, Eur. Phys. J. D **2007**, *45*, 535.
- [47] WURTH, W., MARTINS, M., *Electronic structure and magnetic properties of small deposited transition metal clusters*, Chem. Phys. Solid Surf. **2007**, *12*, 471.
- [48] EELBO, T., WAŚNIEWSKA, M., THAKUR, P., GYAMFI, M., SACHS, B., WEHLING, T. O., FORTI, S., STARKE, U., TIEG, C., LICHTENSTEIN, A. I., WIESENDANGER, R., *Adatoms and Clusters of 3d Transition Metals on Graphene: Electronic and Magnetic Configurations*, Physical Review Letters **2013**, *110*, 136804.
- [49] GAMBARDELLA, P., DHESI, S. S., GARDONIO, S., GRAZIOLI, C., OHRESSER, P., CARBONE, C., *Localized magnetic states of Fe, Co, and Ni impurities on alkali metal films*, Physical Review Letters **2002**, *88*.
- [50] BRUNE, H., GAMBARDELLA, P., *Magnetism of individual atoms adsorbed on surfaces*, Surface Science **2009**, *603*, 1812.
- [51] HABERLAND, H., KLEINERMANN, K., TRÄGER, F., Bergmann-Schäfer, *Lehrbuch der Experimentalphysik Band 5 - Gase, Nanosysteme, Flüssigkeiten*, Cluster, 2nd Ed.; Walter de Gruyter, **2006**; pp 819.
- [52] *Clusters of Atoms and Molecules*; HABERLAND, H., Ed.; Springer, **1994**.
- [53] FARLE, M., *Lecture Notes Magnetism goes Nano - Electron Correlations, Spin Transport, Molecular Magnetism*, Magnetic Nanoparticles; Forschungszentrum Jülich in der Helmholtz Gemeinschaft, **2005**.
- [54] CHEN, K., FIEDLER, S., BAEV, I., BEECK, T., WURTH, W., MARTINS, M., *Hybridization and magnetism in small FePt alloy clusters*, New Journal of Physics **2012**, *14*, 123005.
- [55] FAUTH, K., GOLD, S., HEßLER, M., SCHNEIDER, N., SCHÜTZ, G., *Cluster surface interactions: small Fe clusters driven nonmagnetic on graphite*, Chemical Physics Letters **2004**, *392*, 498.
- [56] AGUILERA-GRANJA, F., MONTEJANO-CARRIZALEZ, J. M., GUIRADO-LÓPEZ, R. A., *Magnetic properties of small 3d and 4d transition metal clusters: The role of a noncompact growth*, Physical Review B **2006**, *73*, 115422.
- [57] AGUILERA-GRANJA, F., VEGA, A., BALBÁS, L. C., *A new family of star-like icosahedral structures for small cobalt clusters*, Chemical Physics **2013**, *415*, 106.
- [58] BILLAS, I. M. L., CHÂTELAIN, A., DE HEER, W. A., *Magnetism from the Atom to the Bulk in Iron, Cobalt, and Nickel Clusters*, Science **1994**, *265*, 1682.
- [59] BILLAS, I. M. L., CHÂTELAIN, A., DE HEER, W. A., *Magnetism of Fe, Co and Ni clusters in molecular beams*, Journal of Magnetism and Magnetic Materials **1997**, *168*, 64.
- [60] KNICKELBEIN, M. B., *Spin relaxation in isolated molecules and clusters: The interpretation of Stern-Gerlach experiments*, J. Chem. Phys. **2004**, *121*, 5281.
- [61] KNICKELBEIN, M. B., *Magnetic moments of bare and benzene-capped cobalt clusters*, The Journal of Chemical Physics **2006**, *125*, 044308.
- [62] KNICKELBEIN, M. B., *Magnetic moments of small bimetallic clusters: Co_nMn_m* , Physical Review B **2007**, *75*, 014401.
- [63] PAYNE, F. W., JIANG, W., BLOOMFIELD, L. A., *Magnetism and Magnetic Isomers in Free Chromium Clusters*, Physical Review Letters **2006**, *97*, 193401.
- [64] PAYNE, F. W., JIANG, W., EMMERT, J. W., DENG, J., BLOOMFIELD, L. A., *Magnetic structure of free cobalt clusters studied with Stern-Gerlach deflection experiments*, Physical Review B **2007**, *75*, 094431.
- [65] DOUGLASS, D. C., COX, A. J., BUCHER, J. P., BLOOMFIELD, L. A., *Magnetic properties of free cobalt and gadolinium clusters*, Physical Review B **1993**, *47*, 12874.
-

- [66] XU, X., YIN, S., MORO, R., LIANG, A., BOWLAN, J., DE HEER, W. A., *Metastability of Free Cobalt and Iron Clusters: A Possible Precursor to Bulk Ferromagnetism*, Physical Review Letters **2011**, *107*, 057203.
- [67] XU, X. S., YIN, S. Y., MORO, R., DE HEER, W. A., *Magnetic moments and adiabatic magnetization of free cobalt clusters*, Physical Review Letters **2005**, *95*, 237209.
- [68] KNICKELBEIN, M. B., *Magnetic ordering in manganese clusters*, Phys. Rev. B: Condens. Matter Mater. Phys. **2004**, *70*, 014424/1.
- [69] COX, A. J., LOUDERBACK, J. G., BLOOMFIELD, L. A., *Experimental observation of magnetism in rhodium clusters*, Physical Review Letters **1993**, *71*, 923.
- [70] KNICKELBEIN, M. B., *Experimental Observation of Superparamagnetism in Manganese Clusters*, Physical Review Letters **2001**, *86*, 5255.
- [71] PEREDKOV, S., NEEB, M., EBERHARDT, W., MEYER, J., TOMBERS, M., KAMPSCHULTE, H., NIEDNER-SCHATTEBURG, G., *Spin and Orbital Magnetic Moments of Free Nanoparticles*, Physical Review Letters **2011**, *107*, 233401.
- [72] PEREDKOV, S., SAVCI, A., PETERS, S., NEEB, M., EBERHARDT, W., KAMPSCHULTE, H., MEYER, J., TOMBERS, M., HOFFERBERTH, B., MENGES, F., NIEDNER-SCHATTEBURG, G., *X-ray absorption spectroscopy of mass-selected transition metal clusters using a cyclotron ion trap: An experimental setup for measuring XMCD spectra of free clusters*, Journal of Electron Spectroscopy and Related Phenomena **2011**, *184*, 113.
- [73] NIEMEYER, M., HIRSCH, K., ZAMUDIO-BAYER, V., LANGENBERG, A., VOGEL, M., KOSSICK, M., EBRECHT, C., EGASHIRA, K., TERASAKI, A., MÖLLER, T., V. ISSENDORFF, B., LAU, J. T., *Spin Coupling and Orbital Angular Momentum Quenching in Free Iron Clusters*, Physical Review Letters **2012**, *108*, 057201.
- [74] LANGENBERG, A., HIRSCH, K., LAWICKI, A., ZAMUDIO-BAYER, V., NIEMEYER, M., CHMIELA, P., LANGBEHN, B., TERASAKI, A., ISSENDORFF, B. V., LAU, J. T., *Spin and orbital magnetic moments of size-selected iron, cobalt, and nickel clusters and their link to the bulk phase diagrams*, arXiv.org, e-Print Arch., Phys. **2014**, 1.
- [75] HIRSCH, K., ZAMUDIO-BAYER, V., LANGENBERG, A., NIEMEYER, M., LANGBEHN, B., MOELLER, T., TERASAKI, A., ISSENDORFF, B. V., LAU, J. T., *Magnetic moments of chromium-doped gold clusters. The Anderson impurity model in finite systems*, arXiv.org, e-Print Arch., Phys. **2013**, 1.
- [76] ZAMUDIO-BAYER, V., LEPPERT, L., HIRSCH, K., LANGENBERG, A., RITTMANN, J., KOSSICK, M., VOGEL, M., RICHTER, R., TERASAKI, A., MOELLER, T., VON, I. B., KUEMMEL, S., LAU, J. T., *Coordination-driven magnetic-to-nonmagnetic transition in manganese doped silicon clusters*, Physical Review B **2013**, *88*, 165402.
- [77] FAUTH, K., MÜNZING, B., *Unterdrückter Impuls*, Physik Journal **2012**, *05/2012*.
- [78] LANGENBERG, A., *Magnetische Momente freier, massenselektierter Eisen-, Cobalt- und Nickelcluster*, Doctoral thesis, **2013**, Technische Universität Berlin.
- [79] HIRSCH, K., LAU, J. T., KLAR, P., LANGENBERG, A., PROBST, J., RITTMANN, J., VOGEL, M., ZAMUDIO-BAYER, V., MOELLER, T., VON ISSENDORFF, B., *X-ray spectroscopy on size-selected clusters in an ion trap: from the molecular limit to bulk properties*, Journal of Physics B-Atomic Molecular and Optical Physics **2009**, *42*.
- [80] HIRSCH, K., ZAMUDIO-BAYER, V., AMESSEDER, F., LANGENBERG, A., RITTMANN, J., VOGEL, M., MOLLER, T., VON ISSENDORFF, B., LAU, J. T., *2p x-ray absorption of free transition-metal cations across the 3d transition elements: Calcium through copper*, Physical Review A **2012**, *85*.

- [81] VOGEL, M., KASIGKEIT, C., HIRSCH, K., LANGENBERG, A., RITTMANN, J., ZAMUDIO-BAYER, V., KULESZA, A., MITRIC, R., MOELLER, T., VON, I. B., LAU, J. T., *2p core-level binding energies of size-selected free silicon clusters: chemical shifts and cluster structure*, Physical Review B **2012**, 85, 195454/1.
- [82] KHANNA, S. N., LINDEROTH, S., *magnetic behavior of clusters of ferromagnetic transition metals*, Physical Review Letters **1991**, 67, 742.
- [83] BUCHER, J. P., DOUGLASS, D. C., BLOOMFIELD, L. A., *Magnetic properties of free cobalt clusters*, Physical Review Letters **1991**, 66, 3052.
- [84] REDDY, B. V., NAYAK, S. K., KHANNA, S. N., RAO, B. K., JENA, P., *Physics of nickel clusters. 2. Electronic structure and magnetic properties*, Journal of Physical Chemistry A **1998**, 102, 1748.
- [85] ANDRIOTIS, A. N., MENON, M., *Tight-binding molecular-dynamics study of ferromagnetic clusters*, Physical Review B **1998**, 57, 10069.
- [86] GUEVARA, J., PARISI, F., LLOIS, A. M., WEISSMANN, M., *Electronic properties of transition-metal clusters: Consideration of the spillover in a bulk parametrization*, Physical Review B **1997**, 55, 13283.
- [87] DONG, C. D., GONG, X. G., *Magnetism enhanced layer-like structure of small cobalt clusters*, Physical Review B **2008**, 78, 020409.
- [88] MA, Q.-M., XIE, Z., WANG, J., LIU, Y., LI, Y.-C., *Structures, stabilities and magnetic properties of small Co clusters*, Physics Letters A **2006**, 358, 289.
- [89] MOKKATH, J. H., *Magnetism, structure and chemical order in small CoPd clusters: A first-principles study*, Journal of Magnetism and Magnetic Materials **2014**, 349, 109.
- [90] FAN, H.-J., LIU, C.-W., LIAO, M.-S., *Geometry, electronic structure and magnetism of small Co_n (n = 2–8) clusters*, Chemical Physics Letters **1997**, 273, 353.
- [91] MARTÍNEZ, G., TANGARIFE, E., PÉREZ, M., MEJÍA-LÓPEZ, J., *Magnetic properties of small cobalt–copper clusters*, Journal of Physics: Condensed Matter **2013**, 25, 216003.
- [92] PÉREZ, M., MUÑOZ, F., MEJÍA-LÓPEZ, J., MARTÍNEZ, G., *Physical and chemical properties of Co_{n-m}Cu_m nanoclusters with n = 2 - 6 atoms via ab-initio calculations*, J Nanopart Res **2012**, 14, 1.
- [93] LAU, J. T., RITTMANN, J., ZAMUDIO-BAYER, V., VOGEL, M., HIRSCH, K., KLAR, P., LOFINK, F., MOELLER, T., VON ISSENDORFF, B., *Size Dependence of L_{2,3} Branching Ratio and 2p Core-Hole Screening in X-Ray Absorption of Metal Clusters*, Physical Review Letters **2008**, 101.
- [94] LAU, J. T., HIRSCH, K., LANGENBERG, A., PROBST, J., RICHTER, R., RITTMANN, J., VOGEL, M., ZAMUDIO-BAYER, V., MOELLER, T., VON ISSENDORFF, B., *Localized high spin states in transition-metal dimers: X-ray absorption spectroscopy study*, Physical Review B **2009**, 79.

4.5 Supplement - Publication - Phys. Rev. Lett. 2011, 107, 233401

PEREDKOV, S., NEEB, M., EBERHARDT, W., MEYER, J., TOMBERS, M., KAMPSCHULTE, H., NIEDNER-SCHATTEBURG, G., *Spin and Orbital Magnetic Moments of Free Nanoparticles*, Physical Review Letters **2011**, 107, 233401

<http://link.aps.org/doi/10.1103/PhysRevLett.107.233401>

Spin and Orbital Magnetic Moments of Free Nanoparticles

S. Peredkov,¹ M. Neeb,² W. Eberhardt,¹ J. Meyer,³ M. Tombers,³ H. Kampschulte,³ and

G. Niedner-Schatteburg³

¹Institut für Optik und Atomare Physik, Technische Universität Berlin, Hardenbergstrasse 36, 10623
Berlin, Germany

²Helmholtz-Zentrum Berlin für Materialien und Energie, BESSY II, Albert-Einstein-Strasse 15, 12489
Berlin, Germany

³Fachbereich Chemie und Forschungszentrum OPTIMAS, TU Kaiserslautern, 67663 Kaiserslautern,
Germany

(Received 27 June 2011; published 30 November 2011)

4.5.0 Abstract

The determination of spin and orbital magnetic moments from the free atom to the bulk phase is an intriguing challenge for nanoscience, in particular, since most magnetic recording materials are based on nanostructures. We present temperature-dependent X-ray magnetic circular dichroism measurements of free Co clusters ($N = 8 - 22$) from which the intrinsic spin and orbital magnetic moments of non-interacting magnetic nanoparticles have been deduced. An exceptionally strong enhancement of the orbital moment is verified for free magnetic clusters which is 4 - 6 times larger than the bulk value. Our temperature-dependent measurements reveal that the spin orientation along the external magnetic field is nearly saturated at 20 K and 7 T, while the orbital orientation is clearly not.

4.5.1 Letter / Content

Free transition metal atoms possess large spin and orbital magnetic moments according to Hund's rules. Bulk formation, on the other hand, causes a substantial attenuation of the spin (m_s) and orbital (m_l) moments. The latter can even be completely quenched in macroscopic systems, as shown by X-ray magnetic circular dichroism (XMCD) measurements on ferromagnetic bulk samples [1, 2]. Thus, one of the main concerns of magnetism is to understand how magnetic properties change when going from the electronic structure of a single atom to the bulk, i.e., when orbital hybridization, geometry, symmetry breaking, electron delocalization, and band formation come into play. Mass-selected clusters are most suitable objects to follow the evolution of magnetism as a function of size. Total magnetic moments (m_{tot}) of free mass-selected clusters have been determined by ingenious

Stern-Gerlach experiments [3-5]. However, spin and orbital magnetic moments of free magnetic particles like molecular magnets and clusters are experimentally unknown due to a lack of magneto sensitive experiments for probing an extremely dilute target density of some attomoles /cm³. Since the orbital moments are influenced more strongly by orbital hybridization and electron delocalization, it is important to quantify them and to study their size and temperature dependence. Do m_s and m_L reveal the same size dependence, or do they vary independently? On which length scale does the orbital momentum get quenched, and when does the spin moment converge to the bulk value? Is there a monotonic size evolution, or do m_s and m_L exhibit a non-scalable size dependence? Do m_s and m_L exhibit the same temperature dependence? Considerable efforts have been invested for the calculation of spin and orbital magnetic moments of free clusters which still await experimental data for comparison and code refinement [6-8]. Large orbital moments are expected to cause a large magnetic anisotropy and thus might play a crucial role in the inherent orientation of magnetic moments along a preferred spatial coordinate of the cluster, an important prerequisite for being used as magnetic data storage material.

Atomic islands, wires, and nanoparticles as well as supported clusters have been explored by XMCD in order to determine size-dependent information and to study the dependence of magnetic moments and anisotropy on dimensionality [9-14]. Common to all these measurements is that the explored particles are in contact with a support material. Extrinsic effects on the magnetic properties are inevitably due to modifications of geometry, electronic structure, charge transfer, and hybridization with the support. Thus, the determination of the intrinsic moments of free magnetic particles is extremely important for both experiment and theory, as the data elucidate the influence of the support on the magnetic properties of application-relevant deposited clusters and, on the other hand, as the measured moments can be used as reference data for highly sophisticated calculations.

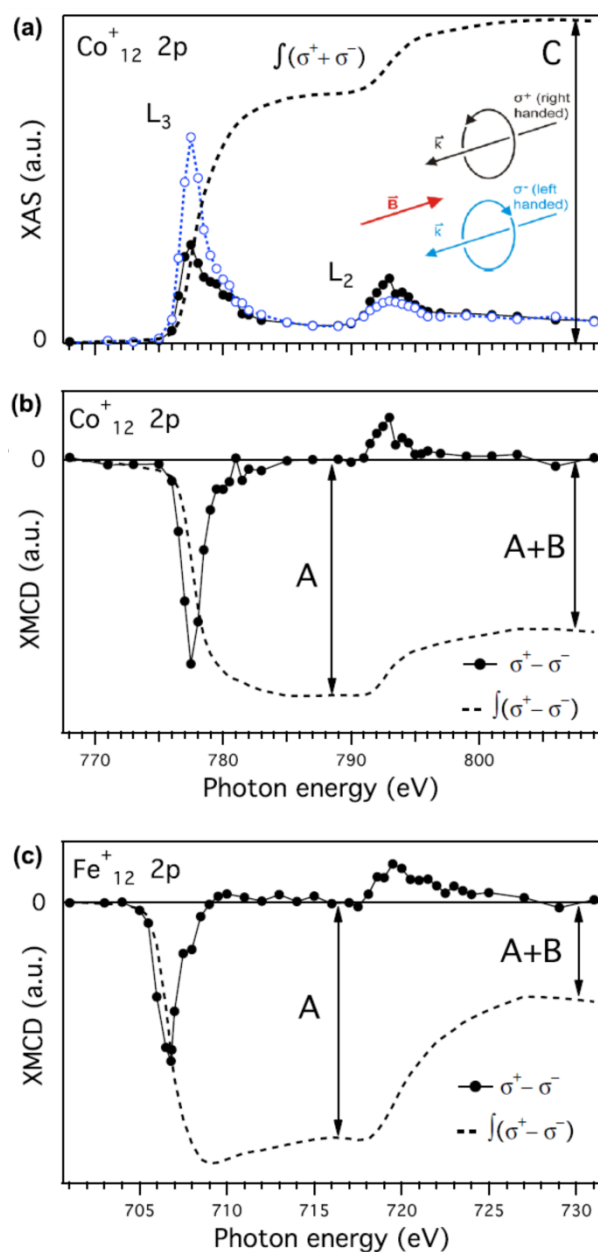


Fig. 1 (color online). **(a)** Circularly polarized x-ray absorption spectra of Co_{12}^+ at the L-edge. The spectrum recorded with negative polarization (σ^-) is shown by open circles and a dotted line (blue), that with positive polarization (σ^+) by filled dots and a full line (black). The relative orientation of polarization, light propagation (\vec{k}), and magnetic field (\vec{B}) is shown in the cartoon. The integration of the sum of both absorption curves is shown as a dashed line (C) which is used for calculation of the magnetic moments according to the magneto-optical sum rules. **(b)** The XMCD spectrum ($\sigma^+ - \sigma^-$) of Co_{12}^+ after subtracting the L-edge-jump intensity. A and B correspond to the area of the L₃ and L₂ dichroic intensity, respectively. The integration of the dichroic intensity is shown as a dashed line (A + B). Note that the large absolute value of (A + B) exhibits a strong orbital moment. **(c)** L-edge XMCD spectrum of Fe_{12}^+ measured under the same conditions

Here we present XMCD data on free "ferromagnetic" nanoparticles which have been used to extract the intrinsic spin and orbital magnetic moments of small Co_N cluster ions as a function of the number of atoms $N = 8 - 22$. Note that Co_N clusters are expected to possess orbital moments that are higher than those of other itinerant ferromagnetic elements like Fe and Ni [7]. The total magnetic moment m_{tot} , which is given by the vector sum of m_s and m_L , is compared with the magnetic moments as obtained from prior Stern-Gerlach experiments [5, 15, 16]. Interestingly, our data are systematically higher than those of Refs. [5, 15] but are close to the magnetic moments of Ref. [16]. We might be able to solve this apparent mismatch by using the different temperature dependence of spin and orbital moments as will be explained in the following.

In order to record XMCD spectra of free mass-selected clusters, a Fourier transform ion cyclotron resonance mass spectrometer has been combined with a soft-X-ray synchrotron beam line at BESSY. The experimental setup has been described in detail in Ref. [17] and Fig. S1 [18]. Fig. 1.a shows L-edge absorption curves of Co_{12}^+ which have been taken at a buffer-gas equilibrated cluster temperature of 20 K using right- and left-handed circular polarization of the x-ray light. The L_3 and L_2 edges are clearly resolved. The XMCD signal $\int(\sigma^+ - \sigma^-)$ at the L_3 edge is very prominent, while it is much smaller at the L_2 edge [Fig. 1(b)].

Magneto-optical sum rules [19-21] have been used to extract the measured projection of the spin and orbital magnetic moments $m_S^{(z)}$ and $m_L^{(z)}$ [22]. The quantization axis z is defined by the direction of the applied magnetic trapping field. For a quantitative determination of spin and orbital magnetic moments, we used Eq. 1 and Eq. 2 of the paper of Chen *et al.* [21]. Rewriting the formula of Ref. [21] by replacing A and B for the corresponding integrated XMCD signal $\int(\sigma^+ - \sigma^-)$ of the L_3 and L_2 edge, respectively, and C for the integral of the sum of the two helicity-dependent absorption curves $\int(\sigma^+ + \sigma^-)$ we obtain

$$m_L^{(z)} = -\frac{4(A+B)}{3C} n_h \quad (1)$$

$$m_S^{(z)} = -\frac{2(A-2B)}{C} n_h - 7T_z \quad (2)$$

$m_L^{(z)}$ and $m_S^{(z)}$ are given per atom in units of μ_B ; n_h represents the number of 3d holes which has been set equal to the bulk value, $n_h = 2.5$ [21]. We use the bulk value instead of the atomic value ($n_h = 3$) in order to take an intra-atomic charge redistribution $4s \rightarrow 3d$ into account. This enables bonding between two adjacent Co atoms [23], as otherwise the $4s\sigma_g$ bond is compensated by an antibonding $4s\sigma_u$ orbital. $\langle T_z \rangle$ corresponds to the expectation value of the spin magnetic dipole operator for the spin quantization axis oriented along z [21, 24], which defines the asymmetry of the intra-atomic spin distribution. It is nonzero in anisotropic bonding environments due to the different

number of spins in the unit cell along different crystallographic directions, but it vanishes when an angular average is performed [25, 26]. According to theory, the absolute value of $7T_z$ for systems with low dimensionality such as surfaces and deposited clusters can range up to 20 % of the spin magnetic moment [24, 27]. In our study we are dealing with freely rotating particles which are not fixed in space. As T_z is a strongly directional value, we have good reasons to assume that T_z , which can adopt values of different sign, averages to a minimum value close to zero.

Applying the above sum rules, the analysis reveals that the measured orbital moments $m_L^{(z)}$ at 20 K and $B = 7$ T are clearly enhanced (2 - 4 times) with respect to the bulk [21], while the measured spin moments $m_S^{(z)}$ of the clusters ($N = 8 - 22$) are less strongly enhanced (< 1.4 times) as summarized in Tab. S2 [18]. Figure 1(c) exemplarily demonstrates that the enhancement of the orbital moment is not just seen for Co clusters but also for small Fe clusters [28]. The XMCD signal ($A + B$) is clearly larger than that of bulk iron, which almost vanishes [21]. The measured orbital moment $m_L^{(z)}$ amounts to $0.25 \mu_B/\text{atom}$ compared to the bulk value of $0.085 \mu_B/\text{atom}$ [21]. According to the classical Langevin equation, which applies for single domain particles, the magnetization of small magnetic particles is expected to scale inversely with the temperature at a given B field [29-31]. Indeed, the measured moments $m_{L,S}^{(z)}$ show a striking temperature dependence as typical for superparamagnetic particles (Fig. 2). Our 7 T strong magnetic field substantially exceeds the Paschen-Back limit for atoms 1 T, and therefore orbital and spin angular momentum can be expected to decouple. This can be quantitatively rationalized by the relatively weak spin-orbit interaction energy of the itinerant 3d metals. The magnetic energy of Co_{11}^+ is 1 - 2 meV /atom at a field strength of 7 T. This energy compares with the spin-orbit splitting of a few meV for the bulk as well as the magnetic anisotropy energy as calculated for the atoms of a Co monolayer [32, 33]. Based on these estimates and our observation of a change in the ratio $m_L^{(z)}/m_S^{(z)}$ with temperature, we apply the classical Langevin equation to fit the temperature dependence of spin and orbital moments separately. According to the Langevin function, the intrinsic magnetic orbital and spin moments m_L and m_S per atom in units of μ_B are given by

$$m_{L,S}^{(z)}(T) = m_{L,S} \left[\coth \left(\frac{Nm_{L,S}\mu_B B}{k_B T} \right) - \frac{k_B T}{Nm_{L,S}\mu_B B} \right] \quad (3)$$

$m_{L,S}^{(z)}$ are the temperature-dependent projected orbital and spin magnetic moments per atom in units of μ_B and N denotes the number of atoms in the cluster. As shown in Fig. 2, a least-squares fit has been used to fit the data $m_L^{(z)}(T)$ and $m_S^{(z)}(T)$ with the above Langevin functions using the intrinsic moments m_L and m_S as fitting parameters. No hints for freezing of the magnetization into a blocked state is observed down to 20 K in agreement with measurements on Co wires [9]. Moreover,

Fig. 2 clearly shows that at 20 K the spin moment is much closer to its saturation limit than the smaller orbital moment. It is obvious that lower temperatures are necessary to saturate the orbital moment due to its smaller magnetic energy. In other words, the alignment of the orbital moment along the external field is weaker than the alignment of the larger spin moment. From this we conclude that spin and orbital moments are decoupled and interact separately with the external field analogous to the Paschen-Back effect in atoms [34].

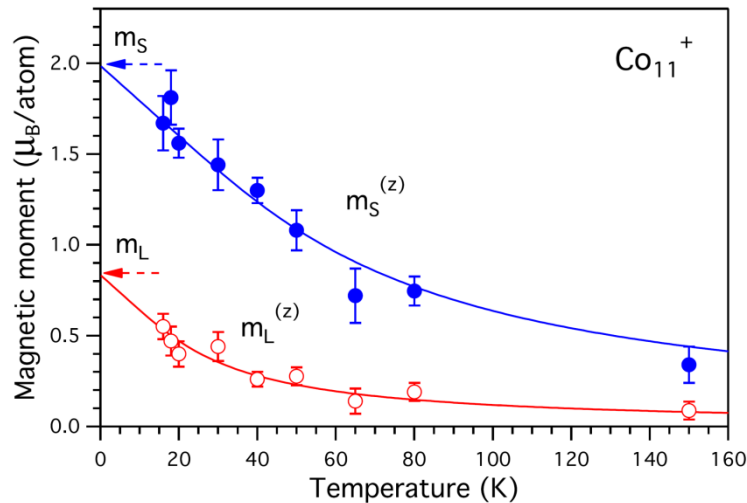


Fig. 2 (color online). Measured spin and orbital magnetic moments ($m_{L,S}^{(z)}$) versus temperature of Co_{11}^+ . The line through the measured moments is a Langevin fit using $B = 7$ T.

Upon scaling $m_L^{(z)}(T)$ and $m_S^{(z)}$ to the saturation limit at $T = 0$ K, the measured moments $m_{L,S}^{(z)}(T = 20\text{K})$ need to be corrected by 15 % and 70 %, respectively, to determine the intrinsic moments m_S and m_L . The corrections become larger the smaller the moments are, as the alignment along the magnetic field direction is thermally less stable. The Langevin-scaled intrinsic spin and orbital moments of the Co_N clusters are plotted in Fig. 3. The moments develop in a non-scalable manner from one cluster size to the next. Seemingly, the spin moment fluctuates more with cluster size N than the orbital moment. A convergence towards the bulk magnetic moments is not obvious up to clusters containing 22 atoms. The intrinsic spin moments of the clusters are in the range $m_S = 2 - 2.7 \mu_B$ per atom, while the orbital moments amount to $m_L = 0.6 - 1 \mu_B$ per atom. Thus the intrinsic orbital moments of the clusters are 4 - 6 times larger than the value of the solid, and the spin moments are enhanced by a factor of 1 - 2. Also, the intrinsic orbital moments of free clusters are enlarged with respect to small atomic islands formed on a crystalline platinum surface [35] as shown in Fig. 3.

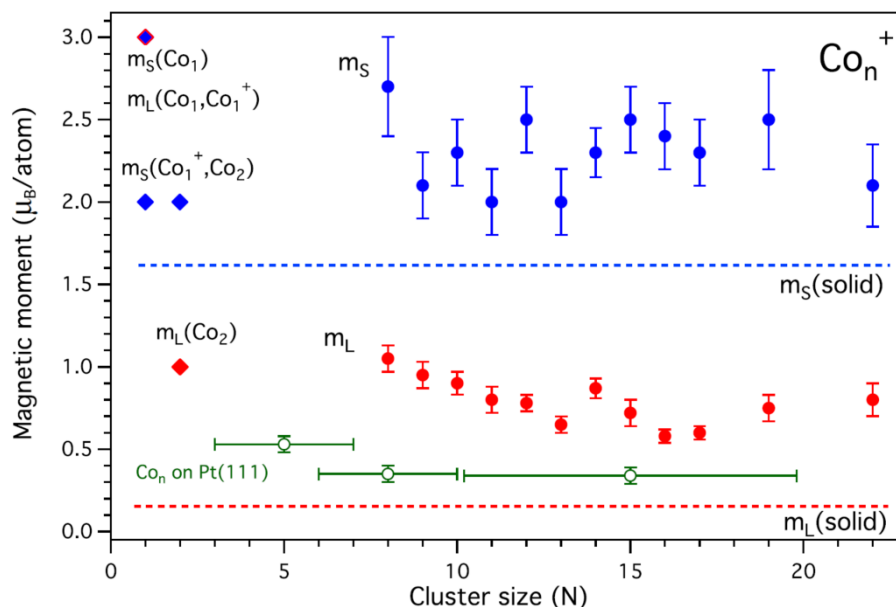


Fig. 3 (color online). Magnetic moments as revealed from XMCD spectra using magneto-optical sum rule analysis. Filled symbols show the intrinsic spin (m_S , blue) and orbital magnetic moments (m_L , red) of the clusters after Langevin scaling of the measured moments ($m_S^{(z)}$, $m_L^{(z)}$) recorded at 20 K and 7 T. The error bar corresponds to the standard deviation from repeated measurements at 778 eV (cf. Fig. S1 [18]). Moments of Co bulk [21] (dotted line) and small atomic islands [35] (green full line) are indicated. Additionally, the corresponding moments of the atom (Co_1^4F ; $\text{Co}_1^+{}^3\text{F}$) and dimer ($\text{Co}_2^5\Delta$) are displayed.

The intrinsic orbital moment of a pentagonal bipyramid with a d-band filling of 2.5 (Co_7) has been calculated to be $0.7 \mu_B/\text{atom}$ for magnetization along the equatorial C_2 axis [6] which comes close to our measured orbital moments. The orbital moment of the dimer $m_L = 1 \mu_B/\text{atom}$, as approximated from Hund's rule for the ground state configuration $^5\Delta$ [23, 36-38], is also similar to m_L of the clusters. However, the orbital moment of the atom (^4F [37], $m_L = 3 \mu_B$) is distinctly larger, which suggests a sudden drop of m_L from the atom to the dimer. Towards larger clusters, m_L further diminishes but rather smoothly. The moment of Co_{13}^+ represents a local minimum which might hint at a highly symmetric structure (I_h) of this cluster. The intrinsic spin moments of the clusters are somewhat higher than the calculated ones, which are in the range $m_S = 1.9 - 2.1 \mu_B/\text{atom}$ for Co_{2-20} [8], while they are smaller than this of the neutral atom ($3 \mu_B$) [39]. Moreover, the XMCD measurements show that the ratio m_L/m_S of the clusters, which is independent of n_h , is 3 - 4 times higher than that of the solid ($m_L/m_S = 0.1$).

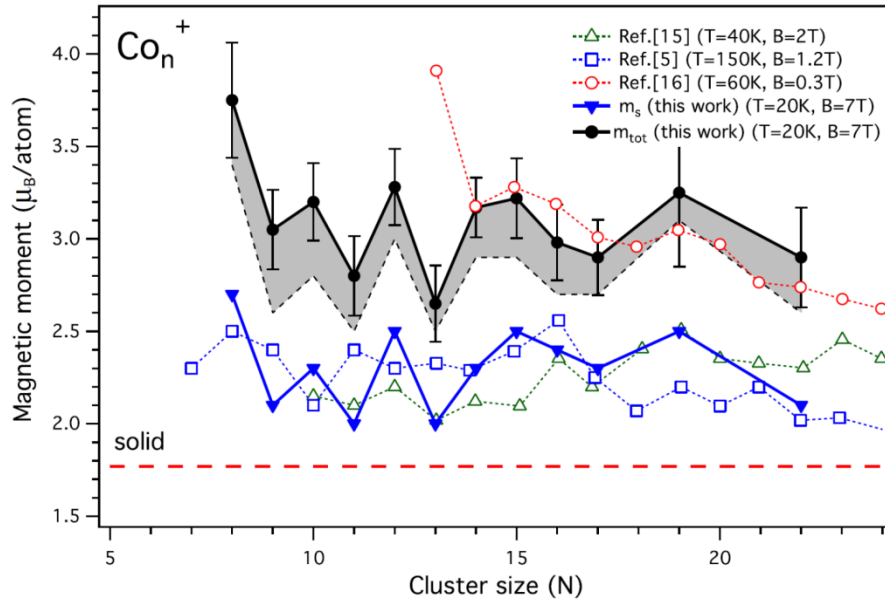


Fig. 4 (color online) Total magnetic moments of Co_N^+ clusters as determined by XMCD (filled dots) in comparison with Stern-Gerlach results (open symbols) taken from Ref. [5, 15, 16]. The spin moments as revealed from XMCD are also shown (filled triangles) [The transition from fully coupled to decoupled moments changes gradually with the strength of the magnetic field. This affects the Langevin scaling of the measured moments which is indicated by the shaded region of the total moment. The boundaries for total coupling and decoupling are shown by the lower line (dotted) and upper line (bold). The intrinsic orbital moment (not shown) drops by 30 % - 40 % when coupled moments are considered while the spin moment hardly ever changes].

In Fig. 4, we compare the total magnetic moments $m_{tot} = m_S + m_L$ as revealed from our XMCD measurements with the results from earlier Stern-Gerlach experiments [5, 15, 16]. In these earlier experiments, the spatial deflection of neutral clusters in an inhomogeneous magnetic field is used as a measure of the total magnetic moment of the clusters. As the Stern-Gerlach data are analyzed by the Langevin model [5, 15, 16], the published data can directly be compared to the sum of our scaled moments. Two of the Stern-Gerlach series [5,15] show very similar results with magnetic moments ranging between 2 and $2.5 \mu_B$ per atom, while another series exhibits much higher moments between 3 and $4 \mu_B$ per atom [16]. Remarkably, the lower Stern-Gerlach data agree with the measured spin moments rather than with the sum of the spin and orbital moment. We therefore conclude that the magnetic moments of Refs. [5, 15] represent basically the spin moment, while the contribution of the orbital magnetic moment is relatively reduced. This might be explained as follows: The data of Xu *et al.* [15] and Knickelbein [5] have been measured with a magnetic field of 1.2 T and 2 T, respectively. It is likely that under these field strengths spin and orbital moments interact rather independently with the external B field similar to our experiment. As established by

our temperature-dependent measurements (Fig. 2), the orbital moment is less aligned along the magnetic field direction than the larger spin moment. For example, the orbital contribution $m_L^{(z)}$ to the measured total magnetic moment is less than 15 % at 1 T and 40 K. The individual temperature dependence of spin and orbital moments must be compensated for by different scaling factors in order to deduce the intrinsic moments. Note that the weaker orbital moment must be scaled more than the larger spin moment (cf. Fig. S3 [18]). In our XMCD experiments, the measured moments are scaled individually according to separate Langevin fits of spin and orbital moments. In Stern-Gerlach experiments, however, such an individual scaling is not possible.

The data of Payne *et al.* [16] have been measured with a considerably lower magnetic field (0.2 - 0.3 T). Under these conditions, spin and orbital moments are most likely coupled by spin-orbit interaction and interact as a total moment with the external magnetic field. In this case, Langevin scaling of the total moment becomes appropriate. This might explain the rather good agreement of the temperature-scaled data of Payne *et al.* [16] with the sum of m_S and m_L as determined from our high-field XMCD measurements in which the uncoupled moments are scaled separately before summing up.

In summary, the present data demonstrate the importance of quantifying spin and orbital moments as a function of temperature in order to analyze the intrinsic magnetic properties of free ferromagnetic particles. A clear Langevin-type temperature dependence has been established for small Co clusters revealing a different temperature scaling of spin and orbital moments under high magnetic field conditions. The data demonstrate that the intrinsic orbital moments of small Co clusters are strongly enlarged by a factor of 4 - 6 in comparison to the bulk. The decomposition of the total moments into spin and orbital moments and their different temperature dependence might help to clarify diverging results of former Stern-Gerlach experiments. The analysis of spin and orbital magnetic moments of free clusters bears high potential for future investigation of application-relevant magnetic storage particles such as magnetic building block clusters, molecular magnets, and magnetic biomolecules.

This work has been supported by the DFG (Nie325/10-1). We are grateful to K. Fauth (University of Würzburg), T. Lau (Helmholtz-Zentrum Berlin), and W. Wurth (University of Hamburg) as well as P. Bechthold and S. Bluegel (Forschungszentrum Jülich) for valuable discussions. We also thank P. Hofmann (Brandenburg University of Technology, Cottbus) for assisting at the UE52 beamline.

4.5.2 References

- [1] G. Schütz, W. Wagner, W. Wilhelm, P. Kienle, R. Zeller, R. Frahm, and G. Materlik, *Phys. Rev. Lett.* **58**, 737 (1987).

- [2] J. Stöhr, *J. Electron Spectrosc. Relat. Phenom.* **75**, 253 (1995).
- [3] M.L. Billas, A. Chatelain, and W.A. de Heer, *Science* **265**, 1682 (1994).
- [4] S.E. Apsel, J.W. Emmert, J. Deng, and L.A. Bloomfield, *Phys. Rev. Lett.* **76**, 1441 (1996).
- [5] M.B. Knickelbein, *J. Chem. Phys.* **125**, 044308 (2006).
- [6] R. Guirado-Lopez, J. Dorantes-Davila, and G. Pastor, *Phys. Rev. Lett.* **90**, 226402 (2003).
- [7] B. Nonas, I. Cabria, R. Zeller, P. Dederichs, T. Huhne, and H. Ebert, *Phys. Rev. Lett.* **86**, 2146 (2001).
- [8] S. Datta, M. Kabir, S. Ganguly, B. Sanyal, T. Saha-Dasgupta, and A. Mookerjee, *Phys. Rev. B* **76**, 014429 (2007).
- [9] P. Gambardella, A. Dallmeyer, K. Maiti, M. Malagoli, W. Eberhardt, K. Kern, and C. Carbone, *Nature (London)* **416**, 301 (2002).
- [10] J.T. Lau, A. Föhlisch, R. Nietubyc, M. Reif, and W. Wurth, *Phys. Rev. Lett.* **89**, 057201 (2002).
- [11] J. Bansmann, A. Kleibert, M. Getzlaff, A. Rodriguez, F. Nolting, C. Boeglin, and K. Meiwes-Broer, *Phys. Status Solidi B* **247**, 1152 (2010).
- [12] K. Fauth, M. Heßler, D. Batchelor, and G. Schütz, *Surf. Sci.* **529**, 397 (2003).
- [13] H. Dürr, S. Dhesi, E. Dudzik, D. Knabben, G. van der Laan, J. Goedkop, and F. Hillebrecht, *Phys. Rev. B* **59**, R701 (1999).
- [14] H. Brune and P. Gambardella, *Surf. Sci.* **603**, 1812 (2009).
- [15] X. Xu, S. Yin, R. Moro, and W. de Heer, *Phys. Rev. Lett.* **95**, 237209 (2005).
- [16] F.W. Payne, W. Jiang, J.W. Emmert, J. Deng, and L.A. Bloomfield, *Phys. Rev. B* **75**, 094431 (2007).
- [17] S. Peredkov, A. Savci, S. Peters, M. Neeb, W. Eberhardt, H. Kampschulte, J. Meyer, M. Tombers, B. Hofferberth, F. Menges, and G. Niedner-Schatteburg, *J. Electron. Spectrosc. Relat. Phenom.* **184**, 113 (2011).
- [18] See Supplemental Material at <http://link.aps.org/supplemental/10.1103/PhysRevLett.107.233401> for a description of the experimental setup (S1), a table showing measured and scaled magnetic moments (S2), and a graph showing scaling factors of magnetic moments as a function of temperature and different magnetic field strengths.
- [19] B. Thole, P. Carra, F. Sette, and G. van der Laan, *Phys. Rev. Lett.* **68**, 1943 (1992).
- [20] P. Carra, B. Thole, M. Altarelli, and X. Wang, *Phys. Rev. Lett.* **70**, 694 (1993).
- [21] C. Chen, Y. Idzerda, H.-J. Lin, N. Smith, G. Meigs, E. Chaban, G. Ho, E. Pellegrin, and F. Sette, *Phys. Rev. Lett.* **75**, 152 (1995).
- [22] By using the Langevin formalism, the intrinsic moments of superparamagnetic particles can be received from the measured moments.
- [23] G. Gutsev, S. Khanna, and P. Jena, *Chem. Phys. Lett.* **345**, 481 (2001).
- [24] O. Sipr, J. Minar, and H. Ebert, *Europhys. Lett.* **87**, 67007 (2009).
- [25] J. Stöhr and R. Nakajima, *IBM J. Res. Dev.* **42**, 73 (1998).
- [26] J. Stöhr and H. König, *Phys. Rev. Lett.* **75**, 3748 (1995).
- [27] R. Wu and A. Freeman, *Phys. Rev. Lett.* **73**, 1994 (1994).
- [28] S. Palutke, I. Baev, M. Martins, W. Wurth, J. Meyer, M. Tombers, G. Niedner-Schatteburg, S. Peredkov, M. Neeb, and W. Eberhardt (to be published).
- [29] S. Khanna and S. Linderoth, *Phys. Rev. Lett.* **67**, 742 (1991).
- [30] J. Bucher, D. Douglass, and L. Bloomfield, *Phys. Rev. Lett.* **66**, 3052 (1991).
- [31] B. Reddy, S. Nayak, S. Khanna, B. Rao, and P. Jena, *J. Phys. Chem. A* **102**, 1748 (1998).
- [32] J. Stöhr, *J. Magn. Magn. Mater.* **200**, 470 (1999).

- [33] G. Daalderop, P. Kelly, and M. Schuurmanns, *Phys. Rev. B* **50**, 9989 (1994).
- [34] M. Knickelbein, *J. Chem. Phys.* **121**, 5281 (2004).
- [35] P. Gambardella, S. Rusponi, M. Veronese, S. Dhesi, C. Grazioli, A. Dallmeyer, I. Cabria, R. Zeller, P. Dederichs, K. Kern, C. Carbone, and H. Brune, *Science* **300**, 1130 (2003).
- [36] H. Wang, Y. Khait, and M. Hoffmann, *Mol. Phys.* **103**, 263 (2005).
- [37] F. Furche and J. Perdew, *J. Chem. Phys.* **124**, 044103 (2006).
- [38] D. Hales and P. Armentrout, *J. Cluster Sci.* **1**, 127 (1990).
- [39] We assume that the extra charge does not much alter the magnetic moments of the ionized clusters, as the single hole is just a small fraction of the total number of valence electrons for $N \geq 8$ atoms (≥ 72 electrons)

4.5.3 Supplementary Material

4.5.3.1 S.1 Experimental setup

The experimental setup has been described in detail in Ref. [1]. A Fourier-Transform-Ion-Cyclotron-Resonance (FT-ICR) mass spectrometer has been combined with a soft-X-ray undulator beamline at BESSY II (UE52-PGM). A Penning-like ICR cell serves both as an ion trap and a mass analyzer. A pulsed laser vaporization source is used for production of a Co-cluster ion beam. The strong (7 T) axial-symmetric magnetic field of the FT-ICR is used for radial confinement of the cluster ions. Axially the cluster ions are trapped by electric fields of ICR trap. The axial magnetic field is not only used for trapping but also for alignment of the magnetic moments. The magnetic field of the superconducting solenoid is directed parallel to the incoming photon beam for maximum XMCD intensity. Moreover, the ICR cell has been modified in order to cool it down cryogenically. This cooling device enables thermalization of the trapped clusters through multiple collisions with a pulsed inert buffer gas (e.g. He, $p \approx 1 \cdot 10^{-6}$ mbar for a few seconds) resulting in cluster temperatures as low as 18 K. In order to record XMCD spectra circularly polarized X-ray radiation (photon flux $\approx 5 \cdot 10^{11} \text{ s}^{-1}$, polarization degree 90 %) has been used which is provided by the UE52-PGM undulator beamline of the BESSY storage ring. Photon helicity-dependent L-edge absorption spectra of trapped Co-cluster ions have been recorded. Core-electron transitions are induced in the stored cluster ions by the absorption of an

X-ray photon. Subsequent internal relaxation produces multiply-ionized mother ions and fragment ions which are individually recorded in the FT-ICR-detection mode. The total fragment signal intensity is proportional to the X-ray absorption probability. The spectra are normalized to the mother cluster intensity and photon flux. We assume that a variation of the trapped cluster density after each refill is the main source of error. This density variation is caused by pulse-to-pulse fluctuations cluster beam. Repeated measurements at the energy of the L_3 -peak maximum were done several times during recording of X-ray absorption spectra (XAS). The two standard deviation ($\pm 2\sigma$) from the repeated measurements is considered as the experimental error of XAS spectra.

4.5.3.2 S.2 Magnetic moments of Co_N clusters

Table I. Magnetic moments of Co_N clusters: $m_L^{(z)}$ and $m_S^{(z)}$ are the measured orbital and spin magnetic moments calculated with Eq. 1 and Eq. 2 in assumption $T_z = 0$ and $n_h = 2.5$. m_L and m_S are the corresponding separately Langevin scaled intrinsic moments. m_{tot} corresponds to the total magnetic moments. Co-bulk (hcp): $m_L = 0.15 \mu_B/\text{atom}$; $m_S = 1.62 \mu_B/\text{atom}$ Ref. [2]

Cluster size Co _N	Measured moment T = 20 K, B = 7 T		Intrinsic moment		
	$m_L^{(z)}$	$m_S^{(z)}$	m_L	m_S	m_{tot}
8	0.6 ± 0.08	2.3 ± 0.25	1.0	2.7	3.7
9	0.52 ± 0.07	1.7 ± 0.2	0.95	2.1	3.1
10	0.5 ± 0.07	1.9 ± 0.2	0.9	2.1	3.2
11	0.47 ± 0.07	1.7 ± 0.15	0.8	2.0	2.8
12	0.47 ± 0.07	2.15 ± 0.2	0.78	2.5	3.3
13	0.37 ± 0.05	1.7 ± 0.2	0.65	2.0	2.7
14	0.6 ± 0.06	2.0 ± 0.15	0.85	2.3	3.2
15	0.47 ± 0.08	2.2 ± 0.15	0.7	2.45	3.2
16	0.36 ± 0.04	2.2 ± 0.2	0.6	2.4	3.0
17	0.38 ± 0.04	2.1 ± 0.2	0.6	2.3	2.9
19	0.54 ± 0.06	2.3 ± 0.3	0.75	2.5	3.3
22 (T = 30 K)	0.5 ± 0.07	1.8 ± 0.25	0.7	2.2	2.9

4.5.3.3 S.3 Langevin scaling factors

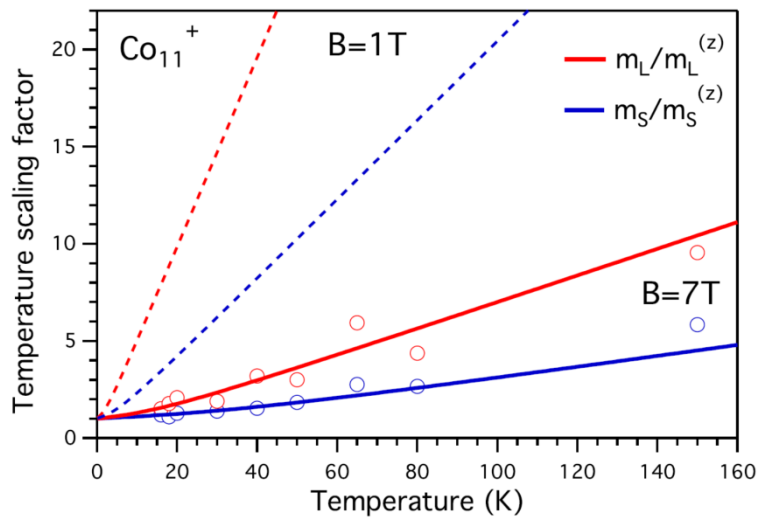


Fig. S3. Langevin-scaling of spin and orbital moment in case of decoupled moments. Note that the temperature scaling factor is larger for the smaller orbital moment than the spin moment. The XMCD measurements have been carried out at 7 T (full line). The corresponding data points of Co_{11}^+ are shown as open circles. For example, at 1 T (broken lines) the scaling disparity would become very prominent. This disparity also changes with temperature

-
- [1] S. Peredkov, A. Savci, S. Peters, M. Neeb, W. Eberhardt, H. Kampschulte, J. Meyer, M. Tombers, B. Hofferberth, F. Menges, and G. Niedner-Schatteburg, *J. Electron Spectrosc. and Relat. Phenom.* **184**, 113 (2011).
- [2] C. Chen, Y. Idzerda, H.-J. Lin, N. Smith, G. Meigs, E. Chaban, G. Ho, E. Pellegrin, and F. Sette, *Phys. Rev. Lett.* **75**, 152 (1995).

5. SPIN AND ORBITAL MAGNETIC MOMENTS OF SMALL CLUSTERS OF THE FERROMAGNETIC 3D ELEMENTS

Experiments with nickel clusters were carried out in cooperation with S. Peredkov^{*}, M. Neeb[#] and W. Eberhardt^{*} and in the case of iron clusters additionally with the group of W. Wurth[§] / M. Martins[§] (^{*}Institut für Optik und Atomare Physik, Technische Universität Berlin, Berlin, Germany; [#]Helmholtz Zentrum Berlin für Materialien und Energie, Berlin, Germany; [§]Institut für Experimentalphysik, Universität Hamburg, Hamburg, Germany). The experimental setup was located at the synchrotron BESSY II / HZB. All spectra were recorded at the undulator beamline UE52-PGM. Experiments were carried out during allocated beamtimes by a team which core members were Matthias Tombers, Sergey Peredkov and me. The experiments on iron clusters were also evaluated by .S. Palutke who joined the experiments on iron clusters

5.1 Introduction

Nearly all of the thirty transition metal atoms have a net spin magnetic moment^[1], but only four elementary metals show a ferromagnetic ordering at room temperature, i.e. iron, cobalt, nickel and gadolinium. The magnetic moments of the 3d ferromagnets iron, cobalt and nickel is almost entirely due to the spin of the 3d electrons^[2]. The orbital magnetic moment is nearly completely quenched in the bulk materials.

The difficulty in understanding the magnetism of the 3d ferromagnets lies in their "split personality"^[2], i.e. the duality between the localized behavior and the delocalized (itinerant) behavior of the electrons. "This duality forms the core of the many body problem and forms the essence of magnetism"^[2]. The band width of the 3d band is about 3 eV whereas the s-p band width is about 10 eV due to the delocalized nature of the s and p electrons. Historically, nickel and cobalt were called strong ferromagnets because their majority bands are fully occupied. Iron was in turn called a weak ferromagnet. The exchange splitting of the valence band is of the order of a few electronvolts for 3d transition metals. The exchange splitting is the largest for iron (2.2 eV^[2]) and the smallest for nickel (0.6 eV^[2]). The order for iron, cobalt and nickel according to the exchange splitting is the same as if ordering the three elements according to the spin magnetic moment.

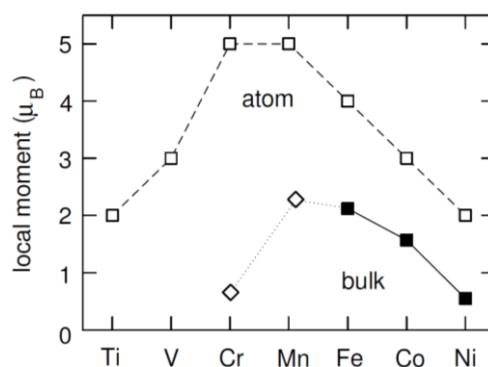


Figure 5.1 Local magnetic moments of isolated 3d atoms (open squares connected by dashed line), ferromagnetic (filled squares connected by solid line) and antiferromagnetic (open diamonds connected by dotted line) 3d bulk metals. The magnetism of the atom includes only the moments due to the 3d electrons. For the bulk metals the experimental spin moments are shown.^[1]

The reduction of dimensions from 3D (bulk samples) to thin films (2D), chains (1D) and atoms (0D) led to the discovery of new phenomena^[1] and spurred a rapid increase in the storage capabilities of hard drives^[3]. However, understanding the new finite size effects is challenging. Some effects can be rationalized by the enhanced surface to bulk ratio in finite sized systems^[1,4]. However, the more complex the new systems become the more parameters have to be considered. This means, that e.g. for a deposited nanoparticle not only the elemental composition but also shape and interaction with the surface material and the surface site become important. Thus, we try to reduce the number of parameters by first studying the isolated cluster without any interaction with an environment^[5,6]. This approach allows us to access the intrinsic magnetic moments without any influences exerted by a supporting material.

The spin and orbital magnetic moments of small nickel Ni_n^+ (Chap. 5.2) and iron Fe_n^+ (Chap. 5.3) clusters will be discussed in the course of this chapter. The found spin and orbital magnetic moments will be compared to theory on neutral cluster and when possible also to theory on the cationic clusters. A comparison to spin and orbital magnetic moments from a different XMCD experiment published by Lau *et al.*^[7-9] will be given for both metals. The chapter will be concluded by a paper draft on the spin and orbital magnetic moments of small Fe_n^+ , Co_n^+ and Ni_n^+ clusters (Chap. 5.5). A detailed comparison of the total magnetic moments by XMCD spectroscopy to prior Stern-Gerlach experiments is included in the paper draft. A key issue of the paper draft is a discussion about the relation of the orbital and spin magnetic moments of the clusters to the bulk and atomic values in terms of scaling laws, i.e. if the magnetic moments follow interpolations between the bulk and atomic values.

5.2 Nickel

5.2.1 Spin and orbital magnetic moment of small nickel clusters

The spin and orbital magnetic moments of small nickel clusters Ni_n^+ ($7 \leq n \leq 18$) are shown in Fig. 5.2a. The magnetic moments were extracted by sum rule analysis from the respective XMCD spectra. The number of 3d holes used to calculate the magnetic moments was set to $n_h = 1.45^{[10,11]}$ which is the respective bulk value. All spectra were recorded under comparable experimental conditions with a cluster temperature of $T_{\text{cluster}} = 20$ K and an external magnetic field of $B = 7$ T. The numerical values of the experimental and intrinsic magnetic moments are given in Tab. 5.1. The orbital magnetic moments show maxima for Ni_{12}^+ and Ni_{15}^+ (Fig. 5.2a).

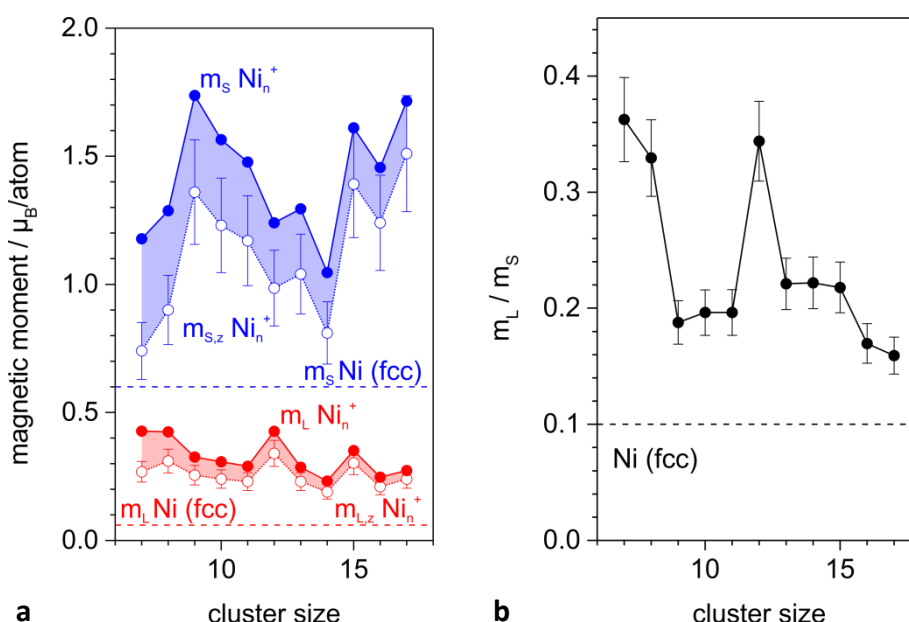


Figure 5.2 (a) Experimental (open circles) and intrinsic (filled circles) spin (blue) and orbital (red) magnetic moments of small nickel clusters Ni_n^+ ($7 \leq n \leq 18$). The total magnetic moments are corrected for field and temperature effects according to Langevin^[9,12-14] and the intrinsic spin and orbital magnetic moments calculated with the help of the m_L / m_s ratio. **(b)** Ratio of orbital to spin magnetic moment m_L / m_s . The values fluctuate around a ratio of 0.2 except for Ni_7^+ , Ni_8^+ and Ni_{12}^+ . The dashed lines indicate the respective bulk value for Ni (fcc)^[15,16].

The remaining cluster sizes show little variation of the orbital magnetic moment. However, for all investigated cluster sizes the orbital magnetic moments are enhanced by a factor of 3 - 5 compared to the value of $0.06 \mu_B/\text{atom}$ for bulk nickel (fcc)^[15,16]. If compared to the orbital moment of the free Ni atom of $3 \mu_B$, the orbital magnetic moments of the clusters only amount to 8 - 15 % of the atomic value. The spin magnetic moments show more pronounced fluctuations than the orbital magnetic moments. The lowest spin magnetic moments were found for Ni_8^+ and Ni_{14}^+ . Ni_{14}^+ represents a

minimum within the investigated size range. As for the orbital magnetic moments, the spin magnetic moments are larger than the bulk value of $0.6 \mu_B/\text{atom}^{[15,16]}$, but only by a factor 2 - 3. The spin magnetic moments are quenched compared to the atomic value of $2 \mu_B$ by 25 - 50 %. This is far less than for the orbital magnetic moment. The ratio of orbital to spin magnetic moment m_L / m_S in the investigated size range fluctuates around a value of 0.2 (Fig. 5.2b). This is twice the bulk value of $m_L / m_S = 0.1$. Ni_7^+ , Ni_8^+ and Ni_{12}^+ show a higher m_L / m_S ratio of about 0.35. A detailed discussion about this topic can be found in the paper draft attached as supplement to this chapter (Chap. 5.5).

Table 5.1 Experimental orbital $m_{L,z}$ and spin $m_{S,z}$ and intrinsic orbital m_L , spin m_S and total m_J magnetic moments of small nickel clusters Ni_n^+ with assumed LS coupling

	Experimental magnetic moments		Magnetic moments		
	/ μ_B/atom		/ μ_B/atom		
	$m_{L,z}$	$m_{S,z}$	m_L	m_S	m_J
Ni_7^+	0.27 ± 0.04	0.75 ± 0.10	0.43 ± 0.06	1.2 ± 0.20	1.6 ± 0.25
Ni_8^+	0.31 ± 0.05	0.90 ± 0.15	0.42 ± 0.06	1.3 ± 0.20	1.7 ± 0.25
Ni_9^+	0.26 ± 0.04	1.35 ± 0.20	0.33 ± 0.05	1.7 ± 0.25	2.1 ± 0.30
Ni_{10}^+	0.24 ± 0.04	1.2 ± 0.20	0.31 ± 0.05	1.6 ± 0.25	1.9 ± 0.30
Ni_{11}^+	0.23 ± 0.04	1.2 ± 0.20	0.29 ± 0.04	1.5 ± 0.20	1.8 ± 0.25
Ni_{12}^+	0.34 ± 0.05	1.0 ± 0.15	0.43 ± 0.06	1.2 ± 0.20	1.7 ± 0.25
Ni_{13}^+	0.23 ± 0.04	1.0 ± 0.15	0.29 ± 0.04	1.3 ± 0.20	1.6 ± 0.20
Ni_{14}^+	0.19 ± 0.03	0.80 ± 0.10	0.23 ± 0.04	1.0 ± 0.15	1.3 ± 0.20
Ni_{15}^+	0.30 ± 0.05	1.4 ± 0.20	0.35 ± 0.05	1.6 ± 0.25	2.0 ± 0.30
Ni_{16}^+	0.21 ± 0.03	1.25 ± 0.20	0.25 ± 0.04	1.5 ± 0.20	1.7 ± 0.25
Ni_{17}^+	0.24 ± 0.04	1.5 ± 0.20	0.27 ± 0.04	1.7 ± 0.25	2.0 ± 0.30

5.2.2 Comparison of experimental data with:

5.2.2.1 Theoretical data

Several theoretical studies on the spin magnetic moments of small nickel clusters have been published within the last years^[14,17-25]. The studies focus on the spin magnetic moments of neutral clusters and either use a tight binding approach^[14,17-19] or a DFT method^[20-25]. Within the last years, a few studies include the spin magnetic moments of singly positively charged clusters Ni_n^+ ^[20,21,25]. The theoretical spin magnetic moments of neutral nickel clusters mostly fluctuates between $0.7 - 1 \mu_B/\text{atom}$ for clusters Ni_n with $n > 7$ (Fig. 5.3a). The spin magnetic moments of Reddy *et al.*^[14] fall below the general trend. The majority of the theoretical m_S values are lower than the experimental m_S values of the present work. The spin magnetic moments of Aguilera-Granja *et al.*^[17] lie above the other data series, i.e. closer to a value of $1.2 \mu_B/\text{atom}$ for clusters smaller than Ni_{20} .

Their values agree reasonably well with our experimentally determined ones for cationic clusters. For Ni_7^+ and Ni_8^+ the calculated moments by Aguilera-Granja *et al.*^[17] are too large. The spin magnetic moments of these two cluster sizes agree well with several other theoretical studies (Fig. 5.3a). However, the calculated moments for the smaller sizes fluctuate much more than for clusters with more than eight atoms per cluster.

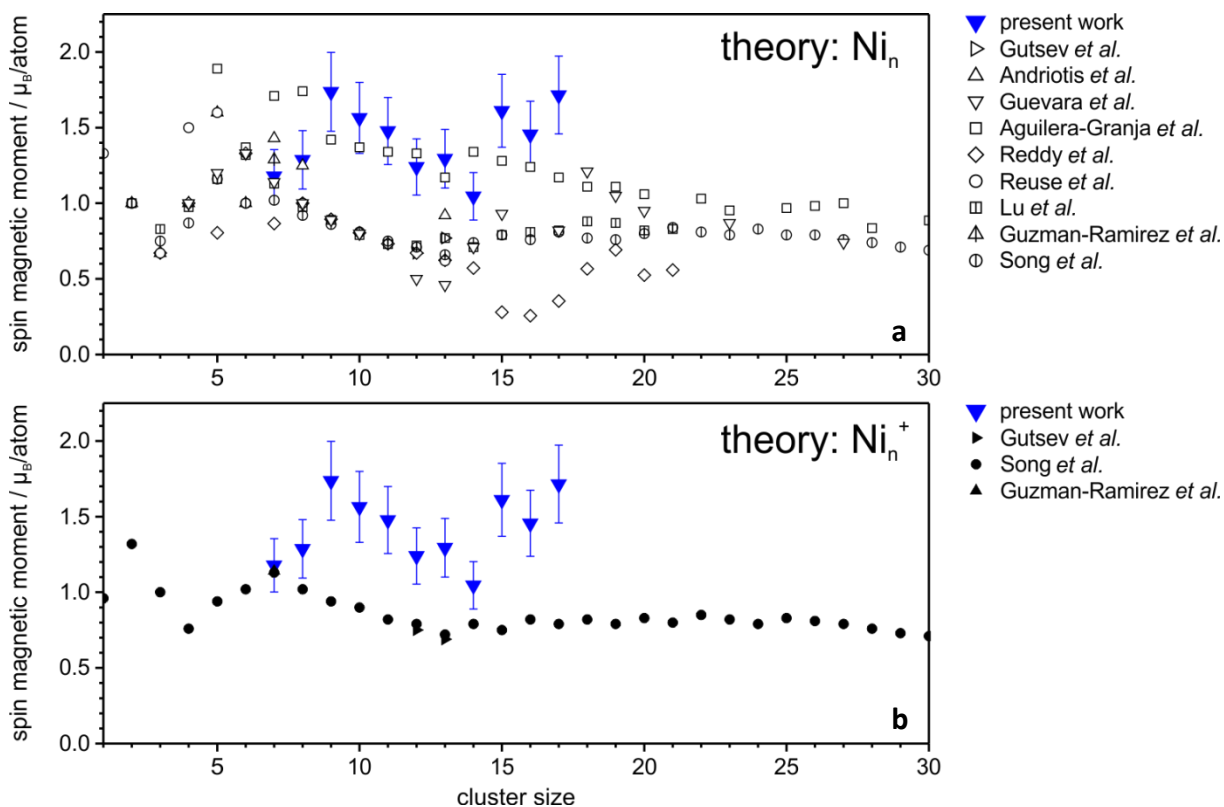


Figure 5.3 Comparison between the spin magnetic moments of Ni_n^+ clusters (filled blue triangles) of the present work with theoretical data of (a) neutral nickel clusters Ni_n ^[14,17-23,25] and (b) cationic clusters Ni_n^+ ^[20,21,25]. Only one theoretical data series agrees with the spin magnetic moments of the present work, i.e. the one of Aguilera-Granja *et al.*^[17]. The exceptions are Ni_7^+ and Ni_8^+ which do not agree with the values of Aguilera-Granja *et al.* but with the several of the other studies. The only agreement with theoretical data of Ni_n^+ clusters can be found for Ni_7^+ . The calculated spin magnetic moments are too low for all other cluster sizes studied by us.

Theoretical data on nickel clusters with fewer atoms per cluster than we studied are included for the sake of completeness. (The spin magnetic moment of the lowest energy isomer was taken from the references in case of several structural isomers for one cluster size, if not indicated otherwise).

All published studies of cationic nickel clusters are based on DFT methods. Gutsev *et al.*^[20] only studied $\text{Ni}_{12}^{0/+}$ and $\text{Ni}_{13}^{0/+}$. Surprisingly, a cluster structure based on an icosahedral geometry is only assigned for Ni_{13}^+ as lowest energy isomer. The spin magnetic moment for Ni_{12}^+ ($0.75 \mu_B/\text{atom}$) and Ni_{13}^+ ($0.69 \mu_B/\text{atom}$) are far lower than the experimentally found m_s values (Fig. 5.3b) Gutsev *et al.*

claim that the cluster structure and consequently also the theoretical spin magnetic moment strongly depend on the chosen DFT method^[20]. Guzman-Ramirez *et al.*^[21] only calculated a spin magnetic moment for Ni_7^+ . The theoretical value agrees with the experimental one. They assigned a capped octahedron as structure for Ni_7^+ . Song *et al.*^[25] calculated spin magnetic moments for cationic nickel clusters Ni_n^+ with $n \leq 30$. They found that the structures of the neutral and singly positively charged clusters are almost identical with the neutral ones with the exceptions of Ni_5^+ and Ni_{28}^+ ^[25]. If we compare the spin magnetic moments found by Song *et al.*^[25] to our experimentally obtained spin magnetic moments, the agreement is not good. The theoretical values are too low over the whole size range investigated by us. The only cluster size for which the theory by Song *et al.*^[25] and our experiment agrees is Ni_7^+ (Fig. 5.3b). Interestingly, the two available theoretical values for Ni_{12}^+ and Ni_{13}^+ agree and both calculated spin magnetic moments for Ni_7^+ agree with each other too.

Guirado-Lopéz *et al.*^[26] published a study in which they calculated orbital magnetic moments for small neutral nickel clusters. Icosahedral structure motifs were assumed for Ni_{13} and Ni_{19} . For the smaller clusters a geometry optimization was done^[14,26,27]. The orbital magnetic moments found by Guirado-Lopéz *et al.* agree for Ni_7 and Ni_{13} with the experimentally determined moments for Ni_7^+ and Ni_{13}^+ (Fig. 5.4). The orbital magnetic moments for Ni_8 and Ni_9 are lower compared to the m_L values of the present work. We did not measure Ni_{19}^+ but the theoretically determined value fits within the general trend determined by the orbital magnetic moments of Ni_{16}^+ and Ni_{17}^+ .

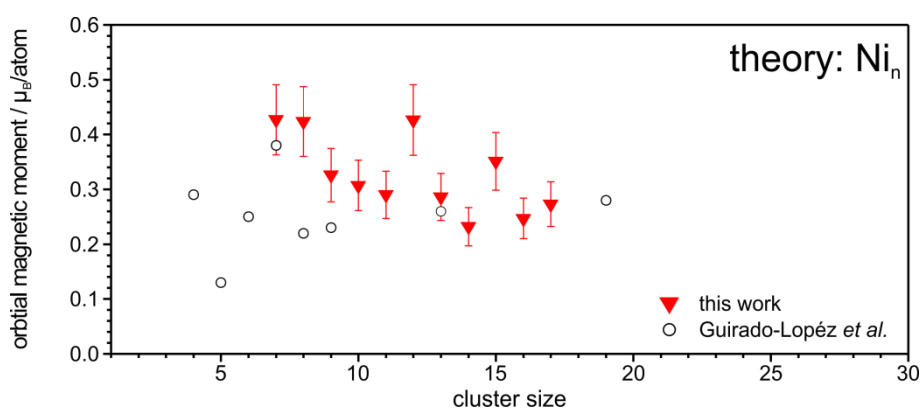


Figure 5.4 Comparison between orbital magnetic moments for Ni_n^+ (filled red triangles) of the present work and theory on neutral Ni_n (open circles) clusters. The theoretically determined orbital magnetic moments by Guirado-Lopéz *et al.*^[26] do agree for Ni_7^+ and Ni_{13}^+ but not for Ni_8^+ and Ni_9^+ . (For the theoretical data: The magnetization direction is a principal C_n symmetry axis z)^[26]

5.2.2.2 XMCD experiments

Lau *et al.*^[7,8] recently published spin and orbital magnetic moments for small nickel clusters Ni_{10}^+ - Ni_{15}^+ obtained by XMCD spectroscopy. Their experimental setup uses a different cluster ion source, ion trap and mass spectrometer but the detection technique is also TIY^[8,9,28,29]. The good agreement between both data sets is a proof of the applicability of TIY as detection technique for the recording of XA and XMCD spectra. The spin as well as orbital magnetic moments agree with each other within the uncertainties of both experiments (Fig. 5.5a). If the m_L / m_S ratio is compared to exclude effects due to the number of 3d holes used in the sum rule analysis and the subtraction of the background stemming from direct photoionization, the agreement is also within the experimental uncertainties for most of the investigated cluster sizes. Ni_{10}^+ is an exception. The m_L / m_S ratio found by Lau *et al.* is about twice of the ratio found by us (Fig. 5.5b). Both experiments find an enhanced m_L / m_S ratio for Ni_{12}^+ compared to the other investigated cluster sizes.

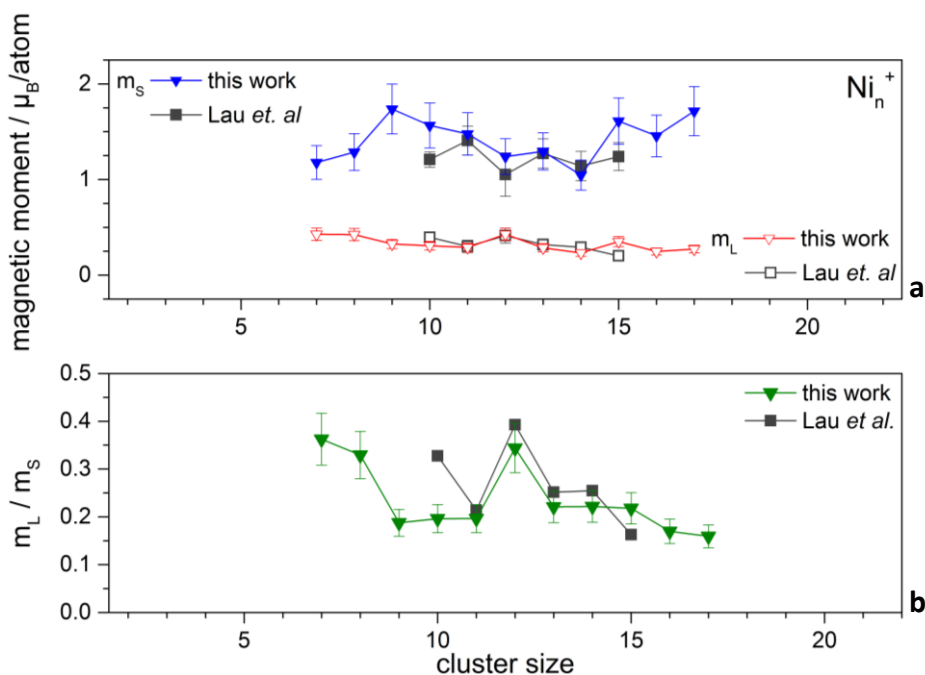


Figure 5.5 Comparison between experimental values for nickel clusters Ni_n^+ from the present work and from Lau *et al.*^[7,8] for the (a) spin (this work, filled blue triangles; Lau *et al.*, filled grey squares) and orbital (this work, open red triangles; Lau *et al.*, open grey squares) magnetic moments and (b) ratio of orbital to spin magnetic moment m_L / m_S (this work, filled green triangles; Lau *et al.*, filled grey squares)

The spin and orbital magnetic moments of both experiments agree well with each other. Also, the ratio of m_L / m_S is in good agreement for both experiments. Ni_{10}^+ is an exception for which m_L / m_S found by Lau *et al.* is about twice the ratio found by us.

5.2.2.3 Stern-Gerlach experiments

A detailed comparison of the total magnetic moments of the present work to the total magnetic moments from Stern-Gerlach experiments will be given in the paper draft in the supplement of this chapter (see Chap. 5.5).

5.3 Iron clusters

5.3.1 Spin and orbital magnetic moment of small iron clusters

The magnetic moments were extracted by sum rule analysis from the respective XMCD spectra. The number of holes in the 3d shell used to calculate the magnetic moments was set to $n_h = 3.4$ ^[30,31]. All XMCD spectra were recorded under comparable experimental conditions with a cluster temperature of $T_{\text{cluster}} = 20$ K and an external magnetic field of $B = 7$ T. The experimental and the intrinsic magnetic moments are given in Tab. 5.2. The spin magnetic moments show a minimum for Fe_{13}^+ (Fig. 5.6a).

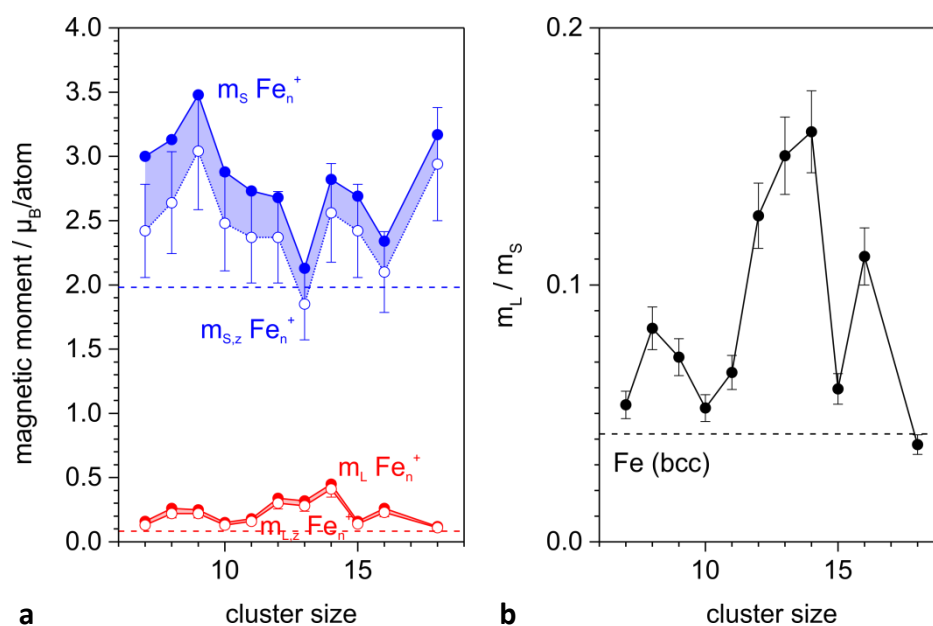


Figure 5.6 (a) Experimental (open circles) and intrinsic (filled circles) spin (blue) and orbital (red) magnetic moments of small iron clusters Fe_n^+ ($7 \leq n \leq 18$). The total magnetic moments are corrected for field and temperature effects according to Langevin^[9,12-14] and the intrinsic spin and orbital magnetic moments calculated with the help of the m_L / m_S ratio. **(b)** ratio of orbital to spin magnetic moment m_L / m_S . The m_L / m_S ratios show strong fluctuations with size although within a small numerical range compared to cobalt (Fig. 4.4) and nickel (Fig. 5.2b) clusters. The dashed lines indicate the respective bulk values for bulk Fe (bcc)^[32].

The spin and orbital magnetic moments for small iron clusters Fe_n^+ ($7 \leq n \leq 18$) are shown in Fig. 5.6a. If the spin and orbital magnetic moments are compared to the bulk values, both contributions are enhanced. If, however, they are compared to the atomic values, the spin and especially the orbital magnetic moments are quenched. The orbital magnetic moment of the investigated cluster sizes only amounts to 6 - 20% of the atomic value. The highest orbital magnetic moment was found for Fe_{14}^+ . The m_L / m_S ratio shows no trend. The values are enhanced compared to the bulk value of 0.042^[32] and show strong fluctuations in the investigated size range (Fig. 5.6b). A detailed discussion about this topic can be found in the paper draft attached as supplement to this chapter (Chap. 5.5)

Table 5.2 Experimental orbital $m_{L,z}$ and spin $m_{S,z}$ and intrinsic orbital m_L , spin m_S and total m_J magnetic moments of small iron clusters Fe_n^+ with assumed LS coupling

	Experimental magnetic moments		Magnetic moments		
	/ μ_B /atom		/ μ_B /atom		
	$m_{L,z}$	$m_{S,z}$	m_L	m_S	m_J
Fe_7^+	0.13 ± 0.02	2.4 ± 0.35	0.16 ± 0.02	3.0 ± 0.45	3.2 ± 0.50
Fe_8^+	0.22 ± 0.03	2.6 ± 0.40	0.26 ± 0.04	3.1 ± 0.50	3.4 ± 0.50
Fe_9^+	0.22 ± 0.03	3.0 ± 0.45	0.25 ± 0.04	3.5 ± 0.50	3.7 ± 0.55
Fe_{10}^+	0.13 ± 0.02	2.5 ± 0.40	0.15 ± 0.02	2.9 ± 0.40	3.0 ± 0.45
Fe_{11}^+	0.16 ± 0.025	2.4 ± 0.35	0.18 ± 0.03	2.7 ± 0.40	2.9 ± 0.40
Fe_{12}^+	0.30 ± 0.045	2.4 ± 0.35	0.34 ± 0.05	2.7 ± 0.40	3.0 ± 0.45
Fe_{13}^+	0.28 ± 0.04	1.9 ± 0.30	0.32 ± 0.05	2.1 ± 0.30	2.5 ± 0.35
Fe_{14}^+	0.41 ± 0.06	2.6 ± 0.40	0.45 ± 0.07	2.8 ± 0.40	3.3 ± 0.50
Fe_{15}^+	0.14 ± 0.02	2.4 ± 0.35	0.16 ± 0.02	2.7 ± 0.40	2.8 ± 0.40
Fe_{16}^+	0.23 ± 0.035	2.1 ± 0.30	0.26 ± 0.04	2.3 ± 0.35	2.6 ± 0.40
Fe_{18}^+	0.11 ± 0.02	3.0 ± 0.40	0.12 ± 0.02	3.2 ± 0.50	3.3 ± 0.50

5.3.2 Comparison of experimental data with:

5.3.2.1 Theoretical data

Numerous theoretical studies have been published on the spin magnetic moment of small neutral iron clusters Fe_n ^[18-21,33-40]. The majority of the theoretical works is based on DFT methods. Only Andriotis *et al.*^[18] and Guevara *et al.*^[19] use a tight binding approach. The general agreement between the theoretical data and the spin magnetic moments of Fe_n^+ clusters of the present work is quite good (Fig. 5.7a). Larger deviations appear for Fe_{13}^+ which shows an exceptionally low spin magnetic moment. This low spin magnetic moment is not reproduced by all theoretical works. However, one has to keep in mind the different charge state of the clusters. The theoretical spin magnetic moments

for clusters with more than ten atoms per clusters tend to be higher than the experimentally determined moments.

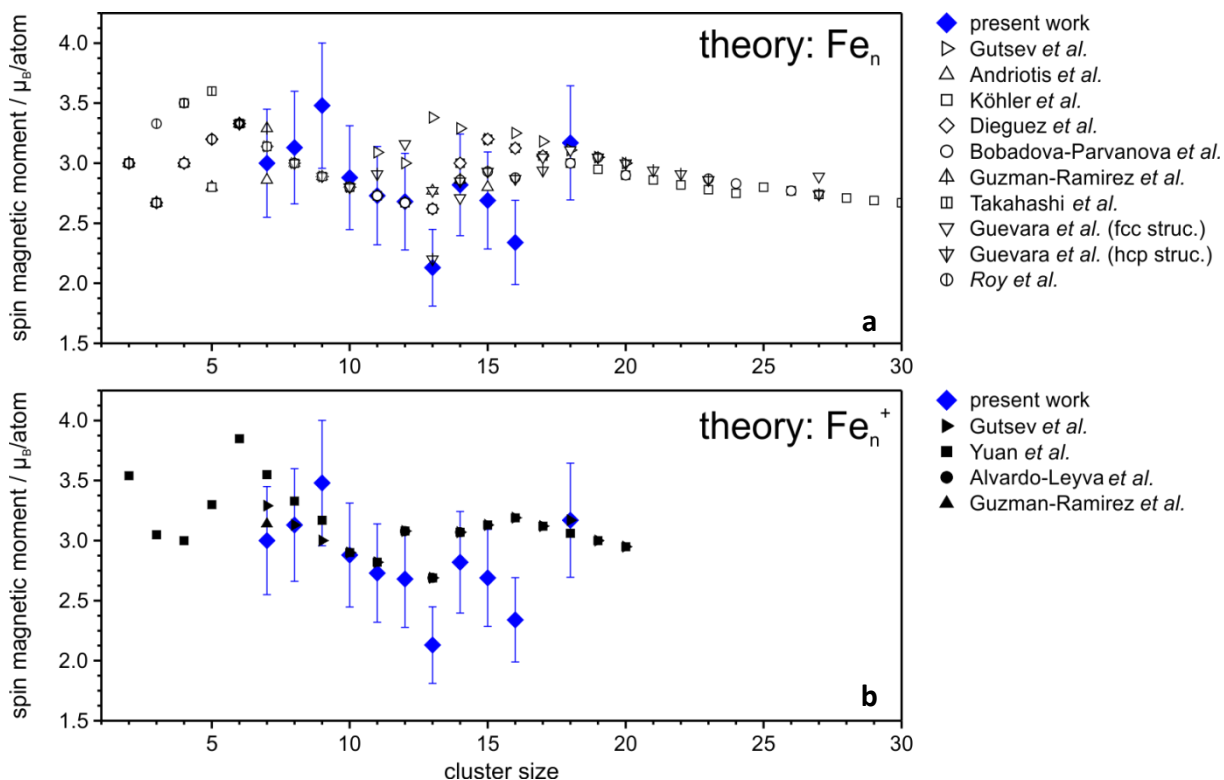


Figure 5.7 Comparison between the spin magnetic moments of cationic Fe_n^+ clusters (filled blue diamonds) of the present work with theoretical data of (a) neutral iron clusters Fe_n ^[18,19,21,34-39] and (b) cationic clusters Fe_n^+ ^[21,36,40,41]. The general agreement between theory and experiment for neutral as well as for cationic iron clusters is good. Deviations occur for individual cluster sizes, e.g. Fe_{13}^+ and Fe_{16}^+ . Theoretical data on iron clusters with fewer atoms per cluster than we studied are included for the sake of completeness. (The spin magnetic moment of the lowest energy isomer was taken from the references in case of several structural isomers for one cluster size, if not indicated otherwise; theoretical values taken from Ref. [40]: Fig. 6, data series denoted GGA+SOC+ U_{eff} ($U = 3$; $J = 0.5$)).

The recently published XMCD results of Fe_n^+ clusters by Lau *et al.*^[9] triggered several theoretical works on singly positively charged iron clusters Fe_n^+ ^[20,21,36,40-42] (Fig. 5.7b). The works of Wu *et al.*^[42] and Alvarado-Leyva *et al.*^[41] focus on the low spin magnetic moment of Fe_{13}^+ . Both groups assume an icosahedral structure with one central iron atom located within the icosahedron. Alvarado-Leyva *et al.*^[41] follow the initial interpretation of Lau *et al.*^[9] of an antiferromagnetic alignment of the central iron atom to the outer twelve iron atoms. Wu *et al.*^[42], on the other hand, found a ferromagnetic alignment of all iron atoms. A promotion electrons into the minority 3d shell reduces the spin magnetic moment of the central iron atom. This in turn reduces the average magnetic moment per iron in Fe_{13}^+ . Although, the presumed origin of the low magnetic moment differs, both

groups still find the same value for the average spin magnetic moment per atom of $2.69 \mu_B/\text{atom}$. This m_s value is still higher than the spin magnetic moment determined by us of $2.1 \mu_B/\text{atom}$ (Fig. 5.7b). The calculated spin magnetic moments of Yuan *et al.*^[40] for Fe_n^+ ($2 \leq n \leq 20$) show a reasonable agreement between theory and experiment. Yuan *et al.* tested several theoretical approaches for the calculation of the spin and orbital magnetic moments. Thus, the one showing the best agreement with the experimental results is shown in Fig. 5.7 and Fig. 5.8. The largest deviations occur for Fe_{13}^+ and Fe_{16}^+ . Guzman-Ramirez *et al.*^[21] found a pentagonal bipyramidal structure with a spin magnetic moment of $3 \mu_B/\text{atom}$ for Fe_7^+ which agrees well with the present experiment.

The study published by Yuan *et al.*^[40] on Fe_n^+ ($2 \leq n \leq 20$) clusters includes besides the spin magnetic moments also the orbital magnetic moments. The agreement between the present experimental results and the moments found by Yuan *et al.*^[40] is reasonably well for clusters $\text{Fe}_n^+ \leq \text{Fe}_{11}^+$ (Fig. 5.8). The experimental orbital magnetic moments for $\text{Fe}_{12}^+ - \text{Fe}_{14}^+$ far exceed the calculated ones. The agreement is better for Fe_{15}^+ and Fe_{18}^+ .

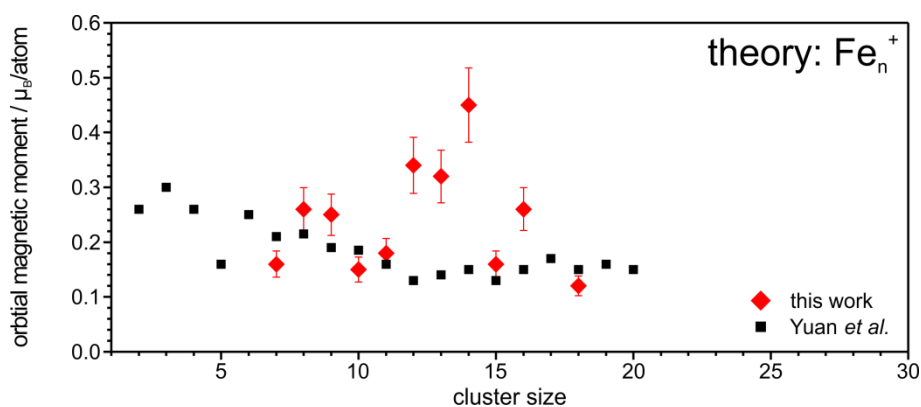


Figure 5.8 Comparison between orbital magnetic moments for Fe_n^+ (filled red diamonds) of the present work and theoretical orbital magnetic moments of cationic Fe_n^+ (filled squares) clusters. The theoretically determined orbital magnetic moments by Yuan *et al.*^[40] do agree reasonably well for the $\text{Fe}_7^+ - \text{Fe}_{11}^+$, Fe_{15}^+ and Fe_{18}^+ with the present experiment. (Theoretical values taken from Ref. [40]: Fig. 7, data series denoted GGA+SOC+ U_{eff} ($U = 3$; $J = 0.5$))

5.3.2.2 XMCD Experiments

If we compare our found spin and orbital magnetic moments to those published by Lau *et al.*^[7-9], the agreement is good (Fig. 5.9a). However, the spin magnetic moments of the present work are lower for iron clusters Fe_n^+ with $n > 10$. We have only for Fe_9^+ found a higher spin magnetic moment than Lau *et al.* The agreement of the orbital magnetic moments is within the uncertainties of both experiments. The agreement of the m_l / m_s ratio is worse than for cobalt and nickel (Fig. 4.6b and Fig. 5.5b). This might be due to the generally lower spin magnetic moment found by us. Fe_9^+ shows

the least agreement between both experiments. Neither spin nor orbital magnetic moments agree which each other for this cluster size. Especially both trends are reversed for Fe_9^+ , i.e. we have found a higher spin and a lower orbital magnetic moment than Lau *et al.* which leads to a large deviation of the m_L / m_S ratio. However, both data series show the minimum in the spin magnetic moment for Fe_{13}^+ .

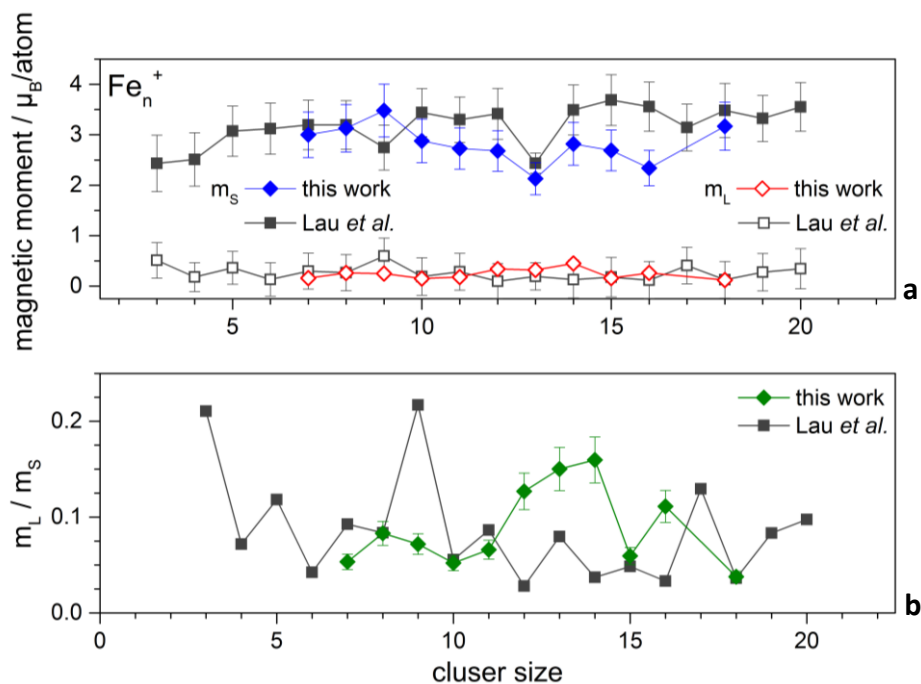


Figure 5.9 Comparison between experimental values for iron clusters Fe_n^+ from the present work and from Lau *et al.*^[7-9] for the (a) spin (this work, filled blue diamonds; Lau *et al.*, filled grey squares) and orbital (this work, open red diamonds; Lau *et al.*, open grey squares) magnetic moments and (b) ratio of orbital to spin magnetic moment m_L / m_S (this work filled, green diamonds; Lau *et al.*, filled grey squares). The spin and orbital magnetic moments of both experiments agree well with each other, i.e. mostly within the error range of both experiments. The spin magnetic moments of the present work are lower than the ones found by Lau *et al.* for clusters with more ten atoms per cluster. The ratio of m_L / m_S shows a worse agreement than for nickel and cobalt (Fig. 4.6a and Fig. 5.4a).

5.3.2.3 Stern-Gerlach experiments

A detailed comparison of the total magnetic moments of the present work to the total magnetic moments from Stern-Gerlach experiments will be given in the paper draft in the supplement of this chapter (see Chap. 5.5).

5.4 References

- [1] BLÜGEL, S., *Lecture Notes Magnetism goes Nano: Electron Correlations, Spin Transport, Molecular Magnetism*, Reduced Dimensions I - Magnetic Moment and Magnetic Structure Forschungszentrum Jülich in der Helmholtz-Gemeinschaft, **2005**
- [2] STÖHR, J., SIEGMANN, H. C., *Magnetism - From Fundamentals to Nanoscale Dynamics*; Springer, **2006**
- [3] DANIEL, E. D., MEE, C. D., *Magnetic recording: The first 100 Years*; IEEE Press: New York, **1998**
- [4] GETZLAFF, M., *Surface Magnetism*; Springer, **2010**
- [5] PEREDKOV, S., NEEB, M., EBERHARDT, W., MEYER, J., TOMBERS, M., KAMPSCHULTE, H., NIEDNER-SCHATTEBURG, G., *Spin and Orbital Magnetic Moments of Free Nanoparticles*, Physical Review Letters **2011**, *107*, 233401
- [6] PEREDKOV, S., SAVCI, A., PETERS, S., NEEB, M., EBERHARDT, W., KAMPSCHULTE, H., MEYER, J., TOMBERS, M., HOFFERBERTH, B., MENGES, F., NIEDNER-SCHATTEBURG, G., *X-ray absorption spectroscopy of mass-selected transition metal clusters using a cyclotron ion trap: An experimental setup for measuring XMCD spectra of free clusters*, Journal of Electron Spectroscopy and Related Phenomena **2011**, *184*, 113
- [7] LANGENBERG, A., *Magnetische Momente freier, massenselektierter Eisen-, Cobalt- und Nickelcluster*, **Doctoral Thesis**, 2013, Technische Universität Berlin
- [8] LANGENBERG, A., HIRSCH, K., LAWICKI, A., ZAMUDIO-BAYER, V., NIEMEYER, M., CHMIELA, P., LANGBEHN, B., TERASAKI, A., ISSENDORFF, B. V., LAU, J. T., *Spin and orbital magnetic moments of size-selected iron, cobalt, and nickel clusters and their link to the bulk phase diagrams*, arXiv.org, e-Print Arch., Phys. **2014**, 1
- [9] NIEMEYER, M., HIRSCH, K., ZAMUDIO-BAYER, V., LANGENBERG, A., VOGEL, M., KOSSICK, M., EBRECHT, C., EGASHIRA, K., TERASAKI, A., MÖLLER, T., v. ISSENDORFF, B., LAU, J. T., *Spin Coupling and Orbital Angular Momentum Quenching in Free Iron Clusters*, Physical Review Letters **2012**, *108*, 057201
- [10] SRIVASTAVA, P., HAACK, N., WENDE, H., CHAUVISTRÉ, R., BABERSCHKE, K., *Modifications of the electronic structure of Ni/Cu(001) as a function of the film thickness*, Physical Review B **1997**, *56*, R4398
- [11] SRIVASTAVA, P., WILHELM, F., NEY, A., FARLE, M., WENDE, H., HAACK, N., CEBALLOS, G., BABERSCHKE, K., *Magnetic moments and Curie temperatures of Ni and Co thin films and coupled trilayers*, Physical Review B **1998**, *58*, 5701
- [12] KHANNA, S. N., LINDEROTH, S., *magnetic behavior of clusters of ferromagnetic transition metals*, Physical Review Letters **1991**, *67*, 742
- [13] BUCHER, J. P., DOUGLASS, D. C., BLOOMFIELD, L. A., *Magnetic properties of free cobalt clusters*, Physical Review Letters **1991**, *66*, 3052
- [14] REDDY, B. V., NAYAK, S. K., KHANNA, S. N., RAO, B. K., JENA, P., *Physics of nickel clusters. 2. Electronic structure and magnetic properties*, Journal of Physical Chemistry A **1998**, *102*, 1748
- [15] CHEN, C. T., SMITH, N. V., SETTE, F., *Exchange, spin-orbit, and correlation effects in the soft-x-ray magnetic-circular-dichroism spectrum of nickel*, Physical Review B **1991**, *43*, 6785
- [16] VOGEL, J., SACCHI, M., *Polarization and angular dependence of the $L_{2,3}$ absorption edges in Ni(110)*, Physical Review B **1994**, *49*, 3230
- [17] AGUILERA-GRANJA, F., BOUARAB, S., LÓPEZ, M. J., VEGA, A., MONTEJANO-CARRIZALES, J. M., IÑIGUEZ, M. P., ALONSO, J. A., *Magnetic moments of Ni clusters*, Physical Review B **1998**, *57*, 12469

- [18] ANDRIOTIS, A. N., MENON, M., *Tight-binding molecular-dynamics study of ferromagnetic clusters*, Physical Review B **1998**, 57, 10069
- [19] GUEVARA, J., PARISI, F., LLOIS, A. M., WEISSMANN, M., *Electronic properties of transition-metal clusters: Consideration of the spillover in a bulk parametrization*, Physical Review B **1997**, 55, 13283
- [20] GUTSEV, G. L., WEATHERFORD, C. W., BELAY, K. G., RAMACHANDRAN, B. R., JENA, P., *An all-electron density functional theory study of the structure and properties of the neutral and singly charged M_{12} and M_{13} clusters: $M = \text{Sc} - \text{Zn}$* , The Journal of Chemical Physics **2013**, 138, 164303
- [21] GUZMÁN-RAMÍREZ, G., SALVADOR, P., ROBLES, J., VEGA, A., AGUILERA-GRANJA, F., *Density functional study of ternary $\text{Fe}_x \text{Co}_y \text{Ni}_z$ ($x + y + z = 7$) clusters*, Theoretical Chemistry Accounts **2012**, 132, 1
- [22] LU, Q. L., LUO, Q. Q., CHEN, L. L., WAN, J. G., *Structural and magnetic properties of Ni_n ($n = 2-21$) clusters*, The European Physical Journal D **2011**, 61, 389
- [23] REUSE, F. A., KHANNA, S. N., *Geometry, electronic structure, and magnetism of small Ni_n ($n = 2 - 6, 8, 13$) clusters*, Chemical Physics Letters **1995**, 234, 77
- [24] REUSE, F. A., KHANNA, S. N., BERNEL, S., *Electronic structure and magnetic behavior of Ni_{13} clusters*, Physical Review B **1995**, 52, R11650
- [25] SONG, W., LU, W.-C., WANG, C. Z., HO, K. M., *Magnetic and electronic properties of the nickel clusters Ni_n ($n < 30$)*, Computational and Theoretical Chemistry **2011**, 978, 41
- [26] GUIRADO-LOPEZ, R. A., DORANTES-DAVILA, J., PASTOR, G. M., *Orbital magnetism in transition-metal clusters: From Hund's rules to bulk quenching*, Physical Review Letters **2003**, 90, 226402
- [27] CASTRO, M., JAMORSKI, C., SALAHUB, D. R., *Structure, bonding, and magnetism of small Fe_n , Co_n , and Ni_n clusters, $n \leq 5$* , Chemical Physics Letters **1997**, 271, 133
- [28] HIRSCH, K., ZAMUDIO-BAYER, V., AMESSEDER, F., LANGENBERG, A., RITTMANN, J., VOGEL, M., MOLLER, T., VON ISSENDORFF, B., LAU, J. T., *2p x-ray absorption of free transition-metal cations across the 3d transition elements: Calcium through copper*, Physical Review A **2012**, 85
- [29] LAU, J. T., RITTMANN, J., ZAMUDIO-BAYER, V., VOGEL, M., HIRSCH, K., KLAR, P., LOFINK, F., MOELLER, T., VON ISSENDORFF, B., *Size Dependence of $L_{2,3}$ Branching Ratio and 2p Core-Hole Screening in X-Ray Absorption of Metal Clusters*, Physical Review Letters **2008**, 101
- [30] SIPR, O., EBERT, H., *Theoretical $\text{Fe } L_{2,3}$ - and K-edge x-ray magnetic circular dichroism spectra of free iron clusters*, Physical Review B **2005**, 72
- [31] STÖHR, J., KÖNIG, H., *Determination of Spin- and Orbital-Moment Anisotropies in Transition Metals by Angle-Dependent X-Ray Magnetic Circular Dichroism*, Physical Review Letters **1995**, 75, 3748
- [32] CHEN, C. T., IDZERDA, Y. U., LIN, H. J., SMITH, N. V., MEIGS, G., CHABAN, E., HO, G. H., PELLEGRIN, E., SETTE, F., *Experimental Confirmation of the X-Ray Magnetic Circular Dichroism Sum Rules for Iron and Cobalt*, Physical Review Letters **1995**, 75, 152
- [33] BOBADOVA-PARVANOV, P., JACKSON, K. A., SRINIVAS, S., HOROI, M., *Density-functional investigations of the spin ordering in Fe_{13} clusters*, Physical Review B **2002**, 66
- [34] BOBADOVA-PARVANOV, P., JACKSON, K. A., SRINIVAS, S., HOROI, M., KOHLER, C., SEIFERT, G., *Scanning the potential energy surface of iron clusters: A novel search strategy*, Journal of Chemical Physics **2002**, 116, 3576
- [35] DIÉGUEZ, O., ALEMANY, M. M. G., REY, C., ORDEJÓN, P., GALLEGO, L. J., *Density-functional calculations of the structures, binding energies, and magnetic moments of Fe clusters with 2 to 17 atoms*, Physical Review B **2001**, 63, 205407

- [36] GUTSEV, G. L., WEATHERFORD, C. A., JENA, P., JOHNSON, E., RAMACHANDRAN, B. R., *Structure and Properties of Fe_n , Fe_n^- , and Fe_n^+ Clusters, $n = 7 - 20$* , The Journal of Physical Chemistry A **2012**, *116*, 10218
- [37] KÖHLER, C., SEIFERT, G., FRAUENHEIM, T., *Density functional based calculations for Fe_n ($n < 32$)*, Chemical Physics **2005**, *309*, 23
- [38] ROY, D. R., ROBLES, R., KHANNA, S. N., *Magnetic moment and local moment alignment in anionic and/or oxidized Fe_n clusters*, The Journal of Chemical Physics **2010**, *132*, 194305
- [39] TAKAHASHI, K., ISOBE, S., OHNUKI, S., *Chemisorption of hydrogen on Fe clusters through hybrid bonding mechanisms*, Applied Physics Letters **2013**, *102*
- [40] YUAN, H. K., CHEN, H., KUANG, A. L., TIAN, C. L., WANG, J. Z., *The spin and orbital moment of Fe_n ($n = 2 - 20$) clusters*, The Journal of Chemical Physics **2013**, *139*
- [41] ALVARADO-LEYVA, P. G., AGUILERA-GRANJA, F., BALBAS, L. C., VEGA, A., *Antiferromagnetic-like coupling in the cationic iron cluster of thirteen atoms*, Physical Chemistry Chemical Physics **2013**, *15*, 14458
- [42] WU, M., KANDALAM, A. K., GUTSEV, G. L., JENA, P., *Origin of the anomalous magnetic behavior of the Fe_{13}^+ cluster*, Physical Review B **2012**, *86*, 174410
- [43] JUN, Y.-W., SEO, J.-W., CHEON, A., *Nanoscaling laws of magnetic nanoparticles and their applicabilities in biomedical sciences*, Accounts of Chemical Research **2008**, *41*, 179
- [44] *Clusters of Atoms and Molecules*; HABERLAND, H., Ed.; Springer, **1994**
- [45] *Metal clusters at surfaces*; MEIWES-BROER, K. H., Ed.; Springer, **2000**
- [46] GLASER, L., CHEN, K., FIEDLER, S., WELLMÖFER, M., WURTH, W., MARTINS, M., *Magnetic properties of small size-selected Co and CoPt clusters on Ni*, Physical Review B **2012**, *86*, 075435
- [47] WURTH, W., MARTINS, M., *Electronic structure and magnetic properties of small deposited transition metal clusters*, Chem. Phys. Solid Surf. **2007**, *12*, 471
- [48] ANTONSSON, E., BRESCH, H., LEWINSKI, R., WASSERMANN, B., LEISNER, T., GRAF, C., LANGER, B., RÜHL, E., *Free nanoparticles studied by soft X-rays*, Chemical Physics Letters **2013**, *559*, 1
- [49] BILLAS, I. M. L., CHÂTELAIN, A., DE HEER, W. A., *Magnetism from the Atom to the Bulk in Iron, Cobalt, and Nickel Clusters*, Science **1994**, *265*, 1682
- [50] WU, Y. Z., SINKOVIC, B., WON, C., ZHU, J., ZHAO, Y., QIU, Z. Q., *Experimental study of the x-ray linear dichroism of NiO films grown on Fe(001)*, Physical Review B **2012**, *85*, 134436
- [51] KNICKELBEIN, M. B., *Nickel clusters: The influence of adsorbates on magnetic moments*, The Journal of Chemical Physics **2002**, *116*, 9703
- [52] KNICKELBEIN, M. B., *Nickel clusters: The influence of adsorbed CO on magnetic moments*, The Journal of Chemical Physics **2001**, *115*, 1983
- [53] APSEL, S. E., EMMERT, J. W., DENG, J., BLOOMFIELD, L. A., *Surface-enhanced magnetism in nickel clusters*, Physical Review Letters **1996**, *76*, 1441
- [54] STÖHR, J., *X-ray magnetic circular dichroism spectroscopy of transition metal thin films*, Journal of Electron Spectroscopy and Related Phenomena **1995**, *75*, 253
- [55] SCHÜTZ, G., WAGNER, W., WILHELM, W., KIENLE, P., ZELLER, R., FRAHM, R., MATERLIK, G., *Absorption of circularly polarized x rays in iron*, Physical Review Letters **1987**, *58*, 737
- [56] GAMBARDILLA, P., RUSPONI, S., VERONESE, M., DHESI, S. S., GRAZIOLI, C., DALLMEYER, A., CABRIA, I., ZELLER, R., DEDERICHS, P. H., KERN, K., CARBONE, C., BRUNE, H., *Giant Magnetic Anisotropy of Single Cobalt Atoms and Nanoparticles*, Science **2003**, *300*, 1130
- [57] DHESI, S. S., DÜRR, H. A., VAN DER LAAN, G., DUDZIK, E., BROOKES, N. B., *Electronic and magnetic structure of thin Ni films on Co/Cu(001)*, Physical Review B **1999**, *60*, 12852

- [58] GAMBARELLA, P., DALLMEYER, A., MAITI, K., MALAGOLI, M. C., EBERHARDT, W., KERN, K., CARBONE, C., *Ferromagnetism in one-dimensional monatomic metal chains*, *Nature* **2002**, *416*, 301
- [59] BANSMANN, J., KLEIBERT, A., GETZLAFF, M., RODRIGUEZ, A. F., NOLTING, F., BOEGLIN, C., MEIWES-BROER, K.-H., *Magnetism of 3d transition metal nanoparticles on surfaces probed with synchrotron radiation - from ensembles towards individual objects*, *Physica Status Solidi B-Basic Solid State Physics* **2010**, *247*, 1152
- [60] LAU, J. T., FÖHLISCH, A., NIETUBYČ, R., REIF, M., WURTH, W., *Size-Dependent Magnetism of Deposited Small Iron Clusters Studied by X-Ray Magnetic Circular Dichroism*, *Physical Review Letters* **2002**, *89*, 057201
- [61] LAU, J. T., FÖHLISCH, A., MARTINS, M., NIETUBYČ, R., REIF, M., WURTH, W., *Spin and orbital magnetic moments of deposited small iron clusters studied by x-ray magnetic circular dichroism spectroscopy*, *New Journal of Physics* **2002**, *4*, 98
- [62] CHEN, K., FIEDLER, S., BAEV, I., BEECK, T., WURTH, W., MARTINS, M., *Hybridization and magnetism in small FePt alloy clusters*, *New Journal of Physics* **2012**, *14*, 123005
- [63] BRUNE, H., GAMBARELLA, P., *Magnetism of individual atoms adsorbed on surfaces*, *Surface Science* **2009**, *603*, 1812
- [64] EELBO, T., WAŚNIEWSKA, M., THAKUR, P., GYAMFI, M., SACHS, B., WEHLING, T. O., FORTI, S., STARKE, U., TIEG, C., LICHTENSTEIN, A. I., WIESENDANGER, R., *Adatoms and Clusters of 3d Transition Metals on Graphene: Electronic and Magnetic Configurations*, *Physical Review Letters* **2013**, *110*, 136804
- [65] SCOTT, G. G., STURNER, H. W., *Magnetomechanical Ratios for Fe-Co Alloys*, *Physical Review* **1969**, *184*, 490
- [66] SCOTT, G. G., *Investigation of the Einstein-de Haas Effect for Cobalt and for the Co-Ni Alloys*, *Physical Review* **1966**, *148*, 525
- [67] SCOTT, G. G., RECK, R. A., *Magnetomechanical ratios and spin and orbital moments for nickel-copper alloys*, *Phys. Rev. B* **1973**, *8*, 233
- [68] NAVE, G., JOHANSSON, S., LEARNER, R. C. M., THORNE, A. P. BRAULT, J. W., *A New Multiplet Table for Fe I*, *Astrophysical Journal Supplement Series* **1994**, *94*, 221
- [69] NIST ASD TEAM. NIST Atomic Spectra Database (ver. 5.1) online <http://physics.nist.gov/asd>. In *National Institute of Standards and Technology, Gaithersburg, MD*, 2013
- [70] NAVE, G., JOHANSSON, S., *The Spectrum of Fe II*, *Astrophysical Journal Supplement Series* **2013**, *204*, 1
- [71] SUGAR, J., CORLISS, C., *Atomic Energy Levels of the Iron Period Elements: Potassium through Nickel*, *Journal of Physical and Chemistry Reference Data* **1985**, *14*, 1
- [72] PICKERING, J. C., RAASSEN, A. J. J., UYLINGS, P. H. M., JOHANSSON, S., *The Spectrum and Term Analysis of Co II*, *Astrophysical Journal Supplement Series* **1998**, *117*, 216
- [73] ULF, L., JAMES, W. B., ANNE, P. T., *Spectrum and term system of neutral nickel, Ni I*, *Physica Scripta* **1993**, *47*, 628
- [74] BERG, C., SCHINDLER, T., NIEDNER-SCHATTEBURG, G., BONDYBEY, V. E., *Reactions of simple hydrocarbons with Nb_n^+ : Chemisorption and physisorption on ionized niobium clusters*, *The Journal of Chemical Physics* **1995**, *102*, 4870
- [75] MARUYAMA, S., ANDERSON, L. R., SMALLEY, R. E., *Direct injection supersonic cluster beam source for FT-ICR studies of clusters*, *Review of Scientific Instruments* **1990**, *61*, 3686
- [76] PROCH, D., TRICKL, T., *A high-intensity multi-purpose piezoelectric pulsed molecular beam source*, *Review of Scientific Instruments* **1989**, *60*, 713

- [77] CARRA, P., THOLE, B. T., ALTARELLI, M., WANG, X., *X-ray circular dichroism and local magnetic fields*, Physical Review Letters **1993**, 70, 694
- [78] THOLE, B. T., CARRA, P., SETTE, F., VANDERLAAN, G., *X-ray circular dichroism as a probe of orbital magnetization*, Physical Review Letters **1992**, 68, 1943
- [79] WU, R., FREEMAN, A. J., *Limitation of the Magnetic-Circular-Dichroism Spin Sum Rule for Transition Metals and Importance of the Magnetic Dipole Term*, Physical Review Letters **1994**, 73, 1994
- [80] SIPR, O., MINAR, J., EBERT, H., *On the importance of the magnetic dipole term T_z in analyzing X-ray magnetic circular dichroism spectra of clusters*, Europhysics Letters **2009**, 87
- [81] ASHCROFT, N. W., MERMIN, N. D., *Festkörperphysik*, 4th ed.; Oldenbourg Verlag München, **2013**
- [82] ELMORE, W. C., *The Magnetization of Ferromagnetic Colloids*, Physical Review **1938**, 54, 1092
- [83] BRUNE, H., GAMBARELLA, P. "Atomic and molecular magnets on surfaces", 2014
- [84] VAZ, C. A. F., BLAND, J. A. C., LAUHOFF, G., *Magnetism in ultrathin film structures*, Reports on Progress in Physics **2008**, 71, 056501
- [85] XU, X., YIN, S., MORO, R., LIANG, A., BOWLAN, J., DE HEER, W. A., *Metastability of Free Cobalt and Iron Clusters: A Possible Precursor to Bulk Ferromagnetism*, Physical Review Letters **2011**, 107, 057203
- [86] PAYNE, F. W., JIANG, W., EMMERT, J. W., DENG, J., BLOOMFIELD, L. A., *Magnetic structure of free cobalt clusters studied with Stern-Gerlach deflection experiments*, Physical Review B **2007**, 75, 094431
- [87] KNICKELBEIN, M. B., *Magnetic moments of bare and benzene-capped cobalt clusters*, The Journal of Chemical Physics **2006**, 125, 044308
- [88] XU, X. S., YIN, S. Y., MORO, R., DE HEER, W. A., *Magnetic moments and adiabatic magnetization of free cobalt clusters*, Physical Review Letters **2005**, 95, 237209
- [89] MARTÍNEZ, G., TANGARIFE, E., PÉREZ, M., MEJÍA-LÓPEZ, J., *Magnetic properties of small cobalt-copper clusters*, Journal of Physics: Condensed Matter **2013**, 25, 216003
- [90] PÉREZ, M., MUÑOZ, F., MEJÍA-LÓPEZ, J., MARTÍNEZ, G., *Physical and chemical properties of $Co_{n-m}Cu_m$ nanoclusters with $n = 2 - 6$ atoms via ab-initio calculations*, Journal of Nanoparticle Research **2012**, 14, 1
- [91] KNICKELBEIN, M. B., *Adsorbate-induced enhancement of the magnetic moments of iron clusters*, Chemical Physics Letters **2002**, 353, 221
- [92] ANDRIOTIS, A. N., MENON, M., *Orbital Magnetism: Pros and Cons for Enhancing the Cluster Magnetism*, Physical Review Letters **2004**, 93, 026402
- [93] RIPS, I., JORTNER, J., *Ion solvation in clusters*, The Journal of Chemical Physics **1992**, 97, 536
- [94] HABERLAND, H., KLEINERMANN, K., TRÄGER, F., **Bergmann-Schäfer**, *Lehrbuch der Experimentalphysik Band 5 - Gase, Nanosysteme, Flüssigkeiten*, Cluster, 2nd Ed.; Walter de Gruyter, **2006**; pp 819
- [95] KOHN, A., WEIGEND, F., AHLRICH, R., *Theoretical study on clusters of magnesium*, Physical Chemistry Chemical Physics **2001**, 3, 711
- [96] BACHELS, T., SCHÄFER, R., *Binding energies of neutral silicon clusters*, Chemical Physics Letters **2000**, 324, 365
- [97] BALETTO, F., FERRANDO, R., *Structural properties of nanoclusters: Energetic, thermodynamic, and kinetic effects*, Reviews of Modern Physics **2005**, 77, 371
- [98] WRIGGE, G., HOFFMANN, M. A., ISSENDORFF, B. V., *Photoelectron spectroscopy of sodium clusters: Direct observation of the electronic shell structure*, Physical Review A **2002**, 65, 063201

- [99] KNICKELBEIN, M. B., YANG, S., *Photoionization studies of niobium clusters: Ionization potentials for Nb₂ - Nb₇₆*, The Journal of Chemical Physics **1990**, *93*, 5760
- [100] WRIGGE, G., ASTRUC HOFFMANN, M., ISSENDORFF, B., HABERLAND, H., *Ultraviolet photoelectron spectroscopy of Nb₄⁻ to Nb₂₀₀⁻*, The European Physical Journal D - Atomic, Molecular, Optical and Plasma Physics **2003**, *24*, 23
- [101] DE HEER, W. A., *The physics of simple metal clusters: experimental aspects and simple models*, Reviews of Modern Physics **1993**, *65*, 611
- [102] ALVAREZ, M. M., KHOURY, J. T., SCHAAFF, T. G., SHAFIGULLIN, M. N., VEZMAR, I., WHETTEN, R. L., *Optical Absorption Spectra of Nanocrystal Gold Molecules*, The Journal of Physical Chemistry B **1997**, *101*, 3706
- [103] DE HEER, W. A. Confinement and size effects in free metal clusters. In *Metal clusters at surfaces*; Meiwes-Broer, K.-H., Ed.; Springer, 2000
- [104] BRECHIGNAC, C., BROYER, M., CAHUZAC, P., DELACRETAZ, G., LABASTIE, P., WÖSTE, L., *Size dependence of inner-shell autoionization lines in mercury clusters*, Chemical Physics Letters **1985**, *120*, 559
- [105] BRÉCHIGNAC, C., BROYER, M., CAHUZAC, P., DELACRETAZ, G., LABASTIE, P., WOLF, J. P., WÖSTE, L., *Probing the Transition from van der Waals to Metallic Mercury Clusters*, Physical Review Letters **1988**, *60*, 275
- [106] PASTOR, G. M., BENNEMANN, K. H. Transition from van der Waals to Metallic Bonding in Clusters. In *Clusters of Atoms and Molecules*; Haberland, H., Ed.; Springer, 1994; Vol. 52
- [107] HARRISON, M. R., EDWARDS, P. P. Electrons in small particles. In *The metallic and non-metallic states of matter*; Edwards, P. P., Rao, C. N. R., Eds.; Francis & Taylor London, 1985
- [108] GETZLAFF, M., *Fundamentals of Magnetism*; Springer, **2008**
- [109] STÖHR, J., *Exploring the microscopic origin of magnetic anisotropies with X-ray magnetic circular dichroism (XMCD) spectroscopy*, Journal of Magnetism and Magnetic Materials **1999**, *200*, 470
- [110] TISCHER, M., HJORTSTAM, O., ARVANITIS, D., HUNTER DUNN, J., MAY, F., BABERSCHKE, K., TRYGG, J., WILLS, J. M., JOHANSSON, B., ERIKSSON, O., *Enhancement of Orbital Magnetism at Surfaces: Co on Cu(100)*, Physical Review Letters **1995**, *75*, 1602
- [111] EINSTEIN, A., DE HAAS, W. J., *Experimenteller Nachweis der Ampereschens Molekularströme*, Verhandlungen Deutsch Physikalische Gesellschaft **1915**, *17*, 152
- [112] KITTEL, C., *On the Gyromagnetic Ratio and Spectroscopic Splitting Factor of Ferromagnetic Substances*, Physical Review **1949**, *76*, 743
- [113] WALLIS, T. M., MORELAND, J., KABOS, P., *Einstein-de Haas effect in a NiFe film deposited on a microcantilever*, Applied Physics Letters **2006**, *89*

5.5 Supplement - Draft - J. Chemical Physics, 2014, in preparation

The following manuscript is intended for publication in the "Journal of Chemical Physics". Our results on the spin and orbital magnetic moments of small clusters of the ferromagnetic 3d metals iron, cobalt and nickel are presented. The manuscript was drafted by me with feedback from Prof. Niedner-Schatteburg and Matthias Tombers. Experiments were carried out by a team as detailed in the introduction to this chapter. All experiments were done in collaboration with the group of

W. Eberhardt (TU Berlin / HZB). The experiments on iron clusters were additionally done in collaboration with the group of W. Wurth (University of Hamburg)

The spin and orbital contributions to the total magnetic moments of free Fe, Co and Ni clusters

Jennifer Meyer, Matthias Tombers, Gereon Niedner-Schatteburg

Fachbereich Chemie and Forschungszentrum OPTIMAS,

Technische Universität Kaiserslautern, 67663 Kaiserslautern, Germany

Sergey Peredkov[§], Wolfgang Eberhardt

Institut für Optik und Atomare Physik, Technische Universität Berlin, Hardenbergstrasse 36, 10623

Berlin, Germany

Matthias Neeb

Helmholtz-Zentrum für Materialien und Energie, BESSY II, Albert-Einstein-Strasse 15,

12489 Berlin, Germany

Steffen Palutke, Michael Martins, Wilfried Wurth

Institut für Experimentalphysik, Universität Hamburg, Luruper Chausee 149, 22761 Hamburg,

Germany

[§] Present address: Max-Planck-Institut fuer Chemische Energiekonversion, Stiftstr. 34-36, 45470, Mülheim an der Ruhr, Germany

5.5.0 Abstract

We present size dependent spin and orbital magnetic moments of cobalt (Co_n^+ , $8 \leq n \leq 22$), iron (Fe_n^+ , $7 \leq n \leq 17$) and nickel cluster (Ni_n^+ , $7 \leq n \leq 17$) cations. X-ray magnetic circular dichroism (XMCD) spectroscopy has been applied to isolated clusters in the gas phase. The spin and orbital magnetic moments are enhanced compared to the corresponding bulk values for all three investigated materials. However, if compared to the atomic value, both contributions are quenched in the investigated clusters. We discuss the application of scaling laws to the size dependent evolution of the spin and orbital magnetic moment per atom in the investigated size range. Both spin and orbit each follow a scaling law, however not the same one.

5.5.1 Introduction

The discussion of magnetic phenomena in homogeneous samples of bulk materials focuses on the dominating exchange coupling of pseudo spins which localize at atomic centers. The concomitant orbital angular momenta of individual electrons quench in the bulk due to orbital hybridization and symmetry reduction. Some orbital angular momenta remain exempt. This gave rise to the adjustable bulk g-factors, and of e.g. 4 - 10 % (Tab. 1) corrections to the spin only g-factor (2.0) in the case of ferromagnetic 3d bulk metals. In the free atoms or ions of those metals, however, the spin and orbital momenta possess values of equal magnitude, e.g. the orbital momentum of a free nickel atom even exceeds its spin momentum. A change in system size obviously induces a change in the electronic structure and along in the magnetic properties.

The evolution of magnetism with sample size and its application has been at the scientific focus for some time^[43,44]. Size selected clusters became favorable objects to follow such evolution^[45-47], and suitable gas phase isolation experiments aim at the determination of intrinsic magnetic moments without the interference of either a supporting surface or of any other environment^[48]. Stern-Gerlach experiments serve to determine the total magnetic moments of isolated transition metal clusters in the gas phase, e.g. shown by de Heer *et al.*^[49] and others^[50-53]. These experiments revealed enhanced magnetic moments compared to the bulk attributed to an enhanced contribution of the orbital magnetic moment. However, Stern-Gerlach experiments conceptually lack the capability to separate the magnetic moment into its spin and orbital contributions. Moreover, the *ab initio* description of the orbital magnetic moment is still a challenge, despite the ongoing progress in the field. The problems arise from the highly correlated nature of the magnetic materials.

X-ray magnetic circular dichroism (XMCD) spectroscopy has proven instrumental to elucidate the spin and orbital contributions to total magnetic moments of bulk samples^[32,54,55]. Recently, it became feasible to conduct XMCD spectroscopy of highly diluted samples in the gas phase^[5,9]. An enhancement of the orbital moment was expected in isolated clusters because enhanced orbital moments were found in low-dimensional samples, e.g. thin films^[56,57], nano structures^[58,59], deposited clusters^[46,60-62] or adatoms^[63,64]. However, both gas phase experiments revealed that the orbital magnetic moment is considerably quenched for small clusters compared to the atomic values. The orbital magnetic moment in free clusters was found to be significantly enhanced compared to the solid. The differences between the spin magnetic moments of the clusters and the bulk or atomic values are less pronounced.

Table 1: magnetic moments of the atom, cluster and bulk for iron, cobalt and nickel in comparison with spin orbit coupling constants (SOC) for the atom / ion and g-factors for the bulk

	Magnetic moment [μ_B /atom]			Landé g-factor	g' factor [§]	g-factor	SOC* constant [cm ⁻¹]
	orbit	spin	total				
Fe ₁ ^a							
⁵ D [Ar]4s ² 3d ⁶	2	4	6	1.50			-104 ⁱ
Fe ₁ ^{+a}							
⁶ D [Ar]4s ¹ 3d ⁶	2	5	7	1.71			-86 ^j
Fe _n ^{+b}	0.24	2.82	3.07	1.85		2.18	
Fe (bcc, bulk) ^c	0.083	1.98	2.063		1.92 ^e	2.09 ^h	
Co ₁							
⁴ F [Ar]4s ² 3d ⁷	3	3	6	1.33			-181 ^k
Co ₁ ⁺							
³ F [Ar]4s ⁰ 3d ⁸	3	2	5	1.40			-238 ^l
Co _n ⁺	0.55	2.28	2.83	1.68		2.49	
Co (hcp, bulk) ^c	0.158	1.55	2.25		1.84 ^f	2.25 ^h	
Ni ₁							
³ F [Ar]4s ² 3d ⁸	3	2	5	1.25			-333 ^m
Ni ₁ ⁺							
² D [Ar]4s ⁰ 3d ⁹	2	1	3	1.33			-603 ^j
Ni _n ⁺	0.33	1.42	1.75	1.68		2.49	
Ni (fcc, bulk) ^d	0.06	0.6	0.66		1.84 ^g	2.18 ^h	

^a magnetic moments for atoms and cations calc. according to Hund's rules

^b average moments of the measured size range of Fe_n⁺, Co_n⁺ & Ni_n⁺, this work

^c magnetic moments from Ref. [32]

^d magnetic moments from Ref. [15,16]

[§] magnetomechanical ratio g': ^e Ref. [65]; ^f Ref. [66], ^g Ref. [67];

^h taken from Ref. [49]

*spin orbit coupling (SOC) constants extracted by Landé interval rule from experimental values: ⁱ Ref. [68,69]; ^j Ref. [69,70]; ^k Ref. [69,71], ^l Ref. [69,72]; ^m Ref. [69,73]

relationship between the different g-factors and g' is given in the Appendix.

A question arising when investigating cluster properties is the following: Does every atom count as in the so called "non-scalable" size regime, or will a trend be followed from the bulk to the atomic value. Various cluster properties follow a scaling law which interpolates between the bulk and the atomic value (Tab. 1). Once, the "non-scalable" size regime is reached individual "every atom counts" fluctuations are superimposed onto the general trend. Therefore, we investigated if the spin and

orbital magnetic moments follow a scaling law. We found that the general trend of the spin and orbital magnetic moments each follow a different scaling law which was not to be expected. Superimposed on this scaling law are non-scalable fluctuations. Implications of this behavior will be discussed in the final section

5.5.2 Experimental methods

The experimental set up consists of a modified Fourier Transform - Ion Cyclotron Resonance - mass spectrometer (FT-ICR; Apex IV Bruker Daltonics) which was coupled to a soft x-ray undulator beamline at the Helmholtz Zentrum Berlin / BEESY II. A detailed description of the experimental set up has been given elsewhere^[5,6]. In brief, the modifications include the possibility to cryogenically cool the ICR cell down to 20 K. Furthermore, the mass spectrometer was equipped with a laser vaporization source^[74,75]. We produce transition metal clusters by focusing a pulsed laser (Nd:YAG, 532 nm, 20 Hz) onto the target material which is ablated into a short transverse helium gas pulse to yield clusters. A homebuilt piezo electric valve provides the gas pulse^[76]. Mono isotopic target materials were used in the case of iron (Oak Ridge National Laboratory, Fe-56, 99.93%) and nickel (Oak Ridge National Laboratory, Ni-58, 99.61%) in order to avoid dilution of the signal intensity due to isotopic distribution. The cluster ion beam is transferred into the ICR cell which serves as ion trap as well as mass analyzer. A cluster size is selected, isolated and cooled down via helium buffer gas to the desired temperature ($T \leq 20$ K). The superconducting magnet ($B = 7$ T) of the FT-ICR aligns the magnetic moments of the cluster ions. X-ray absorption spectra were measured in Total Ion Yield, i.e. the trapped cluster ions are exposed to the x-ray beam and the subsequent fragmentation is measured. By recording mass spectra in dependence of photon energy the whole absorption spectrum could be measured. L edge XMCD spectra were recorded by measuring XAS for both helicities (polarization degree: 90 % @ UE52-PGM). The fragmentation intensities of appearing fragments were added up and then normalized to the photon flux of the x-ray beam and to the parent intensities. As an example the L-edge absorption spectra for both photon polarizations of Ni_7^+ are shown Fig. 1. Dichroic effects are visible at both the L_2 and the L_3 edge which are clearly resolved from each other. The spectrum was recorded at a cluster temperature of 20 K. XMCD spectra were measured for cobalt, iron and nickel cluster cations in the size range from seven to twenty atoms per cluster.

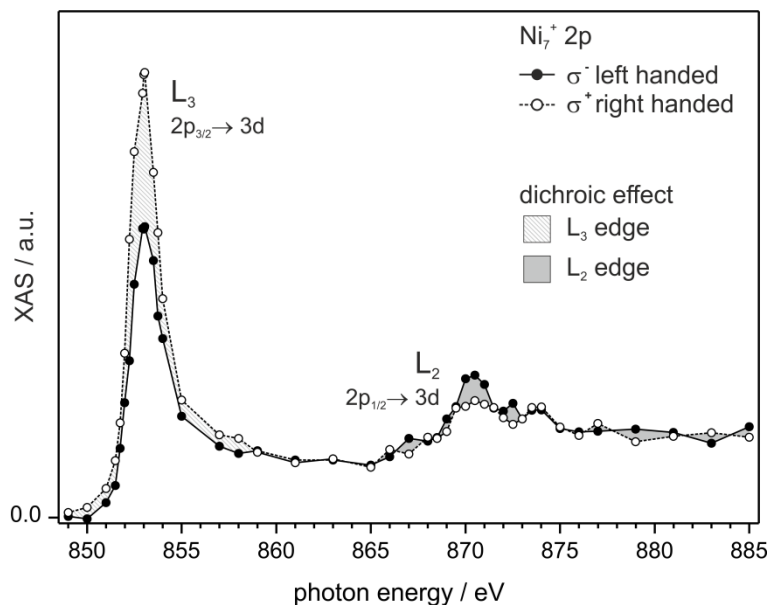


Figure 1 Polarization dependent x-ray absorption spectra for Ni_{12}^{+} at the $L_{2,3}$ edge. The spectra were recorded with negative (open symbols) and positive (filled symbols) circular photon polarization with the propagation direction of the x-ray beam parallel to the magnetic field axis. Shaded areas indicate the x-ray magnetic circular dichroism (XMCD) effects for the L_2 and L_3 edge. Spin and orbital magnetic moments are extracted following the procedure outlined by Chen *et al.*^[32].

The projections of the clusters' spin and orbital magnetic moments upon the quantization axis are extracted from the spectra by magneto optical sum rule analysis^[32,77,78]. The z axis, as quantization axis, coincides with the magnetic field axis of the ICR magnet. The field axis is collinear with the propagation direction of the x-ray beam. We obtain the numerical values of the z components of spin- and orbital moments, $m_{S,z}$ and $m_{L,z}$ ^[32] in units of μ_B , using Eq. (1) and (2).

$$m_{L,z} = -\frac{4(A+B)}{3C} n_h \quad (1)$$

$$m_{S,z} = -\frac{2(A-2B)}{C} n_h - 7T_z \quad (2)$$

The parameters **A** and **B** represent the integrated dichroic effects ($\sigma^+ - \sigma^-$) at the L_2 and L_3 absorption edges of the experimental spectra (Fig. 1). **C** is the sum of spectra of both polarizations ($\sigma^+ + \sigma^-$) which is corrected for non-resonant background absorption^[32]. The application of bulk n_h values is discussed elsewhere^[41]. Calculated moments are given. We set the number of 3d holes to the bulk values with $n_h = 1.45$ ^[10,11] for nickel and $n_h = 3.4$ ^[30,79] for iron following the earlier interpretation for cobalt clusters with n_h being 2.5^[32]. The second term in Eq. (2), $\langle T_z \rangle$, treats a possible anisotropy in the spin distribution of the investigated sample, and it corresponds to a spin asymmetry along the quantization axis. It can contribute up to 20 % to the spin magnetic moment in a highly anisotropic

medium^[80]. It averages out by an angular average^[31]. In our experiment the cluster ions are rotating freely in the ion trap with their moments aligned to the external magnetic field and not locked to the cluster frame. Thus, we may neglect $\langle T_z \rangle$ in our analysis. Finally, we incorporate a 10 % correction for incomplete circular polarization at the beamline.

Small clusters are single domain particles^[2,81] which can be considered to behave superparamagnetic^[12,82,83]. Magnetic moments rotate independent of the cluster frame when the thermal rotational energy exceeds the magnetic crystalline anisotropy energy. Moments lock to the cluster frame below a critical blocking temperature. We found no evidence for a locked moment behavior in our experiment. Therefore, the projection of the magnetic moments upon a quantization axis follows a Langevin function in dependence of temperature and magnetic field strength^[12-14,51]. Thus, the projection of the magnetic moments onto the quantization axis is a function of cluster temperature and applied magnetic field, i.e. intrinsic spin m_s and orbital magnetic moments m_L can be calculated if the cluster temperature and the applied magnetic field strength are known. In the present case of 3d metal clusters, the experimental conditions ($T_{\text{cluster}} = 20$ K and $B_{\text{external}} = 7$ T) correspond to the weak field limit (Zeeman limit). This implies that Russel-Saunders (LS) coupling prevails, and it is the total magnetic moment which aligns to the external magnetic field^[9]. The intrinsic spin and orbital magnetic moments, m_s and m_L , can be calculated from the experimental z components of spin and orbital moments, $m_{s,z}$ and $m_{L,z}$, by Langevin correction.

5.5.3 Results and discussion

5.5.3.1 Magnetic moments of cobalt clusters

The results for cobalt clusters will be addressed briefly as they are discussed in detail elsewhere^[5]. Experimental spin and orbital magnetic moments were corrected for the degree of photon polarization and Langevin corrected for temperature and magnetic field. In the investigated size range (Co_n^+ , $8 \leq n \leq 22$), the orbital moments vary between 0.4 - 0.9 μ_B per atom (Fig. 2). The orbital moment is quenched compared to the atomic value of 3 μ_B . However, it is enhanced compared to the bulk value ($m_L(\text{Co, hcp}) = 0.153 \mu_B$ ^[32]). The orbital moment increases by a factor of 2 - 4 for small clusters. This confirms theoretical predictions that the orbital magnetic moment in small clusters will be larger than the bulk value. Because of the particles' finite size and reduced coordination number at the surface, the 3d electrons are more localized and therefore still retain an orbital moment^[84]. The spin magnetic moment is increased by approximately 1 μ_B per atom compared to the solid. If we compare our spin magnetic moments to those of Lau *et al.*^[8], we find that our spin magnetic moments are systematically higher but show the same general trend (Fig. S2). The orbital magnetic

moments differ slightly but are of the same order (Fig. S2) and show no notable deviations from each other.

The total magnetic moments differ slightly from prior Stern-Gerlach experiments ^[49,85-88]. However, already the results of Stern-Gerlach experiments differ significantly between each other. The present experimental results fall between the differing Stern-Gerlach series. The magnetic moments deduced from the XMCD experiments are larger than the moments from de Heer *et al.* ^[49,85,88] and Knickelbein *et al.* ^[87] but lower than those of Bloomfield *et al.* ^[86]. One has to remember that the investigated clusters in Stern-Gerlach and the present XMCD experiments have a different charge state. While the XMCD experiments are conducted on singly positively charged cluster cations, Stern-Gerlach experiments investigate the neutral cluster.

The extra hole in the cationic cluster due to the positive charge will not alter the electronic, i.e. the magnetic structure, significantly considering the total number of 3d electrons for Co_n^+ with $n \geq 8$ (number of electrons ≥ 72). Going from the neutral species to the mono cation the spin magnetic moment of the whole cluster is expected to change by $1 \mu_B$, i.e. by the spin magnetic moment of the removed electron. Gutsev *et al.* ^[20] calculated the spin magnetic moment for Co_{13} for both charge states. They calculated a spin magnetic moment of $27 \mu_B$ ($2.08 \mu_B/\text{atom}$) for the neutral cluster. The value for the cationic cluster Co_{13}^+ of $26 \mu_B$ ($2 \mu_B/\text{atom}$) agrees with our experimental result of $2 \pm 0.2 \mu_B/\text{atom}$. While Co_{13} retains its geometric structure upon change of the charge state, the geometric structure for Co_{12} alters when removing an electron. The neutral cluster shows the same motif as Co_{13} (hexagonal bilayer) and a spin magnetic moment of $24 \mu_B$ ($2 \mu_B/\text{atom}$). An icosahedral structural motif yielded the most stable conformation for Co_{12}^+ with a spin magnetic moment of $21 \mu_B$ ($1.75 \mu_B/\text{atom}$). Our experimental value of $2.4 \pm 0.2 \mu_B/\text{atom}$ for Co_{12}^+ is slightly higher than the theoretically predicted moments by Gutsev *et al.* ^[20]. Martinez *et al.* ^[89,90] recently calculated spin magnetic moments for positively charged cobalt clusters Co_n^+ ranging from Co_2^+ - Co_{20}^+ . Their spin magnetic moments oscillate around $2 \mu_B/\text{atom}$ for clusters with $n > 7$. Thus, their values are in general lower than the spin magnetic moments found by us.

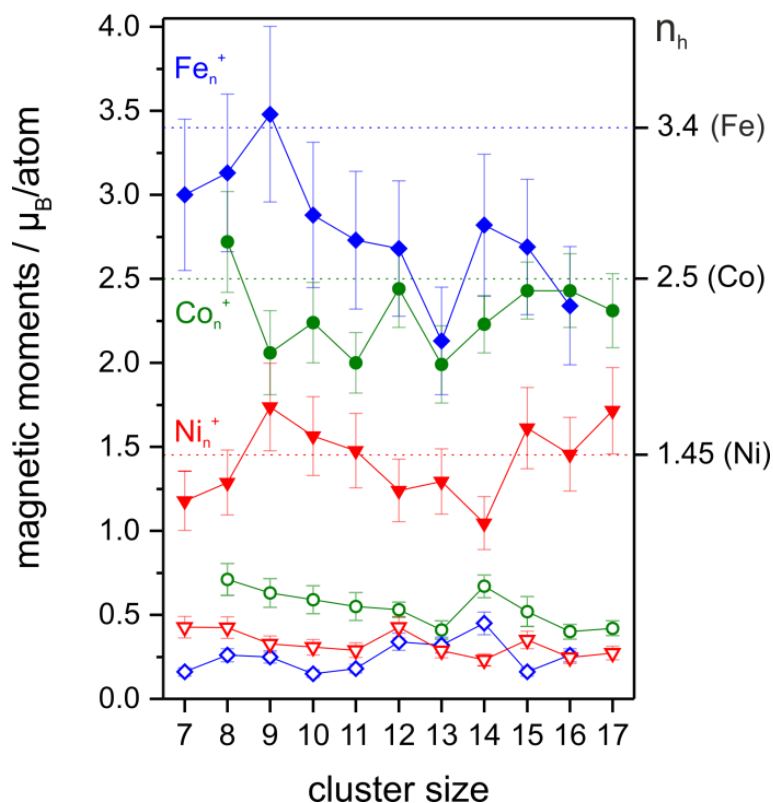


Figure 2 Spin (filled symbols) and orbital (open symbols) magnetic moments of iron Fe_n^+ (diamonds), cobalt Co_n^+ (circles) and nickel Ni_n^+ (triangles) cluster cations. Dashed lines indicate the number of 3d holes used in the calculations of the spin and orbital magnetic moments.

5.5.3.2 Magnetic moments of iron clusters

Spin and orbital magnetic moments of small iron cluster cations Fe_n^+ were measured under the same experimental conditions as the moments of the cobalt cluster cations. The clusters were cooled down to 20 K via collisional in the magnetic field of a 7 Tesla superconducting solenoid. Extracted spin and orbital magnetic moments are scaled to the saturation limit. We investigated iron cluster cations Fe_n^+ in the size range from $7 \leq n \leq 17$ atoms per cluster. Spin as well as orbital magnetic moments are enhanced compared to the bulk value (Fe, bcc) of $1.98 \mu\text{B}/\text{atom}$ for $m_s^{[32]}$ and $0.083 \mu\text{B}/\text{atom}$ for $m_l^{[32]}$. The orbital values range from $0.45 \pm 0.07 - 0.12 \pm 0.02 \mu\text{B}/\text{atom}$ (Fig. 2), which corresponds to a relative increase of about 1.5 to 4 times compared to the bulk values. This increase is less pronounced for the spin magnetic moment (about 1.5 times) with values ranging from $2.1 \pm 0.3 \mu\text{B}/\text{atom}$ for Fe_{13}^+ to $3.5 \pm 0.5 \mu\text{B}/\text{atom}$ for Fe_9^+ . Spin as well as orbital magnetic moment are quenched when compared to the atom (Fe_1 , $[\text{Ar}]4s^23d^6, ^5D$) or to the cation (Fe_1^+ , $[\text{Ar}]4s^13d^6, ^6D$).

If we compare our magnetic moments with those reported by Lau *et al.*^[9], we find that the values for the orbital magnetic moment are of the same order and general trend with the exception of Fe_{14}^+ and

Fe_9^+ (Fig. S2). We obtained a higher value ($0.45 \pm 0.07 \mu_B/\text{atom}$) than Lau *et al.* ($0.14 \mu_B/\text{atom}$) for Fe_{14}^+ while they measured a higher value for Fe_9^+ ($0.6 \mu_B/\text{atom}$) than us ($0.25 \pm 0.04 \mu_B/\text{atom}$).

As for small iron clusters, the spin moment seemingly fluctuates more than the orbital moment. One should bear in mind the different order of magnitude of both contributions. Fe_{13}^+ presents a local minimum in the measured series with its spin magnetic moment being only $2.1 \pm 0.3 \mu_B/\text{atom}$. We find a local maximum at Fe_9^+ ($m_s = 3.4 \pm 0.5 \mu_B/\text{atom}$) (Fig. 2) while the previous study finds a local minimum ($2.7 \mu_B/\text{atom}$)^[9], the deviation falling almost within the range of combined uncertainties. Our experimental spin magnetic moments for Fe_n^+ clusters are in general lower (by up to 10 %) than the previously reported ones.

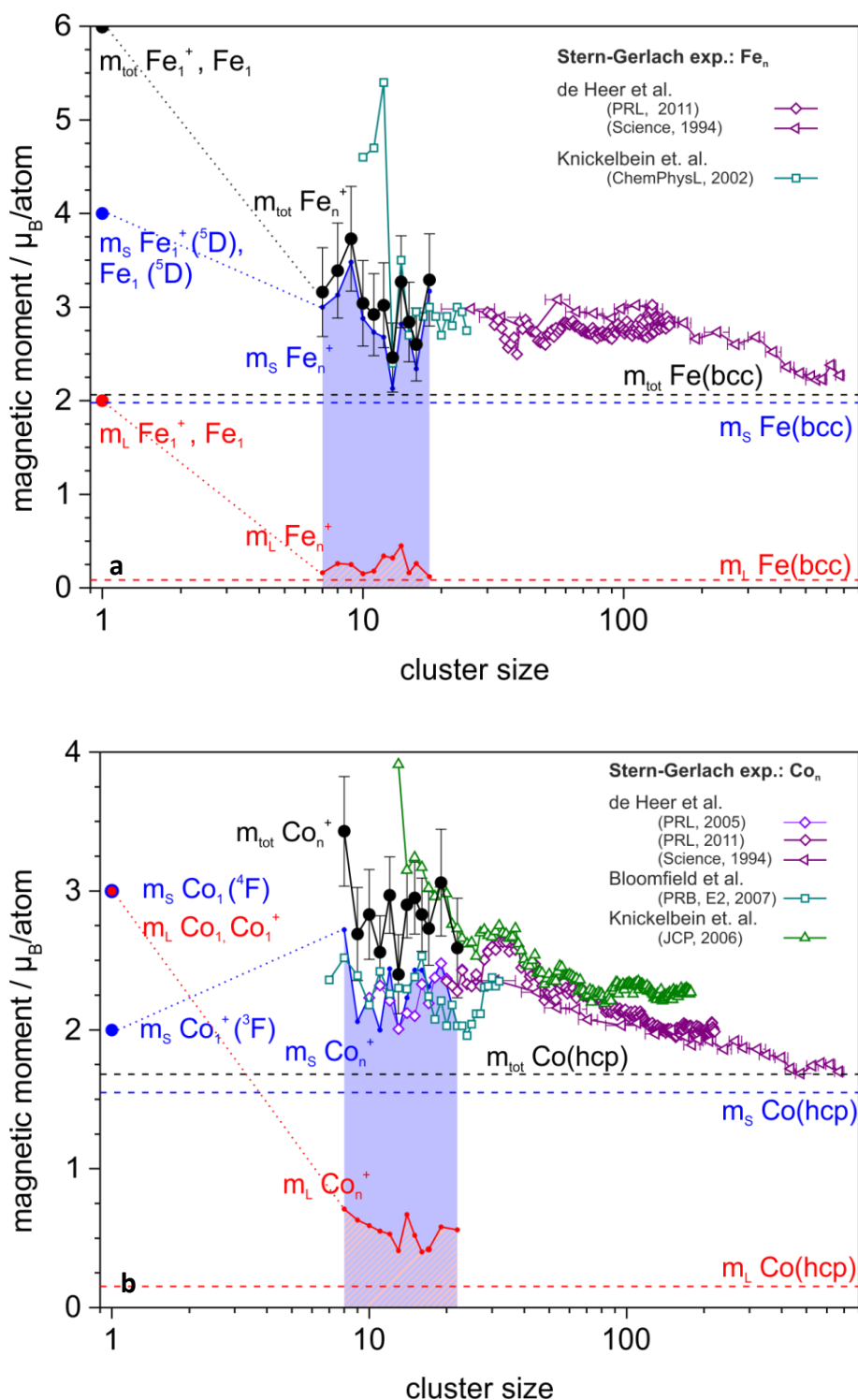
The total magnetic moments of the cluster cations compare well with prior Stern-Gerlach experiments^[49,85,91] of neutral clusters for sizes $n \geq 13$ (Fig. 3a). The magnetic moments deduced from the present experiments are about $2 \mu_B/\text{atom}$ lower than the values obtained by Knickelbein *et al.*^[91] which are approximately $5 \mu_B/\text{atom}$ for $n = 10 - 12$. The size dependence of the total magnetic moments from Stern-Gerlach experiments shows a local minimum at Fe_{13} which corresponds to the local minimum of the spin magnetic moments at Fe_{13}^+ found in XMCD experiments^[9]. Lau *et al.*^[9] argued that this reduced moment is due to an antiferromagnetic coupling of the central Fe atom to the outer twelve iron atoms, if an icosahedral structure is assumed. Recently, theoretical studies on cationic iron Fe_n^+ clusters in the size range from $7 \leq n \leq 20$ ^[36,40] with a focus on Fe_{13}^+ ^[20,41,42] have been published. Theory agrees well with both data sets within error bars and supports the exceptionally low spin magnetic moment found for Fe_{13}^+ despite an ongoing controversy of its origin^[41,42]. Guzman-Ramirez *et al.*^[21] published a value for Fe_7^+ (pentagonal bipyramid) of $3.14 \mu_B/\text{atom}$ which is lower than the two published values by Yuan *et al.*^[40] and Gutsev *et al.*^[36] but closest to the experimental value of $3.0 \pm 0.45 \mu_B/\text{atom}$ found by us.

5.5.3.3 Magnetic moments of nickel clusters

The magnetic moments of small nickel clusters fluctuate with the cluster size as was to be expected in the investigated size regime. The orbital magnetic moments of small nickel cluster cations ($7 \leq \text{Ni}_n^+ \leq 17$) are enhanced compared to the solid (Ni (fcc), $0.06 \mu_B/\text{atom}$ ^[15,16]) as they range from $0.25 - 0.43 \mu_B/\text{atom}$. However, compared to the atomic value Ni_1 of $m_L = 3 \mu_B$ (or the cationic value $\text{Ni}_1^+ = 2 \mu_B$) the orbital moments of the clusters are quenched to about 8 - 10 % of the atomic value (12 - 20 % of the cationic) (Fig. 2). Theory predicts an orbital magnetic moment of an icosahedral Ni_{13} cluster of $0.24 \mu_B/\text{atom}$ ^[92] or $0.32 \mu_B/\text{atom}$ ^[26] and $0.26 \mu_B/\text{atom}$ ^[26] for an fcc-like structure. This compares well with our result of $0.29 \pm 0.04 \mu_B/\text{atom}$. For Ni_7 the calculated value of $0.39 \mu_B/\text{atom}$ ^[26] compares well to the experimental value of $0.43 \pm 0.06 \mu_B/\text{atom}$. The agreement between theory and

5. Spin and orbital magnetic moments of small clusters of the ferromagnetic 3d metals

experiment is worse for Ni_8 and Ni_9 with theoretical values of $0.22 \mu_B/\text{atom}$ ^[26] and $0.25 \mu_B/\text{atom}$ ^[26] compared to $0.42 \pm 0.06 \mu_B/\text{atom}$ for Ni_8^+ and $0.33 \pm 0.06 \mu_B/\text{atom}$ for Ni_9^+ from the current XMCD experiments. The most prominent increase in the orbital moment can be seen for Ni_{12}^+ which is enhanced compared to the neighboring cluster sizes (Fig. 2). The orbital magnetic moment for $\text{Ni}_{10}^+ - \text{Ni}_{15}^+$ obtained by Lau *et al.*^[8] are comparable to ours. Slight deviations occur for Ni_{15}^+ but otherwise the values range within the error bars of both experiments (Fig. S2)



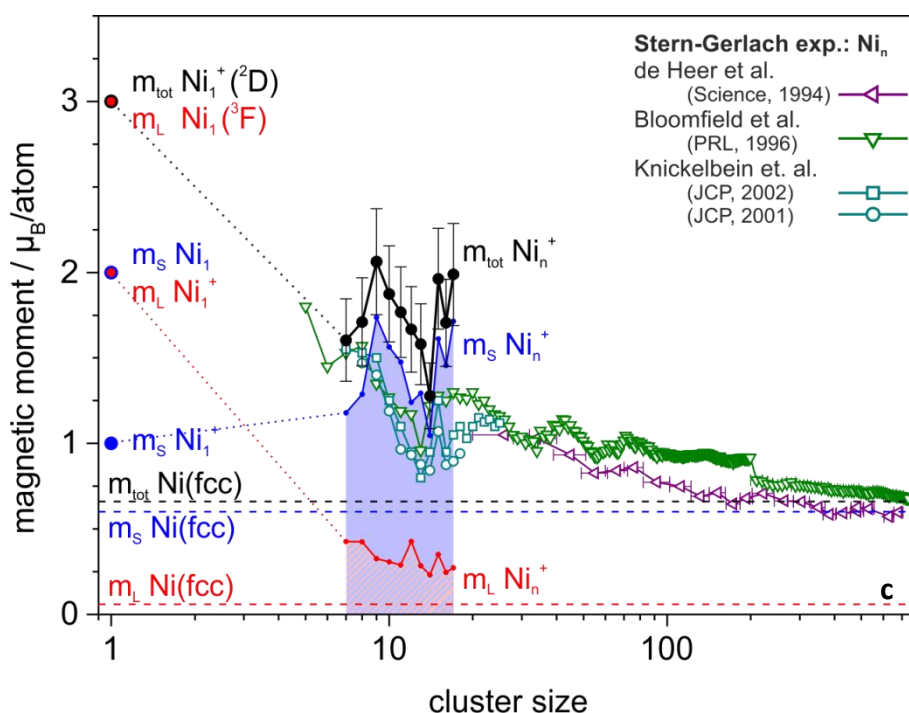


Figure 3 Total Magnetic moments (filled circles) determined by XMCD experiments in comparison with Stern-Gerlach results (open symbols). **(a) Fe_n^+** , **(b) Co_n^+** , **(c) Ni_n^+** Shaded areas indicate the spin (solid, blue) and orbital (hatched, red) magnetic moments. Dashed lines display the magnetic moments of the respective bulk material (Fe & Co Ref. [32], Ni Ref. [15,16]). The magnetic moments of the free atom and cation were calculated according to Hund's rules. Stern-Gerlach results were taken from Ref. [49,85,91] for Fe_n , from Ref. [49,85-88] for Co_n and from Ref. [49,51-53] for Ni_n . For Ref. [85] the magnetic moments for the assigned high spin states are plotted and for Ref. [86] the experimental series denoted E2 is plotted. The Stern-Gerlach experiments investigated a wide cluster size range of up to several hundred atoms per clusters. The magnetic moment does not smoothly approach the bulk value with increasing cluster size but shows an oscillatory behavior. These oscillations are due to electronic and/or geometric shell closures and are superimposed onto the general trend. Our narrow size range does not allow us to detect these oscillations.

The size dependence of the spin magnetic moment is much more pronounced than for the orbital magnetic moment. Experimental spin magnetic moments range from $1.0 \pm 0.15 \mu_B/\text{atom}$ for Ni_{14}^+ to $1.7 \pm 0.25 \mu_B/\text{atom}$ for Ni_9^+ and Ni_{17}^+ . If one compares the m_S data to the spin magnetic moment of the free atom the moments are quenched (Ni, $[\text{Ar}]4s^23d^8$, 3F). There is a nearly degenerate configuration for Ni, i.e. $[\text{Ar}]4s^13d^9$. This configuration is assumed for bulk nickel, giving rise to one single d-hole and a theoretical spin moment of $1 \mu_B/\text{atom}$. The spin magnetic moment is enhanced compared to the solid (Ni (fcc), $0.6 \mu_B/\text{atom}$ ^[15,16]). The size dependence of the spin magnetic moment reveals a local minimum at Ni_{14}^+ . This agrees qualitatively with a local minimum of the prior Stern-

Gerlach experiments in the range of $n = 13 - 14$ ^[51,53,91] (Fig. 3c). The spin magnetic moments of both XMCD experiments agree within combined uncertainties (Fig. S2).

The total magnetic moments of the neutral clusters and cluster cations of cobalt and iron follow the same general trends, i.e. they show pronounced minima for the same cluster sizes, e.g. for Fe_{13} ^[9,85,91]. The absolute values of the total magnetic moments for cobalt and iron are comparable to the values from the Stern-Gerlach experiments. The total magnetic moment of the cationic nickel clusters are higher throughout the measured series but still of the same order. The general trend for the total magnetic moment for cationic nickel clusters, which is dominated by the trend of the spin moment, is the same. However, the whole series deduced from our XMCD experiments seems to be shifted by one atom to larger towards larger clusters compared to Stern-Gerlach experiments ^[51-53].

Gutsev *et al.* ^[20] calculated the spin magnetic moment for $\text{Ni}_{12}^{0/+}$ and $\text{Ni}_{13}^{0/+}$. Ni_{12} and Ni_{12}^+ possess similar structures which are not based on an icosahedral like structure. The calculated spin magnetic moment for the neutral cluster is $8 \mu_B$ ($0.67 \mu_B/\text{atom}$) and $9 \mu_B$ ($0.75 \mu_B/\text{atom}$) for the cationic cluster. However, both values are far below the experimental value of $1.2 \pm 0.2 \mu_B/\text{atom}$. Gutsev *et al.* ^[20] found for the neutral Ni_{13} cluster a magnetic spin moment of $10 \mu_B$ ($0.77 \mu_B/\text{atom}$) and for the corresponding cationic cluster Ni_{13}^+ two almost degenerate lowest energy isomers with $0.69 \mu_B/\text{atom}$ and $0.85 \mu_B/\text{atom}$. As for Ni_{12}^+ , the calculated moments are significantly smaller than the experimental spin magnetic moment of $1.3 \pm 0.2 \mu_B/\text{atom}$ for Ni_{13}^+ . Spin magnetic moments for cationic nickel Ni_n^+ clusters with $n \leq 30$ have been investigated by Song *et al.* ^[25]. However, the theoretically found spin magnetic moments are about $0.3 \mu_B/\text{atom}$ too low. The values found by Song *et al.* increase for smaller clusters and the value for Ni_7^+ agrees with the experimentally found value of $1.2 \mu_B/\text{atom}$. Also, the value found by Guzman-Ramirez *et al.* ^[21] for Ni_7^+ (capped octahedron) agrees with the experimentally found spin magnetic moment.

5.5.3.4 Scaling laws of the spin and orbital contributions to magnetic moments of Fe_n^+ , Co_n^+ and Ni_n^+ clusters?

Within the investigated size range, the obtained spin and orbital moments vary little. The values of the total magnetic moments fall within range of those of previous investigations. Nevertheless, it pays to re-approach the data once more from a broad perspective. If clusters indeed interface between atom and bulk, and if they truly bridge the gap in-between, one would expect a scaling of their properties by size. This scaling should interpolate explicitly between bulk and atom and it should follow predictable trends when scaling from bulk to cluster size ($n \sim 100 - 1000$) throughout the scalable size regime. Reducing sizes further, one anticipates strongly size dependent and non-monotonous jumps in cluster features (as predicted and observed often before), which has

led to the coinage of the term of a "non-scalable" size regime^[93,94]. Note, however, that this term is misleading in so far as the scalability of properties is not obsolete. Instead, "magic cluster size" related variations superimpose onto the prevailing scaling laws. (see Tab. 2 for various common scaling laws). In the present case of magnetic moments and their individual contributions, conceivable scaling laws would read as follows:

$$m_x(n) = m_x(\infty) + \frac{m_x(\infty) - m_x(1)}{n^y} \quad (3)$$

$x = S, L$ and n denotes the cluster size, and the scaling power $y = -\frac{1}{3}, -\frac{1}{2}, -1$ would imply the cases of a scaling correction of "per cluster diameter" (or "per cluster radius"), "per surface area of the cluster" or "per cluster volume" the particular cluster magnetic moments. The given values of bulk magnetic moments and atomic magnetic moments, $m_x(\infty)$ and $m_x(1)$ for $x = S, L$ are taken as asymptotic boundaries. The resulting scaling laws serve to interpolate in between these two limits. Note, that the magnetic moments $m_x(n)$ and $m_x(\infty)$ refer to intensive values, i.e. the magnetic moments are normalized "per atom".

Table 2 Various cluster properties and scaling laws - n refers to the number of particles or atoms per molecule or cluster

cluster property			proportional to
surface tension of a spherical droplet	γ	$1/R^2$	$= n^{-1/2}$
ratio of surface to bulk atoms in a spherical particle	N_s / N_v	$1/R$	$= n^{-1/3}$
binding energy/atom (cohesive energy) ^[95-97]	ϵ_{coh}		$n^{-1/3}$
ionization potential ^[98,99]	I_p		$n^{-1/3}$
electron affinity ^[98,100]	E_a		$n^{-1/3}$
resonance frequency of a spherical metal cluster ^[101-103]	ω_r	$1/R^3$	$= n^{-1}$
autoionization resonance energy of Hg clusters ^[104-106]	δ_n		n^{-1}
average energy level spacing ^[107]	ΔE		n^{-1}
magnetic dipolar interaction ^[108]	E_{mag}		n^{-1}
cluster polarizabilities ^[103]	α_N	R^3	n

In the data of the present study, there is an explicit lack of cluster size dependency throughout the size range covered ($n = 7 - 22$). Inspection of the data compiled in Tab. 1, however, suggests an analysis of the size dependence of normalized moments (per atom) for trends and conceivable scaling laws. Figs. 4a and 4b visualize an attempt to do so for spin and orbital magnetic moments, respectively. The x-axes of diagrams are chosen as $n^{-1/3}$. A data set that would scale by $n^{-1/3}$ ($y = -\frac{1}{3}$, "per diameter") would resemble a straight line. Note, that data following alternative scaling laws would reveal nonlinear curves between the same asymptotes as is indicated in Fig. 4a, b (by

dashed lines) for the case of $y = -1$ ("per cluster volume"). It is gratifying to realize that the recorded cluster data of spin magnetic moments (open data points in Fig. 4a) come close to the conceived scaling law in the three cases, i.e. of Fe_n^+ (blue diamonds), Co_n^+ (green circles) and Ni_n^+ (red triangles). In particular, the scaling "per diameter" ($y = -\frac{1}{3}$) reproduces the experimental data on spin contributions much better than the alternative scaling "per cluster volume" ($y = -1$). One may easily imagine the intermediate case of scaling "per surface area" ($y = -\frac{1}{2}$), and it is obviously not suitable either.

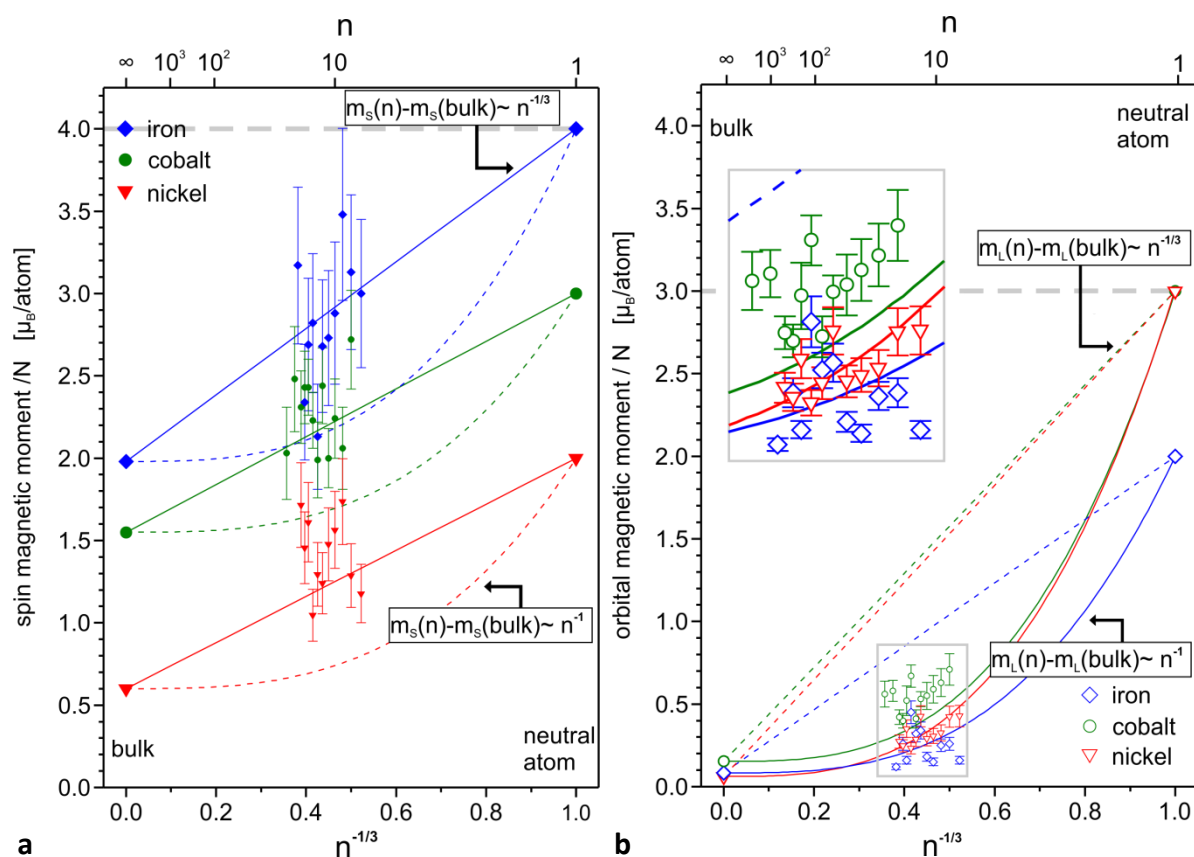


Figure 4 Spin (left) and orbital (right) magnetic moments of size selected clusters in comparison to conceivable trends that would interpolate between bulk metals and neutral atoms. Note, that the recorded spin moments seem to follow an $n^{-1/3}$ trend while orbital moments largely agree with an n^{-1} trend.

There are remarkably different findings in the cases of the orbital magnetic moments (Fig. 4b) of Fe_n^+ (blue diamonds), Co_n^+ (green circles) and Ni_n^+ (red triangles). The cluster values are found in general close to the quenched asymptotic bulk values. For sure, they are not explained by a "per diameter" scaling (dashed lines in Fig. 4b). To our own surprise, however, we find a reasonable agreement with a possible "per cluster volume" scaling law ($y = -1$). Spin and orbital magnetic moments are distinctly different for sure. Inspection of orbital moments in some more detail reveals

that experimental data for Fe_n^+ and Ni_n^+ fit - within their scatter and uncertainties - nicely to the depicted n^{-1} scaling (solid blue and red lines). The experimental data on the orbital moments of Co_n^+ , however, are systematically larger by about 20 % than the scaling prediction (solid green line). Element specific subtleties as such are to be expected. A detailed reasoning, however, remains to future high level theoretical modelling.

Spin moments The spin magnetic moments follow the well-known trend of $n^{-1/3} = 1/(\text{cluster radius})$, like e.g. the ionization potential or the electron affinity (Tab. 2). The general trend is superimposed by individual structures, e.g. the low spin magnetic moment of Fe_{13}^+ or fluctuations introduced by the geometrical structure (Fig. 4a, b). The surface to volume ratio in a spherical particle is directly related to this scaling law $1/(\text{cluster radius}) = (\text{surface area of the cluster})/(\text{cluster volume})$. We conclude from this scaling law that the average spin magnetic moment per atom seems to follow the surface area of the cluster (normalized to the cluster volume). In a first try of an explanation we can follow the argumentation of the enhanced spin magnetic moment at surface and of thin films.

The reduced coordination number at surfaces leads to a stronger localization of the electron wave function and thus to a narrower band width which in turn leads to a higher density of states at surface atoms^[1,83,84]. This leads to an enhanced spin magnetic moment at surfaces. As our measurement averages over all coordination sites (surface and volume), enhanced spin moments at surface sites will lead to an enhancement with respect to the bulk of the average spin magnetic moment per atom in clusters. This leads to a scaling by 1 over area per volume which appears as $n^{-1/3}$ - as observed. This might explain why the surface area is important but we find few individual size effects within our error bars. These individual size effects should be superimposed onto the scaling law. If the investigated size range was to be extended to larger clusters, the trend of $1/(\text{cluster radius})$ should become more pronounced.

Orbital moments The orbital magnetic moment is even more sensitive to the coordination environment than the spin magnetic moment. It is conceivable that the orbital moment is closely related to the delocalization of the electrons within the cluster, .i.e. the forming of a band structure. The hybridization of orbitals and thus the delocalization of electrons leads to a quenching of the orbital moment. Surface layers show an enhanced orbital moment compared to the bulk phase^[57]. This is attributed to the fact that atoms have a lower coordination number than bulk atoms and the 3d states are more localized than in the solid^[54,109,110]. Hence, surface atoms retain more angular orbital momentum than their bulk counterparts. Following this line of thought, the orbital moment should follow the ratio of surface atoms-to-bulk atoms. However, we find a seemingly different scaling of about n^{-1} . It might follow that the general geometry of the clusters influences the orbital

moment more strongly than the spin magnetic moment, i.e. the coordination environment, number of nearest neighbors and bond lengths, etc.. Exceptionally high or low orbital magnetic moments may appear for certain cluster geometries which have an open structure (high orbital magnetic moment) or a high symmetry (small orbital magnetic moment). In the case of the orbital magnetic moment, one might see a significant change if the geometrical motif changes e.g. from icosahedral to bulk like. Our present experiments do not cover a size range which would allow for a conclusive explanation of the observed trend. Currently we are left with tentative suggestions.

Validity of scaling laws It is a general question of concern whether a continuous scaling of magnetic cluster properties amongst atomic and bulk values is to be expected in the first place. Discontinuous (phase) transitions are well conceivable. At least, we are able to phrase a "robust" finding of the present study *without* stating any scaling: Spin and orbit contributions of iron, cobalt and nickel clusters comprising 10 - 20 atoms are closer to bulk than to atomic values. The relative quenching of orbital moments in cluster is higher than that of the spin moments. A final interpretation of the found scaling laws is still pending and will need support from theory. Especially in the case of the orbital magnetic moment as it seems to correlate with the electronic structure of the cluster. Our findings raise conceptual questions that cannot be solved by the present findings on their own. It is mandatory to achieve an appropriate in depth modelling of the prevailing electronic couplings in order to unravel the reasoning for the observed scalings / magnitudes.

5.5.4 Summary and outlook

We have investigated the spin and orbital magnetic moments of small iron, cobalt and nickel clusters. The magnetic moments are enhanced with respect to the values of the bulk material, but quenched with respect to the atomic values. However, we find that the orbital and spin magnetic moments follow different scaling laws, if we interpolate between the atomic and bulk values. The spin follows a "per diameter" asymptote while the orbital magnetic moment follows a "per volume" scaling law. In order to confirm the postulated scaling laws for spin and orbital magnetic moments, we need to extend our data set towards clusters with more "atom-like" character ($n \ll 10$) and clusters with more bulk-like character ($n \gg 20$). If we compare our data for the total magnetic moments to the results obtained from Stern-Gerlach experiments, one would expect the total magnetic moments from both experiments to agree with each other. However, the spin magnetic moments obtained from XMCD experiments agree better with the Stern-Gerlach data than our total magnetic moments. Note, that different Stern-Gerlach series of the same transition metal clusters deviate significantly from each other. However, different XMCD results agree well within the error range of both experiments (Fig. S2) and give the same qualitative results, thus validating the experimental approach and the reliability of the results.

5.5.5 Acknowledgement

This work has been supported by the Deutsche Forschungsgemeinschaft (NIE325/10-1) and in the framework of the Transregional Collaborative Research Center SFB/TRR 88 "3MET.de". We are grateful for valuable discussions with Kai Fauth (University of Würzburg), Tobias Lau (Helmholtz Zentrum Berlin), Paul Bechthold and Stefan Bluegel (Forschungszentrum Jülich). We also thank Patrick Hofmann (Brandenburg University of Technology Cottbus), Stefan Krause and Ruslan Ovsyannikov (Helmholtz Zentrum Berlin) for assistance at the beamline UE52-PGM at BESSY II.

5.5.6 Appendix

The magnetomechanical ratio g' can be deduced from gyromagnetic experiments by the Einstein-de Haas effect^[111] (rotation induced by change of the magnetization). g' differs from the g factor determined by Ferromagnetic resonance (FMR) experiments. The definition of g' includes J_{tot} and thus a contribution of the orbital angular momentum J_{orbit} (L). The definition of g , on the other hand, only includes the spin angular momentum J_{spin} ($= S$)^[112,113]. The value of the free electron, i.e. the spin only value, is equal to two for g and g' . However, the deviation due to the orbital angular momentum results in $g > 2$ and $g' < 2$.

$$g' = \frac{2m_e}{e} \frac{M}{J_{tot}} = \frac{2m_e}{e} \frac{M}{J_{spin} + J_{orbit}} \quad (4)$$

$$g = \frac{2m_e}{e} \frac{M}{J_{spin}} \quad (5)$$

$$\frac{g'}{g} = \frac{J_{spin}}{J_{spin} + J_{orbit}} = \frac{S}{S + L} \quad (6)$$

5.5.7 References

The references for the manuscript are included in the general reference list of this chapter (Chap. 5.5).

5.5.9 Supplementary material

5.5.9.1 S.1 Application of scaling laws

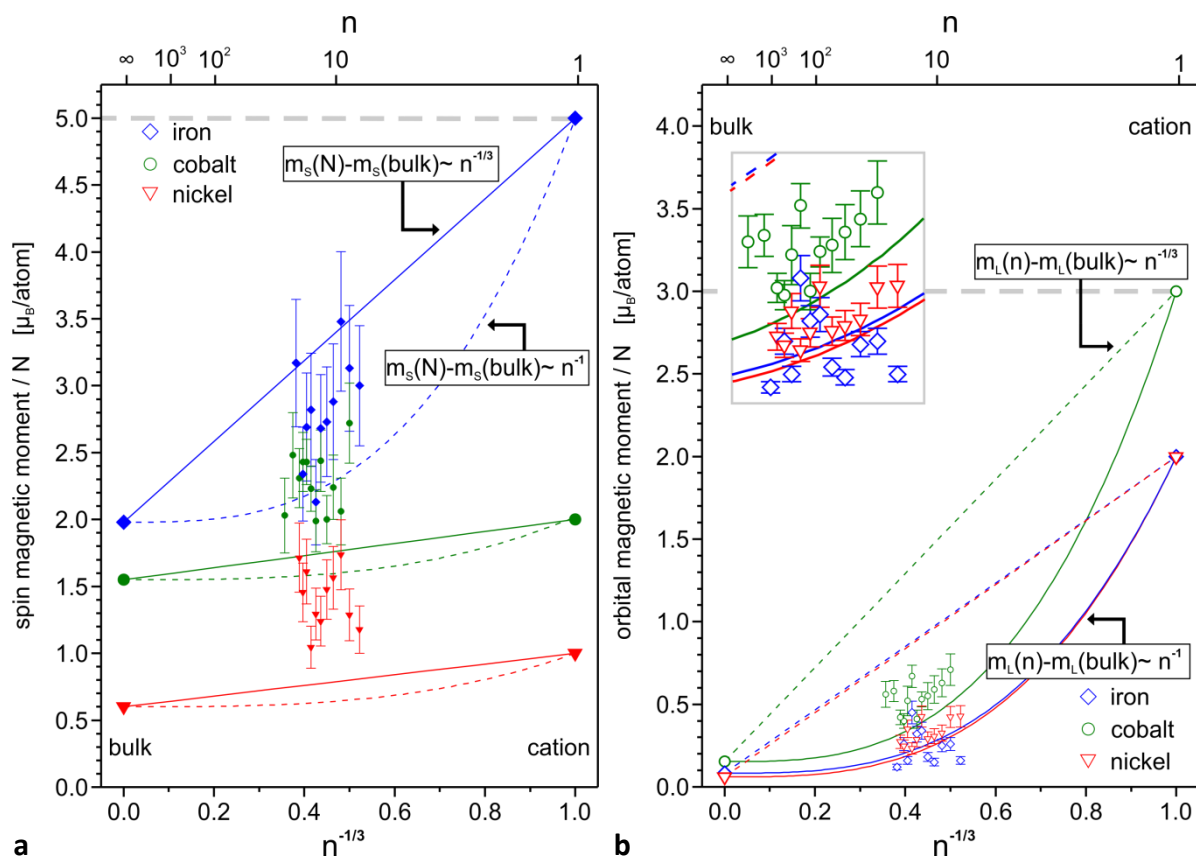


Figure S1 Spin (left) and orbital (right) magnetic moments of size selected clusters in comparison to conceivable trends that would interpolate between bulk metals and cationic atoms. Note, that these trends do agree much less with the recorded XMCD data as the trends depicted in Fig. 4a and 4b, where neutral atoms serve as reference points instead.

5.5.9.2 S.2 Comparison of spin and orbital magnetic moments

Fig. S2 gives a direct comparison of the spin and orbital magnetic moments of free clusters. The data sets are from two independent experiments. Both experiments use XMCD spectroscopy to access the spin and orbital magnetic moments.

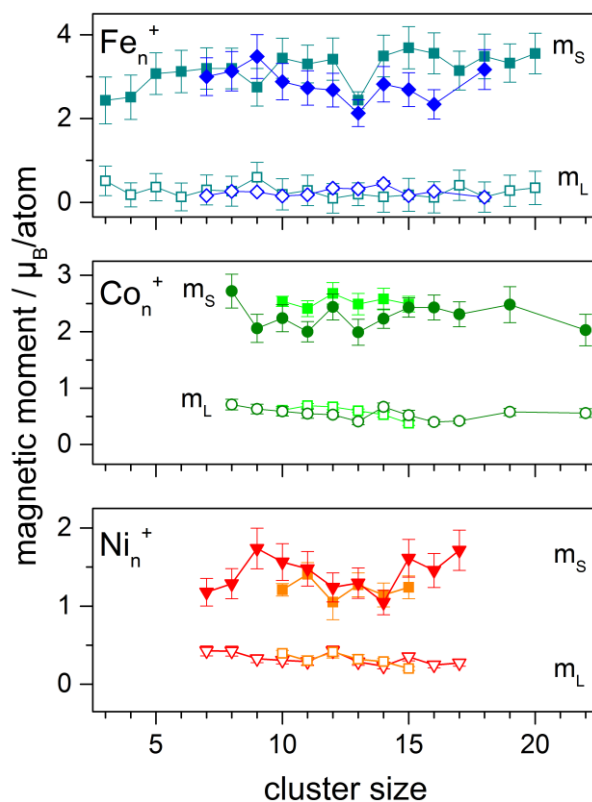


Figure S2 Comparison of spin and orbital magnetic moments for Fe_n^+ (top), Co_n^+ (middle) and Ni_n^+ (bottom) clusters from this study and data obtained by Lau *et al.*^[7-9] (squares in all three panels). The orbital magnetic moments are represented by open and the spin magnetic moments by filled symbols. The found magnetic moments agree well with each other within the error bars of both experiments. Our spin magnetic moments are systematically lower for iron and cobalt clusters but are of the same order. Overall the results found by the two experiments agree well with each other.

5.5.9.3 S.3 Numerical values of spin and orbital magnetic moments

Table S3a Comparison of experimental and theoretical spin magnetic moments in μ_B /atom

	Exp. ^a	Theo. ^b	Exp. ^c		Exp. ^a	Exp. ^d		Exp. ^a	Exp. ^d
Fe₇⁺	3.0 ± 0.45	3.29	3.1 ± 0.45				Ni₇⁺	1.2 ± 0.20	
Fe₈⁺	3.1 ± 0.50	3.13	3.2 ± 0.45	Co₈⁺	2.7 ± 0.30	2.2 ± 0.10	Ni₈⁺	1.3 ± 0.20	
Fe₉⁺	3.5 ± 0.50	3.00	2.8 ± 0.40	Co₉⁺	2.0 ± 0.25	2.0 ± 0.10	Ni₉⁺	1.7 ± 0.25	
Fe₁₀⁺	2.9 ± 0.40	2.90	3.4 ± 0.45	Co₁₀⁺	2.25 ± 0.25	2.5 ± 0.10	Ni₁₀⁺	1.6 ± 0.20	1.2 ± 0.10
Fe₁₁⁺	2.7 ± 0.40	2.82	3.3 ± 0.40	Co₁₁⁺	2.0 ± 0.20	2.4 ± 0.15	Ni₁₁⁺	1.5 ± 0.20	1.4 ± 0.15
Fe₁₂⁺	2.7 ± 0.40	3.08	3.4 ± 0.50	Co₁₂⁺	2.4 ± 0.20	2.7 ± 0.20	Ni₁₂⁺	1.2 ± 0.20	1.05 ± 0.20
Fe₁₃⁺	2.1 ± 0.30	2.69	2.45 ± 0.40	Co₁₃⁺	2.0 ± 0.20	2.5 ± 0.20	Ni₁₃⁺	1.3 ± 0.20	1.3 ± 0.15
Fe₁₄⁺	2.8 ± 0.40	3.07	3.5 ± 0.50	Co₁₄⁺	2.2 ± 0.20	2.6 ± 0.20	Ni₁₄⁺	1.0 ± 0.15	1.15 ± 0.15
Fe₁₅⁺	2.7 ± 0.40	3.13	3.7 ± 0.50	Co₁₅⁺	2.4 ± 0.20	2.5 ± 0.15	Ni₁₅⁺	1.6 ± 0.25	1.25 ± 0.15
Fe₁₆⁺	2.3 ± 0.35	3.19	3.7 ± 0.50	Co₁₆⁺	2.4 ± 0.20		Ni₁₆⁺	1.5 ± 0.20	
				Co₁₇⁺	2.3 ± 0.20		Ni₁₇⁺	1.7 ± 0.25	
Fe₁₈⁺	3.2 ± 0.50	3.17	3.5 ± 0.50						
				Co₁₉⁺	2.5 ± 0.30				
				Co₂₂⁺	2.0 ± 0.30				

^a this work; ^b see Ref. [36]; ^c see Ref. [9]; ^d see Ref. [7,8]

Table S3b Comparison of experimental orbital magnetic moments in μ_B /atom

	Exp ^a	Exp ^b		Exp ^a	Exp ^d		Exp ^a	Exp ^d
Fe₇⁺	0.16 ± 0.02	0.30 ± 0.35				Ni₇⁺	0.43 ± 0.06	
Fe₈⁺	0.26 ± 0.04	0.28 ± 0.35	Co₈⁺	0.71 ± 0.10	0.87 ± 0.035	Ni₈⁺	0.42 ± 0.06	
Fe₉⁺	0.25 ± 0.04	0.60 ± 0.35	Co₉⁺	0.63 ± 0.09	0.49 ± 0.03	Ni₉⁺	0.33 ± 0.05	
Fe₁₀⁺	0.15 ± 0.02	0.21 ± 0.35	Co₁₀⁺	0.59 ± 0.08	0.61 ± 0.03	Ni₁₀⁺	0.31 ± 0.05	0.40 ± 0.04
Fe₁₁⁺	0.18 ± 0.03	0.29 ± 0.35	Co₁₁⁺	0.55 ± 0.08	0.69 ± 0.04	Ni₁₁⁺	0.29 ± 0.04	0.30 ± 0.06
Fe₁₂⁺	0.34 ± 0.05	0.09 ± 0.35	Co₁₂⁺	0.53 ± 0.05	0.67 ± 0.05	Ni₁₂⁺	0.43 ± 0.06	0.41 ± 0.08
Fe₁₃⁺	0.32 ± 0.05	0.20 ± 0.25	Co₁₃⁺	0.41 ± 0.06	0.60 ± 0.03	Ni₁₃⁺	0.29 ± 0.04	0.32 ± 0.06
Fe₁₄⁺	0.45 ± 0.07	0.14 ± 0.35	Co₁₄⁺	0.67 ± 0.07	0.53 ± 0.04	Ni₁₄⁺	0.23 ± 0.04	0.29 ± 0.04
Fe₁₅⁺	0.16 ± 0.02	0.19 ± 0.40	Co₁₅⁺	0.52 ± 0.09	0.38 ± 0.04	Ni₁₅⁺	0.35 ± 0.05	0.20 ± 0.025
Fe₁₆⁺	0.26 ± 0.04	0.13 ± 0.40	Co₁₆⁺	0.40 ± 0.04		Ni₁₆⁺	0.25 ± 0.04	
			Co₁₇⁺	0.42 ± 0.04		Ni₁₇⁺	0.27 ± 0.04	
Fe₁₈⁺	0.12 ± 0.02	0.13 ± 0.35						
			Co₁₉⁺	0.58 ± 0.06				
			Co₂₂⁺	0.56 ± 0.08				

^a this work; ^b see Ref. [9]; ^d see Ref. [7,8]

6. SINGLE MOLECULE MAGNETS

Experiments on Single Molecule Magnets (SMMs) were carried out in collaboration with the group of T. Lau (Helmholtz Zentrum Berlin für Materialien und Energie (HZB), Berlin, Germany). We used the experimental setup called NanoClusterTrap which is operated by the group of T. Lau (Chap. 6.2.2) together with an electrospray ionization (ESI) source. Our group provided the ESI source. The beamtime team consisted of M. Tombers, A. Ławicki, V. Zaimundo-Bayer and myself. All XA and XMCD spectra were recorded at the soft x-ray undulator beamline UE52-PGM at BESSY II/HZB. The SMMs were synthesized in the group of A. Powell (Karlsruher Institute of Technology, Karlsruhe, Germany) in the framework of the Collaborative Research Center TRR88/3MET.

6.1 Introduction

Magnetism is a bulk property linked to the 3D lattice structure of the respective metal or alloy. The quest for new magnetic materials and magnetic phenomena led to reduced dimensionalities of the samples. The reduced dimension or finite size of thin films (2D) or nanoparticles or clusters (1D) resulted in new quantum phenomena due to confinement effects^[1-4]. The ultimate reduction of dimensionality would be a single atom / molecule (0D) as a magnetic entity, i.e. the complete localization of the magnetic moment on one ferromagnetic core without any influence due to packing effects^[1]. In this case, the intramolecular forces dominate the magnetic behavior as the intermolecular or long range interactions are negligible. The unique magnetic features of SMMs make them possible candidates for applications in physics, magneto-chemistry, biology, biomedicine, and material sciences^[5-8] and recently as bits in quantum computing^[8-12].

The most important physical property identifying a molecule as an SMM^[5,13] is a slow relaxation of the magnetization at low temperatures^[14-16] and the occurrence of a hysteresis loop upon reversal of the magnetization^[14,16,17]. "Under these conditions a single molecule becomes like a tiny magnet, in the sense that if magnetized by an applied field it retains the magnetization for days"^[16]. The archetypical SMM is the Mn₁₂-ac ([Mn₁₂O₁₂(CH₃COO)₁₆(H₂O)₄] complex^[18] (Fig. 6.1).

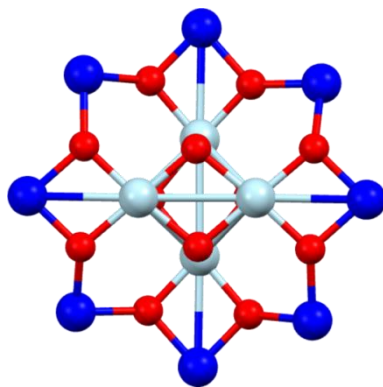


Figure 6.1 $[\text{Mn}_{12}\text{O}_{12}]$ unit of a Mn_{12} SMM. The inner Mn^{IV} atoms (light blue) and the outer Mn^{III} atoms (dark blue) couple antiferromagnetically. Thus, Mn_{12} has got a ferromagnetic ground state with $S = 10$.^[5,18-20]

An SMM behavior is not dependent on the size of the magnetic core, i.e. the number of atoms involved, but centers on two ground state properties:

- a large ground state spin moment S
- a uniaxial/easy axis (Ising-type) anisotropy (Fig. 6.2)

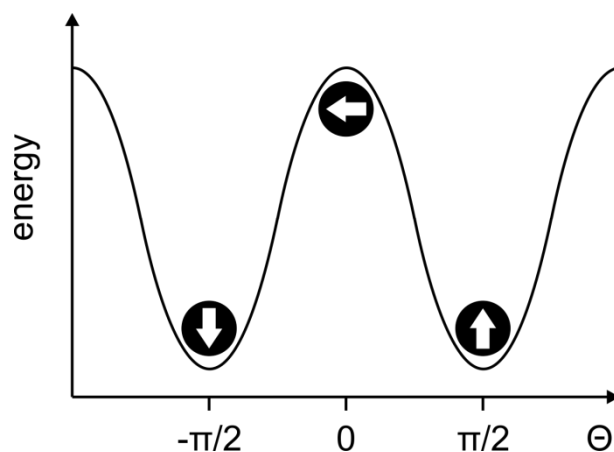


Figure 6.2 Energy of an Ising (easy) axis type magnet as a function of the angle Θ of the magnetization from the easy axis^[15]. The orientations of the magnetization at $\Theta = 2/\pi$ and $\Theta = -2/\pi$ are equal in energy and represent the energy minimum.

The large ground state spin gives rise to the magnetic moment and thus it is favorable to couple as many spins as possible. The easy axis (Ising-type) anisotropy leads to a double well ground state (Fig. 6.2). The blocking temperature is defined as the temperature needed to overcome the barrier which separates the two spin orientations. The higher the blocking temperature is, the longer is the relaxation time of the system due to thermal excitations. Additionally, relaxation of the

magnetization due to tunneling was found for SMMs. This quantum effect is evident in the hysteresis loops as distinct steps in the curve^[14-16,21,22]. The origin of the anisotropy can be complex due to the anisotropies' tensorial nature. The anisotropy can stem from a single atom and / or from the spatial orientation of individual paramagnetic building blocks. Despite continuing efforts of synthetic chemists, Mn₁₂-ac still is one of the SMMs showing the highest blocking temperature. Therefore, a lot of studies focus on the archetypical SMM family of Mn₁₂^[5,13,20,23-33]. Additionally, a second group of iron based molecules, e.g. Fe₈^[34-38] and Fe₄^[25,39,40] have gained a lot of attention because of their high ground states spins and blocking temperatures. The design of SMMs is more and more driven by a rational approach but serendipity still plays a major role in the discovery of new SMMs^[15].

The combination of 3d transition metals, which have got a high spin moment in the ground state, and the high anisotropy of lanthanides has attracted a lot of attention^[22,41-46]. The present chapter focusses on a [Fe₄Ln₂] complex based on a wheel structure^[47] (Fig. 6.5a). The complex contains two Fe^{III} (hs) - Fe^{III} (hs) (hs = high spin) units in which the Fe atoms couple ferromagnetically to each other. The coupling of the two units to each other is mediated via the lanthanide ions. The coupling depends on the lanthanide present and can either be antiferromagnetic (Lu)^[47] or ferromagnetic (Er, Dy, Tb, Gd, Ho)^[47,48].

XMCD spectroscopy of SMMs has been established during the last decade^[20,25,33,34,49-59]. The element sensitivity of the technique allows the determination of the individual contributions of several elements and also gives direct experimental access to the coupling scheme within the SMMs^[49-51,60]. So far, XMCD experiments have either been conducted on solid (crystal or powder samples) or deposited molecules. The intermolecular interactions within a solid SMM are far weaker than the intramolecular interactions but they still might influence the spectrum. In the case of deposited Mn₁₂-ac, it is known that the SMM behavior is lost upon deposition due to the interactions with the support^[20,25,61]. In the investigation of SMMs, a next step is the recording of XMCD spectra of truly isolated SMMs in the gas phase. Gasphase XMCD^[62-67] and XA^[68] spectra of ions and small clusters have recently been reported. In the following, the first polarization dependent gas phase XA spectra for [Fe₄Ln₂] based SMMs will be presented after a short introduction into the experimental methods.

6.2 Experimental methods

6.2.1 Electrospray Ionization (ESI)

6.2.1.1 ESI process

Electrospray Ionization (ESI) is one of the most frequently used ionization methods in modern mass spectrometry applications^[69-72]. ESI is an atmospheric pressure ionization (API) method, i.e. the analyte ions are produced at atmospheric pressure and then are transferred into the UHV region of the mass spectrometer^[71,73-76] by a suitable interface. John Fenn titled his Nobel lecture "Wings for Molecular Elephants"^[77]. The title highlights the fact that ESI is one of the softest ionization techniques available. The ESI technique has been extensively reviewed within the last years, e.g. in Refs. [70,71,78-82]. Initially developed for biomolecular applications^[83-86], ESI has become an important tool in the characterization of metal organic and coordination complexes^[43,87-93].

The analyte is dissolved in a volatile solvent, e.g. acetonitrile or methanol. Then the solution is sprayed through a needle. A nebulizing gas (in our case nitrogen) is concentrically following around the spray needle (Fig. 6.3). The gas flow reduces the surface tension of the solvent, allows higher flow rates, provides more stable spray conditions and smaller droplets^[73,94-97]. However, analyte ions are not created during the spray process. They have already to be present in the solution. An electric field gradient of 3 - 6 kV between the spray needle and the entrance to the mass spectrometer is applied. The electric field gradient causes a charge separation in the solution and the forming of a cone from which the droplets are released^[98,99]. The individual droplets are driven apart by their Coulomb repulsion. Each droplet carries excess charges. As soon as the Rayleigh limit^[100] is reached, which is due to the shrinking of the droplet by evaporation of solvent molecules, the droplet will disintegrate into smaller droplets because the Coulomb repulsion exceeds the surface tension. This process is called Coulomb fission or Coulomb explosion. Recent work, however, has shown that the droplets do not explode but eject smaller droplets^[101-104]. This droplet jet fission starts at a macroscopic scale and takes place several times until the droplet reaches a state in which it resembles a large cluster or microdroplet. The free ion is released from this micro droplet. The final process of the ion release is controversially discussed in the literature^[101,102,105] and two models exist:

- Ion evaporation model (IEM)^[106,107]

The desolvated ion is produced by a direct evaporation of the ion from the surface of the highly charged microdroplet^[108].

- Charge residue model (CRM)^[109-111]

The model assumes that at the end of the fission cascade the droplet is so small that it only contains one analyte ion. The remaining solvent molecules successively evaporate and a complete desolvation is reached in the end.

6.2.1.2 ESI source

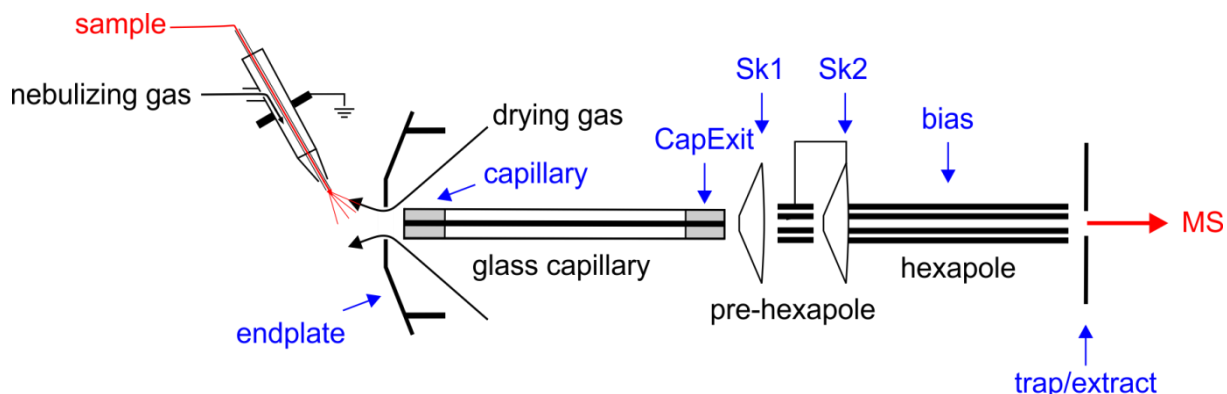


Figure 6.3 Scheme of the Bruker Apollo™ I ESI source^[112]. All major components are indicated. Voltages applied to individual elements are written in blue. The sample is sprayed through a needle held at ground. The electric field gradient is provided by a bias to the endplate. The hexapole can be used as an ion trap. In the present work, it was only used as an ion guide by keeping trap/extract at a constant voltage. Standard values used during the experiment are given in Tab. 6.1. (Sk = Skimmer)

In the present work, we used a Bruker-APOLLO™ I ESI source (Fig. 6.3). After the ESI process, the free analyte ions are transferred into the high vacuum region of the mass spectrometer through a glass capillary (diameter 0.5 mm, length 20 cm). Heated nitrogen gas is flowing around the entrance of the glass capillary to evaporate the solvent molecules off the droplets. The glass capillary is the vacuum interface of the ESI source. A second differential pumping stage is created by a skimmer within the ESI source. The ions are then transferred by a hexapole ion guide into a hexapole ion trap. In the present work, we did not use the trapping function of the hexapole but only used the hexapole as guide, i.e. the Apollo™ I as a continuous ion source. A typical set of ESI parameters used by us is given in Tab. 6.1.

Table 6.1 Typical set of ESI parameters used during the experiments presented later in the chapter. Individual elements to which the voltages are applied are indicated in Fig. 6.3.

parameter		
drying gas (N ₂)	T / °C	180
	p / psi	30
nebulizing gas (N ₂)	p / psi	22
	endplate / V	-5.300
	capillary / V	-6.500
	CapExit / V	90
	Sk1 / V	50
	Sk2 / V	16
	hexapole	RF / MHz
	amplitude / V	600
	bias / V	6.8
	trap/extract / V	-0.5

6.2.2 ClusterNanoTrap

The ESI source was attached to the NanoClusterTrap^[64-66,113,114] experimental endstation operated by the group of Tobias Lau (Fig. 6.4). The instruments design is optimized for the recording of XA^[68,115] and XMCD^[64-67] spectra of free ions and clusters in the gas phase.

Ions leaving the ESI source are injected into a hexapole ion guide which can be operated between 0.5 - 2 MHz. The length of the rods was adjusted to account for the different source geometry of the ESI source compared to gas aggregation source which is usually attached to the NanoClusterTrap. The hexapole ion guide is followed by a quadrupole mass filter (Extrel, GP-203D) with an m/z range of 4000 m/z . A set of electrostatic lenses is used to subsequently focus the ion beam into a quadrupole bending unit. The ion beam is bent by 90° onto the x-ray beam axis. The lenses are horizontally cut in half in order to compensate for the Lorentz' Force exerted by the stray field of the 5 T superconducting solenoid once the magnetic field is switched on. After the ion beam is bended by 90°, a quadrupole ion guide transfers the ions into the linear quadruple ion trap located within the field of a superconducting 5 T magnet (Fig. 6.4).

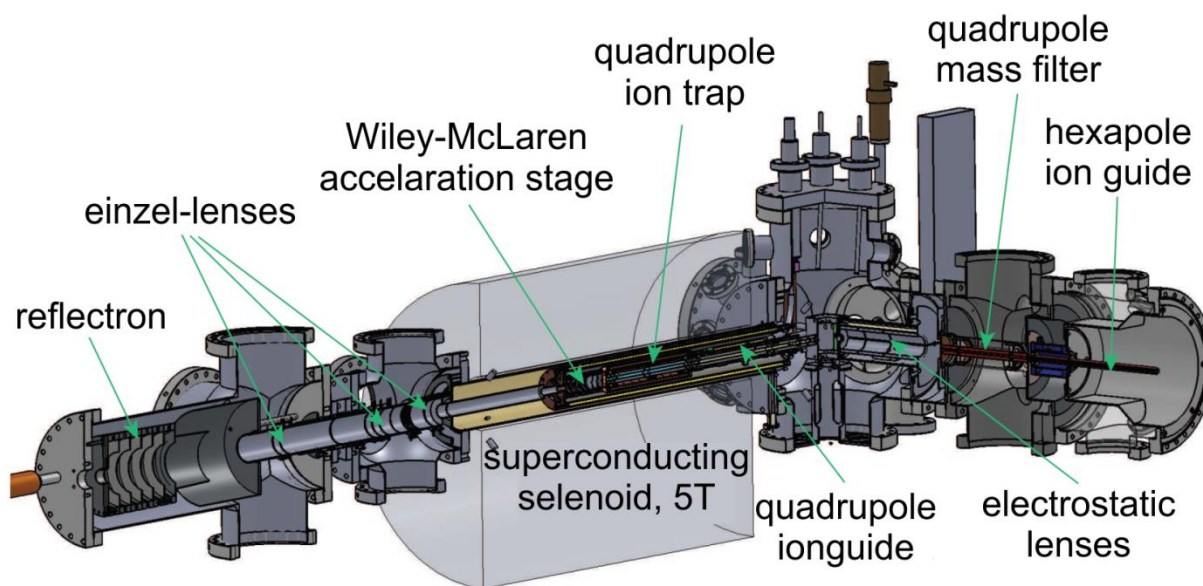


Figure 6.4 NanoClusterTrap setup^[113]

The setup was designed and built by the groups of Tobias Lau and Bernd von Issendorff. The magnet is provided by Akira Terasaki. The drawing shows the major building blocks of the instrument, i.e. ion guides, the linear quadrupole ion trap and the time of flight mass spectrometer. A cluster source is not attached in this drawing.

The trap is surrounded by cooling shields, one cooled by liquid nitrogen and the other by liquid helium. Helium buffer gas which is cooled by heat exchange is added to the trap. It is used to force the ions on axis and to cool the trapped ions down to the desired temperature. The trap electrodes are actively coupled to the helium reservoir. Nevertheless, the RF of the ion trap heats up the stored ions. The cluster temperature is higher than the reading of the temperature sensor located at the side electrodes of the ion trap. A temperature reading of 5 K at the side electrodes translates into a cluster temperature of approximately 12 ± 3 K^[113]. An additional dipole RF field tuned to the cyclotron frequency of He^+ is applied to the trap's electrodes to eject He^+ ions from the trap. During the admittance of the x-ray beam into the trap, He atoms are ionized by direct photoionization. This process has a low cross section but the high number of He atoms present in the trap compensates for the low cross section. The high density of He^+ ions is problematic because it can suppress the cluster signal and spark discharges^[113,114].

A modified reflectron time of flight (ToF) mass spectrometer is used for the recording of the Total Ion Yield (TIY) spectra. If monoenergetic ions are accelerated by an electric field, the electric energy is transformed into kinetic energy. All ions have the same kinetic energy. In a field-free region, the ions disperse according to their mass-to-charge ratio. The standard^[116-118] reflectron ToF mass spectrometer was modified by Bernd von Issendorff with three einzel-lenses located within the first

drift region of the flight tube. This modification became necessary because the first part of the drift region is located within the inhomogeneous field of the magnet. The einzel-lenses can be used to correct perturbations of the ion trajectories caused by the magnetic field. A GaAsP diode is used to record the incident photon flux during the experiment. The NanoClusterTrap was attached to the UE52-PGM beamline at the synchrotron BESSY II/HZB.

6.3 [Fe₄Ln₂] Single Molecule Magnets

A new cyclic coordination complex with an [Fe₄Ln₂] core was synthesized in the group of A. Powell. Its structure is based on the so called ferric wheel^[119,120].

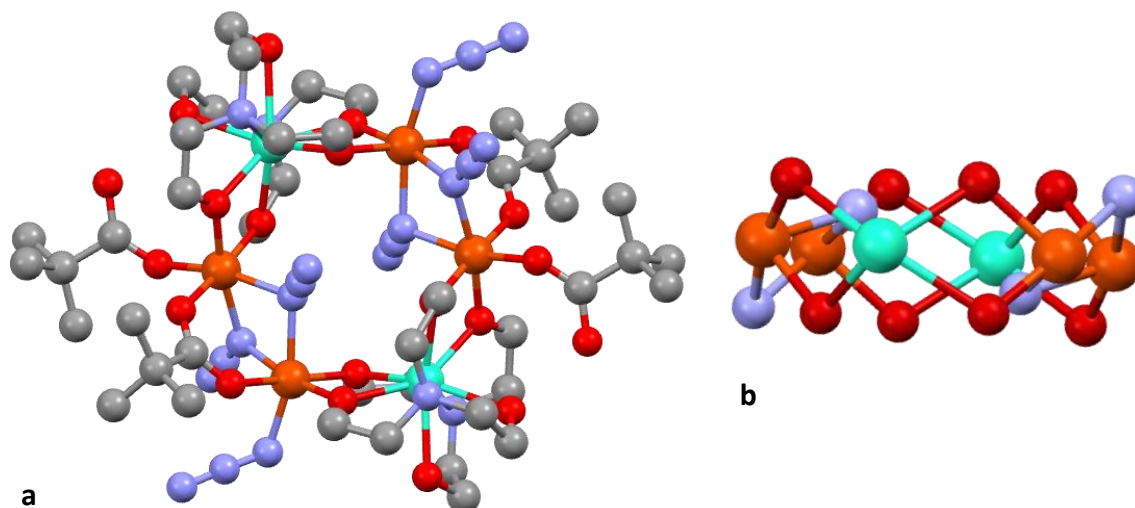


Figure 6.5 (a) molecular structure of [Fe₄Ln₂] ([Fe^{III}₄Ln^{III}₂(Htea)₄(piv)₆(N₃)₄]; teaH₃ = triethanolamine; pivH = pivalic acid), hydrogens are omitted for clarity **(b)** Fe₄Ln₂ core of the wheel highlighting the planar arrangement of the metal ions. (Ln = light green, Fe = orange, O = red, N = purple, C = grey)^[19,47,48]

The central ring is built up by two [Fe^{III}₂(N₃)₂(piv)₃]⁺ dimers which are bridge by two lanthanide centers (Fig. 6.5). The iron dimers consist of two Fe^{III} (hs) ions. Each lanthanide cation has an octa coordination geometry provided by two nitrogen atoms and six oxygen atoms. The coordination geometry can best be described as distorted square antiprismatic^[47]. The nitrogen atoms are provided by the triethanolamine molecules which form the bridges to the Fe ions. The Fe ions are octahedrally coordinated in a cis N₂O₄ geometry^[47]. The complex has been synthesized in several compositions by exchanging the lanthanide ion (Ln = Er, Lu, Gd, Tb, Dy, Ho) and investigating the resulting changes of the magnetic properties. The Fe-Fe coupling in the two dimers is ferromagnetic.

However, the coupling of the dimers across the lanthanide bridge to each other depends on the lanthanide ion present in the complex^[47,48]. We had access to the [Fe₄Gd₂] (Gd = 4f⁷ 5d¹ 6s²) and [Fe₄Tb₂] (Tb = [Xe] 4f⁹ 6s²) complex. The coupling across the lanthanide is ferromagnetic for both lanthanides according to the group of A. Powell^[48].

6.3.1 X-ray absorption spectra of [Fe₄Tb₂]⁺ and [Fe₄Gd₂]⁺

We recorded the x-ray absorption spectrum of [Fe₄Tb₂]⁺ with horizontally polarized light at the iron L_{2,3} edge. The spectrum was taken at room temperature and without external magnetic field (Fig. 6.7). The spectrum shows two energetically separated transitions which are the L₃ and L₂ edges. The splitting of the edges of about 10 eV corresponds to the spin orbit splitting of the 2p_{1/2} and 2p_{3/2} levels. The iron ions are in an octahedral coordination geometry with four oxygen and two nitrogen atoms coordinated to each iron ion (Fig. 6.5a and inset Fig. 6.6).

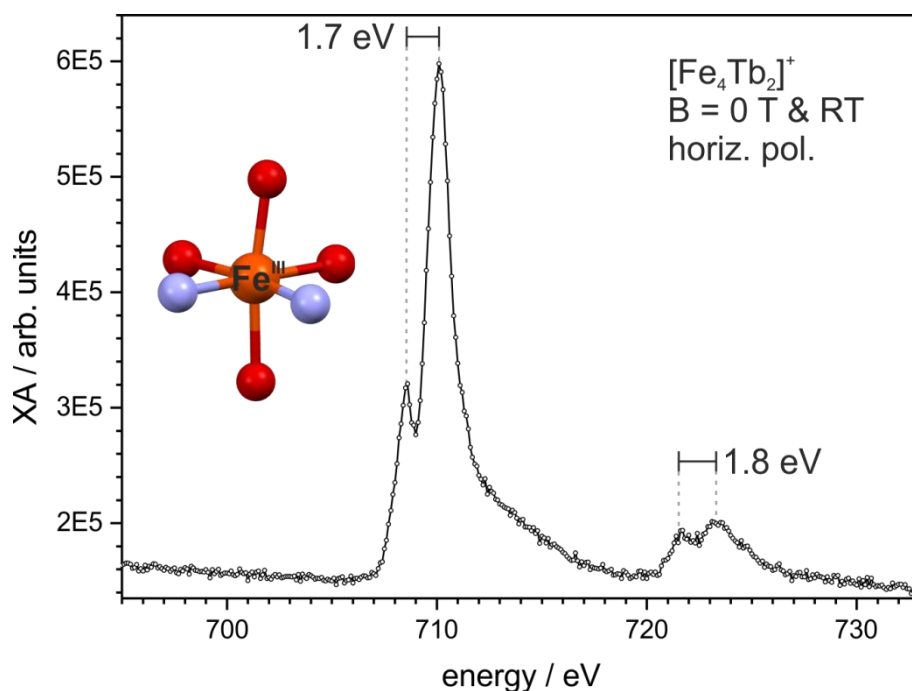


Figure 6.6 XA spectrum of [Fe₄Tb₂]⁺ recorded at the iron L_{2,3} edge with horizontally polarized x-rays at room temperature and without magnetic field (energy resolution approx. 250 meV). The splitting of the L₂ and L₃ edges into two peaks is due to a multiplett splitting. The shape of the edges is typical for a distorted octahedral coordination of an Fe^{III} hs state^[33,39,40]. The inset shows the *cis*-N₂O₄ coordination environment of the iron ions^[19,47,48] (Fe = orange, O = red, N = purple).

The Fe^{III} atoms are in the high spin state^[47]. The Fe^{III} in a *O_h* symmetry has an ⁶A₁ ground state with no first-order spin orbit splitting^[33]. Therefore, the crystal field splitting 10 *Dq*^[121] is responsible for the overall shape of the spectrum^[33]. The spectrum of [Fe₄Tb₂]⁺ shows a two-peak shape which is characteristic for Fe^{III} high spin complexes^[33,39,40]. The splitting of the peaks is about 1.7 eV. In

octahedral Fe^{III} (hs) complexes with Fe-O and / or Fe-N coordinating ligands $10 Dq$ is known to be about 2 eV^[33,122-124]. The spectrum of the SMM Fe_4 ^[40], which contains four Fe^{III} high spin atoms, is given as comparison (Fig. 6.7). The spectral shapes of both spectra are identical thus confirming the presence of Fe^{III} (hs) ions also in the cationic complex $[\text{Fe}_4\text{Tb}_2]^+$ after the ESI process.

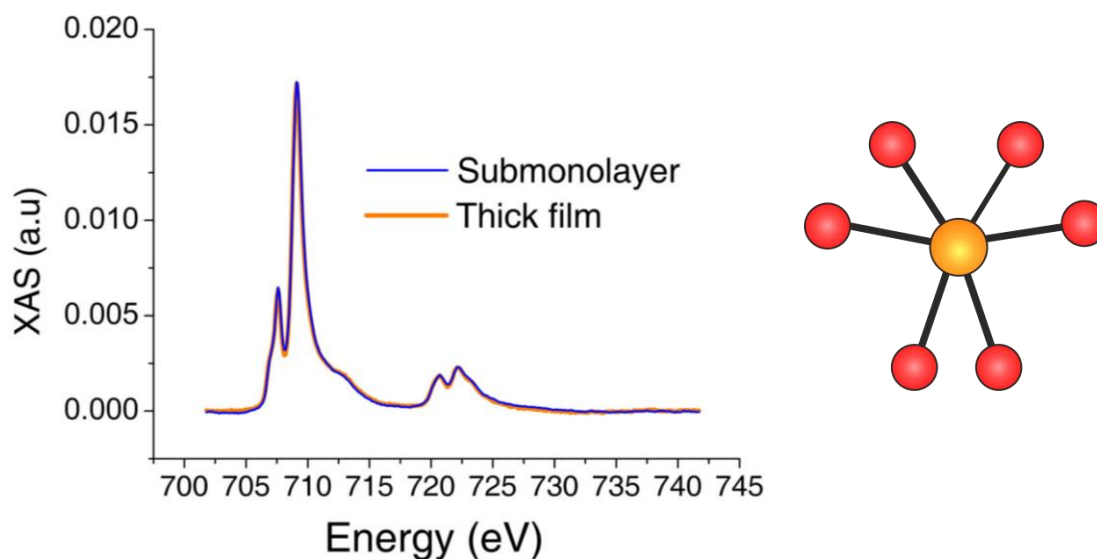


Figure 6.7 Comparison between the average XA spectra of the thick film and of the monolayer deposit of Fe_4 recorded at $T = 4.5$ K and with an induction of 5 T^[40] (taken from the suppl. material of Ref. [40]) The Fe^{III} high spin centers in the SMM Fe_4 are in a distorted octahedral coordination sphere (see inset; Fe = orange, oxygen = red) ($\text{Fe}_4 = [\text{Fe}_4(\text{L})_2(\text{dpm})_6]$; $\text{H}_3\text{L} = 11$ -(acetythio)-2,2-bis(hydroxymethyl)undecan-1-ol, Hdpm = dipivalonylmethane)

We were able to record polarization dependent XA spectra for $[\text{Fe}_4\text{Gd}_2]^+$ and $[\text{Fe}_4\text{Tb}_2]^+$ at the iron $L_{2,3}$ edges. The spectra of both complexes show the spectral shape typical for high spin Fe^{III} ions (Fig. 6.8). The spectra were recorded with a trap temperature of less than 6 K. The ion temperature after thermalization with pre-cooled He buffer gas can be estimated to be 12 - 15 K^[113]. The magnetic field was set to 5 T. The spectral features for both complexes are located at the same energies. Thus, confirming that the lanthanide ion has no significant influence on the coordination geometry of the iron atoms.

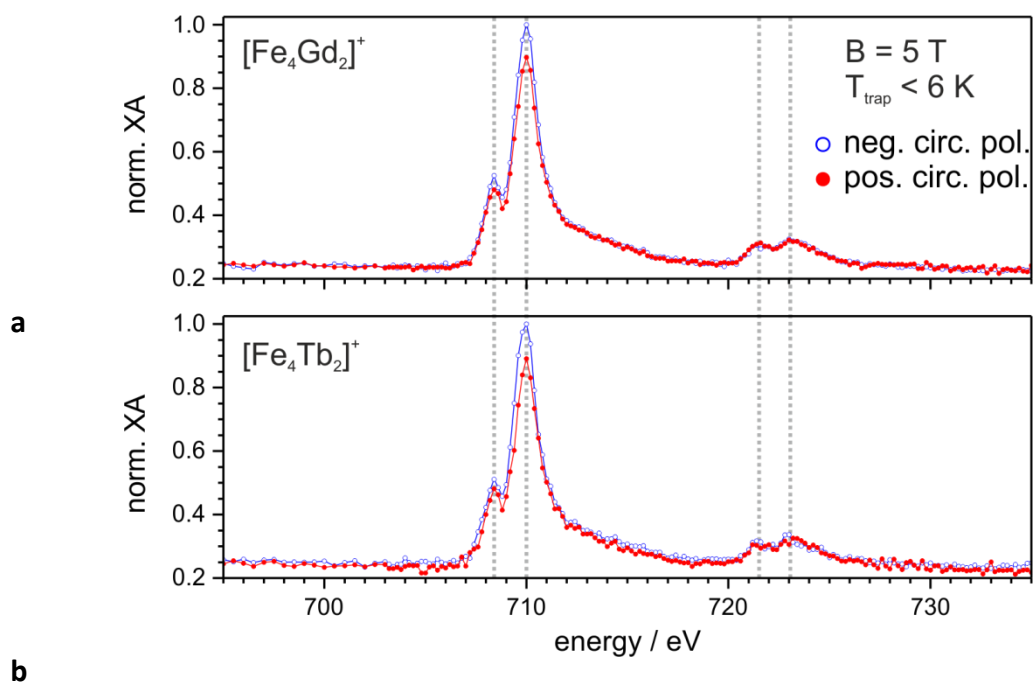


Figure 6.8 Polarization dependent XA spectra of **(a)** $[\text{Fe}_4\text{Gd}_2]^+$ and **(b)** $[\text{Fe}_4\text{Tb}_2]^+$. The spectral shapes for both complexes are identical. A small dichroic effect is visible at the L_3 edge but none at the L_2 edge. Each pair of spectra was normalized to the highest absorption intensity, i.e. the absorption intensity at the L_3 edge recorded with negative circularly polarized photons.

A small dichroic effect is visible in both spectra at the L_3 edge but none at the L_2 edge. The dichroic effect for the Tb containing complex is larger than for the Gd one (Fig. 6.9). This might be an indication that the $[\text{Fe}_4\text{Tb}_2]$ is indeed the stronger SMM as proposed by the group of A. Powell^[48]. They also proposed a ferromagnetic coupling of the two Fe_2 -units. Their proposed model is based on results from a combination of Mössbauer spectroscopy, SQUID and HF-EPR measurements. We can neither confirm nor contradict their assumptions. We need more reliable experimental conditions, than we had during recording the shown spectra (unstable x-ray beam), to be able to evaluate the XMCD spectrum by sum rule analysis. We also need to know the coupling scheme of the Fe_2 units to the lanthanide ions for a complete evaluation of the magnetic moments within the complex. The coupling of the iron centers to the lanthanide ions could not be assigned because experiments at the lanthanide $M_{4,5}$ edge ($3d \rightarrow 4f$) were not possible at the time.

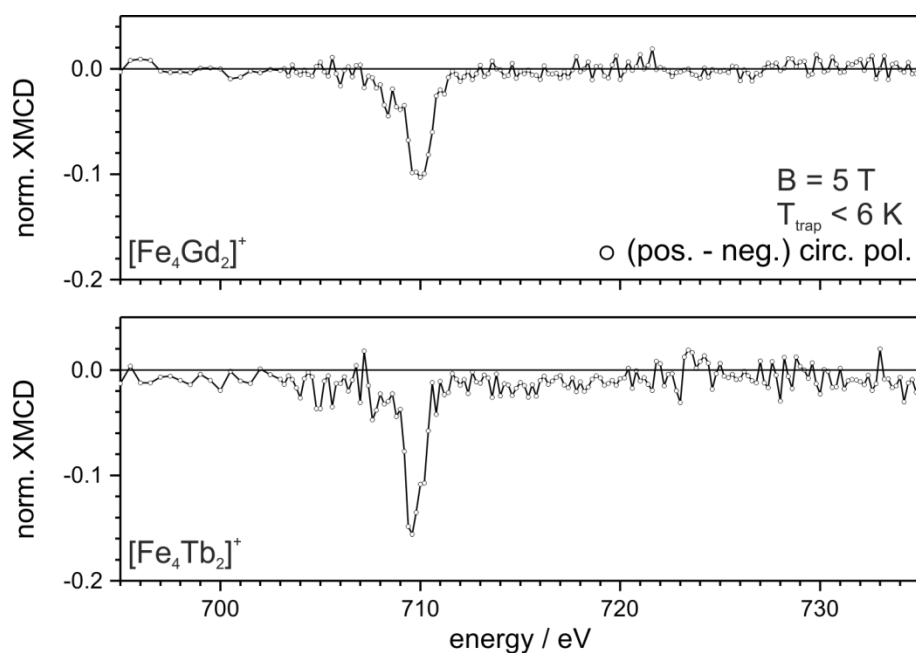


Figure 6.9 Normalized XMCD spectra of $[\text{Fe}_4\text{Gd}_2]^+$ and $[\text{Fe}_4\text{Tb}_2]^+$ at the iron $L_{2,3}$ edge. Both complexes only show a small dichroic effect at the L_3 edge at approximately 710 eV. The dichroic effect is larger for $[\text{Fe}_4\text{Tb}_2]^+$ than for $[\text{Fe}_4\text{Gd}_2]^+$.

6.4 References

- [1] SRAJER, G., LEWIS, L. H., BADER, S. D., EPSTEIN, A. J., FADLEY, C. S., FULLERTON, E. E., HOFFMANN, A., KORTRIGHT, J. B., KRISHNAN, K. M., MAJETICH, S. A., RAHMAN, T. S., ROSS, C. A., SALAMON, M. B., SCHULLER, I. K., SCHULTHESS, T. C., SUN, J. Z., *Advances in nanomagnetism via X-ray techniques*, Journal of Magnetism and Magnetic Materials **2006**, 307, 1.
- [2] *Lecture Notes Magnetism goes Nano: Electron Correlation, Spin Transport, Molecular Magnetism*; Forschungszentrum Jülich in der Helmholtz Gemeinschaft, **2005**.
- [3] FREEMAN, A. J., WU, R.-Q., *Electronic structure theory of surface, interface and thin-film magnetism*, Journal of Magnetism and Magnetic Materials **1991**, 100, 497.
- [4] FREEMAN, A. J., BADER, S. D., *Magnetism beyond 2000*, Journal of Magnetism and Magnetic Materials **2003**, 200, 1999.
- [5] SESSOLI, R., GATTESCHI, D., CANESCHI, A., NOVAK, M. A., *Magnetic bistability in a metal ion cluster*, Nature **1993**, 365, 141.
- [6] GATTESCHI, D., *Molecular Magnetism: A basis for new materials*, Advanced Materials **1994**, 6, 635.
- [7] *Localized and itinerant Molecular Magnetism: From Molecular Assemblies to the Devices*; CORONADO, E., DELHAËS, P., GATTESCHI, D., MILLER, J., Eds.; Kluwer Academic Publishers: Dordrecht, **1996**; Vol. 321.
- [8] SCHNACK, J., *Lecture Notes Magnetism goes Nano - Electron Correlations, Spin Transport, Molecular Magnetism*, Quantum Theory of Molecular Magnetism; Forschungszentrum Jülich in der Helmholtz Gemeinschaft, **2005**.
- [9] LEUENBERGER, M. N., LOSS, D., *Quantum computing in molecular magnets*, Nature **2001**, 410, 789.

- [10] WANG, X., ZANARDI, P., *Quantum entanglement and Bell inequalities in Heisenberg spin chains*, Physics Letters A **2002**, 301, 1.
- [11] LEE, C.-F., LEIGH, D. A., PRITCHARD, R. G., SCHULTZ, D., TEAT, S. J., TIMCO, G. A., WINPENNY, R. E. P., *Hybrid organic-inorganic rotaxanes and molecular shuttles*, Nature **2009**, 458, 314.
- [12] AROMI, G., AGUILA, D., GAMEZ, P., LUIS, F., ROUBEAU, O., *Design of magnetic coordination complexes for quantum computing*, Chemical Society Reviews **2012**, 41, 537.
- [13] CANESCHI, A., GATTESCHI, D., SESSOLI, R., BARRA, A. L., BRUNEL, L. C., GUILLOT, M., *Alternating-current susceptibility, high-field magnetization, and millimeter band EPR evidence for a ground $S = 10$ state in $Mn_{12}O_{12}(CH_3COO)_{16}(H_2O)_4 \cdot 2CH_3COOH \cdot 4H_2O$* , Journal of the American Chemical Society **1991**, 113, 5873.
- [14] WERNSDORFER, W., *Adv. Chem. Phys.*, Classical and Quantum Magnetization Reversal Studied in Nanometer-Sized Particles and Clusters; John Wiley & Sons, Inc., **2007**; pp 99.
- [15] GATTESCHI, D. S., ROBERTA; VILLIAN JACQUES, *Molecular Nanomagnets*; Oxford University Press, **2006**.
- [16] GATTESCHI, D., SESSOLI, R., *Quantum tunneling of magnetization and related phenomena in molecular materials*, Angew. Chem., Int. Ed. **2003**, 42, 268.
- [17] CANESCHI, A., GATTESCHI, D., SANGREGORIO, C., SESSOLI, R., SORACE, L., CORNIA, A., NOVAK, M. A., PAULSEN, C., WERNSDORFER, W., *The molecular approach to nanoscale magnetism*, J. Magn. Magn. Mater. **1999**, 200, 182.
- [18] LIS, T., *Preparation, structure, and magnetic properties of a dodecanuclear mixed-valence manganese carboxylate*, Acta Crystallographica Section B **1980**, 36, 2042.
- [19] *X-ray diffraction experiments by S. Schmidt, AK Powell, Karlsruhe Institute of Technology.*
- [20] MANNINI, M., SAINCTAVIT, P., SESSOLI, R., CARTIER DIT MOULIN, C., PINEIDER, F., ARRIO, M.-A., CORNIA, A., GATTESCHI, D., *XAS and XMCD Investigation of Mn₁₂ Monolayers on Gold*, Chemistry – A European Journal **2008**, 14, 7530.
- [21] SESSOLI, R., *Chilling with Magnetic Molecules*, Angew. Chem., Int. Ed. **2012**, 51, 43.
- [22] STAMATATOS, T. C., TEAT, S. J., WERNSDORFER, W., CHRISTOU, G., *Enhancing the Quantum Properties of Manganese-Lanthanide Single-Molecule Magnets: Observation of Quantum Tunneling Steps in the Hysteresis Loops of a {Mn₁₂Gd} Cluster*, Angewandte Chemie-International Edition **2009**, 48, 521.
- [23] PEDERSON, M. R., KHANNA, S. N., *Electronic structure and magnetism of Mn₁₂O₁₂ clusters*, Phys. Rev. B: Condens. Matter Mater. Phys. **1999**, 59, R693.
- [24] PEDERSON, M. R., KHANNA, S. N., *Magnetic anisotropy barrier for spin tunneling in Mn₁₂O₁₂ molecules*, Physical Review B **1999**, 60, 9566.
- [25] MANNINI, M., PINEIDER, F., SAINCTAVIT, P., JOLY, L., FRAILE-RODRÍGUEZ, A., ARRIO, M.-A., CARTIER DIT MOULIN, C., WERNSDORFER, W., CORNIA, A., GATTESCHI, D., SESSOLI, R., *X-Ray Magnetic Circular Dichroism Picks out Single-Molecule Magnets Suitable for Nanodevices*, Advanced Materials **2009**, 21, 167.
- [26] NOVAK, M. A., SESSOLI, R., Nato Advanced Science Institutes Series, Series E, Applied Sciences, *Quantum Tunneling of Magnetization - Qtm '94*, AC susceptibility relaxation studies on a manganese organic cluster compound: Mn₁₂-ac, Gunther, L., Barbara, B., Eds., **1995** Vol. 301; pp 171.
- [27] NOVAK, M. A., SESSOLI, R., CANESCHI, A., GATTESCHI, D., *Magnetic properties of a Mn cluster organic compound*, J. Magn. Magn. Mater. **1995**, 146, 211.
- [28] SESSOLI, R., MANNINI, M., PINEIDER, F., CORNIA, A., SAINCTAVIT, P., *XAS and XMCD of single molecule magnets*, Springer Proc. Phys. **2010**, 133, 279.

- [29] SESSOLI, R., TSAI, H. L., SCHAKE, A. R., WANG, S., VINCENT, J. B., FOLTING, K., GATTESCHI, D., CHRISTOU, G., HENDRICKSON, D. N., *High-spin molecules: [Mn₁₂O₁₂(O₂CR)₁₆(H₂O)₄]*, Journal of the American Chemical Society **1993**, *115*, 1804.
- [30] THOMAS, L., LIONTI, F., BALLOU, R., GATTESCHI, D., SESSOLI, R., BARBARA, B., *Macroscopic quantum tunnelling of magnetization in a single crystal of nanomagnets*, Nature **1996**, *383*, 145.
- [31] VAN, W. C., *Magnetic anisotropy from density functional calculations. Comparison of different approaches: Mn₁₂O₁₂ acetate as a test case*, J. Chem. Phys. **2009**, *130*, 194109/1.
- [32] BARRA, A. L., *High- and multi-frequency EPR study of Mn₁₂: A new technique for studying new objects*, Inorg. Chim. Acta **2008**, *361*, 3564.
- [33] GHIGNA, P., CAMPANA, A., LASCIALFARI, A., CANESCHI, A., GATTESCHI, D., TAGLIAFERRI, A., BORGATTI, F., *X-ray magnetic-circular-dichroism spectra on the superparamagnetic transition-metal ion clusters Mn-12 and Fe-8*, Physical Review B **2001**, *64*.
- [34] GHIGNA, P., CAMPANA, A., LASCIALFARI, A., CANESCHI, A., GATTESCHI, D., TAGLIAFERRI, A., BORGATTI, F., *X-ray magnetic-circular-dichroism spectra of the superparamagnetic transition-metal ion clusters Mn₁₂ and Fe₈. [Erratum to document cited in CA136:47067]*, Phys. Rev. B: Condens. Matter Mater. Phys. **2002**, *65*, 109903/1.
- [35] LETARD, I., SAINCTAVIT, P., CARTIER, C., KAPPLER, J.-P., GHIGNA, P., GATTESCHI, D., DODDI, B., *Remnant magnetization of Fe₈ high-spin molecules: X-ray magnetic circular dichroism at 300 mK*, J. Appl. Phys. **2007**, *101*, 113920/1.
- [36] WIEGHARDT, K., POHL, K., JIBRIL, I., HUTTNER, G., *Hydrolysis products of the monomeric amine complex (C₆H₁₅N₃)FeCl₃ - The structure of the octameric iron(III) cation of (C₆H₁₅N₃)₆Fe₈(μ-3-O)(μ-2-OH)₁₂Br₇(H₂O)Br₈(H₂O)*, Angewandte Chemie-International Edition in English **1984**, *23*, 77.
- [37] BARRA, A. L., DEBRUNNER, P., GATTESCHI, D., SCHULZ, C. E., SESSOLI, R., *Superparamagnetic-like behavior in an octanuclear iron cluster*, Europhysics Letters **1996**, *35*, 133.
- [38] CIANCHI, L., DEL GIALLO, F., SPINA, G., REIFF, W., CANESCHI, A., *Spin dynamics study of magnetic molecular clusters by means of Mossbauer spectroscopy*, Physical Review B **2002**, *65*.
- [39] PERFETTI, M., PINEIDER, F., POGGINI, L., OTERO, E., MANNINI, M., SORACE, L., SANGREGORIO, C., CORNIA, A., SESSOLI, R., *Grafting Single Molecule Magnets on Gold Nanoparticles*, Small **2014**, *10*, 323.
- [40] MANNINI, M., PINEIDER, F., SAINCTAVIT, P., DANIELI, C., OTERO, E., SCIANCALEPORE, C., TALARICO, A. M., ARRIO, M.-A., CORNIA, A., GATTESCHI, D., SESSOLI, R., *Magnetic memory of a single-molecule quantum magnet wired to a gold surface*, Nat. Mater. **2009**, *8*, 194.
- [41] KAROTISIS, G., KENNEDY, S., TEAT, S. J., BEAVERS, C. M., FOWLER, D. A., MORALES, J. J., EVANGELISTI, M., DALGARNO, S. J., BRECHIN, E. K., *Mn₄(III)Ln₄(III) Calix 4 arene Clusters as Enhanced Magnetic Coolers and Molecular Magnets*, Journal of the American Chemical Society **2010**, *132*, 12983.
- [42] MEREACRE, V., LAN, Y., CLERAC, R., AKO, A. M., WERNSDORFER, W., BUTH, G., ANSON, C. E., POWELL, A. K., *Contribution of Spin and Anisotropy to Single Molecule Magnet Behavior in a Family of Bell-Shaped Mn₁₁Ln₂ Coordination Clusters*, Inorganic Chemistry **2011**, *50*, 12001.
- [43] BHUNIA, A., GAMER, M. T., UNGUR, L., CHIBOTARU, L. F., POWELL, A. K., LAN, Y., ROESKY, P. W., MENGES, F., RIEHN, C., NIEDNER-SCHATTEBURG, G., *From a Dy(III) Single Molecule Magnet (SMM) to a Ferromagnetic [Mn(II)Dy(III)Mn(II)] Trinuclear Complex*, Inorganic Chemistry **2012**, *51*, 9589.
- [44] BANIODEH, A., MEREACRE, V., MAGNANI, N., LAN, Y., WOLNY, J. A., SCHUENEMANN, V., ANSON, C. E., POWELL, A. K., *Para versus meta ligand substituents as a means of directing magnetic*

- anisotropy in Fe₂Dy₂ coordination clusters*, Chem. Commun. (Cambridge, U. K.) **2013**, 49, 9666.
- [45] MEREACRE, V., BANIODEH, A., ANSON, C. E., POWELL, A. K., *Effect of Ligand Substitution on the Interaction Between Anisotropic Dy(III) Ions and Fe-57 Nuclei in Fe₂Dy₂ Coordination Clusters*, Journal of the American Chemical Society **2011**, 133, 15335.
- [46] LINH, P., ABBOUD, K. A., WERNSDORFER, W., CHRISTOU, G., *Synthesis, structure and magnetic properties of Fe₄(III)Ln₂(III) (Ln = Gd, Tb, Dy, Ho) and (Fe₄Y₂III)-Y-III clusters*, Polyhedron **2013**, 66, 205.
- [47] SCHMIDT, S., PRODIUS, D., NOVITCHI, G., MEREACRE, V., KOSTAKIS, G. E., POWELL, A. K., *Ferromagnetic heteronuclear {Fe₄(Er,Lu)₂} cyclic coordination clusters based on ferric wheels*, Chemical Communications **2012**, 48, 9825.
- [48] SCHMIDT, S., KOO, C., PRODIUS, D., MEREACRE, V., ANSON, C., KOSTAKIS, G. E., NOVITCHI, G., PARK, J., HEERMAN, D. W., KLINGELER, R., POWELL, A. K., *Combined magnetic susceptibility, HF-ESR and ⁵⁷Fe Mössbauer measurements on a ferromagnetic FeLn single molecule magnet* conference poster, **2013**
- [49] CORRADINI, V., GHIRRI, A., GARLATTI, E., BIAGI, R., DE RENZI, V., DEL PENNINO, U., BELLINI, V., CARRETTA, S., SANTINI, P., TIMCO, G., WINPENNY, R. E. P., AFFRONTI, M., *Magnetic Anisotropy of Cr₇Ni Spin Clusters on Surfaces*, Advanced Functional Materials **2012**, 22, 3706.
- [50] DREISER, J., PEDERSEN, K. S., BIRK, T., SCHAU-MAGNUSSEN, M., PIAMONTEZE, C., RUSPONI, S., WEYHERMUELLER, T., BRUNE, H., NOLTING, F., BENDIX, J., *X-ray Magnetic Circular Dichroism (XMCD) Study of a Methoxide-Bridged Dy-III-Cr-III Cluster Obtained by Fluoride Abstraction from cis-[(CrF₂)-F-III(phen)₂]⁺*, Journal of Physical Chemistry A **2012**, 116, 7842.
- [51] DREISER, J., PEDERSEN, K. S., PIAMONTEZE, C., RUSPONI, S., SALMAN, Z., ALI, M. E., SCHAU-MAGNUSSEN, M., THUESSEN, C. A., PILIGKOS, S., WEIHE, H., MUTKA, H., WALDMANN, O., OPPENEER, P., BENDIX, J., NOLTING, F., BRUNE, H., *Direct observation of a ferri-to-ferromagnetic transition in a fluoride-bridged 3d-4f molecular cluster*, Chemical Science **2012**, 3, 1024.
- [52] MORONI, R., CARTIER, D. M. C., CHAMPION, G., ARRIO, M. A., SAINTAVIT, P., VERDAGUER, M., GATTESCHI, D., *X-ray magnetic circular dichroism investigation of magnetic contributions from Mn(III) and Mn(IV) ions in Mn₁₂-ac*, Phys. Rev. B: Condens. Matter Mater. Phys. **2003**, 68, 064407/1.
- [53] MORONI, R., GHIGNA, P., BONACCHI, D., CANESCHI, A., ROVAI, D., *X-ray magnetic circular dichroism investigation of the superparamagnetic transition-metal ion-cluster r-Mn₁₂Bz*, Inorg. Chim. Acta **2008**, 361, 3887.
- [54] MORO, F., BIAGI, R., CORRADINI, V., EVANGELISTI, M., GAMBARDELLA, A., DE, R. V., DEL, P. U., CORONADO, E., FORMENT-ALIAGA, A., ROMERO, F. M., *Electronic and Magnetic Properties of Mn₁₂ Molecular Magnets on Sulfonate and Carboxylic Acid Prefunctionalized Gold Surfaces*, J. Phys. Chem. C **2012**, 116, 14936.
- [55] MORO, F., CORRADINI, V., EVANGELISTI, M., BIAGI, R., DE, R. V., DEL, P. U., CEZAR, J. C., INGLIS, R., MILIOS, C. J., BRECHIN, E. K., *Addressing the magnetic properties of sub-monolayers of single-molecule magnets by X-ray magnetic circular dichroism*, Nanoscale **2010**, 2, 2698.
- [56] BADÍA-ROMANO, L., BARTOLOMÉ, F., BARTOLOMÉ, J., LUZÓN, J., PRODIUS, D., TURTA, C., MEREACRE, V., WILHELM, F., ROGALEV, A., *Field-induced internal Fe and Ln spin reorientation in butterfly {Fe₃LnO₂} (Ln = Dy and Gd) single-molecule magnets*, Physical Review B **2013**, 87, 184403.
- [57] CHABOY, J., BARTOLOME, F., GARCIA, L. M., CIBIN, G., *Evidence of quadrupolar transitions in the circular dichroism at the neodymium L₂ and L₃ edges*, Physical Review B **1998**, 57, R5598.

- [58] CHABOY, J., MARCELLI, A., GARCIA, L. M., BARTOLOME, J., KUZMIN, M., MARUYAMA, H., KOBAYASHI, K., KAWATA, H., IWAZUMI, T., *X-ray circular magnetic dichroism (XMCD) as a probe of the dynamics of the spin reorientation transitions in Nd₂Fe₁₄B and Er₂Fe₁₄B systems*, *Europhysics Letters* **1994**, *28*, 135.
- [59] HAMAMATSU, T., YABE, K., TOWATARI, M., OSA, S., MATSUMOTO, N., RE, N., POCHABA, A., MROZINSKI, J., GALLANI, J.-L., BARLA, A., IMPERIA, P., PAULSEN, C., KAPPLER, J.-P., *Magnetic interactions in Cu(II)-Ln(III) cyclic tetranuclear complexes: Is it possible to explain the occurrence of SMM behavior in Cu-II-Tb-III and Cu-II-Dy-III complexes?*, *Inorganic Chemistry* **2007**, *46*, 4458.
- [60] MANNINI, M., TANCINI, E., SORACE, L., SAINCTAVIT, P., ARRIO, M.-A., QIAN, Y., OTERO, E., CHIAPPE, D., MARGHERITI, L., CEZAR, J. C., SESSOLI, R., CORNIA, A., *Spin Structure of Surface-Supported Single-Molecule Magnets from Isomorphous Replacement and X-ray Magnetic Circular Dichroism*, *Inorganic Chemistry* **2011**, *50*, 2911.
- [61] GRUMBACH, N., BARLA, A., JOLY, L., DONNIO, B., ROGEZ, G., TERAZZI, E., KAPPLER, J. P., GALLANI, J. L., *Loss of single-molecule-magnet behavior of a Mn₁₂-based compound assembled in a monolayer*, *Eur. Phys. J. B* **2010**, *73*, 103.
- [62] PEREDKOV, S., NEEB, M., EBERHARDT, W., MEYER, J., TOMBERS, M., KAMPSCHULTE, H., NIEDNER-SCHATTEBURG, G., *Spin and Orbital Magnetic Moments of Free Nanoparticles*, *Physical Review Letters* **2011**, *107*, 233401.
- [63] PEREDKOV, S., SAVCI, A., PETERS, S., NEEB, M., EBERHARDT, W., KAMPSCHULTE, H., MEYER, J., TOMBERS, M., HOFFERBERTH, B., MENGES, F., NIEDNER-SCHATTEBURG, G., *X-ray absorption spectroscopy of mass-selected transition metal clusters using a cyclotron ion trap: An experimental setup for measuring XMCD spectra of free clusters*, *Journal of Electron Spectroscopy and Related Phenomena* **2011**, *184*, 113.
- [64] HIRSCH, K., ZAMUDIO-BAYER, V., LANGENBERG, A., NIEMEYER, M., LANGBEHN, B., MOELLER, T., TERASAKI, A., ISSENDORFF, B. V., LAU, J. T., *Magnetic moments of chromium-doped gold clusters. The Anderson impurity model in finite systems*, *arXiv.org, e-Print Arch., Phys.* **2013**, *1*.
- [65] LANGENBERG, A., HIRSCH, K., LAWICKI, A., ZAMUDIO-BAYER, V., NIEMEYER, M., CHMIELA, P., LANGBEHN, B., TERASAKI, A., ISSENDORFF, B. V., LAU, J. T., *Spin and orbital magnetic moments of size-selected iron, cobalt, and nickel clusters and their link to the bulk phase diagrams*, *arXiv.org, e-Print Arch., Phys.* **2014**, *1*.
- [66] NIEMEYER, M., HIRSCH, K., ZAMUDIO-BAYER, V., LANGENBERG, A., VOGEL, M., KOSSICK, M., EBRECHT, C., EGASHIRA, K., TERASAKI, A., MÖLLER, T., V. ISSENDORFF, B., LAU, J. T., *Spin Coupling and Orbital Angular Momentum Quenching in Free Iron Clusters*, *Physical Review Letters* **2012**, *108*, 057201.
- [67] ZAMUDIO-BAYER, V., LEPPERT, L., HIRSCH, K., LANGENBERG, A., RITTMANN, J., KOSSICK, M., VOGEL, M., RICHTER, R., TERASAKI, A., MOELLER, T., VON, I. B., KUEMMEL, S., LAU, J. T., *Coordination-driven magnetic-to-nonmagnetic transition in manganese doped silicon clusters*, *Physical Review B* **2013**, *88*, 165402.
- [68] HIRSCH, K., ZAMUDIO-BAYER, V., AMESSEDER, F., LANGENBERG, A., RITTMANN, J., VOGEL, M., MOLLER, T., VON ISSENDORFF, B., LAU, J. T., *2p x-ray absorption of free transition-metal cations across the 3d transition elements: Calcium through copper*, *Physical Review A* **2012**, *85*.
- [69] *Mass Spectrometry in Drug discovery*; ROSSI, D. T., SINZ, M. W., Eds.; Marcel Dekker: New York, **2002**.
- [70] ARDREY, R. E., *Liquid Chromatography-Mass Spectrometry - An Introduction*; Wiley: Chichester, **2003**.

- [71] SIUZAK, G., *The expanding role of mass spectrometry in biotechnology*, 2nd ed.; MCC Press: San Diego, **2006**.
- [72] *Modern Mass Spectrometry*; SCHALLEY, C. A., Ed.; Springer: New York, **2003**.
- [73] GROSS, J. H., *Mass Spectrometry*; Springer, **2011**.
- [74] FENN, J., MANN, M., MENG, C., WONG, S., WHITEHOUSE, C., *Electrospray ionization for mass spectrometry of large biomolecules*, *Science* **1989**, *246*, 64.
- [75] FENN, J. B., MANN, M., MENG, C. K., WONG, S. F., WHITEHOUSE, C. M., *Electrospray ionization—principles and practice*, *Mass Spectrometry Reviews* **1990**, *9*, 37.
- [76] SMITH, R. D., LOO, J. A., EDMONDS, C. G., BARINAGA, C. J., UDSETH, H. R., *New developments in biochemical mass spectrometry: electrospray ionization*, *Analytical Chemistry* **1990**, *62*, 882.
- [77] FENN, J. B., *Electrospray Wings for Molecular Elephants (Nobel Lecture)*, *Angewandte Chemie International Edition* **2003**, *42*, 3871.
- [78] COLE, R. B., *Electrospray ionization mass spectrometry: fundamentals, instrumentation, and applications*; Wiley, **1997**.
- [79] COLE, R. B., *Electrospray and MALDI mass spectrometry: fundamentals, instrumentation, practicalities and biological applications*; Wiley, **2011**.
- [80] ROHNER, T. C., LION, N., GIRAULT, H. H., *Electrochemical and theoretical aspects of electrospray ionisation*, *Physical Chemistry Chemical Physics* **2004**, *6*, 3056.
- [81] CECH, N. B., ENKE, C. G., *Practical implications of some recent studies in electrospray ionization fundamentals*, *Mass Spectrometry Reviews* **2001**, *20*, 362.
- [82] MORA, J. F. D. L., VAN BERKEL, G. J., ENKE, C. G., COLE, R. B., MARTINEZ-SANCHEZ, M., FENN, J. B., *Electrochemical processes in electrospray ionization mass spectrometry*, *Journal of Mass Spectrometry* **2000**, *35*, 939.
- [83] AMAD, M. A. H., CECH, N. B., JACKSON, G. S., ENKE, C. G., *Importance of gas-phase proton affinities in determining the electrospray ionization response for analytes and solvents*, *Journal of Mass Spectrometry* **2000**, *35*, 784.
- [84] SCHALLEY, C. A., *Supramolecular chemistry goes gas phase: the mass spectrometric examination of noncovalent interactions in host–guest chemistry and molecular recognition*, *International Journal of Mass Spectrometry* **2000**, *194*, 11.
- [85] CRISTONI, S., BERNARDI, L. R., *Development of new methodologies for the mass spectrometry study of bioorganic macromolecules*, *Mass Spectrometry Reviews* **2003**, *22*, 369.
- [86] HECK, A. J. R., VAN DEN HEUVEL, R. H. H., *Investigation of intact protein complexes by mass spectrometry*, *Mass Spectrometry Reviews* **2004**, *23*, 368.
- [87] MENGES, F., *Structure and Reactivity of Isolated Mononuclear and Oligonuclear Metal Complexes*, Doctoral thesis, **2013**, Technische Universität Kaiserslautern.
- [88] TAGHIZADEH, G. L., KERNER, C., FARSAPOUR, S., MENGES, F., SUN, Y., NIEDNER-SCHATTEBURG, G., THIEL, W. R., *C-H Activation at a Ruthenium(II) Complex - The Key Step for a Base-Free Catalytic Transfer Hydrogenation?*, *Eur. J. Inorg. Chem.* **2013**, *2013*, 4305.
- [89] LAGUTSCHENKOV, A., *Structure and reactivity of solvated transition metal ions and complexes*, Doctoral thesis, **2008**, Technische Universität Kaiserslautern.
- [90] COLTON, R., D'AGOSTINO, A., TRAEGER, J. C., *Electrospray mass spectrometry applied to inorganic and organometallic chemistry*, *Mass Spectrometry Reviews* **1995**, *14*, 79.
- [91] POON, G. K., BISSET, G. G. F., PRAKASH, M., *Electrospray ionization mass spectrometry for analysis of low-molecular-weight anticancer drugs and their analogues*, *Journal of the American Society for Mass Spectrometry* **1993**, *4*, 588.

- [92] FAVARO, S., PANDOLFO, L., TRALDI, P., *The behaviour of [Pt(η -3-allyl)XP(C₆H₅)₃] complexes in electrospray ionization conditions compared with those achieved by other ionization methods*, Rapid Communications in Mass Spectrometry **1997**, *11*, 1859.
- [93] FEICHTINGER, D., PLATTNER, D. A., *Direct Proof for O₂MnV (salen) Complexes*, Angewandte Chemie International Edition in English **1997**, *36*, 1718.
- [94] BRUINS, A. P., COVEY, T. R., HENION, J. D., *Ion spray interface for combined liquid chromatography/atmospheric pressure ionization mass spectrometry*, Analytical Chemistry **1987**, *59*, 2642.
- [95] COVEY, T. R., BRUINS, A. P., HENION, J. D., *Comparison of thermospray and ion spray mass spectrometry in an atmospheric pressure ion source*, Organic Mass Spectrometry **1988**, *23*, 178.
- [96] COVEY, T. R., BONNER, R. F., SHUSHAN, B. I., HENION, J., BOYD, R. K., *The determination of protein, oligonucleotide and peptide molecular weights by ion-spray mass spectrometry*, Rapid Communications in Mass Spectrometry **1988**, *2*, 249.
- [97] IKONOMOU, M. G., BLADES, A. T., KEBARLE, P., *Electrospray-ion spray: a comparison of mechanisms and performance*, Analytical Chemistry **1991**, *63*, 1989.
- [98] ZELENY, J., *Instability of Electrified Liquid Surfaces*, Physical Review **1917**, *10*, 1.
- [99] TAYLOR, G., *Disintegration of Water Drops in an Electric Field*, Proceedings of the Royal Society of London. Series A. Mathematical and Physical Sciences **1964**, *280*, 383.
- [100] RAYLEIGH, L., *XX. On the equilibrium of liquid conducting masses charged with electricity*, Philosophical Magazine Series 5 **1882**, *14*, 184.
- [101] KEBARLE, P., *A brief overview of the present status of the mechanisms involved in electrospray mass spectrometry*, Journal of Mass Spectrometry **2000**, *35*, 804.
- [102] COLE, R. B., *Some tenets pertaining to electrospray ionization mass spectrometry*, Journal of Mass Spectrometry **2000**, *35*, 763.
- [103] KEBARLE, P., TANG, L., *from ions in solution to ions in the gas phase - the mechanism of electrospray mass spectrometry*, Analytical Chemistry **1993**, *65*, 972A.
- [104] DUFT, D., ACHTZEHN, T., MULLER, R., HUBER, B. A., LEISNER, T., *Coulomb fission: Rayleigh jets from levitated microdroplets*, Nature **2003**, *421*, 128.
- [105] FENN, J. B., ROSELL, J., MENG, C. K., *In electrospray ionization, how much pull does an ion need to escape its droplet prison?*, Journal of the American Society for Mass Spectrometry **1997**, *8*, 1147.
- [106] THOMSON, B. A., IRIBARNE, J. V., *Field induced ion evaporation from liquid surfaces at atmospheric pressure*, The Journal of Chemical Physics **1979**, *71*, 4451.
- [107] IRIBARNE, J. V., THOMSON, B. A., *On the evaporation of small ions from charged droplets*, The Journal of Chemical Physics **1976**, *64*, 2287.
- [108] LABOWSKY, M., FENN, J. B., FERNANDEZ DE LA MORA, J., *A continuum model for ion evaporation from a drop: effect of curvature and charge on ion solvation energy*, Analytica Chimica Acta **2000**, *406*, 105.
- [109] FELITSYN, N., PESCHKE, M., KEBARLE, P., *Origin and number of charges observed on multiply-protonated native proteins produced by ESI*, International Journal of Mass Spectrometry **2002**, *219*, 39.
- [110] DOLE, M., MACK, L. L., HINES, R. L., MOBLEY, R. C., FERGUSON, L. D., ALICE, M. B., *Molecular Beams of Macroions*, The Journal of Chemical Physics **1968**, *49*, 2240.
- [111] MACK, L. L., KRALIK, P., RHEUDE, A., DOLE, M., *Molecular Beams of Macroions. II*, The Journal of Chemical Physics **1970**, *52*, 4977.

- [112] *The Apollo™ API source: Operations manual & user's guide (version 1.0)*; Bruker Daltonics Inc., Billerica, MA, USA, **2001**.
- [113] LANGENBERG, A., *Magnetische Momente freier, massenselektierter Eisen-, Cobalt- und Nickelcluster*, Doctoral thesis, **2013**, Technische Universität Berlin.
- [114] HIRSCH, K., *Electronic and Magnetic Properties of Impurities Embedded in Non-Magnetic Finite Hosts*, Doctoral thesis, **2013**, Technische Universität Berlin.
- [115] HIRSCH, K., LAU, J. T., KLAR, P., LANGENBERG, A., PROBST, J., RITTMANN, J., VOGEL, M., ZAMUDIO-BAYER, V., MOELLER, T., VON ISSENDORFF, B., *X-ray spectroscopy on size-selected clusters in an ion trap: from the molecular limit to bulk properties*, Journal of Physics B-Atomic Molecular and Optical Physics **2009**, *42*.
- [116] BOESL, U., WEINKAUF, R., SCHLAG, E. W., *Reflectron time-of-flight mass spectrometry and laser excitation for the analysis of neutrals, ionized molecules and secondary fragments*, International Journal of Mass Spectrometry and Ion Processes **1992**, *112*, 121.
- [117] GOHL, W., KUTSCHER, R., LAUE, H. J., WOLLNIK, H., *Time-of-flight mass spectrometry for ions of large energy spread*, International Journal of Mass Spectrometry and Ion Physics **1983**, *48*, 411.
- [118] WILEY, W. C., MCLAREN, I. H., *Time of Flight Mass Spectrometer with Improved Resolution*, Review of Scientific Instruments **1955**, *26*, 1150.
- [119] TAFT, K. L., DELFS, C. D., PAPAETHYMIU, G. C., FONER, S., GATTESCHI, D., LIPPARD, S. J., *[Fe(OMe)₂(O₂CCH₂Cl)₁₀] a molecular ferris wheel*, Journal of the American Chemical Society **1994**, *116*, 823.
- [120] TAFT, K. L., LIPPARD, S. J., *Synthesis and structure of [Fe(OMe)₂(O₂CCH₂Cl)₁₀] a molecular ferric wheel*, Journal of the American Chemical Society **1990**, *112*, 9629.
- [121] VAN DER LAAN, G., THOLE, B. T., *Strong magnetic x-ray dichroism in 2p absorption spectra of 3d transition-metal ions*, Physical Review B **1991**, *43*, 13401.
- [122] PELLEGRIN, E., HAGELSTEIN, M., DOYLE, S., MOSER, H. O., FUCHS, J., VOLLATH, D., SCHUPPLER, S., JAMES, M. A., SAXENA, S. S., NIESEN, L., ROGOJANU, O., SAWATZKY, G. A., FERRERO, C., BOROWSKI, M., TJERNBERG, O., BROOKES, N. B., *Characterization of Nanocrystalline γ -Fe₂O₃ with Synchrotron Radiation Techniques*, physica status solidi (b) **1999**, *215*, 797.
- [123] PENG, G., VAN ELP, J., JANG, H., QUE, L., ARMSTRONG, W. H., CRAMER, S. P., *L-edge x-ray absorption and x-ray magnetic circular dichroism of oxygen-bridged dinuclear iron complexes*, Journal of the American Chemical Society **1995**, *117*, 2515.
- [124] KUIPER, P., SEARLE, B. G., RUDOLF, P., TJENG, L. H., CHEN, C. T., *X-ray magnetic dichroism of antiferromagnet Fe₂O₃: The orientation of magnetic moments observed by Fe 2p x-ray absorption spectroscopy*, Physical Review Letters **1993**, *70*, 1549.

7. SUMMARY & OUTLOOK

Spin and orbital magnetic moments of small isolated iron Fe_n^+ ($7 \leq n \leq 18$), cobalt Co_n^+ ($8 \leq n \leq 22$) and nickel ($7 \leq n \leq 17$) clusters were presented in this thesis. The magnetic moments were experimentally determined by x-ray magnetic circular dichroism (XMCD) spectroscopy. Extending our work done on small clusters, first gas phase x-ray absorption spectra (XAS) and XMCD experiments were carried out on Single Molecule Magnets (SMMs).

An experimental scheme had to be devised to record XA spectra of isolated clusters in the gas phase. A Fourier Transform - Ion Cyclotron Resonance (FT-ICR) mass spectrometer was used as means of detection. The commercially available instrument (Apex IV, Bruker Daltonics) had been modified to accommodate a laser vaporization source set 90° off axis with respect to the magnetic field axis which coincides with the x-ray beam axis. Additionally, a cryo ICR cell had been installed to be able to cool the ICR cell and subsequently also the clusters down to 20 K. The cryo ICR cell was designed by H. Kampschulte and first test experiments were carried out by him^[1]. The instrument was coupled to the soft x-ray undulator beamline UE52-PGM ($E_{\text{ph}} < 1500$ eV) at the synchrotron facility BESSY II at the Helmholtz Zentrum Berlin für Materialien und Energie (HZB), Berlin, Germany. Circularly polarized photons were available and the photon polarity could be switched allowing us to record XMCD spectra. An efficient cooling routine for the cluster ions had to be established prior to the recording of XMCD spectra. A pulse of helium was added as means to cool the clusters down. A series of experiments varying the amount of buffer gas was conducted to ensure a sufficient number of collisions with precooled helium gas to thermalize the cluster temperature to the helium buffer gas temperature. The amount of buffer gas was increased until the spectral shape of the XMCD spectrum did not change anymore. All spectra were recorded in Total Ion Yield (TIY) mode. The experimentally accessible magnetic moments are the projections onto the quantization axis which coincides with the magnetic field axis or in a classic picture the magnetization of the sample. Therefore, the experimental magnetic moments had to be corrected for insufficient alignment due to the finite external magnetic field and the cluster temperature of $T > 0$ K and the finite external magnetic field. This was achieved by Langevin correction of the experimental magnetic moments. The validity of this approach was proven by a series of temperature dependent experiments on Co_{11}^+ .

The spin and orbital magnetic moments of small cobalt clusters Co_n^+ ($8 \leq n \leq 22$) found by us are enhanced compared to bulk Co (hcp). The orbital magnetic moments are enhanced by a

factor of 3 - 5. The spin moment is about 50 % higher in the clusters than in the bulk. When the cluster moments are compared to the atomic values ($\text{Co}_1 = {}^3\text{F}$), both contributions are quenched in the investigated clusters, e.g. the orbital magnetic moment is only about 13 - 20 % of the atomic value. On the other hand, the spin magnetic moment retains most of its atomic value, i.e. 65 - 90 %. The enhancement of the magnetic moments in clusters relative to the bulk can be rationalized by the large surface to bulk ratio in clusters. Surface atoms have fewer nearest neighbors than bulk atoms and thus crystal field effects cannot quench the orbital angular momentum to the same extent as in the bulk. Also, the spin magnetic moment is enhanced at surfaces and thin films due to the electrons more localized character.

The spin and orbital magnetic moments m_s and m_L of the cobalt clusters in this thesis have been reevaluated with respect to a prior publication^[2] to account for a discussion about the Langevin / Brillouin correction of the experimentally determined values $m_{s,z}$ and $m_{L,z}$. The question addressed the coupling of angular moments. The discussion centered on the question if a magnetic field of 7 T is strong enough to overcome the spin orbit coupling and an individual alignment of $m_{s,z}$ and $m_{L,z}$ to the external magnetic field will result. If the spin orbit coupling is stronger than the interaction with the magnetic field, an alignment of the total angular momentum will be the case. This effects the Langevin correction in the way that either spin or orbital magnetic moments are individually scaled or the total moment is scaled. Then spin and orbital magnetic moments can be calculated from the scaled total magnetic moment due to the constant $m_{L,z} / m_{s,z} = m_L / m_s$ ratio if $m_{L,z}$ will be corrected. Our initial assumption of decoupled moments was proven wrong. The data was reevaluated by Langevin correction of the total magnetic moment. The changes after reevaluation are small for the spin magnetic moment. However, in the case of the orbital magnetic moment they are significant. The reevaluated moments are about 50% lower than the initially assumed ones.

We extended our study of the magnetism of small clusters to the clusters of the two other ferromagnetic 3d transition metals iron and nickel. Small iron Fe_n^+ ($7 \leq n \leq 18$) and nickel Ni_n^+ ($7 \leq n \leq 17$) clusters also show enhanced orbital and spin magnetic moments with respect to the bulk materials. The orbital magnetic moments again are quenched to a few percent of the atomic value comparable to cobalt. The iron cluster series shows a minimum in the spin magnetic moment for Fe_{13}^+ . This minimum can be attributed to an antiferromagnetic coupling of the central iron atom within the icosahedron to the twelve outer Fe atoms. A second theoretical model assumes a ferromagnetic coupling of the central Fe atom to the remaining Fe atoms. However, a change in the electronic structure of the central iron atom, i.e. a different occupation of the 3d orbitals, leads to a reduced spin magnetic moment. Nickel clusters show a minimum in the spin magnetic moment for Ni_{14}^+ . This is somewhat surprising as the minimum is typically expected for a thirteen atomic cluster

for which a highly symmetrical icosahedral structure is usually assumed. This is the case for the Stern-Gerlach experiments on neutral nickel clusters Ni_n . If the XMCD results are compared to those of Stern-Gerlach experiments, it becomes evident that the trend in the total magnetic moment reflects that of our measurements but for a displacement by one atom. The whole data series is shifted towards larger clusters by one atom in our nickel data with respect to the Stern-Gerlach experiments. Such a deviation cannot be found in the cases of iron or cobalt. Theory is of no help in the interpretation for nickel and cobalt up until now. There is only limited data available on the spin magnetic moments of cationic clusters which is generally about $0.5 \mu_B/\text{atom}$ too low over the by us investigated size range. The available theory on neutral clusters shows a large spread. This does not allow us to draw any meaningful conclusions. Only in the case of iron the theory is more reliable as there is a general trend within theory. However, we can compare our data to the data recently published by Lau *et al.*^[3-5]. The data sets of both experiments show a good agreement within the error bars of both experiments for most cluster sizes of three studied elements. This validates the approach of recording XMCD spectra by TIY and extracting spin and orbital magnetic moments for isolated clusters in the gas phase by sum rule analysis.

Cluster properties often follow a general trend which can be visualized as an interpolation, i.e. a scaling law, between the atomic and the bulk values. Fluctuations due to individual cluster size effects are superimposed onto the general trend for small cluster sizes in the so called non-scalable size regime. The spin and orbital magnetic moment each follow such a scaling law but interestingly not the same. The spin magnetic moment follows the well-known trend of $n^{-1/3} = 1/(\text{cluster radius})$ (n = number of atoms per cluster, assumption of a spherical particle). This trend is related to the surface to volume ratio of a spherical particle. The orbital magnetic moment, on the other hand, follows an $1/n = 1/(\text{cluster radius})^3 = 1/(\text{cluster volume})$. Is it still not known why both moments interpolate differently between the atom and bulk. We can just speculate as to why. The average spin magnetic moment per atom seems to follow the surface area of the cluster. The reduced coordination number at surfaces leads to a stronger localization of the electron wave function and thus to a narrower band width which in turn leads to a higher density of states. This leads to an enhanced magnetic moment at surfaces because of further accessible energy levels which can be filled and thus a larger imbalance of spin up and spin down holes. As we measure an averaged moment over all coordination sites, enhanced moments at surface sites will lead to an enhanced spin magnetic moment per atom compared to the bulk material. The spin magnetic moments of strong ferromagnets (filled majority band) are rather robust against changes of the surface topology^[6]. The investigated iron, cobalt and nickel clusters all have filled majority bands. This might explain why the surface area is important but that there are few individual size effects within our error bars. If the investigated size range was to be extended to larger clusters, the trend of $1/(\text{cluster radius})$ should

be become more pronounced as larger clusters develop a surface and a bulk-like core. However, the cluster geometry might still deviate from the bulk structure even for clusters containing a few hundred atoms per cluster. On the other hand, the orbital magnetic moment is much more sensitive to the coordination environment than the spin magnetic moment. Therefore, it might follow the general geometric structure of the clusters, i.e. the coordination environment, number of nearest neighbors and bond lengths, etc.. Exceptionally high or low orbital magnetic moments may appear for certain cluster geometries which have a high symmetry (small orbital magnetic moment) or an open or unsymmetrical structure (high orbital magnetic moment). In the case of the orbital magnetic moment, one might see a significant change if the geometrical motif changes e.g. from icosahedral to bulk like. Our experiments do not cover a size range which allows a final explanation of the observed trends.

From a purely experimental point of view, it would be highly desirable to enhance the duty cycle of the experiment. The time needed to pump out the He gas, which is necessary to cool down the clusters, makes the experiment extremely slow in terms of recording speed of the XA spectra. A pre-cooling of the clusters prior to injection into the ICR cell would result in a significantly faster experimental procedure. A comparable experimental setup to the Apex IV used in for the presented cluster experiments is currently being modified to pre-cool ions in a hexapole trap before transfer into the ICR cell^[7].

The element sensitivity allows the study of alloyed systems and the deduction of the contributions of the individual elements to the overall magnetic properties of the cluster. First experiments with cobalt + gold / rhodium composite systems $[\text{Co}_n\text{Rh}_1]^+$ and $[\text{Co}_n\text{Au}_1]^+$ have been done^[8]. The difference between the two heteroatoms is that rhodium is the heavier homologue of cobalt whereas gold is diamagnetic. Hence, both elements should exert a different influence on the magnetic structure of the cluster. These experiments are to be extended by adding further rhodium and gold atoms and by exchanging the cobalt by iron and nickel. Additionally, small cluster alloys with a maximum of four atoms per cluster of the elements iron, cobalt and nickel $[\text{Fe}_n\text{Co}_m\text{Ni}_l]^+$ ($n + m + l \leq 4$) are to be studied within the framework of the collaborative research center TRR88 / 3MET. The influence of an adsorbate or a support material on the magnetism of a system can be quite large. Thus, the study of these effects is of fundamental importance for future applications. In a first step, information about the electronic but also about the geometric structure can be gained by varying adsorbates from weakly binding nitrogen to strongly binding carbon monoxide. The different coordination strengths of the ligands allow an estimate about how easily the electronic and thus the magnetic structure of a certain cluster can be influenced by interactions with an environment.

Single Molecule Magnets are small magnetic entities which magnetism does not depend on any spatial arrangement, i.e. a 1D to 3D structure. The intramolecular forces dominate over the long range intermolecular interactions. Thus, each molecule (0D) is a magnet in itself. First experiments were done on isolated SMMs in the gas phase. Therefore, the NanoClusterTrap setup, operated by the group of T. Lau (HZB, Berlin, Germany), was equipped with an electrospray ionization source. First XA and XMCD spectra were recorded of SMMs $[\text{Fe}_4\text{Ln}_2]$ (Ln = Gd, Tb) containing 3d transition metal atoms and lanthanide atoms, which were synthesized in the group of A. Powell (Karlsruher Institute of Technology (KIT), Karlsruhe, Germany). Polarization dependent XA spectra at the iron $L_{2,3}$ edge could be recorded. The spectra show the typical spectral shape of Fe^{III} high spin ions. An evaluation of the spectra by sum rule analysis has not been possible yet.

The next step in the investigation of SMMs by our group will be the recording of XMCD spectra of $[\text{Fe}_4\text{Ln}_2]$ complexes which can be analyzed by sum rule analysis at the iron $L_{2,3}$ edge. If the experimental moments shall be Langevin / Brillouin corrected, the coupling of the Fe and lanthanide ions needs to be known. Therefore, an XMCD spectrum at the lanthanide $M_{4,5}$ edge has to be recorded of such quality that the coupling of the lanthanides to the iron can be deduced from the XMCD spectrum. The groups of A. Powell (KIT) and of H.-J. Krüger (University of Kaiserslautern, Kaiserslautern, Germany) synthesize and investigate magnetic molecules and spin cross over complexes in the framework of the collaborative research center TRR88/3MET. These systems will be at the focus of further investigations. Additionally to XMCD spectra at high and low temperatures, magnetization curves and temperature dependent experiments will be carried out to learn more about coupling schemes within heterogeneous system as well as blocking and cross over temperatures.

7.1 References

- [1] KAMPSCHULTE, H., *Entwicklung einer Tieftemperatur FT-ICR Zelle und ihre Charakterisierung mittels Reaktionskinetiken und Synchrotron-Spektroskopie*, Doctoral thesis, **2010**, Technische Universität Kaiserslautern.
- [2] PEREDKOV, S., NEEB, M., EBERHARDT, W., MEYER, J., TOMBERS, M., KAMPSCHULTE, H., NIEDNER-SCHATTEBURG, G., *Spin and Orbital Magnetic Moments of Free Nanoparticles*, Physical Review Letters **2011**, *107*, 233401.
- [3] LANGENBERG, A., *Magnetische Momente freier, massenselektierter Eisen-, Cobalt- und Nickelcluster*, Doctoral thesis, **2013**, Technische Universität Berlin.
- [4] LANGENBERG, A., HIRSCH, K., LAWICKI, A., ZAMUDIO-BAYER, V., NIEMEYER, M., CHMIELA, P., LANGBEHN, B., TERASAKI, A., ISSENDORFF, B. V., LAU, J. T., *Spin and orbital magnetic moments of size-selected iron, cobalt, and nickel clusters and their link to the bulk phase diagrams*, arXiv.org, e-Print Arch., Phys. **2014**, 1.

- [5] NIEMEYER, M., HIRSCH, K., ZAMUDIO-BAYER, V., LANGENBERG, A., VOGEL, M., KOSSICK, M., EBRECHT, C., EGASHIRA, K., TERASAKI, A., MÖLLER, T., v. ISSENDORFF, B., LAU, J. T., *Spin Coupling and Orbital Angular Momentum Quenching in Free Iron Clusters*, Physical Review Letters **2012**, *108*, 057201.
- [6] BLÜGEL, S., *Lecture Notes Magnetism goes Nano: Electron Correlations, Spin Transport, Molecular Magnetism*, Reduced Dimensions I - Magnetic Moment and Magnetic Structure Forschungszentrum Jülich in der Helmholtz-Gemeinschaft, **2005**.
- [7] MOHRBACH, J., *Charakterisierung ausgewählter Übergangsmetallkomplexe mittels infrarot induzierter Multiphotonendissoziation (IR-MPD) bei tiefen Temperaturen*, Diploma thesis, **2013**, Technische Universität Kaiserslautern.
- [8] content of the Doctoral thesis of M. Tombers

8. ZUSAMMENFASSUNG & AUSBLICK

Diese Dissertation befasst sich mit spin- und bahnmagnetischen Momenten kleiner isolierter Eisen- Fe_n^+ ($7 \leq n \leq 18$), Cobalt- Co_n^+ ($8 \leq n \leq 22$) und Nickelcluster Ni_n^+ ($7 \leq n \leq 17$). Die magnetischen Momente wurden experimentell mittels Röntgenzirkulardichroismus (XMCD = X-ray magnetic circular dichroism) bestimmt. Erste Röntgenabsorptions- und XMCD-Spektren in der Gasphase isolierter Einzelmolekülmagnete (Single Molecule Magnets = SMMs) wurden als Ergänzung und Weiterführung der Experimente an isolierten Übergangsmetallclustern durchgeführt.

Zunächst musste eine experimentelle Methodik zur Aufnahme von Röntgenabsorptionsspektren isolierter Cluster in der Gasphase mittels Massenspektrometrie etabliert werden. Zur Detektion der Cluster wurde ein Fourier Transform - Ionen Zyklotron Resonanz (FT-ICR) Massenspektrometer genutzt. Das kommerziell erworbene Gerät (Apex IV, Bruker Daltonic) wurde um eine Laserverdampfungsquelle ergänzt. Diese wurde um 90° versetzt zur Magnetfeldachse angebracht, welche mit der Ausbreitungsrichtung des Röntgenstrahls zusammenfällt. Weitergehend wurde eine Kryo-ICR Zelle installiert um die ICR Zelle, und damit auch die Cluster, auf bis zu 20 K zu kühlen. Der Aufbau wurde von H. Kampschulte im Rahmen seiner Promotion entwickelt und die Funktionalität mittels erster temperaturabhängiger Testexperimente überprüft^[1]. Der experimentelle Aufbau wurde mit der Undulatorbeamline UE52-PGM am Synchrotron BESSY II (Helmholtz Zentrum Berlin für Materialien und Energie, Berlin, Deutschland) verbunden. Die Beamline liefert Röntgenstrahlung im sogenannten "weichröntgen" Bereich ($E_{\text{hv}} < 1500 \text{ eV}$). Zirkular polarisierte Röntgenstrahlung ist an der UE52-PGM zugänglich und die Möglichkeit die Polarität der Photonen um zu kehren, erlaubt die Aufnahme von XMCD-Spektren. Jedoch musste vor der Aufnahme von XMCD-Spektren, eine effiziente Routine zur Kühlung der Cluster gefunden werden. Zur Thermalisierung der Cluster wurde ein Puls vorgekühltes Helium als Puffergas zugegeben. Um die Thermalisierung der Cluster auf die Temperatur des Heliumpuffergases sicherzustellen, d.h. eine genügende Anzahl von Kollisionen zwischen Clustern und Puffergas, wurde eine Reihe von Experimenten durchgeführt in denen die Gasmenge kontinuierlich erhöht wurde bis sich keine Änderungen mehr im XMCD-Spektrum ergaben. Alle Spektren wurden über die Fragmentationsintensitäten nach Absorption der Röntgenstrahlung gemessen, d.h. im sogenannten Total Ion Yield (TIY) Modus. Bei den experimentell erhaltenen magnetischen Momenten handelt sich um die Projektionen der intrinsischen Momente auf die Quantisierungsachse, welche mit der Magnetfeldachse zusammenfällt, oder um die Magnetisierung der Probe im klassischen Bild. Da die Momente unter den gegebenen

experimentellen Bedingungen von $T > 0$ K und endlichem Magnetfeld unvollständig ausgerichtet sind, müssen die intrinsischen Momente über eine Brillouin- oder Langevinkorrektur der gemessenen Werte errechnet werden. Die Anwendbarkeit dieser Methodik wurde durch eine Reihe temperaturabhängiger Experimente an Co_{11}^+ bestätigt.

Die spin- und bahnmagnetische Momente kleiner Cobaltcluster Co_n^+ ($8 \leq n \leq 22$) sind im Vergleich zum Festkörper (Co = hcp) erhöht. Das Bahnmoment ist um einen Faktor von 3 - 5 verstärkt. Das Spinmoment ist jedoch nur um ca. 50 % im Vergleich zum Festkörper erhöht. Vergleicht man hingegen die gemessenen Werte der Cluster mit den atomaren Werten ($\text{Co}_1 = {}^3\text{F}$), so stellt man fest, dass beide Anteile in den untersuchten Clustern verringert sind. Nur etwa 13 - 20 % des atomaren Orbitalmoments bleiben im Cluster erhalten. Im Gegensatz dazu, ergibt sich für das Spinmoment ein Anteil von circa 65 - 90 % des atomaren Wertes. Durch das größere Oberflächen-zu-Festkörper-Verhältnis lassen sich die erhöhten spin- und bahnmagnetischen Momente in Clustern im Vergleich zum Festkörper verstehen. Oberflächenatome weisen in der Regel eine geringere Koordinationszahl auf als Atome im Inneren des Festkörpers. Daher können Kristallfeld- und Ligandeneffekte das Bahnmoment an der Oberfläche nicht so effektiv aufheben wie im Inneren des Festkörpers. Die stärkere Lokalisation der Elektronen an der Oberfläche führt in einer komplexen Form ebenfalls zu einem erhöhten Spinmoment für Oberflächenatome.

Im Vergleich zu bereits publizierten Werten^[2], wurden die intrinsischen Spin und Bahnmomente kleiner Cobaltcluster, im Rahmen dieser Arbeit nochmals neu berechnet, d.h. die Langevinkorrektur der experimentellen Werte nochmals durchgeführt. Diese Neuevaluierung beruht auf einer Diskussion, ob die Wechselwirkung mit den externen Magnetfeld von $B = 7$ T stark genug ist, um die Spinbahnkopplung zu überwinden und Spin- und Bahnmoment zu entkoppeln. Die individuelle Ausrichtung der Spin- und Bahnmomente würde sich in einer unabhängigen Skalierung beider Momente widerspiegeln. Überwiegt die Spinbahnkopplung richtet sich das totale magnetische Moment zum externen Magnetfeld aus und dieses wird dann mittels Langevin korrigiert. Die intrinsischen spin- und bahnmagnetischen Momente können mit Hilfe des konstant bleibenden Verhältnisses von Bahn- zu Spinmoment $m_{L,z}/m_{S,z} = m_L/m_S$ berechnet werden. Die von uns ursprünglich angenommene Entkopplung der Momente stellte sich als falsch heraus. Daher wurde eine Neuevaluierung der Momente im Rahmen dieser Arbeit vorgenommen. Aufgrund der unterschiedlichen Größenordnung von Spin- und Bahnmoment, ergibt sich für das Spinmoment nur eine geringfügige Änderung. Dahingegen sind die neu skalierten Bahnmomente um circa 50 % niedriger als die ursprünglich angenommenen Werte.

Die von uns durchgeführten Experimente wurden auf die Cluster der beiden verbleibenden ferromagnetischen 3d Übergangsmetalle Eisen und Nickel ausgedehnt. Kleine Eisencluster

Fe_n^+ ($7 \leq n \leq 18$) und Nickelcluster Ni_n^+ ($7 \leq n \leq 17$) zeigen ebenfalls erhöhte Spin- und Bahnmomente im Vergleich zum jeweiligen Festkörper. Die Bahnmomente der Cluster sind wie im Falle der Cobaltcluster auf circa 10 % Prozent der atomaren Werte gequenchet. Die spinmagnetischen Momente der Eisencluster weisen ein Minimum bei Fe_{13}^+ auf. Nimmt man eine ikosaedrische Struktur mit einem zentralen, inneren Fe-Atom an, so kann das verringerte Spinmoment durch eine antiferromagnetisch Kopplung des inneren Fe-Atoms zu den äußeren zwölf Fe-Atomen zustande kommen. Ein weiteres theoretisches Modell nimmt eine vollständige ferromagnetische Ordnung im Cluster an. Allerdings, ist das Spinmoment des zentralen Fe-Atoms auf Grund einer von den äußeren Atomen abweichenden elektronischen Struktur, d.h. Besetzungsänderung der 3d Zustände, stark verringert. Da von uns ein über alle Fe-Atome gemittelttes Spinmoment gemessen wird, ergibt sich so ein Minimum für das gemittelte spinmagnetische Moment pro Cluster. Für Nickelcluster finden wir ein Minimum für das spinmagnetische Moment bei Clustergröße Ni_{14}^+ . Dieser Fund überrascht insoweit, als allgemein ein Minimum im Spinmoment für einen Cluster mit dreizehn Atomen und der damit einhergehenden Annahme einer hochsymmetrischen ikosaedrischen Struktur erwartet wird. Dies ist der Fall in Stern-Gerlach Experimenten, die an neutralen Nickelclustern durchgeführt wurden. Vergleicht man die Ergebnisse der Stern-Gerlach Experimente mit unseren Ergebnissen aus XMCD-Experimenten, so ergibt sich ein vergleichbarer Verlauf der magnetischen Momente als Funktion der Clustergröße. Jedoch ist die Kurve für unsere XMCD Experimente um ein Atom pro Cluster zu größeren Clustern im Vergleich zu den Stern-Gerlach Daten verschoben. Diese Abweichung der beiden Kurven von einander wurde weder für Cobalt noch für Eisen gefunden. Theoretische Daten stellen bisher keine Hilfe bei der Interpretation der Cobalt und Nickel Daten dar. Für kationische Cluster gibt es bisher nur eine geringe Anzahl an Studien und deren berechnete spinmagnetische Momente liegen im Allgemeinen circa $0,5 \mu_B$ / Atom unter den experimentellen Daten im von uns untersuchten Größenbereich. Die theoretischen Studien für neutrale Cluster weisen eine enorm große Streuung der Werte auf und lassen daher keine aussagekräftigen Schlüsse zu. Einzig für Eisen ergibt sich ein genereller Trend innerhalb der berechneten Spinmomente. Jedoch ist es uns möglich unsere Daten mit den kürzlich veröffentlichten Daten aus XMCD Experimenten von Lau *et al.*^[3-5] zu vergleichen. Der Vergleich beider Datensätze ergibt eine relativ gute Übereinstimmung beider Experimente innerhalb der Fehlerbalken für die meisten Clustergrößen. Diese Übereinstimmung kann als Bestätigung für den experimentellen Ansatz magnetische Momente isolierter Cluster in der Gasphase mittels "Total Ion Yield" Spektroskopie zu messen gewertet werden.

Clustereigenschaften folgen häufig einen generellen Trend, der sich als Interpolation ("scaling law") zwischen dem atomaren und dem Festkörperwert darstellen lässt. Im Bereich kleiner Cluster, dem sogenannten nicht skalierbarem Größenbereich, sind diesem generellem Trend häufig Fluktuationen auf Grund von Clustergrößeneffekten überlagert. Sowohl das Spin- als auch das Bahnmoment folgen

einem solchen Trend, interessanterweise jedoch nicht dem Selben. Das Spinmoment folgt der allgemein bekannten $n^{-1/3} = 1/(\text{Clusterradius})$ Interpolation ($n = \text{Anzahl an Atomen pro Cluster}$, kugelsymmetrischer Cluster angenommen). Der Trend folgt der Anzahl von Oberflächen zu inneren Atomen in einem kugelsymmetrischen Teilchen. Das Bahnmoment dagegen folgt einer $1/N = 1/(\text{Clusterradius})^3 = 1/(\text{Clustervolumen})$ Interpolation. Bisher kann nur spekuliert werden, warum die beiden Beiträge zum magnetischen Moment einer unterschiedlichen Interpolation zwischen Atom und Festkörper folgen. Das über alle Atome im Cluster gemittelte Spinmoment scheint der geometrischen Oberfläche zu folgen. Die verringerte Anzahl nächster Nachbarn an der Oberfläche im Vergleich zum Festkörper, d.h. eine vom Festkörper abweichende Koordinationsgeometrie, führt zu einer stärkeren Lokalisierung der Elektronenwellenfunktion. Dies wiederum führt zu schmäleren Energiebändern und einer erhöhten Zustandsdichte am Fermi-Niveau und erlaubt daher die Besetzung weiterer Zustände und führt so zu einem erhöhten Spinmoment für Oberflächenatome, auf Grund einer verstärkten Ungleichbesetzung von "spin up" and "spin down" Zuständen. Da wir ein gemitteltes Moment über alle Atome im Cluster unabhängig von ihrer individuellen Koordinationsgeometrie messen, führen erhöhte Spinmomente für Oberflächenatome zu einem erhöhten Spinmoment pro Atom im Vergleich zum Festkörper. Einer Änderung der Oberflächentopologie hat einen relativ geringen Einfluss auf das Spinmoment für starke Ferromagnete, d.h. Ferromagnete mit vollständig gefülltem Majoritätsband^[6]. Bei allen von uns untersuchten Clustern handelt es sich um starke Ferromagnete. Dies könnte eine mögliche Erklärung dafür sein, warum die geometrische Oberfläche einen Einfluss hat, wir aber im Rahmen unserer Fehlerbalken nur wenige Clustergrößeneffekte für das Spinmoment sehen. Eine Ausweitung des untersuchten Clustergrößenbereichs könnte Aufschluss darüber geben, ob das Spinmoment tatsächlich $1/(\text{Clusterradius})$ folgt, da größere Cluster eine Oberfläche und einen festkörperähnlichen Kern ausbilden. Jedoch weicht die Clustergeometrie selbst für Cluster mit mehreren hundert Atomen pro Cluster noch häufig von der Festkörperstruktur ab. Im Gegensatz zum Spinmoment reagiert das Bahnmoment sehr viel empfindlicher auf eine Änderung der Koordinationsgeometrie. Daher könnte man spekulieren, ob das Bahnmoment nicht stärker der geometrischen Struktur der Cluster, d.h. der Koordinationsumgebung, Anzahl nächster Nachbarn, Bindungslänge, etc., folgt. Clustergrößenabhängige Schwankungen im Bahnmoment könnten mit hochsymmetrischen (sehr kleines Bahnmoment) oder sehr offenen oder unsymmetrischen (großes Bahnmoment) Clusterstrukturen einhergehen. Das Bahnmoment könnte daher bei einer Änderung des grundlegenden Strukturmotives, z.B. von einer ikosaedrischen zur Festkörperstruktur, eine signifikante Änderung erfahren. Allerdings erlaubt der von uns untersuchte Größenbereich noch keine abschließende Bewertung der beiden Interpolationen.

Ausgehend von rein experimentellen Gesichtspunkten wäre es wünschenswert den "duty cycle" des Experiments zu erhöhen. Die benötigte Zeit um das zur Thermalisierung benötigte Helium wieder abzupumpen macht das Experiment sehr langsam bezogen auf die Aufnahme von Röntgenabsorptionsspektren. Eine Kühlung der Cluster in einer vorgelagerten Falle würde die Geschwindigkeit der Datenaufnahme stark erhöhen. Ein zu dem in dieser Arbeit verwendetem FT-ICR-MS vergleichbares Gerät wird zurzeit in Kaiserslautern mit einer solchen Vorkühlung ausgestattet. Die Ionen werden in einer Hexapolfalle gekühlt bevor sie in die ICR-Zelle transferiert werden^[7]. Die Elementspezifität der Röntgenabsorptionsspektroskopie erlaubt es heterogene Systeme zu untersuchen und weiterhin die Anteile der einzelnen Elemente zum Magnetismus des Gesamtsystems zu bestimmen. Erste Experimente an legierten Cobalt + Gold / Rhodium Systemen der Zusammensetzung $[\text{Co}_n\text{Rh}_1]^+$ und $[\text{Co}_n\text{Au}_1]^+$ wurden bereits durchgeführt^[8]. Die beiden verwendeten Heteroatome unterscheiden sich in ihrer elektronischen Struktur. Während Rhodium das schwerere Homologe des Cobalts ist, ist Gold diamagnetisch. Daher sollten die beiden Elemente einen unterschiedlichen Einfluss auf die magnetische Struktur der Cobaltcluster ausüben. Diese Experimente sollen ausgeweitet werden, in dem weitere Rhodium- und Goldatome pro Cluster legiert werden und weiterhin Cobalt durch Eisen und Nickel ersetzt wird. Im Rahmen des Sonderforschungsbereichs TRR88/3MET werden heterogene Cluster der ferromagnetischen 3d Metalle untersucht werden, mit maximal vier Atomen pro Cluster $[\text{Fe}_m\text{Co}_n\text{Ni}_l]^+$ ($m + n + l \leq 4$). Der Magnetismus eines Systems/Clusters kann durch Adsorbate oder Substrate stark beeinflusst werden und daher sind Studien zu diesen Effekten von großer Bedeutung in Bezug auf spätere technische Anwendungen. Informationen über die elektronische aber auch über die geometrische Struktur können durch Variation der Bindungsstärken etwaiger Liganden (N_2 schwach gebunden bis CO stark gebunden) erhalten werden. Durch die Reaktion des Systems auf Liganden mit unterschiedlichen Bindungsstärken lässt sich abschätzen wie leicht ein System elektronisch beeinflussbar ist.

Einzelmolekülmagnete sind magnetische Systeme deren Magnetismus nicht von einer räumlichen Anordnung der Moleküle abhängt, d.h. die langreichweitigen Wechselwirkungen sind vernachlässigbar gegenüber den intramolekularen Wechselwirkungen und jedes Molekül kann als kleiner individueller Magnet angesehen werden. Wir haben erste Experimente an isolierten Einzelmolekülmagneten in der Gasphase durchgeführt. Eine Elektrosprayionisationsquelle (ESI) wurde an den NanoClusterTrap-Aufbau, der von T. Lau (HZB, Berlin, Deutschland) betrieben wird, angebaut. Ein Einzelmolekülmagnet, welcher sowohl 3d als auch 4f Metalle enthielt $[\text{Fe}_4\text{Ln}_2]$ ($\text{Ln} = \text{Gd}, \text{Tb}$), wurde in der Arbeitsgruppe von A. Powell (Karlsruher Institute of Technology, Karlsruhe, Deutschland) synthetisiert und uns zur Verfügung gestellt. Erste Röntgenabsorptions- und XMCD-Spektren konnten an der Eisen $L_{2,3}$ Kante aufgenommen werden. Die Spektren zeigen die für Fe^{III} high spin Ionen

typischen Absorptionsmuster. Eine Auswertung der Spektren mittels Summenanalyse ist jedoch auf Grund der Datenqualität nicht möglich.

Die Experimente an $[\text{Fe}_4\text{Ln}_2]$ werden fortgeführt werden um ein XMCD Spektrum in ausreichende Qualität zu erhalten, auf das die Summenanalyse an der Eisen $L_{2,3}$ Kante angewendet werden kann. Sollen aus die intrinsischen magnetischen Momente mittels Langevin- oder Brillouinkorrektur bestimmt werden, muss dazu allerdings die Kopplung der Eisenatome zu den Lanthanoidatomen bekannt sein. Dies ist durch ein XMCD Spektrum an der $M_{4,5}$ Kante der Lanthanoide möglich. In den Gruppen von A. Powell (KIT) und H.-J. Krüger (Technische Universität Kaiserslautern, Kaiserslautern, Deutschland) werden im Rahmen des Sonderforschungsbereichs TRR88 / 3MET magnetische Moleküle und Spincrossover Komplexe synthetisiert und untersucht. Auf diesen Systemen wird der experimentelle Fokus der nächsten Strahlzeiten liegen. Neben XMCD-Spektren bei hohem Magnetfeld und tiefen Temperaturen, werden Magnetisierungskurven und temperaturabhängige Messungen durchgeführt werden. Aus diesen Experimenten lassen sich Informationen zu "Blocking"- und "Spincrossover"-Temperaturen ziehen sowie Informationen zu den Kopplungsstärken und -schemen innerhalb heterogener Systeme erhalten.

8.1 Referenzen

- [1] KAMPSCHULTE, H., *Entwicklung einer Tieftemperatur FT-ICR Zelle und ihre Charakterisierung mittels Reaktionskinetiken und Synchrotron-Spektroskopie*, Doctoral thesis, **2010**, Technische Universität Kaiserslautern.
- [2] PEREDKOV, S., NEEB, M., EBERHARDT, W., MEYER, J., TOMBERS, M., KAMPSCHULTE, H., NIEDNER-SCHATTEBURG, G., *Spin and Orbital Magnetic Moments of Free Nanoparticles*, Physical Review Letters **2011**, *107*, 233401.
- [3] LANGENBERG, A., *Magnetische Momente freier, massenselektierter Eisen-, Cobalt- und Nickelcluster*, Doctoral thesis, **2013**, Technische Universität Berlin.
- [4] LANGENBERG, A., HIRSCH, K., LAWICKI, A., ZAMUDIO-BAYER, V., NIEMEYER, M., CHMIELA, P., LANGBEHN, B., TERASAKI, A., ISSENDORFF, B. V., LAU, J. T., *Spin and orbital magnetic moments of size-selected iron, cobalt, and nickel clusters and their link to the bulk phase diagrams*, arXiv.org, e-Print Arch., Phys. **2014**, *1*.
- [5] NIEMEYER, M., HIRSCH, K., ZAMUDIO-BAYER, V., LANGENBERG, A., VOGEL, M., KOSSICK, M., EBRECHT, C., EGASHIRA, K., TERASAKI, A., MÖLLER, T., V. ISSENDORFF, B., LAU, J. T., *Spin Coupling and Orbital Angular Momentum Quenching in Free Iron Clusters*, Physical Review Letters **2012**, *108*, 057201.
- [6] BLÜGEL, S., *Lecture Notes Magnetism goes Nano: Electron Correlations, Spin Transport, Molecular Magnetism*, Reduced Dimensions I - Magnetic Moment and Magnetic Structure Forschungszentrum Jülich in der Helmholtz-Gemeinschaft, **2005**.

- [7] MOHRBACH, J., *Charakterisierung ausgewählter Übergangsmetallkomplexe mittels infrarot induzierter Multiphotonendissoziation (IR-MPD) bei tiefen Temperaturen*, Diploma thesis, **2013**, Technische Universität Kaiserslautern.
- [8] content of the Doctoral thesis of M. Tombers

A. APPENDIX

A.1 Theoretical Background

A.1.1 Spectroscopic splitting factor g & magnetomechanical ratio g'

The magnetic moment of an electron precesses around a magnetic field \mathbf{H} with a given frequency ω , the so called Larmor frequency:

$$\omega = -\gamma H \quad (\text{Eq. A.1})$$

with γ being the gyromagnetic ratio:

$$\gamma = \frac{qg\mu_0}{2m_e} \quad (\text{Eq. A.2})$$

q	charge
g	spectroscopic splitting factor
μ_0	Bohr magneton
m_e	electron mass

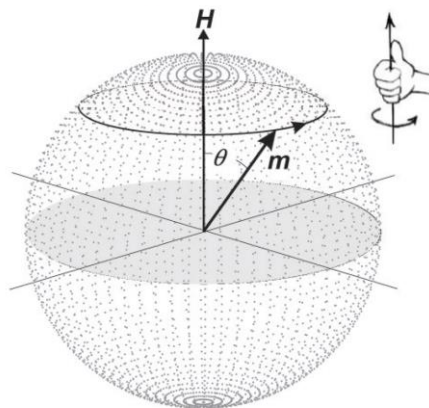


Figure A.1 Precessing of a magnetic moment \mathbf{m} around a magnetic field \mathbf{H} . The precession direction is defined by the gyromagnetic moment, i.e. the electron charge $q = -e$. ω is independent of the angle θ enclosed by \mathbf{m} and \mathbf{H} ^[1].

The spectroscopic splitting factor g or g-factor is a material dependent factor which is deduced by ferromagnetic resonance experiments (FMR). The deviation from the spin only value of $g = 2.0$ due to

the orbital magnetic moment can be calculated according to Kittel's formula^[1-3] for small orbital magnetic moments:

$$\frac{g-2}{2} = \frac{m_L}{m_S} \quad (\text{Eq. A.3})$$

m_S spin magnetic moment
 m_L orbital magnetic moment

The definition of g used for FMR experiments is given by Eq. A.4 and includes on the spin contribution^[2,4].

$$g = \frac{2m_e}{e} \frac{M}{J_{spin}} \quad (\text{Eq. A.4})$$

M Magnetization
 J angular momentum per unit volume
 m_e electron mass
 e elementary charge

The Magnetomechanical ratio g' , deduced from gyromagnetic experiments^[2,4] (Einstein - de Haas effect^[5-7]), is defined according to Kittel^[2] as:

$$g' \frac{e}{2m_e} = \frac{\Delta(M_{spin}+M_{orb})}{\Delta(J_{spin}+J_{orb})} \quad (\text{Eq. A.5})$$

$g \neq g'$ in case that the angular magnetic moment is coupled to the lattice structure. Their relation is given by the following equation:

$$\frac{g'}{g} = \frac{J_{spin}}{J_{spin}+J_{orb}} = \frac{S}{S+L} \quad (\text{Eq. A.6})$$

One should remember that $g > 2$ and $g' < 2$. It is evident from Eq. A.4 that the magnetomechanical ratio g' corresponds to the Landé g-factors^[6].

A.1.2 References

- [1] STÖHR, J., SIEGMANN, H. C., *Magnetism - From Fundamentals to Nanoscale Dynamics*; Springer, **2006**.
- [2] KITTEL, C., *On the Gyromagnetic Ratio and Spectroscopic Splitting Factor of Ferromagnetic Substances*, Physical Review **1949**, 76, 743.
- [3] PELZL, J., MECKENSTOCK, R., SPODDIG, D., SCHREIBER, F., PFLAUM, J., FRAIT, Z., *Spin-orbit-coupling effects on g-value and damping factor of the ferromagnetic resonance in Co and Fe films*, Journal of Physics: Condensed Matter **2003**, 15, S451.

- [4] WALLIS, T. M., MORELAND, J., KABOS, P., *Einstein–de Haas effect in a NiFe film deposited on a microcantilever*, Applied Physics Letters **2006**, 89.
- [5] EINSTEIN, A., DE HAAS, W. J., *Experimenteller Nachweis der Ampereschen Molekularströme*, Verhandlungen Deutsch Physikalische Gesellschaft **1915**, 17, 152.
- [6] DEMTRÖDER, *Experimental Physik III - Atome, Moleküle und Festkörper*, 4th ed.; Springer Verlag Heidelberg, **2010**.
- [7] *Gerthsen Physik*; 20th ed.; MESCHÉDE, D., Ed.; Springer **2010**.

A.2 Experimental methods - GAMBIT setup

A.2.1 Total Ion Yield spectroscopy of isolated clusters

Fig. A.2 to A.4 give an example of TIY spectroscopy. Mass spectra of Ni_{13}^+ are presented. The mass spectra were recorded after exposure of the clusters to the x-ray beam. Each mass spectrum was recorded with a different photon energy of the x-ray. The energy range spans 3 eV with 852 eV being the energy of the L_3 resonance.

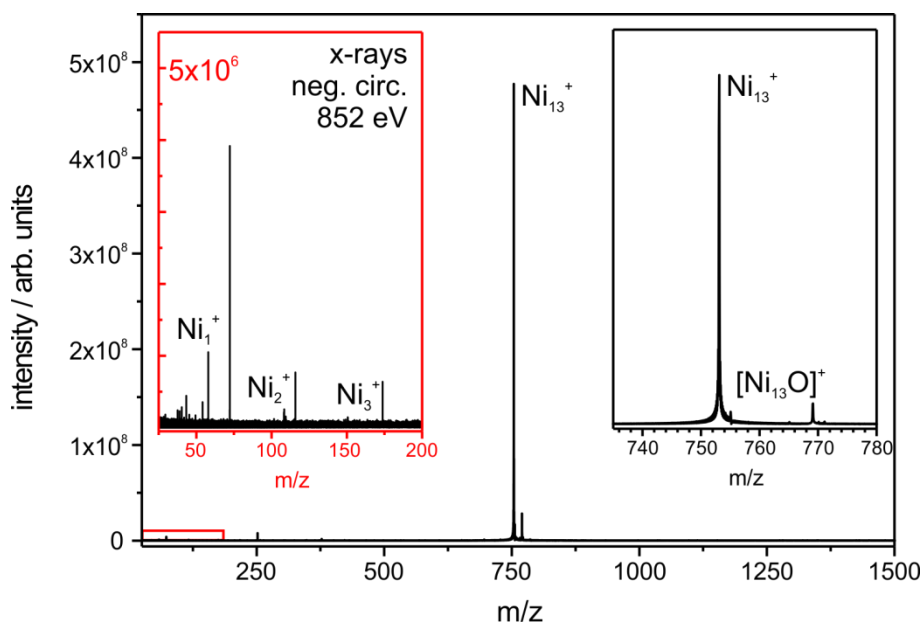


Figure A.2 Mass spectrum of Ni_{13}^+ after irradiation with x-ray photons with a photon energy of 852 eV

The photon energy was set to one electron volt below the resonance at the L_3 edge. The inset marked in red shows the fragments Ni_1^+ , Ni_2^+ and Ni_3^+ . The highest peak at m/z 72 is a noise peak. The shown spectrum is the sum of ten single mass spectra. The cluster temperature is about 20 K.

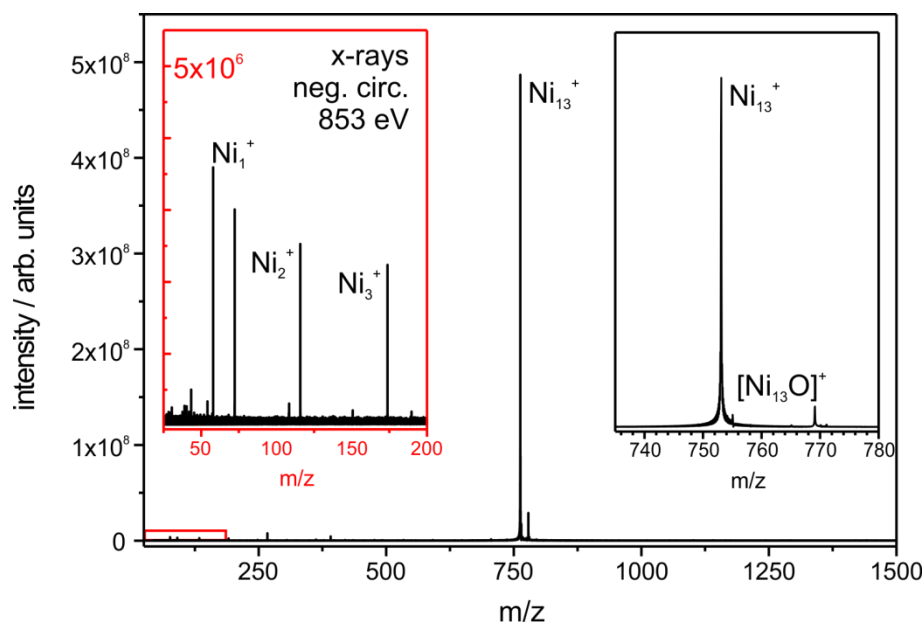


Figure A.3 Mass spectrum of Ni_{13}^+ after irradiation with x-ray photons with a photon energy of 853 eV

The photon energy was set to the resonance at the L_3 edge. The inset marked in red shows the fragments Ni_1^+ , Ni_2^+ and Ni_3^+ . The shown spectrum is the sum of ten single mass spectra. The cluster temperature is about 20 K.

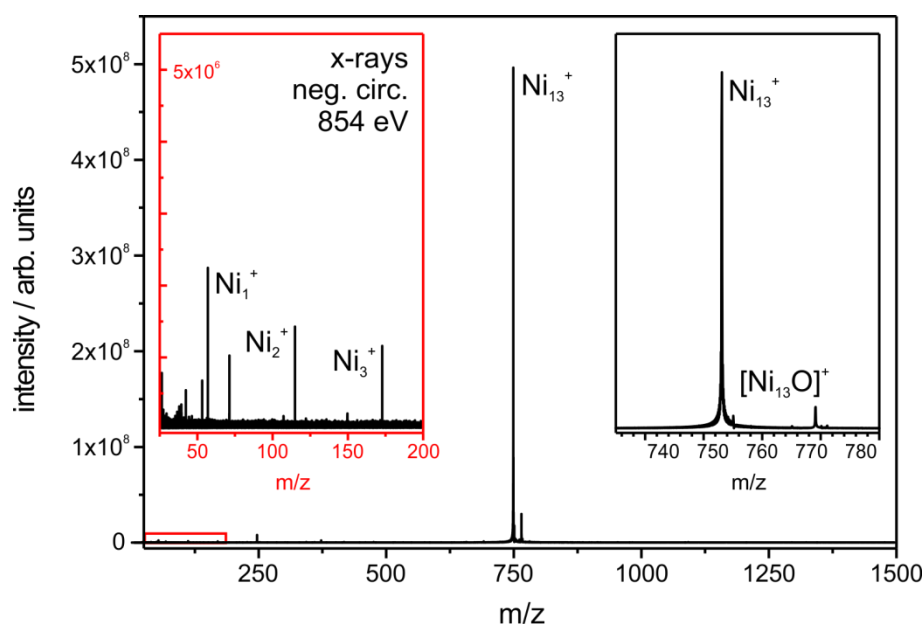


Figure A.4 Mass spectrum of Ni_{13}^+ after irradiation with x-ray photons with a photon energy of 854 eV

The photon energy was set to one electron volt above the resonance at the L_3 edge. The inset marked in red shows the fragments Ni_1^+ , Ni_2^+ and Ni_3^+ . The shown spectrum is the sum of ten single mass spectra. The cluster temperature is about 20 K.

A.2.2 Collisional cooling

Fig. A.5 to A.9 show the normalized polarization dependent x-ray absorption spectra recorded to define the amount of helium buffer gas needed to cool down the cluster. The spectra are normalized by setting the highest XA intensity at the L_3 edge to one. The inset shows the XMCD spectrum for the pair of polarization dependent XA spectra.

(*) Experiments of isolated Co_{11}^+ were not possible at the time of the experiment. A set of three clusters Co_{10}^+ , Co_{11}^+ and Co_{12}^+ was selected with Co_{11}^+ as the most intense peak.

Table A.1 Parameter set for buffer gas dependent experiments

p_{\max} ICR cell after pulse / mbar	$p^{(\#)}$ General Valve / bar	opening time GV / ms	pump down delay / s	irradiation time / s	p ICR cell opening shutter / mbar	p ICR cell detection / mbar
$1.7 \cdot 10^{-7}$	≈ 1	1.7	6	8	-(^s)	$4.0 \cdot 10^{-9}$
$5.5 \cdot 10^{-7}$	≈ 1	2.2	8	8	-(^s)	$1.9 \cdot 10^{-9}$
$8.9 \cdot 10^{-7}$	< 1	8.7	8	8	$1.4 \cdot 10^{-8}$	$2.4 \cdot 10^{-9}$
$9.3 \cdot 10^{-7}$	≈ 0.6	8.3	8	8	$7.5 \cdot 10^{-9}$	$1.2 \cdot 10^{-9}$
$1.0 \cdot 10^{-6}$	≈ 0.35	9.9	8	8	$1.4 \cdot 10^{-8}$	$2.0 \cdot 10^{-9}$

([#]) He backing pressure on the gas line

(^s) no values recorded

p_{\max} (ICR cell)	after gas pulse	maximum pressure reading after the pulse of helium buffer gas into the UHV region
p (ICR cell)	opening shutter	pressure reading after pump down delay, i.e. at the opening of the shutter and admittance of the x-ray beam into the ICR cell
p (ICR cell)	detection	pressure reading after closing the shutter and at the detection time of the mass spectrum
p (General Valve)		backing pressure at the General Valve used to produce the pulse of helium buffer gas
opening time GV		time the General Valve (GV) opens to release gas
pump down delay		time needed to pump out the helium buffer gas
irradiation time		exposure time of the clusters to the x-ray beam

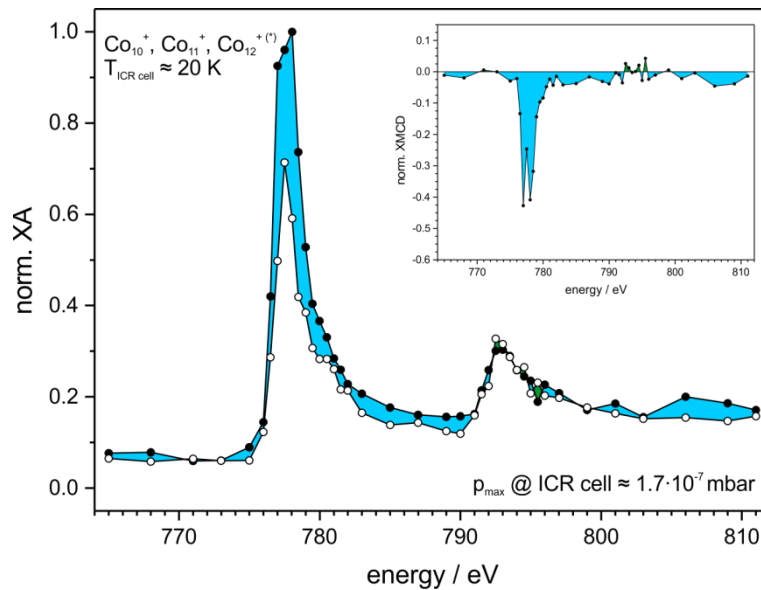


Figure A.5 Polarization dependent XAS of Co_{10}^+ , Co_{11}^+ & Co_{12}^+ at the $L_{2,3}$ edge for a maximum helium buffer gas pressure in the UHV region of $1.7 \cdot 10^{-7}$ mbar (μ^- = solid symbols and μ^+ = open symbols)

The inset shows the XMCD spectrum calculated from the polarization dependent XA spectra. Blue areas indicate a negative dichroic effect and green areas a positive dichroic effect.

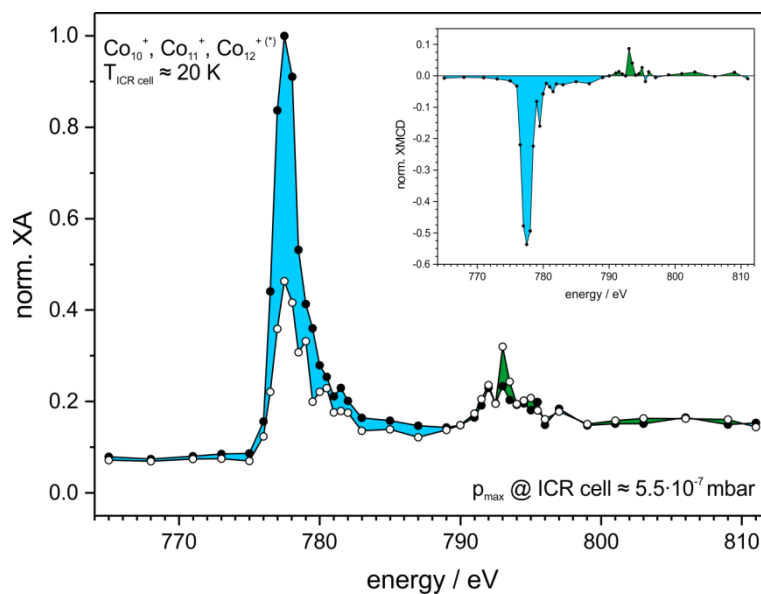


Figure A.6 Polarization dependent XAS of Co_{10}^+ , Co_{11}^+ & Co_{12}^+ at the $L_{2,3}$ edge for a maximum helium buffer gas pressure in the UHV region of $5.5 \cdot 10^{-7}$ mbar (μ^- = solid symbols and μ^+ = open symbols)

The inset shows the XMCD spectrum calculated from the polarization dependent XA spectra. Blue areas indicate a negative dichroic effect and green areas a positive dichroic effect.

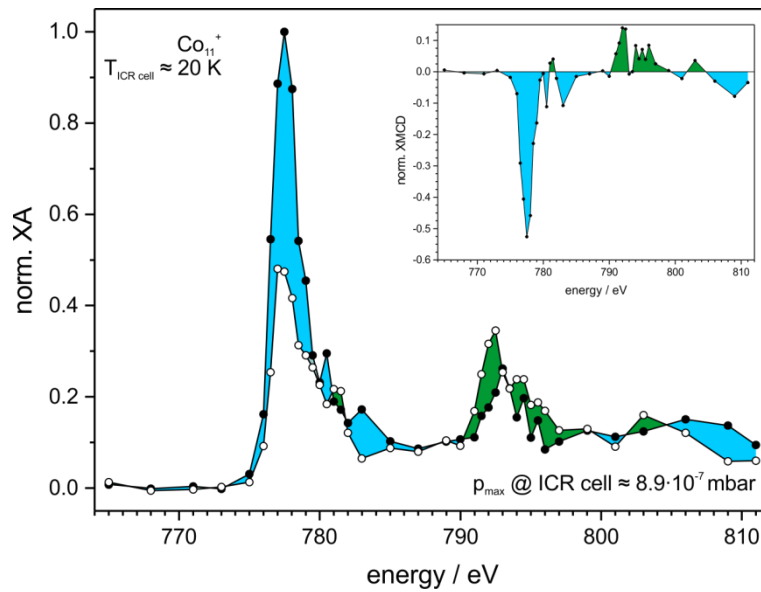


Figure A.7 Polarization dependent XAS of Co_{11}^{+} at the $L_{2,3}$ edge for a maximum helium buffer gas pressure in the UHV region of $8.9 \cdot 10^{-7}$ mbar (μ^{-} = solid symbols and μ^{+} = open symbols)

The inset shows the XMCD spectrum calculated from the polarization dependent XA spectra. Blue areas indicate a negative dichroic effect and green areas a positive dichroic effect.

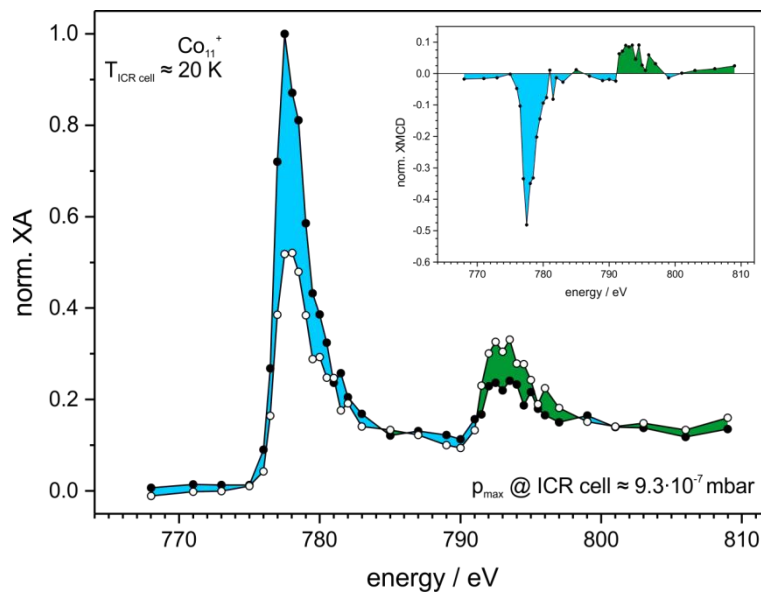


Figure A.8 Polarization dependent XAS of Co_{11}^{+} at the $L_{2,3}$ edge for a maximum helium buffer gas pressure in the UHV region of $9.3 \cdot 10^{-7}$ mbar (μ^{-} = solid symbols and μ^{+} = open symbols)

The inset shows the XMCD spectrum calculated from the polarization dependent XA spectra. Blue areas indicate a negative dichroic effect and green areas a positive dichroic effect.

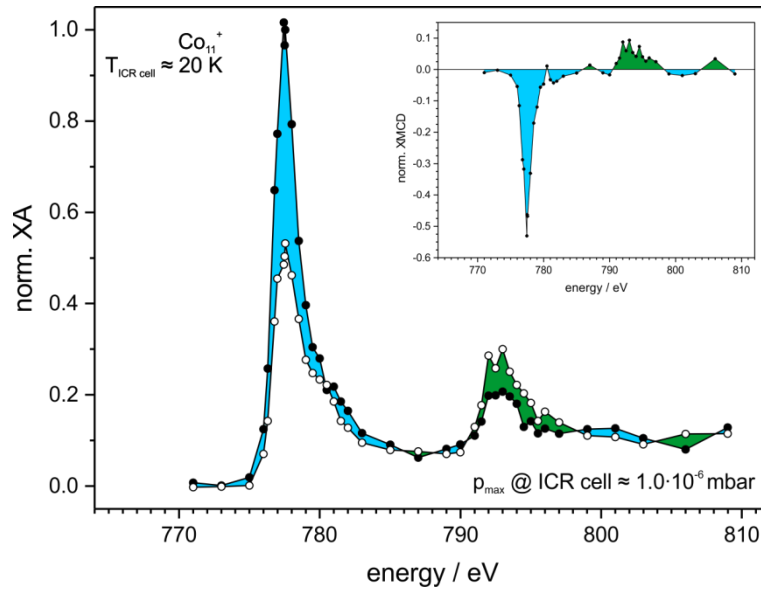


Figure A.9 Polarization dependent XAS of Co_{11}^+ at the $L_{2,3}$ edge for a maximum helium buffer gas pressure in the UHV region of $1 \cdot 10^{-6}$ mbar (μ^- = solid symbols and μ^+ = open symbols)

The inset shows the XMCD spectrum calculated from the polarization dependent XA spectra. Blue areas indicate a negative dichroic effect and the green areas indicate a positive dichroic effect.

A.2.3. Scaling of the experimental magnetic moments

The experimental spin and orbital magnetic moments of Co_{11}^+ used for the confirmation of a Langevin-like behavior of the cluster magnetization are shown in Tab. A.2.

Table A.2 Experimental spin and orbital magnetic moments of the temperature dependent experiments of Co_{11}^+

$T_{\text{ICR cell}}$ / K	T_{cluster} / K	$m_{S,z}$ / μ_B/atom	$m_{L,z}$ / μ_B/atom	$m_{J,z}$ / μ_B/atom
$20^{(*)}$	150 ± 50	0.34 ± 0.10	0.09 ± 0.05	0.45 ± 0.15
88	80 ± 1	0.75 ± 0.08	0.19 ± 0.05	0.84 ± 0.13
67	65 ± 1	0.72 ± 0.15	0.14 ± 0.07	0.86 ± 0.22
$50^{(+)}$	50 ± 1	1.08 ± 0.11	0.28 ± 0.05	1.36 ± 0.16
43	40 ± 1	1.30 ± 0.07	0.26 ± 0.04	1.56 ± 0.11
33	30 ± 1	1.44 ± 0.14	0.44 ± 0.08	1.88 ± 0.22
$20^{(+)}$	20 ± 2	1.56 ± 0.08	0.40 ± 0.07	1.96 ± 0.15
19.5	18.5 ± 5	1.81 ± 0.15	0.47 ± 0.08	2.28 ± 0.22
20	16 ± 5	1.67 ± 0.15	0.55 ± 0.07	2.22 ± 0.22

Fig. A.10 to A.18 show the normalized x-ray absorption spectra recorded to explicitly measure the temperature dependence of the XMCD effect for isolated clusters in the gas phase. The spectra are normalized by setting the highest XA intensity of a pair of polarization dependent XA spectra at the L_3 edge to one. The inset shows the XMCD spectrum for the pair of XA spectra. Tab. A.3 gives the parameter set used for collisional cooling of the clusters.

(*) Experiments of isolated Co_{11}^+ were not possible at the time of the experiment. A set of three clusters Co_{10}^+ , Co_{11}^+ and Co_{12}^+ was instead selected with Co_{11}^+ as the central peak.

(#) Experiments of isolated Co_{11}^+ were not possible at the time of the experiment. The isolation of only Co_{11}^+ led to a strong reduction of the cluster intensity. $[\text{Co}_{11}\text{H}_2]^+$ had to be included in the experiments to ensure a sufficient parent cluster intensity.

(+) Spin and orbital magnetic moments are extrapolated from the dichroic effect at the L_3 edge.

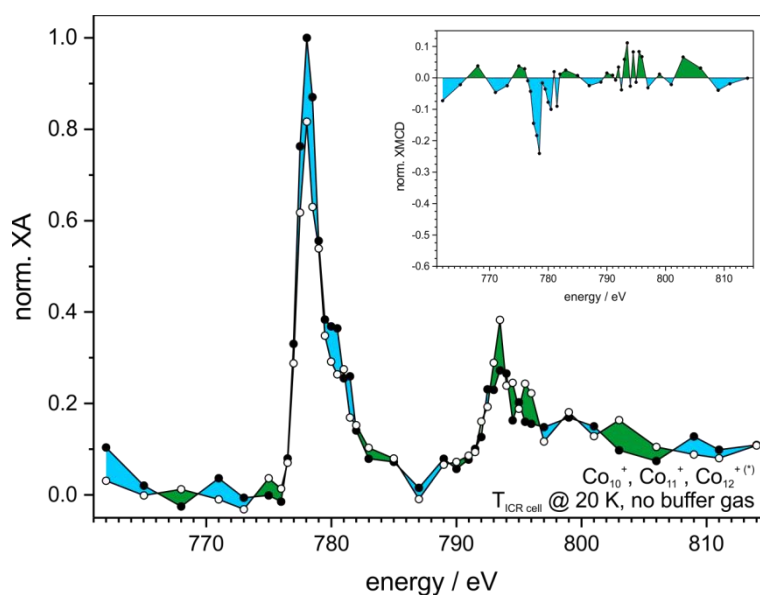


Figure A.10 Polarization dependent XAS of Co_{11}^+ at the $L_{2,3}$ edge with $T_{\text{ICR cell}} = 20$ K but without helium buffer gas (μ^- = solid symbols and μ^+ = open symbols)

The cluster temperature is defined by the supersonic expansion in the source region and is estimated to be about 150 K. The inset shows the XMCD spectrum calculated from the polarization dependent XA spectra. Blue areas indicate a negative dichroic effect and the green areas indicate a positive dichroic effect.

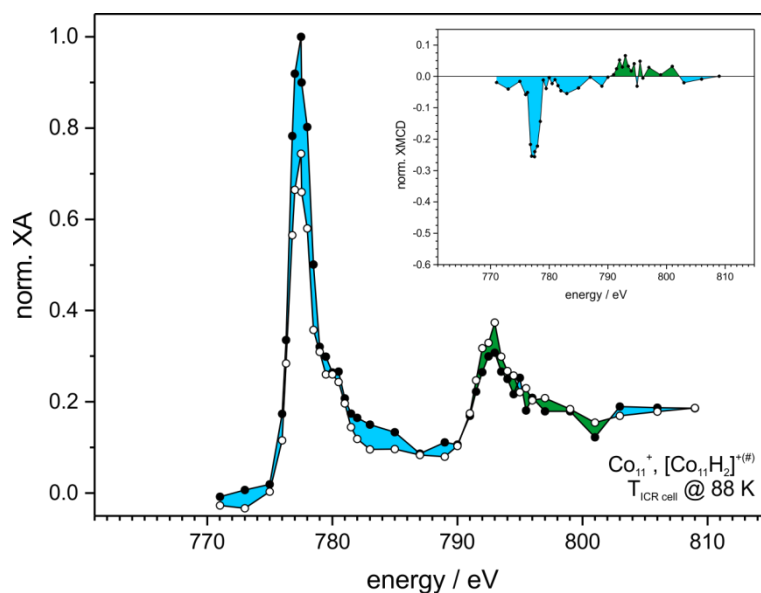


Figure A.11 Polarization dependent XAS of Co_{11}^+ at the $L_{2,3}$ edge at $T_{\text{ICR cell}} = 88 \text{ K}$ (μ^- = solid symbols and μ^+ = open symbols)

The spectrum was recorded with helium buffer gas to thermalize the clusters to the cell temperature. The cluster temperature of this measurement was estimated to be approximately 80 K. The inset shows the XMCD spectrum calculated from the polarization dependent XA spectra. Blue areas indicate a negative dichroic effect and the green areas indicate a positive dichroic effect.

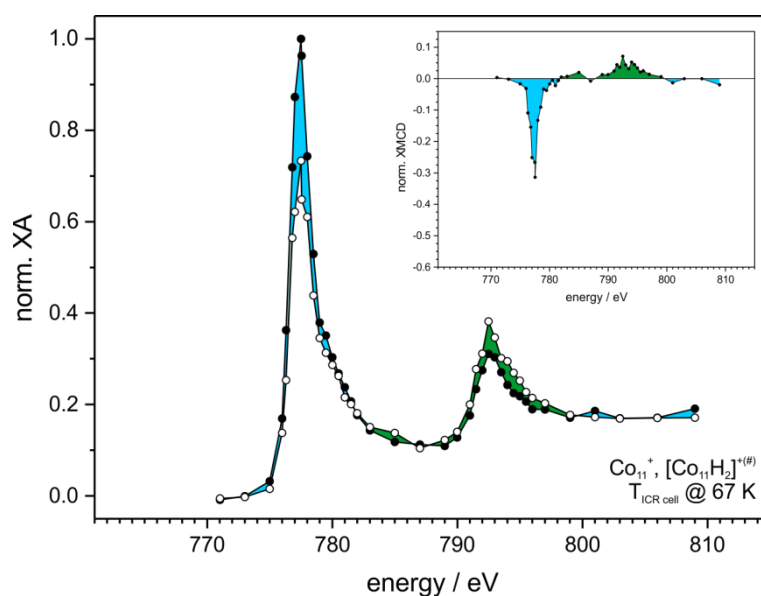


Figure A.12 Polarization dependent XAS of Co_{11}^+ at the $L_{2,3}$ edge with $T_{\text{ICR cell}} = 67 \text{ K}$ (μ^- = solid symbols and μ^+ = open symbols)

The spectrum was recorded with helium buffer gas to thermalize the clusters to the cell temperature. The inset shows the XMCD spectrum calculated from the polarization dependent XA spectra. Blue areas indicate a negative dichroic effect and the green areas indicate a positive dichroic effect.

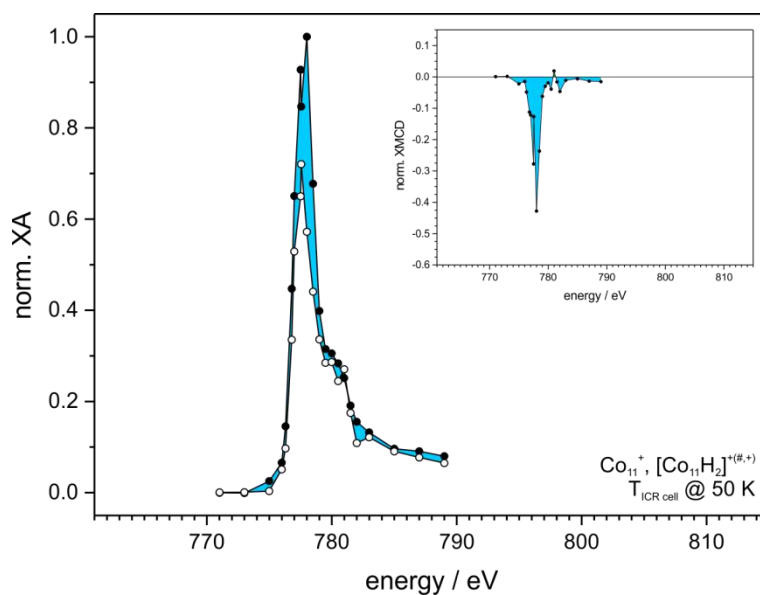


Figure A.13 Polarization dependent XAS of Co_{11}^+ at the L_3 edge with $T_{\text{ICR cell}} = 50 \text{ K}$ (μ^- = solid symbols and μ^+ = open symbols)

The spectrum was recorded with helium buffer gas to thermalize the clusters to the cell temperature. The inset shows the XMCD spectrum calculated from the polarization dependent XA spectra. Blue areas indicate a negative dichroic effect and the green areas indicate a positive dichroic effect.

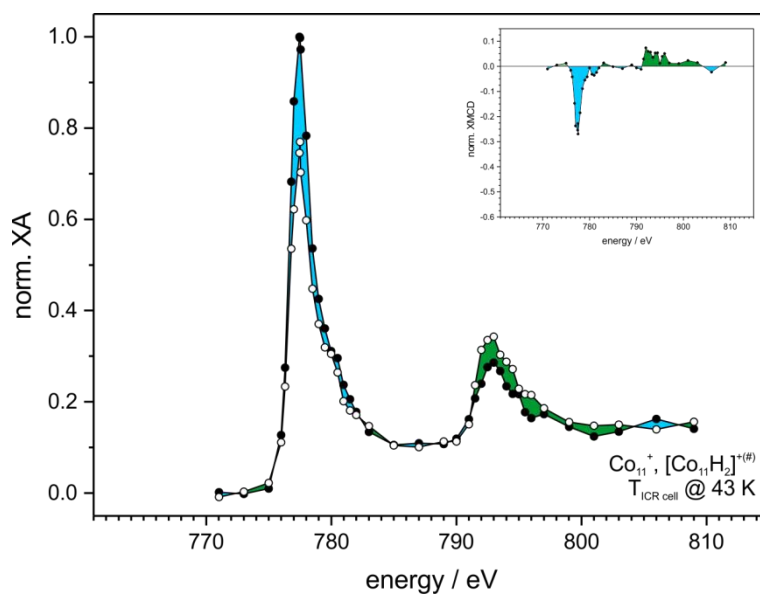


Figure A.14 Polarization dependent XAS of Co_{11}^+ at the $L_{2,3}$ edge with $T_{\text{ICR cell}} = 43 \text{ K}$ (μ^- = solid symbols and μ^+ = open symbols)

The spectrum was recorded with helium buffer gas to thermalize the clusters to the cell temperature. The inset shows the XMCD spectrum calculated from the polarization dependent XA spectra. Blue areas indicate a negative dichroic effect and the green areas indicate a positive dichroic effect.

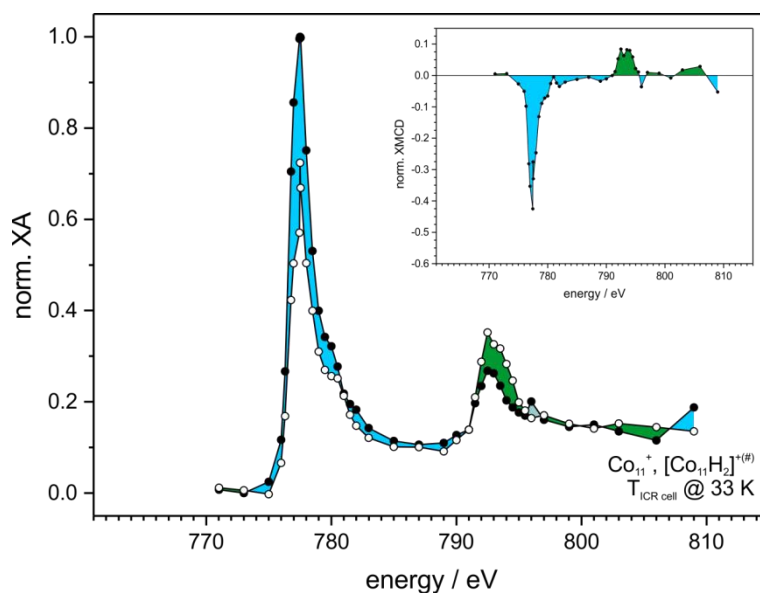


Figure A.15 Polarization dependent XAS of Co_{11}^+ at the $L_{2,3}$ edge with $T_{\text{ICR cell}} = 33 \text{ K}$ (μ^- = solid symbols and μ^+ = open symbols)

The spectrum was recorded with helium buffer gas to thermalize the clusters to the cell temperature. The inset shows the XMCD spectrum calculated from the polarization dependent XA spectra. Blue areas indicate a negative dichroic effect and the green areas indicate a positive dichroic effect.

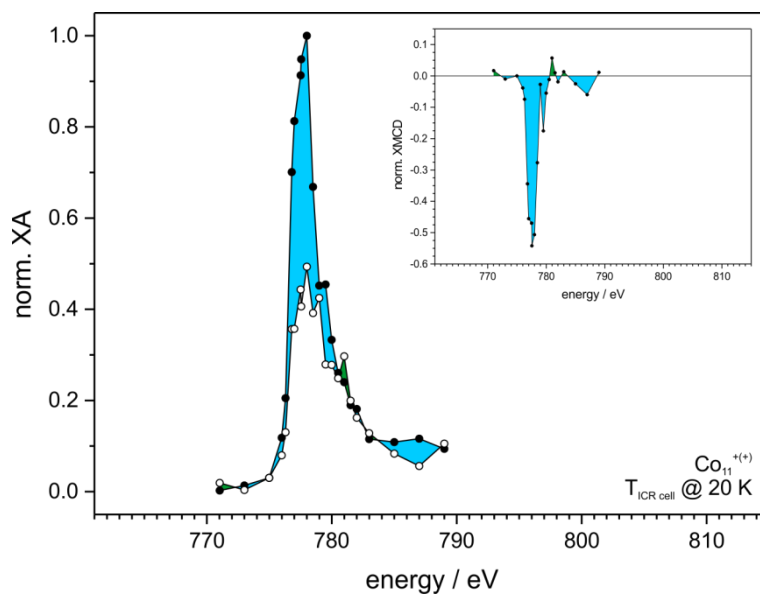


Figure A.16 Polarization dependent XAS of Co_{11}^+ at the L_3 edge with $T_{\text{ICR cell}} = 20 \text{ K}$ (μ^- = solid symbols and μ^+ = open symbols)

The spectrum was recorded with helium buffer gas to thermalize the clusters to the cell temperature. The inset shows the XMCD spectrum calculated from the polarization dependent XA spectra. Blue areas indicate a negative dichroic effect and the green areas indicate a positive dichroic effect.

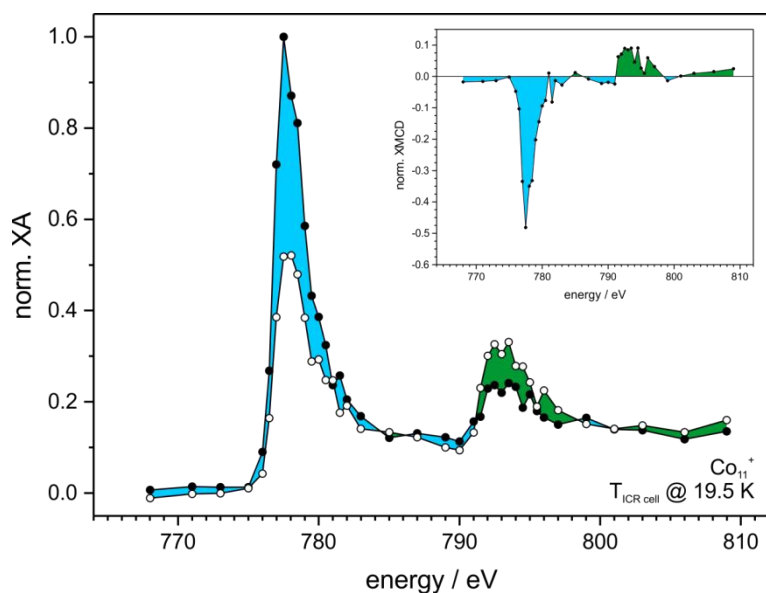


Figure A.17 Polarization dependent XAS of Co_{11}^+ at the $L_{2,3}$ edge with $T_{\text{ICR cell}} = 19.5 \text{ K}$ (μ^- = solid symbols and μ^+ = open symbols)

The spectrum was recorded with helium buffer gas to thermalize the clusters to the cell temperature. The cluster temperature for this measurement was estimated to be approximately 18.5 K. The inset shows the XMCD spectrum calculated from the polarization dependent XA spectra. Blue areas indicate a negative dichroic effect and the green areas indicate a positive dichroic effect.

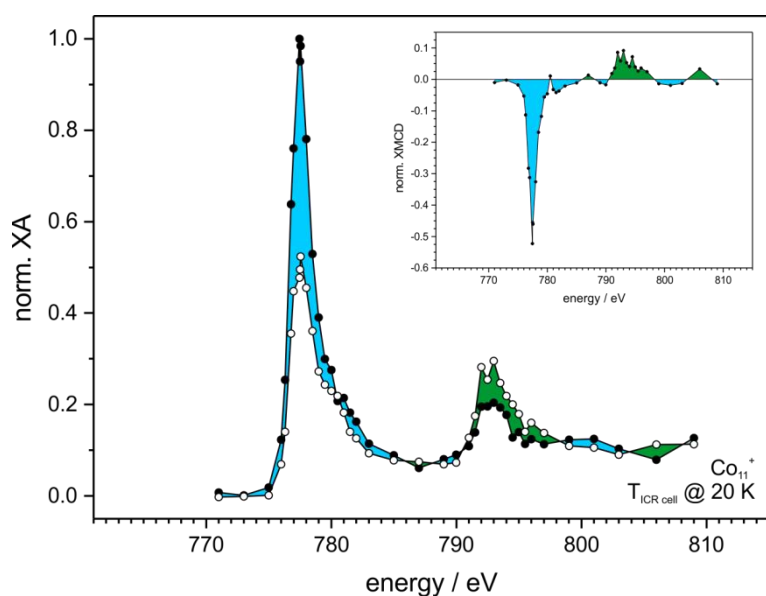


Figure A.18 Polarization dependent XAS of Co_{11}^+ at the $L_{2,3}$ edge with $T_{\text{ICR cell}} = 20 \text{ K}$ (μ^- = solid symbols and μ^+ = open symbols)

The spectrum was recorded with helium buffer gas to thermalize the clusters to the cell temperature. The cluster temperature for this measurement was estimated to be approximately 16 K. The inset shows the XMCD spectrum calculated from the polarization dependent XA spectra. Blue areas indicate a negative dichroic effect and the green areas indicate a positive dichroic effect.

Table A.3 Parameter set used for collisional cooling in temperature dependent experiments for Co_{11}^+

T cluster	p GV ^(#)	opening time GV	pump down delay	irradiation time	p _{max} ICR cell after pulse	p ICR cell opening shutter	p ICR cell detection
/ K	/ bar	/ ms	/ s	/ s	/ mbar	/ mbar	/ mbar
150 ± 50	-	-	-	4		no gas pulse	
80 ± 1	≈ 0.5	8.8	8	8	≈ 8·10 ⁻⁷	1.1·10 ⁻⁸	1.6·10 ⁻⁹
65 ± 1	≈ 0.6	8.8	8	8	≈ 8·10 ⁻⁷	1.0·10 ⁻⁸	1.5·10 ⁻⁹
50 ± 1	≈ 0.6	8.8	8	8	8.4·10 ⁻⁷	1.0·10 ⁻⁸	1.3·10 ⁻⁹
40 ± 1	≈ 0.5	9.9	8	8	9.0·10 ⁻⁷	1.0·10 ⁻⁸	1.0·10 ⁻⁹
30 ± 1	≈ 0.5	9.9	8	8	9.5·10 ⁻⁷	1.0·10 ⁻⁸	2.0·10 ⁻⁹
20 ± 2	≈ 0.6	8.8	8	8	9.8·10 ⁻⁷	7.0·10 ⁻⁹	1.5·10 ⁻⁹
18.5 ± 5	≈ 0.6	8.3	8	8	9.3·10 ⁻⁷	7.5·10 ⁻⁹	1.2·10 ⁻⁹
16 ± 5	≈ 0.35	9.9	8	8	1.0·10 ⁻⁶	1.4·10 ⁻⁸	2.0·10 ⁻⁹

^(#) He backing pressure on the gas line

Langevin and Brillouin correction for the total magnetic moment $m_{J,z}$ for each of the nine temperature dependent experiments are given in Fig. A.20 and A.21. Fig. A.19 gives the Landé g-factors of the total magnetic moments used for the Brillouin correction of the total experimental magnetic moments $m_{J,z}$. Fig. A.22 and A.23 show the scaling of the spin magnetic moment and the curves for the orbital magnetic moment are given in Fig. A.24 and A.25.

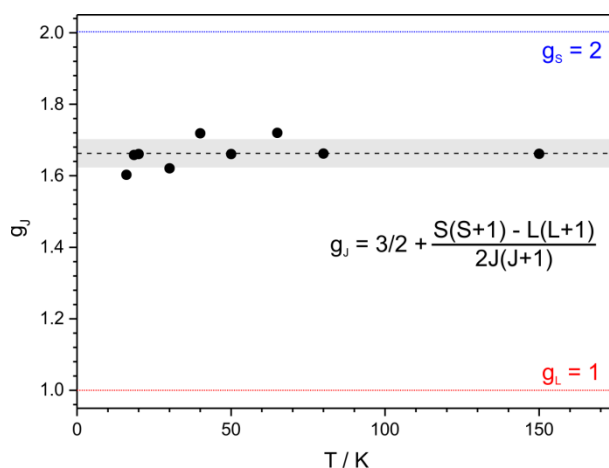


Figure A.19 Landé g-factors of the total magnetic moment m_J of the temperature dependent measurements of Co_{11}^+ . The g-factor of the spin magnetic moment, i.e. the electron, is given by the blue dotted line. The red dotted line gives the g-factor of the orbital magnetic moment. The dashed line gives the mean value and the shaded area indicates the standard deviation ($\sigma(g_J) = 0.038$)

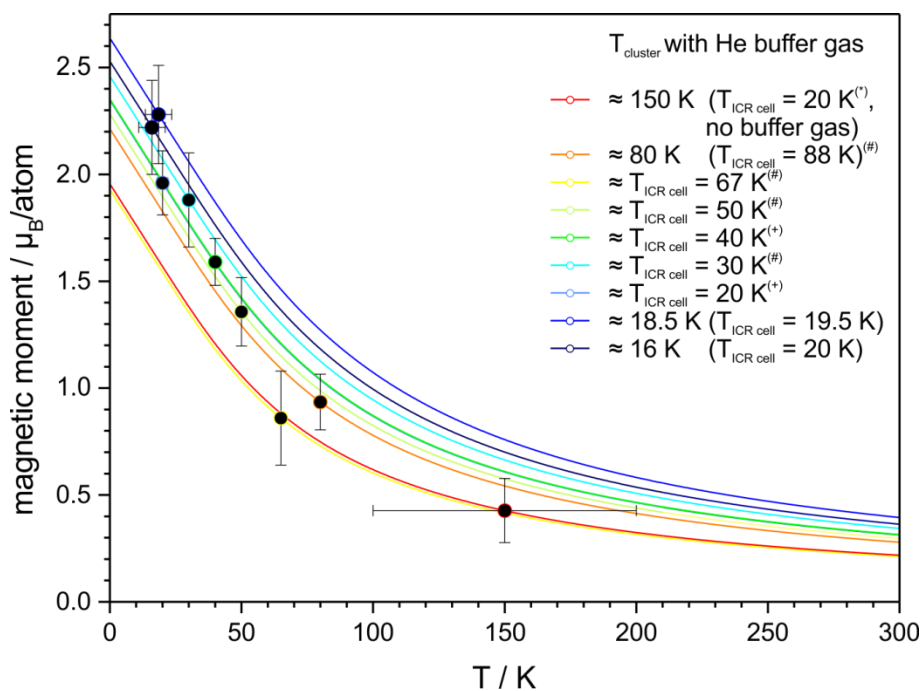


Figure A.20 Langevin scaling of the experimental total magnetic moment $m_{J,z}$ of individual temperature dependent experiments of Co_{11}^+ . The experimental total magnetic moments $m_{J,z}$ (solid symbols) are scaled to the intrinsic magnetic moment m_J .

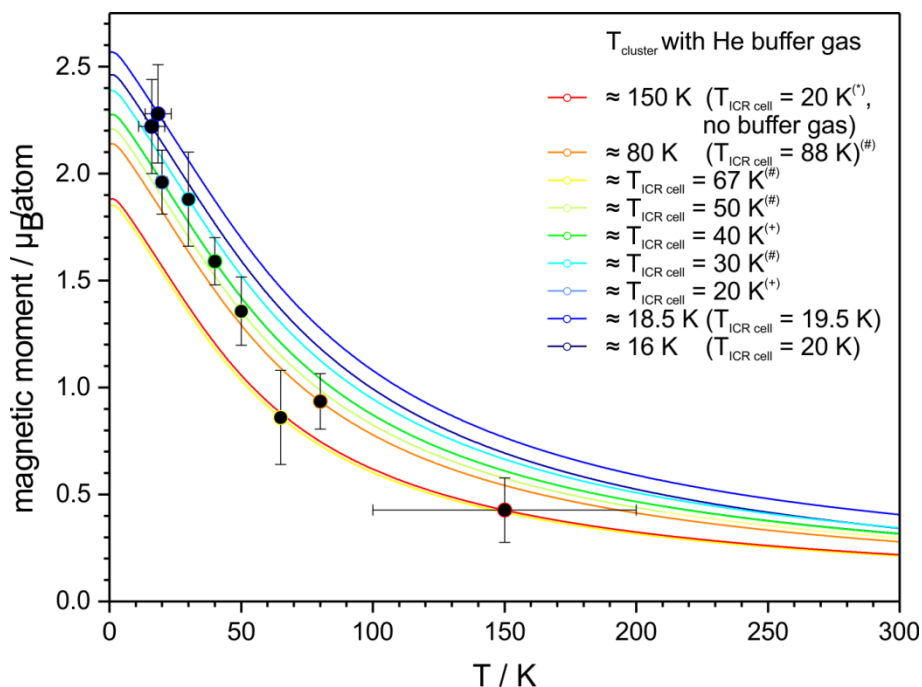


Figure A.21 Brillouin scaling of the experimental total magnetic moment $m_{J,z}$ of individual temperature dependent experiments of Co_{11}^+ . The experimental total magnetic moments $m_{J,z}$ (solid symbols) are scaled to the intrinsic magnetic moment m_J .

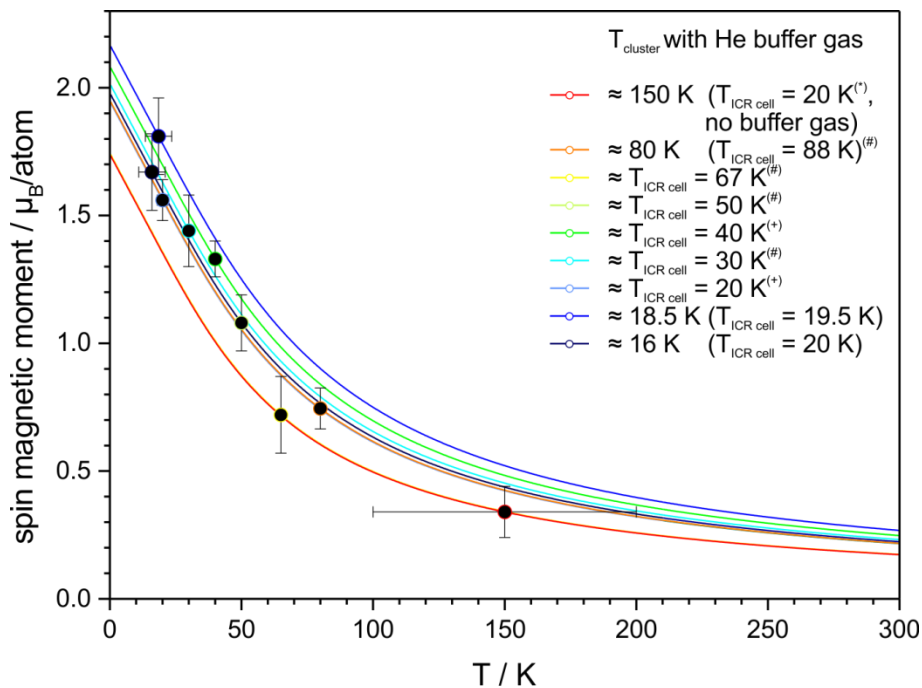


Figure A.22 Langevin scaling of the experimental spin magnetic moment $m_{s,z}$ of individual temperature dependent experiments of Co_{11}^+ . The experimental spin magnetic moments $m_{s,z}$ (solid symbols) are scaled to the intrinsic spin magnetic moment m_s .

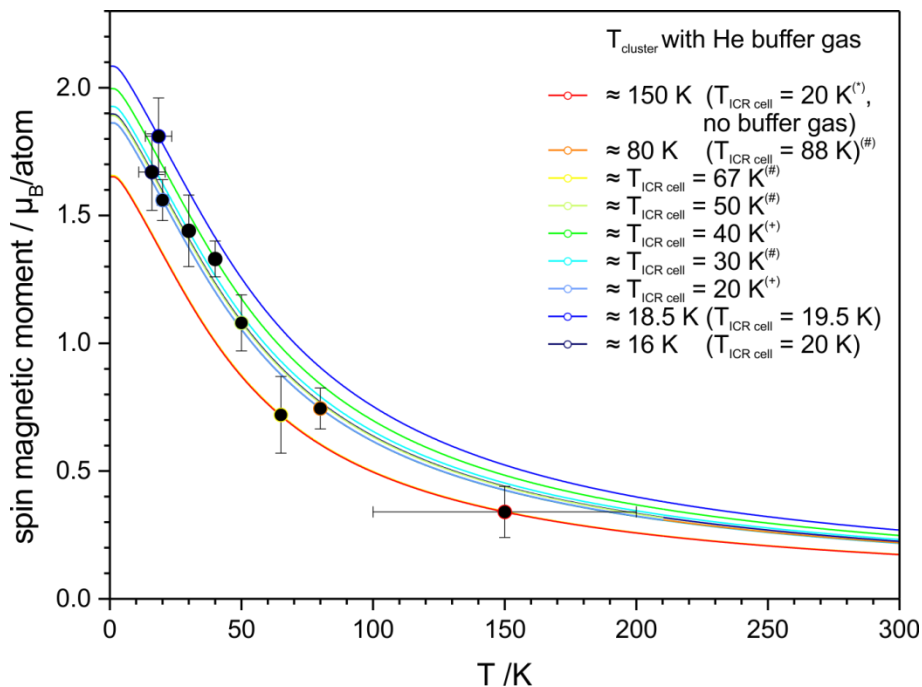


Figure A.23 Brillouin scaling of the experimental spin magnetic moment $m_{s,z}$ of individual temperature dependent experiments of Co_{11}^+ . The experimental spin magnetic moments $m_{s,z}$ (solid symbols) are scaled to the intrinsic spin magnetic moment m_s .

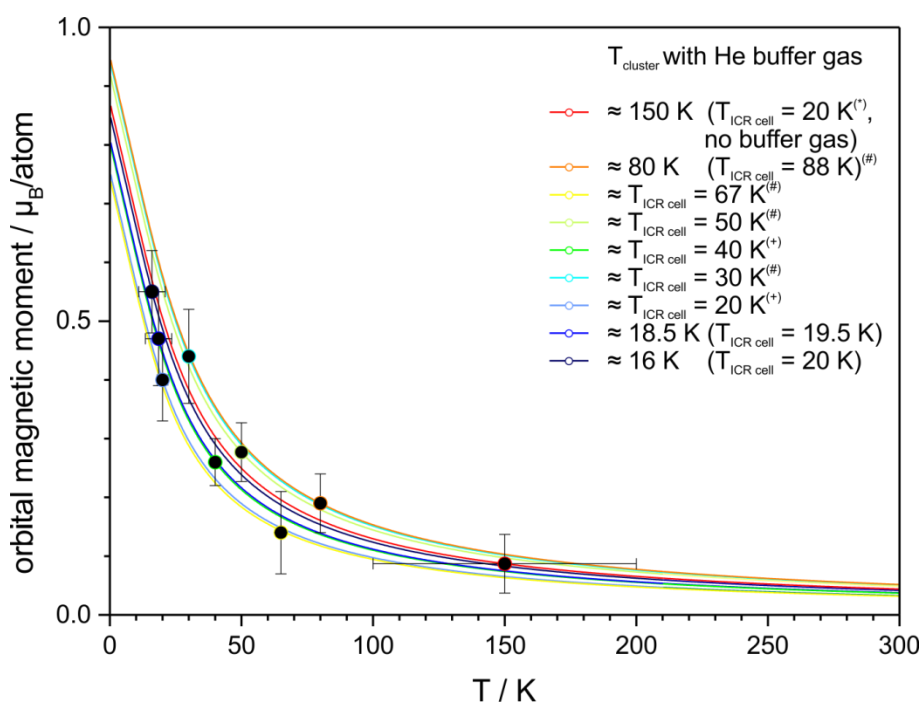


Figure A.24 Langevin scaling of the experimental orbital magnetic moment $m_{L,z}$ of individual temperature dependent experiments of Co_{11}^+ . The experimental orbital magnetic moments $m_{L,z}$ (solid symbols) are scaled to the intrinsic orbital magnetic moment m_L .

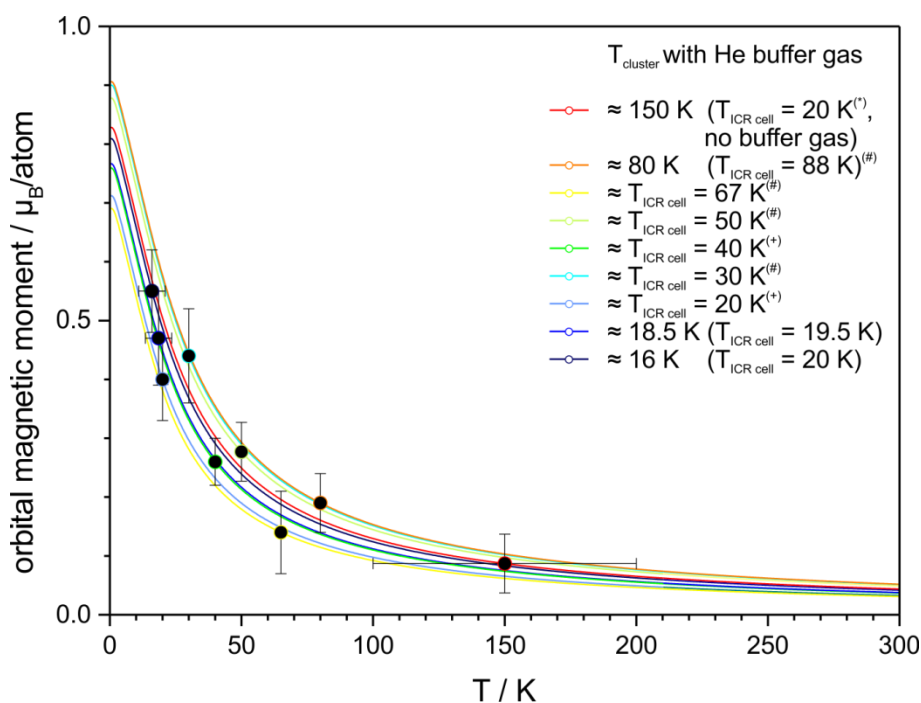


Figure A.25 Brillouin scaling of the experimental orbital magnetic moment $m_{L,z}$ of individual temperature dependent experiments of Co_{11}^+ . The experimental orbital magnetic moments $m_{L,z}$ (solid symbols) are scaled to the intrinsic orbital magnetic moment m_L .

The intrinsic magnetic moments after correction are given in Fig. A.26 - A.28. The intrinsic magnetic moments after Brillouin correction of m_j are displayed in Fig. A.26. The intrinsic moments after the individual scaling of $m_{S,z}$ and $m_{L,z}$ according to Langevin (Fig. A.27) or Brillouin (Fig. A.28) are also shown. The ratio of m_L / m_S after Brillouin scaling for both approaches is given in Fig. A.29.

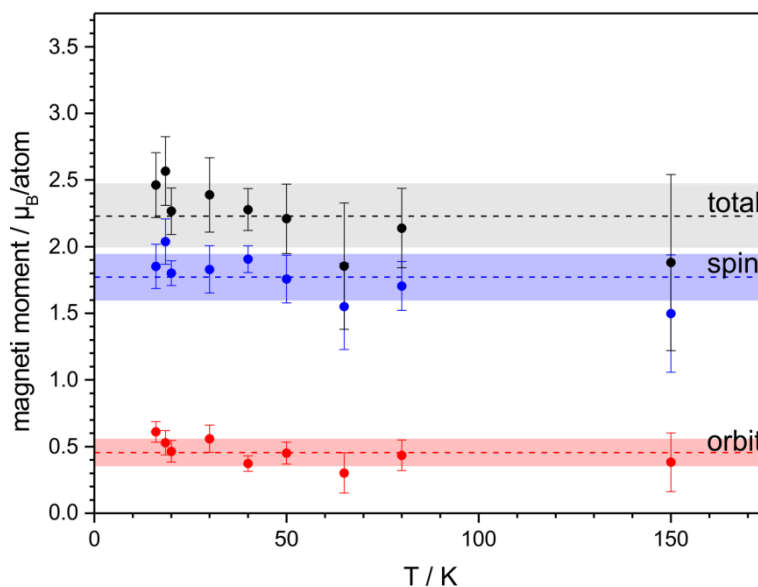


Figure A.26 Total magnetic moments m_j of Co_{11}^+ after Brillouin scaling of $m_{j,z}$ of the temperature dependent experiments

The scaling of the total magnetic moment preserves the ratio of $m_{L,z} / m_{S,z}$. Thus, the ratio of $m_{L,z} / m_{j,z}$ and $m_{S,z} / m_{j,z}$ respectively are preserved too and the values for m_S and m_L can be calculated from m_j .

The three dashed lines give the mean values of m_S , m_L and total m_j . The shaded area represents two times the standard deviation from the mean value ($\sigma(m_j) = 0.240$, $\sigma(m_S) = 0.168$, $\sigma(m_L) = 0.098$)

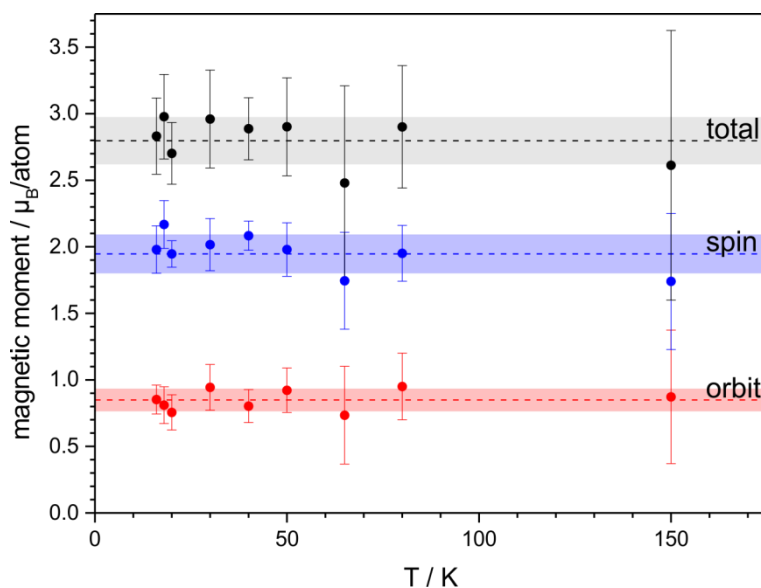


Figure A.27 Spin and orbital magnetic moments m_s and m_L of Co_{11}^+ after Langevin scaling of $m_{s,z}$ and $m_{L,z}$ of the temperature dependent experiments. The total magnetic moments m_j are calculated as the sum of m_s and m_L . The three dashed lines give the mean values of m_s , m_L and m_j . The shaded area represents the standard deviation from the mean value ($\sigma(m_j) = 0.172$, $\sigma(m_s) = 0.141$, $\sigma(m_L) = 0.080$).

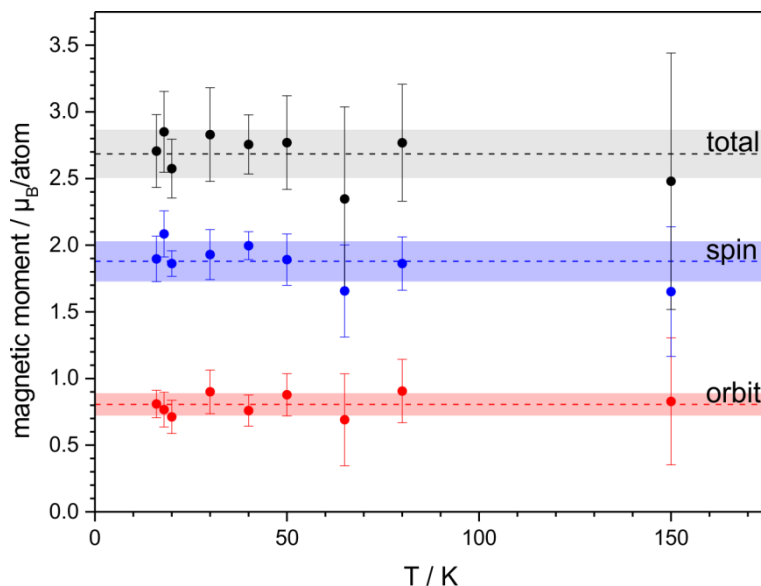


Figure A.28 Spin and orbital magnetic moments m_s and m_L of Co_{11}^+ after Brillouin scaling of $m_{s,z}$ and $m_{L,z}$ of the temperature dependent experiments. The total magnetic moments m_j are calculated as the sum of m_s and m_L . The three dashed lines give the mean values of spin, orbital and total magnetic moment. The shaded area represents the standard deviation from the mean value (2σ , with $\sigma(m_j) = 0.176$, $\sigma(m_s) = 0.146$, $\sigma(m_L) = 0.079$).

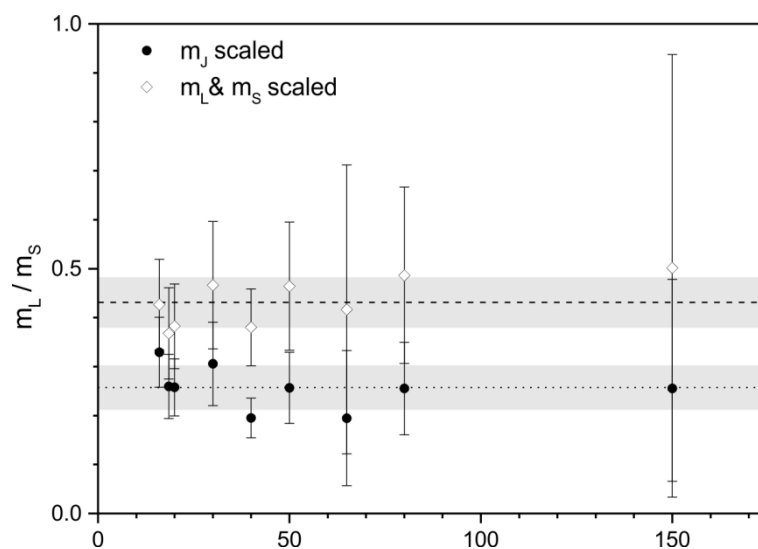


Figure A.29 Ratio of orbital to spin magnetic moment m_L / m_S after Brillouin correction

If m_j is scaled the m_L / m_S ratio is the same as the $m_{L,z} / m_{S,z}$ ratio (solid symbols; the dotted line gives the mean value and the shaded area is two times the standard deviation, $\sigma = 0.044$). If spin and orbital magnetic moments are scaled independently the m_L / m_S ratio differs from the $m_{L,z} / m_{S,z}$ ratio (open symbols; the dashed line gives the mean value and the shaded area is two times the standard deviation, $\sigma = 0.050$).

A.3 List of symbols

A	vector potential
A	integral dichroic effect at the L ₃ edge
A	prefactor ($= 2\pi^2\alpha_r\hbar\omega$)
<i>a</i>	lattice parameter
a⟩	electronic ground state
B	magnetic induction, magnetic flux density; [B] = T
B	integral dichroic effect at the L ₂ edge
$\frac{\partial B}{\partial z}$	magnetic field gradient
B(γ)	Brillouin function
b⟩	excited electronic state
C	integral intensity of ($\mu^+(E)+\mu^-(E)$), corrected for direct photo ionization
C	Curie constant
$C_m^{(l)}$	Racah's spherical tensor operators / normalized spherical harmonics operator
<i>c</i>	orbital angular momentum quantum number of the core state
<i>c</i>	velocity of light
d_{Nb}	Nb-Nb distance
$10Dq$	crystal field splitting an octahedral ligand field
<i>d</i>	deflection
$E_{anisotropy}$	anisotropy energy within a single domain particle energy barrier between the two preferential orientations of the sample magnetization
<i>e</i>	elementary charge
f⟩	final combined electron and photon state
E	energy
ΔE	average energy level spacing
E_a	electron affinity
E_F	Fermi level
E_{hv}	photon energy
E_{bin}	binding energy
E_{kin}	kinetic energy
E_{mag}	magnetic dipolar interaction

$e_{\alpha,p}^q$	coefficients (angular part of the transition matrix elements expressed by Racah's spherical tensor operators)
F_{cf}	Centrifugal force
F_L	Lorentz Force
f_c	cyclotron frequency
g	g-factor, spectroscopic splitting factor
g	Landé g-factor
g'	magnetomechanical ratio
g_L	Landé g-factor of the orbital angular momentum
g_S	Landé g-factor of the spin angular momentum
g_J	Landé g-factor of the total angular momentum
H	magnetic field strength; $[H] = m/A$
\hat{H}_{int}	interaction Hamiltonian for resonant x-ray absorption
h	Planck's constant
\hbar	Planck's constant / 2π
I_{res}	resonance intensity
$ i\rangle$	combined initial electron and photon state
J	angular moment per unit volume
J	total angular moment; $J = L + S$
J_z	projection of J on the quantization axis z
J	exchange energy per atom
J_{exch}	exchange energy between 3d electrons
j_+ / j_-	spin orbit split states ($j_{+/-} = l \pm s$)
K	absorption edge corresponding to an excitation from the 1s state
k	wave vector
k_B	Boltzmann constant
$l (L)$	(total) orbital angular momentum quantum number
l	orbital angular momentum quantum number of the final state
I_p	ionization potential
L	orbital angular momentum
L_z	projection of L on the quantization axis z
$L(y)$	Langevin function
L_2	absorption edge corresponding to the $2p_{1/2} \rightarrow 3d$ transition
L_3	absorption edge corresponding to the $2p_{3/2} \rightarrow 3d$ transition
M	magnetization

M	transition matrix element
M_4	absorption edge corresponding to the $3d_{3/2} \rightarrow 4f$ transition
M_5	absorption edge corresponding to the $3d_{5/2} \rightarrow 4f$ transition
m	ion mass
m_e	electron mass
m	magnetic moment
$m_x(n)$	size dependent magnetic moment
$m_c(m_l)$	orbital magnetic quantum number of the core (final) state
m_J	total magnetic moment
$m_{J,z}$	total magnetic moment projected onto the quantization axis
m_l	orbital magnetic quantum number
m_L	orbital magnetic moment
$m_{L,z}(m_L^{(z)})$	orbital magnetic moment projected onto the quantization axis
m_s	spin magnetic quantum number
m_S	spin magnetic moment
$m_{S,z}(m_S^{(z)})$	spin magnetic moment projected onto the quantization axis
m_L / m_S	ratio of orbital to spin magnetic moment
m/z	mass-to-charge ratio
$n(N)$	number of particles or atoms per cluster
$N(E)$	density of states
$N(E_F)$	density of states at the Fermi level
n	principal quantum number
n_h	number of holes in the valence shell
O_h	point group, distorted octahedral symmetry
P_α^q	dipole operator
p	momentum operator
p	pressure
q	photon angular momentum; $[q] = \hbar$
q	ion charge; $q = z \cdot e$
R	radius of a spherical droplet
R	radial part of the transition matrix element
$R_{n,l}(r)$	radial part of the electron wavefunction
r	length operator
r	radius of the ion orbit within the ICR cell
r	(interatomic) distance

r_{AB}	interatomic distance
r_d	radius of the 3d shell
r_{WS}	Wigner-Seitz radius
S	total spin angular momentum quantum number
S_z	projection of S on the quantization axis z
s	spin angular momentum quantum number
T	temperature
T_B	blocking temperature
T_C	Curie temperature
$T_{cluster}$	cluster temperature
$T_{ICR\ cell}$	readout of the temperature sensor located at the ICR cell
T_{if}	transition probability per unit time for resonant x-ray absorption
$\langle T_z \rangle$	magnetic dipole term
v_x	velocity of the ion in the x-direction
v_{xy}	velocity of the ion in the xy-plane
W_{solid}	bulk work function
$Y_{l,m}(\vartheta, \phi)$	Spherical Harmonics
z	number of charges
z	quantization axis
α	quantization axis in Cartesian coordinates; $\alpha = x, y$ or z
α_f	fine structure constant
α_N	cluster polarizability
γ	gyromagnetic ratio
γ	surface tension of spherical droplet
$\delta(E_F)$	exchange splitting of the spin up and spin down band
δ_n	autoionization resonance energy
$\boldsymbol{\epsilon}$	unit photon polarization vector
ϵ_{coh}	cohesive energy
ϵ_0	dielectric constant
ϵ_i	energy level of the initial state
ϵ_f	energy level of the final state
λ	wavelength; $[\lambda] = \text{nm}$
λ_0	period length of the magnetic array of an undulator
Θ	angle enclosed by a magnetic moment \mathbf{m} and an external magnetic field \mathbf{H}
Θ	angle between the magnetization and the easy axis

Θ_N	Néel temperature
μ_B	Bohr magneton: magnetic moment of the electron
μ_r	relative magnetic permeability
μ_0	magnetic permeability of free space
μ_1, μ_2	magnetic dipole
$\mu^0 (E)$	XA spectrum recorded with horizontally (linearly) polarized photons
$\mu^- (E)$	XA spectrum recorded with negative circularly polarized photons
$\mu^+ (E)$	XA spectrum recorded with positive circularly polarized photons
ν	photon frequency
$\rho(\epsilon_f)$	density of final states per unit energy
σ	standard deviation
$\sigma^0 (E)$	horizontally (linearly) polarized photons
$\sigma^- (E)$	negative circularly polarized photons
$\sigma^+ (E)$	positive circularly polarized photons
ϕ	work function
ϕ	Fibonacci number = 1.618
χ	magnetic susceptibility
$\chi^{\text{collective}}$	magnetic susceptibility of material exhibiting collective magnetism
χ^{dia}	diamagnetic susceptibility
χ^{Langevin}	susceptibility of Langevin-Paramagnetism
χ^{Pauli}	susceptibility of Pauli-Paramagnetism
$\chi_{s,ms}$	spin part of the electron wave function
Ω_0	atomic volume
ω	photon frequency (= $2\pi \cdot \nu$)
ω	Larmor frequency, precession frequency of a magnetic moment around a magnetic field
ω_c	angular velocity of an ion in the ICR trap
ω_r	resonance frequency of a spherical metal cluster

A.4 List of publications & conference contributions

A.4.1 Publications

X-ray absorption spectroscopy of mass-selected transition metal clusters using a cyclotron ion trap:

An experimental setup for measuring XMCD spectra of free clusters

PEREDKOV, S., SAVCI, A., PETERS, S., NEEB, M., EBERHARDT, W., KAMPSCHULTE, H., **MEYER, J.**, TOMBERS, M.,
HOFFERBERTH, B., MENGES, F., NIEDNER-SCHATTEBURG, G.

Journal of Electron Spectroscopy and Related Phenomena **2011**, *184*, 113.

<http://www.sciencedirect.com/science/article/pii/S0368204810003026>

Spin and orbital magnetic moments of free nanoparticles

PEREDKOV, S., NEEB, M., EBERHARDT, W., **MEYER, J.**, TOMBERS, M., KAMPSCHULT, H., NIEDNER-SCHATTEBURG, G.,
Physical Review Letters **2011**, *107*, 233401

<http://link.aps.org/doi/10.1103/PhysRevLett.107.233401>

Synthesis and Characterization of a Potential Anti-Cancer Candidate, MTX-Gelonin Conjugate

BADR, M., KOPP, CH., THEISON, S., **MEYER, J.**, TROMMER, W.

Biological Chemistry **2014**, accepted

Atomic and electronic structure of free niobium nanoclusters: simulation of the $M_{4,5}$ -XANES spectrum of Nb_{13}^+

KRAVTSOVA, A., LOMACHENKO, K., SOLDATOV, A., **MEYER, J.**, NIEDNER-SCHATTEBURG, G., PEREDKOV, S.,
EBERHARDT, W., NEEB, M.

Journal of Electron Spectroscopy and Related Phenomena, **2014**, accepted,
DOI: 10.1016/j.elspec.2014.07.005

<http://www.sciencedirect.com/science/article/pii/S0368204814001534>

The spin and orbit contributions to the total magnetic moments of free Fe, Co and Ni clusters

MEYER, J., TOMBERS, M., NIEDNER-SCHATTEBURG, G., PEREDKOV, S., EBERHARDT, W., NEEB, M., PALUTKE, S.,
MARTINS, M., WURTH, W.

Journal of Chemical Physics, **2014**, in preparation

A.4.2 Conference contributions

A.4.2.1 Talks

April 2014 "Magnetic properties of transition metal clusters and complexes probed by XMCD spectroscopy"

Gordon Research Seminar (GRS) on "Molecular and Ionic Clusters", Barga, Italy

- Oct. 2012 "Spin and orbital magnetic moments of isolated transition metal oligomers
International Workshop on Metal-to-Metal communications in Oligonuclear Complexes, Meeting of the Collaborative Research Center TRR 88 / 3MET, TU Kaiserslautern, Kaiserslautern, Germany
- Aug. 2012 "X-ray magnetic circular dichroism spectroscopy of transition metal clusters"
Meeting of the "3MET" magnetism section, TU Kaiserslautern, Kaiserslautern, Germany
- July 2012 "X-ray magnetic circular dichroism spectroscopy of transition metal clusters"
Meeting of the "3MET" gas phase group, Karlsruhe Institute of Technology, Karlsruhe, Germany
- April 2012 "X-ray magnetic circular dichroism spectroscopy of transition metal clusters"
Workshop OPTIMAS Carl Zeiss PhD Programm, Annweiler, Germany
- Feb. 2012 "Spin and Orbital moments of isolated clusters: Synchrotron radiation elucidates nanomagnetism" (HotTopic)
Gordon Research Conference (GRC) on "Molecular and Ionic Clusters", Ventura, CA, USA
- March 2011 "Spin and orbit moments of super paramagnetic cobalt clusters from XMCD
Investigation of isolated ions by the GAMBIT experiment"
Spring Meeting of the German Physical Society (DPG) - "Atom and Molecular Physics" section, Dresden, Germany

A.4.2.2 Poster presentations

- April/May 2014 GRS & GRC on "Molecular and Ionic Clusters", Barga, Italy
- Feb. 2012 GRC on "Molecular and Ionic Clusters", Ventura, CA, USA
- Nov/Dez 2011 HZB User's Meeting, Helmholtz Zentrum Berlin für Materialien und Energie, Berlin, Germany
- Oct. 2011 Workshop of the Collaborative Research Center TRR88/3MET, Bad Bergzabern, Germany

July 2011	GRC on "Clusters, Nanostructure & Nanocrystals", South Hadley, MA, USA
June 2011	Annual Meeting of the German Bunsensociety of Physical Chemistry, Berlin, Germany
Dec. 2010	HZB User's Meeting, Helmholtz Zentrum Berlin für Materialien und Energie, Berlin, Germany

A.5 Danke

Herrn Prof. Gereon Niedner-Schatteburg möchte ich für die Betreuung, die gute Zusammenarbeit und den mir eingeräumten Freiraum während meiner Promotion danken.

Herrn Prof. Markus Gerhards danke ich für die Übernahme des Zweitgutachtens und Prof. Werner Thiel danke ich für die Übernahme des Prüfungsvorsitzes.

Danke an Matthias Tombers für's gemeinsame Leiden, Durchhalten und manchmal auch Jubeln an der Beamline zu allen Tages und Nachtzeiten.

Sergey Peredkov möchte für die Wissensweitergabe, das gemeinsame Durchhalten während der Strahlzeiten und die stete Hilfsbereitschaft danken.

Matthias Neeb möchte ich für organisatorische Unterstützung vor Ort bei BESSY und die zahlreichen wissenschaftlichen Diskussionen danken.

Der "alten Garde" Lars Barzen, Christine Merkert, Fabian Menges, Anita Röthke, Britta Pfeffer, Stephanie Jaberg und Heinrich Kampschulte danke ich für die Hilfe beim Einstieg in die physikalische Chemie und die Weitergabe von Wissen und wertvollen Tipps und Tricks.

Ein besonderes Danke geht an Lars für die stete Hilfsbereitschaft und Lösung von PC-Problemen und die unzähligen Telefonate, die uns in Berlin nicht vereinsamen ließen.

Christine danke ich für die schöne gemeinsame Zeit in unserem Büro, wenn ich denn mal da war.

Allen aktuellen Mitgliedern des Arbeitskreises GNS die zur freundlichen Atmosphäre im Arbeitskreis beitragen: Matthias Tombers, Thomas Kolling, Jennifer Mohrbach, Johannes Lang, Maximilian Gaffga, Joachim Hewer, Sebastian Dillinger, Jonathan Meyer, Yvegeni Nosenko, Dimitri Imanbaev, Sebastian Kruppa und Christoph Rhien.

Jennifer Mohrbach, Joachim Hewer, Anke Stamm, Markus Becherer, Steffen Palutke, Ivan Baev, Denins Dielemann, Jeroen Jalink, Arkadiusz Ławicki, Vicente Zamundio-Bayer möchte für die Unterstützung während diversen Strahlzeiten danken. Tobias Lau möchte ich für die Möglichkeit danken, den NanoClusterTrap Aufbau nutzen zu können.

Ein Danke geht an das BESSY Personal für die Unterstützung an der Beamline und Hilfe bei Problemen aller Art. Ein besonderer Dank geht an Patrick Hofmann, Stefan Krause und Ruslan Ovsyannikov für Einführung in die Beamline und Unterstützung wenn's mal wieder "brannte".

Ein Danke geht an alle die in irgendeiner Weise am GAMBIT Projekt beteiligt waren und nicht namentlichen erwähnt sind.

Den Mitarbeitern in der Metall- und Elektronikwerkstatt (in Kaiserslautern und am BESSY) danke ich für die vielen beratenden Gespräche und die unkomplizierte Hilfe, wenn's mal wieder eilig war.

Danke, an alle aktuellen und ehemaligen Mitglieder der physikalischen und theoretischen Chemie für die schönen und lustigen Stunden im Kaffeezimmer.

Sebastian Schmidt und Valeriu Mereacre von der Gruppe von Annie Powell (KIT) möchte ich für die Bereitstellung der Einzelmolekülmagnete danken.

Ein besonderer Dank gilt unseren guten Seelen Hilde Seelos, Sibylle Heieck und Inge Krull im Sekretariat der physikalischen und theoretischen Chemie und allen übrigen guten Seelen, auch dem Team der Nutzerbetreuung / Pforte / Gästehaus bei BESSY, die fast immer alles möglich machten.

Danke an alle meine Freunde für die Unterstützung während der letzten Jahre. Ein ganz ganz großes Danke geht an Christiane Lohr, dafür das sie immer ein offenes Ohr, aufmunternde Worte und Zeit für mich hatte.

Danke an meine Familie und ganz besonders an meine Eltern für die Unterstützung, aufmunternde Worte und daran dass sie immer an mich geglaubt haben.

Eine Dankesliste kann nie vollständig sein, daher gilt dieser Abschnitt allen denjenigen, die sich nicht in der obigen Liste wiederfinden, weil ich sie übersehen oder vergessen habe. Fühlt euch an dieser Stelle gedankt.

A.6 Curriculum Vitae

Dipl.-Chem. Jennifer Meyer

email: jdmeyer@chemie.uni-kl.de

- Nov. 2009 - July 2014 TU Kaiserslautern, Dep. of Chemistry, Kaiserslautern, Germany
Doctoral thesis in the group von Prof. Dr. G. Niedner-Schatteburg
Topic: "Spin and orbital contributions to the magnetic moment of transition metal clusters and complexes" (grade "*summa cum laude*")
- April 2009 - Nov. 2009 TU Kaiserslautern, Dep. of Chemistry, Kaiserslautern, Germany
Diplomathesis in the group of Prof. Dr. G. Niedner-Schatteburg
Topic: " Inbetriebnahme einer Laserverdampfungsquelle mit "pick up" Einheit & Reaktionen kationischer Tantalcluster mit kleinen Kohlenwasserstoffen" (grade: 1.0)
- Sep. 2008 - Feb. 2009 Johns Hopkins University / Department of Chemistry, Baltimore, MD, USA
study abroad program
- Oct. 2004 - Nov. 2009 TU Kaiserslautern, Dep. of Chemistry, Kaiserslautern, Germany
Diploma in Chemistry (overall grade 1.0)
- Aug. 1997 - March 2004 Priv. St. Josef Gymnasium Biesdorf, Biesdorf, Germany
German Abitur (overall grade 1.2)
- Aug. 1995 - June 1997 "Orientierungsstufe für Realschule und Gymnasium der Otto-Hahn Realschule und des St. Willibrod Gymnasiums", Bitburg, Germany

Internships

- Sep. 2008 - Feb. 2009 Johns Hopkins University / Department of Chemistry, group of Kit Bowen, Baltimore, MD, USA
UV photo electron spectroscopy
- May 2008 - Aug. 2008 TU Kaiserslautern, Dep. of Physics, group of Martin Aeschlimann
photo emission electron microscopy (PEEM)

July 2004 - Sep. 2004 Bitburger Braugruppe GmbH, Abteilung Technische Qualitätskontrolle, Bitburg
summer job, Analytics

Research visits

04. Aug. - 23. Aug. 2013 @ Universität Innsbruck, group of Paul Scheier, Innsbruck, Österreich

Sep. 2008 - Feb. 2009 @ Johns Hopkins University, group of Kit Bowen, Baltimore, MD, USA

May 2009 @ Centre Laser Infrarouge d'Orsay (CLIO), Université de Paris Sud, Frankreich,
EPITOPES Project

Feb. 2008 @ Centre Laser Infrarouge d'Orsay (CLIO), Université de Paris Sud, Frankreich,
EPITOPES Project

All experiments conducted within the GAMBIT project (Generalized abstraction of magnetic moments by ion trapping at BESSY) need polarized synchrotron radiation and were carried out at the undulator beamline UE52-PGM at the synchrotron BESSY II (Helmholtz Zentrum Berlin für Materialien und Energie, Berlin, Germany).

Eidesstattliche Erklärung

Hiermit bestätige ich, Jennifer Meyer, dass die vorliegende Arbeit gemäß der Promotionsordnung des Fachbereichs Chemie der Technischen Universität Kaiserslautern selbständig und unter der Verwendung der angegebenen Quellen und Hilfsmittel angefertigt wurde.

Kaiserslautern, im Juni 2014
